

JAERI-M  
85-104

JAERI TANDEM, LINAC & V.D.G.  
ANNUAL REPORT

1984

April 1, 1984 — March 31, 1985

July 1985

Department of Physics

日 本 原 子 力 研 究 所  
Japan Atomic Energy Research Institute

JAERI-Mレポートは、日本原子力研究所が不定期に公刊している研究報告書です。

入手の問合わせは、日本原子力研究所技術情報部情報資料課（〒319-11茨城県那珂郡東海村）あて、お申しこしてください。なお、このほかに財団法人原子力弘済会資料センター（〒319-11茨城県那珂郡東海村日本原子力研究所内）で複写による実費頒布をおこなっております。

JAERI-M reports are issued irregularly.

Inquiries about availability of the reports should be addressed to Information Division, Department of Technical Information, Japan Atomic Energy Research Institute, Tokai-mura, Naka-gun, Ibaraki-ken 319-11, Japan.

© Japan Atomic Energy Research Institute, 1985

---

編集兼発行	日本原子力研究所
印刷	日立高速印刷株式会社

JAERI TANDEM, LINAC & V.D.G.  
Annual Report  
1984

April 1, 1984 - March 31, 1985

Department of Physics  
Tokai Research Establishment, JAERI

( Received June 26, 1985 )

This annual report describes research activities which have been performed with the JAERI tandem accelerator, the electron linear accelerator and the Van de Graaff accelerator from April 1, 1984 to March 31, 1985. Summary reports of 53 papers, publications, personnel and a list of cooperative researches with universities are contained.

Keywords: JAERI TANDEM, e-LINAC, V.D.G., Atomic & Solid State Physics, Material Science, Nuclear Chemistry, Nuclear Physics, Neutron Physics, Annual Report

Editors    Naomoto Shikazono  
            Masashi Iizumi  
            Mitsuhiko Ishii  
            Yuuki Kawarasaki  
            Michio Maruyama  
            Hiroshi Okashita  
            Kunio Ozawa  
            Yoichi Suto

原研タンデム，リニアック，バンデグラフ加速器59年度年次報告

日本原子力研究所東海研究所物理部

(1985年6月26日受理)

本年次報告は，原研タンデム，リニアック及びバンデグラフ加速器で，1984年4月1日から1985年3月31日までの間に東海研で行われた研究活動を取りまとめたものである。

1) 加速器運転と開発研究，2) 原子及び固体物理，3) 材料の放射線損傷，4) 核化学，5) 核物理 及び6) 中性子物理の6部門にまたがる53編の研究報告，公表された文献，関与した職員及び大学との協力研究のリストを収録している。

---

(編集者) 鹿園 直基・飯泉 仁・石井 三彦・河原崎雄記・丸山 倫夫・岡下 宏・小沢 国夫・  
須藤 洋一



Insulating Column Structure in the  
Tandem Pressure Vessel

PREFACE

This annual report covers the research works performed with the tandem accelerator, the electron linear accelerator and the Van de Graaff accelerator during the period from April 1, 1984 to March 31, 1985. All the accelerators were in good condition during the past one year as before.

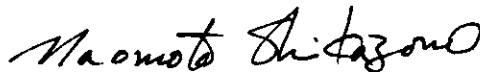
A majority of the research works have been carried out with heavy ions accelerated by the tandem accelerator. The electron linear accelerator has been used mainly for measurements of neutron cross sections in the medium energy region. Some works on atomic and solid state physics have been carried out at the Van de Graaff accelerator.

The subjects of our research activities are as follows:

- 1) Atomic and solid state physics
- 2) Radiation effects in materials
- 3) Nuclear chemistry
- 4) Nuclear physics
- 5) Neutron physics.

In the period, more than 70 staff members of JAERI have worked in the five fields of researches, and about 100 colleagues of universities and institutions outside JAERI have joined and collaborated in these studies. Some theoretical studies related to the subjects and the developments in the accelerator technology including a preliminary study of a superconducting cavity for a tandem booster are also reported.

A joint seminar on atomic physics, solid state physics and material science in the energy region of tandem accelerators was held at Tokai Research Establishment of JAERI, January 9-11, 1985 and several experimental results described in this annual report were presented in the seminar.



Naomoto Shikazono  
Director,  
Department of Physics

## CONTENTS

I	ACCELERATOR OPERATION AND DEVELOPMENT .....	1
1.1	Tandem Accelerator Operation .....	3
1.2	An Extension to the 350 kV Negative Ion Injector for the JAERI Tandem Accelerator .....	5
1.3	Production and Acceleration of Tellurium and Nitrogen Ions at the JAERI Tandem Accelerator .....	8
1.4	Control System for JAERI Tandem Accelerator .....	10
1.5	Development of Ion Optics Computer Code .....	13
1.6	Development of Superconducting RF Cavity for Heavy Ion Booster .....	16
1.7	Electron Linac Operation and Improvements .....	19
II	ATOMIC AND SOLID STATE PHYSICS .....	23
2.1	Beam-Foil Spectra of Chlorine Ions in High Energy Region (II) .....	25
2.2	Ion Beam Analysis on Nb-Mo Alloy with Energetic Heavy Ions .....	29
2.3	Defect Production and Recovery in Copper Irradiated with Energetic Ions .....	33
2.4	Transmission Sputterings of Molybdenum and Silver by High-Energy Heavy Ions .....	37
2.5	The Preliminary Study with the Light Scattering Equipment .....	41
2.6	Measurement of Mean Projected Ranges of High Energy Ions .....	45
2.7	Molecular Effect of O and Al K $\alpha$ X-Ray Yields from Al <sub>2</sub> O <sub>3</sub> Films for H <sup>+</sup> and H <sub>2</sub> <sup>+</sup> Ions .....	49
2.8	Deuterium Retention in TiC Crystals Prepared by Zone Melting Methods .....	53
2.9	Ion Beam Analysis on $\alpha$ -SiC Crystal Irradiated with Ar Ions .....	58
2.10	Computer Simulation Study of Low Energy Radiation Damage in Molybdenum .....	62
2.11	Electron Capture and Loss Cross Sections for 300 keV to 1.50 MeV Carbon Atoms in Collision with Helium .....	66
2.12	Characteristics of Gas Stripper Cell for Production of Multi-Charged Ions .....	70
III	RADIATION EFFECTS IN MATERIALS .....	75
3.1	Irradiation Effects with Heavy Ions on Alkali Halides (II) .....	77
3.2	Irradiation Damage in Lithium Oxide .....	81

3.3	IR, UV and ESR Studies of Polyvinylidene Fluoride Irradiated with Heavy Ions .....	87
3.4	Residual Radioactivities in Silicon and Germanium Irradiated with Various High-Energy Heavy-Ions .....	89
3.5	X-Ray Diffraction Topographic Observation of Silicon Single Crystals Irradiated with Energetic Heavy Ions .....	93
3.6	Radiation Damage of Materials Ion-Irradiated at Low Temperature .....	97
3.7	Track Formation in Evaporated Films of Germanium, Silicon and Titanium .....	100
3.8	TEM Observation of Cascade Damage Structure in Pure Nickel .....	104
3.9	Irradiation Induced Defects of Dual Phase (Austenite and Ferrite; Duplex) Stainless Steel .....	105
3.10	Near Surface Modification of $\alpha$ -Al <sub>2</sub> O <sub>3</sub> by Nb Implantation .....	106
3.11	Temperature Dependence of Damage Profile in Helium-Irradiated Stainless Steel .....	110
3.12	Effect of Solute Carbon Content on the Distribution of Helium Bubble and Dislocation Loop in Ti-Modified Type 316 Stainless Steels Irradiated with Helium Ions .....	114
3.13	Microstructural Evolution in N Ion Irradiated Stainless Steel ..	118
3.14	Damage Structure in Ion-Irradiated Si <sub>3</sub> N <sub>4</sub> .....	122
3.15	Irradiation Effect with Light Ions on Some Ceramics and Glasses .....	124
IV	NUCLEAR CHEMISTRY .....	127
4.1	Nuclear Chemistry of Actinoids (III) $^{16}\text{O} + ^{238}\text{U}$ and $^{12}\text{C} + ^{242}\text{Pu}$ Reactions .....	129
4.2	Decay of the Compound Nuclei Produced in the Reactions of $^{197}\text{Au}$ Induced by $^{16}\text{O}$ and $^{12}\text{C}$ .....	132
4.3	Nucleon Transfer Reaction of Gold Induced by Heavy Ions .....	135
4.4	A Study of the Decay of $^{121}\text{Ba}$ .....	139
4.5	A Study of the Existence of the Low- $\ell$ Cutoff by Isomer-Ratio Measurement .....	143
4.6	Preparation of $^{237}\text{Pu}$ from $^{237}\text{Np}$ Irradiated with Deuterons .....	147
V	NUCLEAR PHYSICS .....	149
5.1	Studies of Nuclei with Proton and Neutron Numbers of 50 to 82 .....	151
5.2	Inclusive and Coincidence Measurements for Strongly Damped Reactions in the System $^{37}\text{Cl} + ^{48}\text{Ti}$ .....	155



5.3	Magnetic Substate Population in $^{12}\text{C} + ^{12}\text{C}$ Inelastic Scattering ...	159
5.4	Incomplete Fusion of the $^{16}\text{O} + ^{27}\text{Al}$ Reaction .....	163
5.5	A Study of Limiting Angular Momenta in Fusion Reaction.....	167
5.6	Pre-Equilibrium Emission of Light Particles in the Heavy Ion Reactions.....	171
5.7	Enhancement of Sub-Barrier Fusion Cross Section Due to Neck Formation .....	173
5.8	Low-Lying Isovector Collective States and the Interacting Boson Model .....	174
5.9	Renormalization of g-Boson Effects in the Interacting-Boson Hamiltonian .....	176
VI	NEUTRON PHYSICS.....	179
6.1	Scattering of 12.8 MeV Neutrons from $^{28}\text{Si}$ .....	181
6.2	Measurements of Fast Neutron Scattering Cross Sections of Aluminum	185
6.3	Neutron Resonance Parameters of $^{142}\text{Ce}$ .....	190
6.4	Neutron Capture and Transmission Measurements at a 55 m Station of the JAERI Linac.....	194
VII	PUBLICATIONS.....	199
7.1	Publications in Journals and Proceedings.....	201
7.2	Contributions to Scientific and Technical Meetings .....	208
VIII	PERSONNEL AND COMMITTEES.....	219
8.1	Personnel .....	221
8.2	Tandem Steering Committee .....	226
8.3	Tandem Consultative Committee .....	227
8.4	Tandem Program Advisory Committee .....	228
IX	CO-OPERATIVE RESEARCHES .....	229

# I ACCELERATOR OPERATION AND DEVELOPMENT

## 1.1 TANDEM ACCELERATOR OPERATION

## Tandem Accelerator Group

## Department of Physics, JAERI

Accelerator operation

The scheduled operation for experiments was performed through the past one year containing three short periods for the scheduled maintenance. The following are summary of the operation from April 1, 1984 to March 31, 1985.

## 1) Time distribution by terminal voltage

16-17 MV	28 days	19.2 %	10-11 MV	24 days	16.4 %
15-16	18	12.3	9-10	7	4.8
14-15	41	28.1	8- 9	1	0.7
13-14	9	6.2	7- 8	3	2.0
12-13	9	6.2	4- 5	4	2.7
11-12	2	1.4			

## 2) Time distribution by projectile

D	23 days	15.7 %	Ni	3 days	2.0 %
B	1	0.7	Se	1	0.7
C	19	13.0	Br	2	1.4
O	43	29.5	Te	1	0.7
F	3	2.0	I	2	1.4
Si	1	0.7	Au	2	1.4
S	20	13.7	Bi	1	0.7
Cl	24	16.4			

## 3) Time distribution by activity

Operation for research	149 days	40.8 %
Atomic and solid state physics	19	
Radiation effects in materials	19	
Nuclear chemistry	24	
Nuclear physics	52	
Fast neutron physics	24	
Accelerator development	11	
Voltage conditioning	40	11.0
Operation training	6	1.6
Scheduled maintenance (3 tank openings)	102	28.0
Unscheduled repair (1 tank opening)	7	1.9
Holidays and vacation	61	16.7

Tank openings

The accelerator was opened three times for the scheduled maintenance and once for the unexpected repair in the period.

## 1) May 9-June 21, 1984

Scheduled maintenance.

Improvement of the negative ion injector.

## 2) July 17-23, 1984

Unscheduled repair. Repair of the mechanical joint between the rotating shaft and the 10 KVA terminal generator.

## 3) October 12-November 6, 1984

Scheduled maintenance.

Trial of the hydrogen discharge cleaning for the accelerating tubes in the lowest 7 MV modules.

Repair of the mechanical joint between the rotating shaft and the 15 KVA terminal generator.

## 4) February 22-March 26, 1985

Scheduled maintenance.

The second hydrogen discharge cleaning for the accelerating tubes in the lowest 7 MV modules.

Improvement and development

The 350 KV negative ion injector was improved to perform simultaneous operation of the plural ion sources, to ensure reliable operation of the terminal devices, and to assure safety of maintenance crew in the terminal. It has been confirmed through the accelerator running after the improvement that these purposes were achieved as expected.

An automated control of the accelerator is being developed to save operator manpower and to offer more efficient machine times to experimentors. An automatic setting of the operating parameters is recently getting usable by the scaling method in which a desirable parameter set for new ion and energy is calculated from the stored reference parameter set.

The hydrogen discharge was tried to improve the voltage holding of the tubes. The discharge current, time, hydrogen pressure and flow rate were 8 A, 5 hours, .03 Torr and .1 atm·cm<sup>3</sup>/sec, respectively. In the 2nd trial, lower current 2.5-5.5A and higher flow rate .25 atm·cm<sup>3</sup>/sec were used. The tube conditioning has been intermittently carried out through the scheduled running. Any definite result, however, has not been got yet.

## 1.2 AN EXTENSION TO THE 350KV NEGATIVE ION INJECTOR FOR THE JAERI TANDEM ACCELERATOR

Eisuke MINEHARA, Tadashi YOSHIDA, Shinichi ABE,  
Shuhei KANAZAWA, Katsuzo HORIE, Yoshihiro TSUKIHASHI  
and Susumu HANASHIMA

Accelerators Division, Department of Physics, JAERI

We have accelerated various heavy ions for a very short interval of about one or two days on the average during the scheduled operation. Such runnings of the ion sources forced us to start them up rapidly and to cool them down suddenly, and resulted in frequent malfunctionings, short lifetimes, lesser current intensities, and instabilities of the ion sources. In addition, reliability of all devices in the 350 KV negative ion injector had not been satisfied, and personal safety of the operation crew had not been insured completely in the injector platform since the installation of the accelerator.

In order to remove these defects, an extension to the injector has been constructed and tested recently.<sup>1)</sup>

Purpose of the extension is described as follows:

- (1) to increase reliability of all devices in the injector,
- (2) to exclude completely any unsafe operation in the injector, and
- (3) simultaneous operation of plural ion sources.

In order to realize these three items, we added another high voltage platform, developed several devices and improved most of devices used in the old injector. The extended injector was arranged in the ion source room as illustrated in fig. 1.

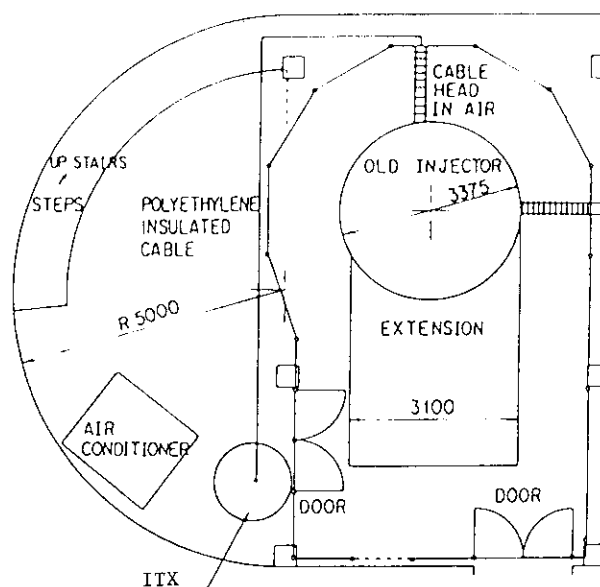


Fig. 1 Arrangement of the extension, old injector, isolation transformer in the ion source room.

What we had done are as follows:

- (1) a platform having about  $9\text{m}^2$  rectangular area added to the circular old platform as shown in fig. 2,
- (2) an epoxy resin and  $\text{SF}_6$  gas insulated high voltage isolation transformer (ITX) as shown in fig. 3,
- (3) electrostatic shielding sheets, cages and ducts against high voltage racks, the ion sources and high voltage cables,
- (4) an independent set of turbomolecular vacuum pump station for each ion source beam line,
- (5) an independent set of high voltage and low voltage power supplies for each ion source,
- (6) four independent sets of ion source gas metering system, and a warning and absorbing system of poisonous gas, and
- (7) expansion of control system for simultaneous running of the four ion sources.

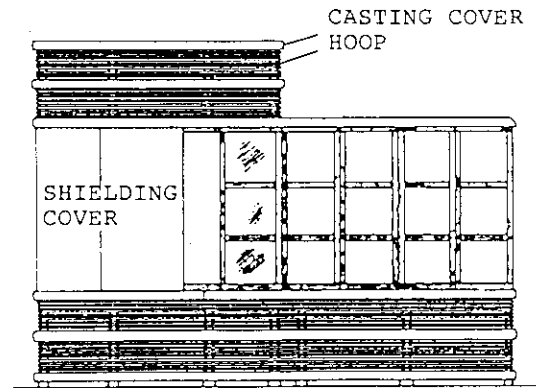


Fig. 2 Extended injector.

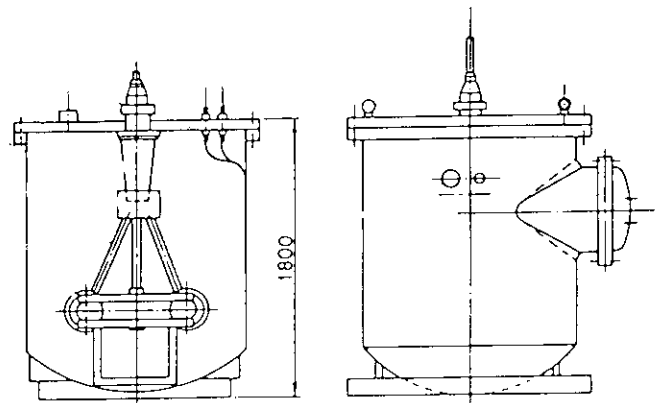


Fig. 3 Epoxy resin and  $\text{SF}_6$  gas insulated high voltage isolation transformer.

The maximum voltage of the improved injector was observed to be 300 KV, and it was confirmed that the new configuration of the injector did not deteriorate the voltage performance seriously. The ITX has been working with no trouble since the installation. The vacuum system has been working continuously with no trouble for about one year. Before the expansion of the injector control system, its reliability and accuracy were not satisfactory. Now we can read and control precisely all parameters. All devices at high voltage were completely covered with grounded metal sheets or ducts, or plastic sheets except for the ion sources. Therefore, we could greatly reduce the possibilities that the operation crew working on the platform were seriously

injured by receiving electric shocks.

we are using three negative ion sources (a negative sputter source, a heinicke penning source with radial extraction, and a direct extraction duoplasmatron source). Even when one of the ion sources feeds ion beams to the accelerator, we can tune the others. Thus, it takes only a few minutes to switch ion sources with enough and stable current. As it has not been necessary to prepare and to tune them up rapidly, the ion sources condition have been usually experienced to be very stable. Available currents of most ions have been recently found to become several tens % to a few hundred % higher than before. The interval of the ion sources became longer to some extent than before. After the extended injector became available, we have been able to run the whole injector system very steadily, and have had few troubles concerning about the items of extension.

Reference:

- (1) E. Minehara, T. Yoshida, S. Abe, S. Kanazawa, S. Hanashima, K. Horie and Y. Tsukihashi: Proc. 5th Symp. on Accelerator Science and Technology, Tsukuba, Ibaraki, September 26-28, 1984, pp. 422-424.

### 1.3 PRODUCTION AND ACCELERATION OF TELLURIUM AND NITROGEN IONS AT THE JAERI TANDEM ACCELERATOR

Eisuke MINEHARA, Tadashi YOSHIDA, Shinichi ABE,  
Shuhei KANAZAWA, Chiaki KOBAYASHI, Susumu KANDA  
and Susumu HANASHIMA

Accelerators Division, Department of Physics, JAERI

Ions of  $^{130}\text{Te}$  and  $^{14}\text{N}$  have been successfully accelerated by the JAERI tandem accelerator. Negatively charged atomic and molecular ions of them were obtained from a negative ion sputter source (NISS as an abbreviation) and a Heinicke penning ion source with radial extraction (HPIG), respectively. Details of the ion sources were already reported in the previous papers.<sup>1,2)</sup>

Powder cones of ZnTe, CdTe and PbTe which were fabricated by using cellulose binders were tested and found to be usable. The cone of PbTe was applied to accelerate a Te ion beam. Several kinds of gas mixtures containing carbon and nitrogen were tested to know how much current of  $\text{CN}^-$  ion we could get from them, and how stable and how long they worked. A 66%  $\text{CF}_4$  and 34%  $\text{N}_2$  gas mixture was selected after this test, and applied to accelerate a nitrogen ion beam because this mixture is safer than other gas mixtures. As this gas mixture is not only nonflammable but also nonpoisonous in the contrary to the gas mixtures containing  $\text{CH}_4$  and  $\text{NH}_3$  gases, we can handle them very safely.

Typical results are shown in table 1 and 2. Table 1 contains typical parameters of the ion sources, negative ion currents and ion source materials. Typical beam current, final energy, charge state and so on are summarized in table 2.

#### References

- 1) E. Minehara, S. Abe, C. Kobayashi and S. Kikuchi: Proc. 4th Symp. on Ion Sources and Ion Application Technology, Tokyo, June 24-26, 1981, p. 261.
- 2) S. Abe, E. Minehara, C. Kobayashi and S. Kikuchi: Proc. 6th Symp. on Ion Sources and Ion-Assisted Technology, Tokyo, June 7-9, 1982, p. 185.



Table 1 Typical parameters of the ion sources, negative ion currents and ion source materials

Ion source	NISS	NISS	NISS	HPIG	HPIG
Beam species	Te <sup>-</sup>	Te <sup>-</sup>	Te <sup>-</sup>	CN <sup>-</sup>	CN <sup>-</sup>
Negative Ion Current	1200nA	2000nA	1100nA	2000nA	4000nA
Ion Source Materials	CdTe	ZnTe	PbTe	66%CF <sub>4</sub> <sup>+</sup> 34%N <sub>2</sub>	50%CH <sub>4</sub> <sup>+</sup> 50%NH <sub>3</sub>
Extraction Voltage/Current	25KV/.3mA	25KV/.4mA	25KV/.5mA	--	--
Acceleration Voltage	--	--	--	25KV	25KV
Einzel Lens Voltage	18.8KV	19.0KV	18.8KV	--	--
Focus Voltage	13.5KV	13.5KV	13.4KV	5KV	3KV
Ionizer Voltage	5.8V	5.9V	5.8V	--	--
Oven Current	0.18A	0.19A	0.17A	--	--
Source Pressure	--	--	--	400 micron	500 micron
System Pressure	9*10 <sup>-7</sup>	8*10 <sup>-7</sup>	9*10 <sup>-7</sup>	7*10 <sup>-6</sup>	8*10 <sup>-6</sup> Torr

Table 2 Beam Currents and operational parameters of the tandem accelerator

Element	Atomic Number/ Mass Number	Ion Source Material	Negative Ion	Charge State	Beam Current	
					Ion Source/ Analyzed	Final Energy
Te	52/130	PbTe	Te <sup>-</sup>	13 <sup>+</sup>	1100nA/10pnA	190MeV
N	7/14	CF <sub>4</sub> +N <sub>2</sub>	CN <sup>-</sup>	5 <sup>+</sup>	1000nA/60pnA	80MeV

## 1.4 CONTROL SYSTEM FOR JAERI TANDEM ACCELERATOR

Susumu HANASHIMA, Eisuke MINEHARA, Isao OHUCHI, Katsuzo HORIE, Shuhei KANAZAWA, Susumu KANDA, Tadashi YOSHIDA and Yoshihiro TSUKIHASHI

Department of Physics, JAERI

1. Development of automated accelerator control

In the previous report, we have reported about computer aided automated parameter setting for JAERI tandem<sup>1)</sup>. In the method, a set of parameters that provides enough beam transportation for some ion beam is used as reference. The set of parameters for new ion beam are calculated to give the same optical effect to the new ion beam as the reference. Tests of the method( we call it scaling method) were continued and expanded. A computer program for the parameter setting have been expanded to transport molecular ion beams from negative ion injector. Many kinds of ion beams were transported by the method. In the tests, it has been demonstrated that even a faint beam can be transported through the tandem in a few minutes by the scaling method. It is because the method does not need monitoring of beam current for the parameter setting. The scaling was used for acceleration tests of new kinds of ion beams. We will use the method for daily operation of the tandem.

2. Modification of the system for an expansion of the negative ion injector

Negative ion injector of the tandem have been expanded. Modification of the control system was needed for the new injector.

With the expansion of the injector, many objectives of control and monitoring( we call them beam line components ) were added and several beam components were modified. Many data in the program of the control system have been modified. In the work, a method of management of these data has been changed for easier and more reliable maintenance. In the new method, a directory of the beam line component is used as primary data and all the data program and all pointers in the sub-modules of the control program are generated from the directory through generation programs or pre-processor for the source code of the modules. Usual maintenance of data is made only on the directory and there is no

duplication in the primary data. Thus, integrity of the data is maintained.

Several CAMAC modules have been relocated in a CAMAC crate on the injector deck. New type of CAMAC module for an analog light link system was developed and has been used. The module is used to control devices on high potential decks. Signals are transferred through plastic fibers as frequency of light pulses and electrical isolation is maintained. In the module, conversions between frequency and digital value are made with PLL frequency synthesizer or frequency counter. We call the module D/F-F/D module. The module has 5 control channels and 8 monitoring channels in a single width CAMAC module. The optical fiber connectors are directly connected to channels in the module. Voltage to frequency(V/F) and frequency to voltage(F/V) conversion technic is utilized in a module on the high potential deck of the link. It was also rebuilt. Compared with the previous light link system, reliability and accuracy have been greatly improved in the new system<sup>3)</sup>.

#### 4. Improvement of accuracy of devices

Improvement of accuracy of beam optical elements is inevitable for computer aided beam transportation. New type of analog isolaters for control of electro-magnetic devices are developed and all module previously used have been replaced with the new ones to improve the accuracy.

A prototype of new current logarithmic amplifier for monitoring of beam current was made. It was tested in the accelerator system and good results were obtained. It can measure small current of up to 10 pA with good long term stability.

#### 5. Optical serial highway for the injector

One serial highway loop has been added to the control system and dedicated for control of the injector. Thus, operation of the injector has become free from troubles of communications around the main accelerator. For the loop, an optical highway system has been used for better surge immunity and greater band width. Commercially available U-port adapters(model 5211, Lecroy, U.S.A.) have been used. Transfer rate of data is 5 M bytes per second. The optical fiber used is a graded index type silica fiber with core diameter of 50 micro meters, clad diameter of 125 micro meters, band width of 200MHz•Km and numerical aperture of 0.2(GC•50/125•3002, Fuzikura, Japan). Figure 1 shows cross section of the

fiber cord. The fiber cord gives electrical isolation between the deck of the injector and ground. Usually, the deck is biased up -200 KV from ground potential.

#### 6. High voltage tests of an optical fiber

The optical fiber used in the injector highway was put through the column structure of the tandem and high voltage tests were made. At first, complete cord with PVC sheath was tested. Next, line element without PVC sheath and tension member was tested. The cord could not withstand high voltages in both cases. We will examine other types of fibers.

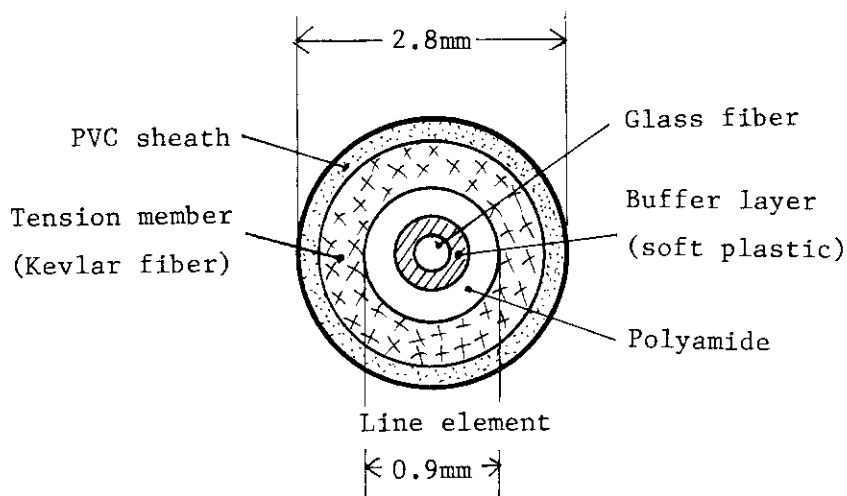


Fig.1 Cross section of optical cord(GC-50/125-3002).

#### References

- 1) S. Hanashima et al. : JAERI Tandem Annual Report 1983, JAERI-M 84-129 (1984) pp. 10-11.
- 2) S. Hanashima et al. : Proceedings of the 5th Symposium on Accelerator Science and Technology (1984) pp. 420-421.
- 3) S. Hanashima et al. : Proceedings of the 5th Symposium on Accelerator Science and Technology (1984) pp. 425-427.

## 1.5 DEVELOPMENT OF ION OPTICS COMPUTER CODE

Shiroh KIKUCHI, Suehiro TAKEUCHI and Eisuke MINEHARA

Department of Physics, JAERI

A computer code BEAM has been developed for the ion optics calculation of the tandem accelerator system. The one of the aims of the code is to obtain the optimum parameters of the devices, especially those for the magnetic and electrostatic Q-lenses, at the tandem operation. The other is to see the aspect of the beam trajectory visibly on a picture display.

The calculation is performed by using a VAX-11/780 computer equipped with the picture display, which is set for the data analyzing computer system. An example of the results is shown in Table 1 and Fig. 1. The output parameters in Table 1 are obtained by using the input parameters, typed in from the computer terminal, and the device configuration list housed in a disk as a file. The parameters for the magnetic Q-lenses are tentatively represented in units of ampere-turn.

Fig.1 is the display of the beam trajectory calculated by using the parameters shown in Table 1. The beam line, actually curved by bending magnets, is depicted as a stretched straight line. The directions  $X$  and  $Z$  indicate those of horizontal and vertical, respectively, at the starting point of the traveling of the ion beam. The axis  $S$  is so chosen that it coincides with the beam axis. The symbols  $\sqcup$  and  $\sqcap$  with the respective names show the lengths and aperture gaps of individual devices. Those without names indicate accelerator tube units of the bottom, middle and top sections.

The trajectory shown is the envelope of  $^{16}\text{O}$  beam with the final energy of 50 MeV. Such a relatively low energy beam requires low terminal voltage, accordingly small potential gradient, in the accelerator tube. Since the small potential gradient weakens the beam focusing effect, seven units in the top section, in the present example, are shorted to make it larger.

Detailed improvement of the code is still now in progress.

Table 1 Input and output parameters of the calculation

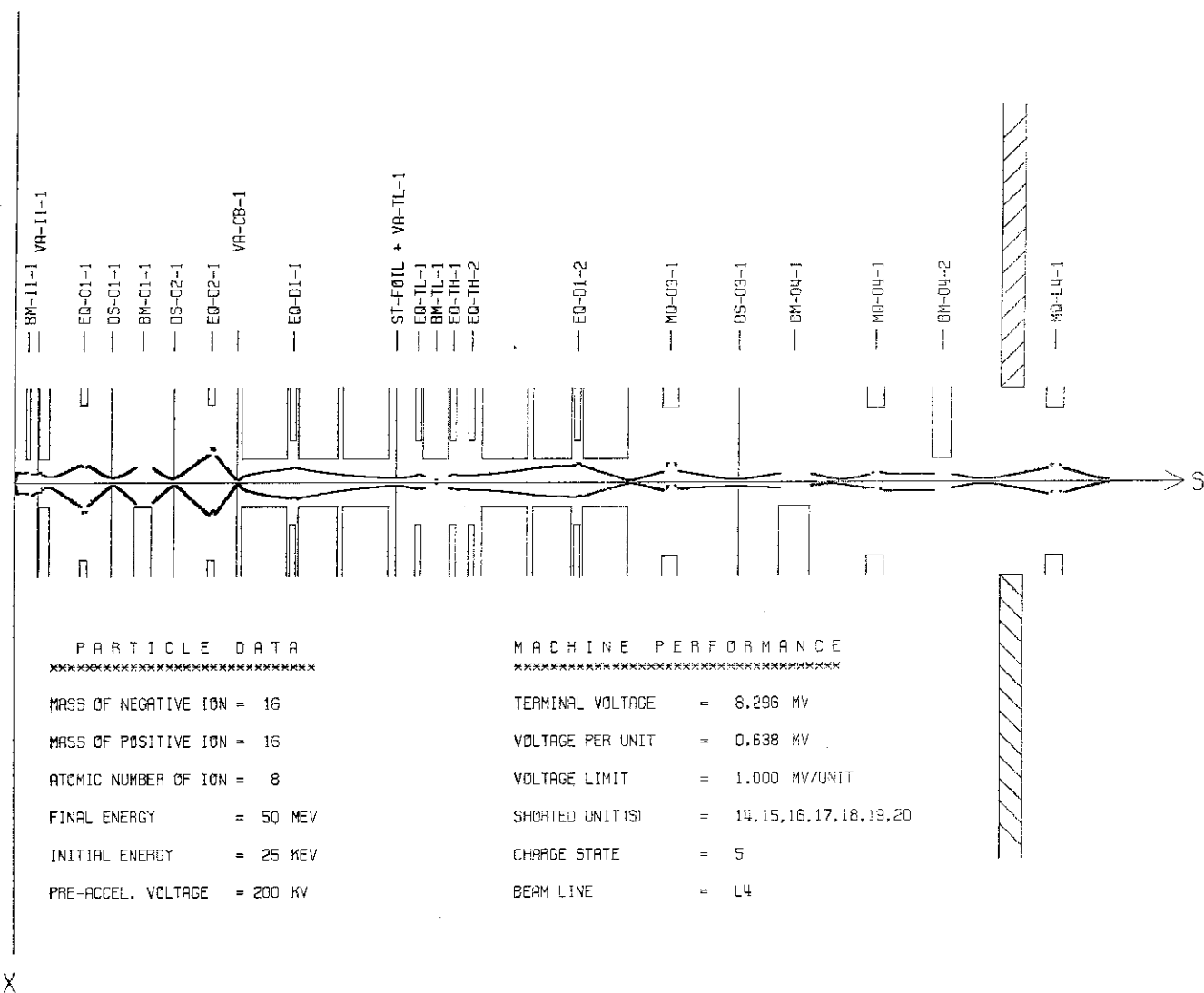
## \*\*\*\*\* INPUT \*\*\*\*\*

Negative particle-mass (in a.m.u.)	=	16
Positive particle-mass (in a.m.u.)	=	16
Atomic number of the particle	=	8
Final particle energy	=	50.0 MEV
Ion source	:	Sputter Cone
Stripper	:	Foil
Beam line	:	L4
Initial beam: rx_max, rz_max	=	1.0, 1.0 mm
drx_max, drz_max	=	29.0, 29.0 mrad
Initial energy	=	25.0 KEV
Pre-acceleration voltage	=	200.0 KV
Terminal voltage limit / unit	=	1.00 MV
Shorted unit	:	14,15,16,17,18,19,20

## \*\*\*\*\* OUTPUT \*\*\*\*\*

Terminal Voltage	=	8.296 MV
Voltage per tube-unit	=	0.638 MV
Charge state	=	5
DS-01-1	Gap_X	= 4.00 mm
	Gap_Z	= 6.00 mm
DS-02-1	Gap_X	= 4.00 mm
	Gap_Z	= 6.00 mm
DS-03-1	Gap_X	= 5.00 mm
	Gap_Z	= 4.00 mm
EQ-01-1	Element 1,3	= 4.56 KV
	" 2	= 5.18 KV
EQ-02-1	Element 1,3	= 4.79 KV
	" 2	= 5.39 KV
EQ-D1-1	Element 1,3	= 17.31 KV
	" 2	= 21.67 KV
EQ-TL-1	Element 1,3	= 12.45 KV
	" 2	= 14.68 KV
EQ-TH-1	Element 1,3	= 8.93 KV
	" 2	= 10.87 KV
EQ-TH-2	Element 1,3	= 0.00 KV
	" 2	= 0.00 KV
EQ-D1-2	Element 1,3	= 21.44 KV
	" 2	= 26.88 KV
MQ-03-1	Element 1,3	= 3658.3 A-T
	" 2	= 2218.3 A-T
MQ-04-1	Element 1,3	= 1071.0 A-T
	" 2	= 1081.0 A-T
MQ-L4-1	Element 1,3	= 1336.2 A-T
	" 2	= 1240.0 A-T
BM-I1-1	Field strength	= 2.2849 KG
BM-01-1	Field strength	= 2.7788 KG
BM-TL-1	Field strength	= 4.7271 KG
BM-04-1	Field strength	= 4.5244 KG
BM-04-2	Field strength	= 4.5599 KG

Z



X

Fig. 1 Display of the beam trajectory and the device configuration of the tandem accelerator system. Meanings of the device names are:

BM- : bending magnet  
 DS- : double slit  
 EQ- : electrostatic Q-lens  
 MQ- : magnetic Q-lens  
 ST- : stripper  
 VA- : variable aperture.

## 1.6 DEVELOPMENT OF SUPERCONDUCTING RF CAVITY FOR HEAVY ION BOOSTER

Suehiro TAKEUCHI and Naomoto Shikazono

Department of Physics, JAERI

RF superconductivity has become useful accelerator technology for heavy ions, since Argonne National Laboratory and Stony Brook (State University of N.Y.) successfully developed superconducting split-ring resonators using niobium and lead-plated copper, respectively as the superconductor. At present, quarter wave line resonators are being vigorously developed at many laboratories, stimulated by the work of Ben-Zvi and Brennan at Stony Brook<sup>1)</sup>. Combining the superiority of niobium to lead-plated copper as the RF superconductor and good electrical and mechanical properties of quarter wave line resonator, niobium quarter wave line resonators seem to be the most promising choice for superconducting heavy ion accelerating cavities. In fact, a record-high accelerating field of 4.7 MV/m was obtained with a niobium quarter wave line resonator at ANL in early 1984<sup>2)</sup>. The authors, therefore, decided to develop a niobium quarter wave line resonator for the heavy ion boosting linac proposed for the JAERI tandem accelerator.

The following were done in fiscal year of 1984 in order to start the development. A test cryostat 66 cm in diameter and 150 cm high was made. It has a 33 liter liquid helium dewar and a room 57 cm in diameter and 87 cm high under the dewar for a resonator to be tested. A test RF circuit with phase lock loop was constructed. Niobium materials for two resonators were prepared. Niobium-copper plates for the cavity housing were explosively bonded by a domestic company. The purity is modestly high as RF superconductor. A trial of making a quarter wave line resonator using the materials has not been done yet. A normal-conducting quarter wave line model resonator was made and the electric and magnetic fields were measured after the resonant frequency was tuned to 128 MHz by adjusting the length of the center conductor. The properties obtained with the model are shown in Table 1. The transit



time factor, efficiency of acceleration, is shown in Fig. 1. It can be seen that heavy ions, over wide range of ion velocities, can be accelerated with high acceleration efficiency. The optimum ion velocity is  $0.1c$ , where  $c$  is the light velocity. The resonator designed is illustrated in Fig. 2.

Table 1 Properties of a quarter wave line resonator.

Resonant Frequency	128 MHz
Optimum Velocity $\beta_0 (=v_0/c)$	0.1
Transit Time Factor at $\beta_0=0.1$	0.9
RF Stored Energy/ $E_a^{2*}$	$0.046 \text{ Joules}/(\text{MV/m})^2$
Peak Surface Fields/ $E_a^*$	
Electric	4.6
Magnetic	$75 \text{ G}/(\text{MV/m})$
Inside Length along Beam Axis	0.15 m

\*  $E_a$  = accelerating field level

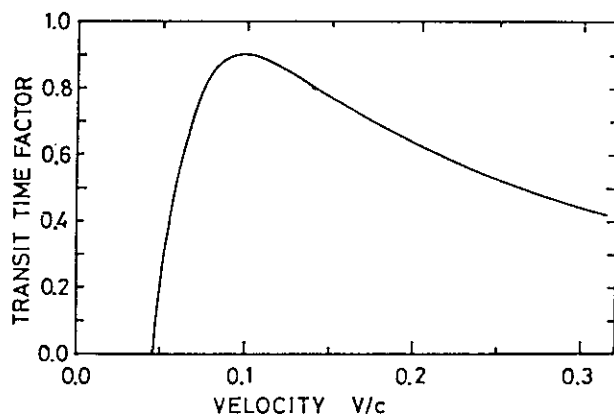


Fig.1 Transit time factor of  $\beta_0=0.10$  quarter wave line resonator.

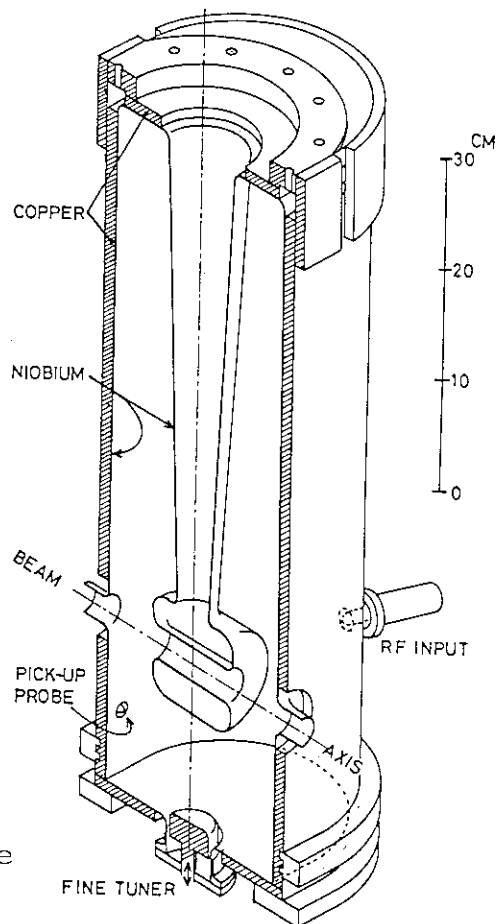


Fig.2 Cut-away view of a quarter wave line resonator.

References

- 1) I. Ben-Zvi and J.M. Brennan: Nucl. Instr. and Meth. 212(1983)73.
- 2) K.W. Shepard, S. Takeuchi and G.P. Zinkann: IEEE Transactions on Magnetism MAG-21(1985)146.

## 1.7 ELECTRON LINAC OPERATION AND IMPROVEMENTS

## Electron Linac Group

Accelerators Division, Department of Physics, JAERI

Operation

The 120 MeV JAERI electron linear accelerator (linac)<sup>1)</sup> has been routinely operated for the measurement of various neutron cross sections (neutron nuclear data), for 90% of the total machine time. The measurement in higher precision by a time-of-flight method requires the following linac performance as a pulsed neutron source: 1) higher peak beam current, 2) shorter beam pulse width and 3) higher pulse repetition rate. Main improvements of the performance were carried out to aim at these points and the endeavours for this purpose have been continued, since this linac was remodeled in 1972. Recent achievements in last few years are found elsewhere in some detail.<sup>2),3),4),5)</sup>

In addition to neutron cross section measurement, the linac has been used for other research programs spending a small part of the machine time (<10%): for solid-state-physics study by neutron diffraction and for radioisotope production by  $\gamma$ -ray irradiation.

Table 1 shows the contents of machine time devoted to the above

Table 1 Machine Time and Output Beam by Research Program in 1984

Research Program	Time (h)	Ratio (%)	Energy (MeV)	Rate (pps)	Length (nsec)	Ave. Current ( $\mu$ A)
Neutron Cross Section (Time of Flight Method)	1253	89.3	100~130	600	25 30	~53
Solid-state Physics (Neutron Diffraction)	106	7.5	100	150	1000	35
Radioisotope Production	3	0.2	60	150	1000	15
Tuning and Test Operation	42	3.0	100~130	600	25~1000	~53
<u>Total</u>	<u>1404</u>	<u>100.0</u>				

research programs together with the linac operating conditions in last fiscal year (FY) 1984.

#### Improvement

The recent improvement on the pulse modulator units made the linac operation at higher repetition rate (600 pps) possible, while the previous rate was limited to 300pps. The repair of the pulse modulators, which produced high-power pulses (250 kV, 250 A) to drive high-power klystron amplifiers, was funded in FY 1983. Main items for the repair and improvement of the modulator are summarized as follows: 1) replacement of the reverse-current-absorbing circuits of an end-of-clipper type by those of a reverse-diode type immersed in more-efficient-cooling oil-filled cases, 2) renewal of the triggering circuits to the main thyatron (ITT KU275C), replacing small thyatron (5C22) by silicon controlled rectifiers (IR 68RS160) together with their compact power supply circuit units and 3) renewal of the master pulse-trigger generator and the time distributors. The old ones were of vacuum tube circuits and the new ones are of semiconductor devices, to control finer trigger timing to each modulator unit. The 600 pps routine operation was started from the beginning of FY 1984 after two months' test operation of 450 pps. Satisfactory operation was experienced during last year.

Other improvements and preparation are as follows. 1) The TV-monitor displays were provided for the linac operation status, i.e., beam energy, average current, repetition rate, pulse width and operator's name. Four displays were prepared and located in the related rooms. 2) Preparation of the data logging system for the linac operation has been continued. The microcomputer-based system started its function partly last year; recording the control time, the beam time, the operation status, the cooling-water temperature and so on. 3) The interlock system has been renewed by adding the sensing points and replacing the old one of hard wired and relay logic by the NIM modules of IC logic. The new system has a total of 240 sensing points and 80 points were already accomplished in FY 1984. This was designed to be connected with a microcomputer for ease of checking. Software preparation is also in progress. 4) Three stainless-steel vacuum chambers of the beam deflection systems were replaced by aluminum ones in order to reduce residual activities along the beam transport system. This reduced the activity strength to less than one twentieth.

### Maintenance

Major replacements for the linac component are itemized: 1) three main klystron amplifiers (ITT-8568), 2) two thyratrons (F-175), 3) four capacitors used in the pulse-forming network in the pulse modulators and 4) insulation oil.

In addition to the ordinary maintenance, the following were carried out last year: 1) repair of the linac building, 2) renewal of the air conditioner for the control and modulator rooms, 3) renewal of the target cooling system and 4) modification of the klystron cooling system.

### References

- 1) H.Takekoshi et al.: JAERI-1238 (1975).
- 2) Y.Kawarasaki et al.: Proceedings of the 4th Symposium on Accelerator Science and Technology in Saitama (1982) 41.
- 3) K.Mashiko et al.: Proceedings of the 5th Symposium on Accelerator Science and Technology in Tsukuba (1984) 74.
- 4) K.Mashiko et al.: Proceedings of the 8th Meeting on Linac in Tokyo (1983) 8.
- 5) K.Mashiko et al.: Proceedings of the 9th Meeting on Linac in Kyoto (1984) 4.

## II      ATOMIC AND SOLID STATE PHYSICS

## 2.1 BEAM-FOIL SPECTRA OF CHLORINE IONS IN HIGH ENERGY REGION (II)

Masao SATAKA, Kunio OZAWA, Kiyoshi KAWATSURA, Kuniaki MASAI<sup>+</sup>, Keishi ISHII\*, Akio OOTUKA\*\*, Ken-ichiro KOMAKI\*\*, Fuminori FUJIMOTO\*\*, Akira KIKUCHI\*\*\* and Tetsuo KITAHARA\*\*\*\*

Department of Physics, JAERI, \*Faculty of Engineering, Kyoto University, \*\*College of General Education, University of Tokyo, \*\*\*Faculty of Engineering, Ibaraki University, \*\*\*\*Yamanashi Medical University

Atomic data for the structure of highly ionized atom are of importance in basic atomic physics, astrophysics and plasma physics. Especially, these data are indispensable for plasma diagnostics and plasma modeling in thermo-nuclear fusion.

We have reported the first results on the experimental study of atomic structure of highly ionized atomic structure by beam-foil technique<sup>1)</sup>. As the extension of Ref. 1, we have made measurements of spectral lines covering a wide wavelength range and measurements of life times of highly ionized chlorine atom. The experimental apparatus consists of a target chamber and a 2.2 m grazing incidence spectrometer. These are differentially pumped with use of two turbo molecular pumps. In the target chamber, target carbon foils are mounted on a wheel which can be translated 30 cm parallel to the ion beams for the life time measurement. The accuracy and reproducibility of foil motion is within 0.05 mm. The ion beams are monitored by a biased Faraday cup behind the foil. The foil position is moved with use of stepping motor, each step corresponds to a preset value of integrated current measured by a Faraday cup. Spectral scans are also made automatically by step scanning, normalized to the integrated current.

The spectrum of foil-excited chlorine ions measured at beam energy 80 MeV is shown in Figure 1. The foils mounted on the wheel had thickness of 15  $\mu\text{g}/\text{cm}^2$ . Wavelength range is between 230 and 470 Å. Many of the

---

+Present address: Institute of Plasma Physics, Nagoya University

strong lines were identified with use of the results of Ishii et al.<sup>2)</sup>, Forester et al.<sup>3)</sup> and Fawcett<sup>4)</sup> and the tabulation of Kelly<sup>5)</sup>. Most of those lines can be attributed to  $\Delta n=0$  transitions belonging to Cl XII - Cl XV. The lines attributed to ions of high charge states are dominant, for example 384 Å and 415 Å lines belonging Cl XV resonance doublet ( $2s^2 2s_{1/2} - 2p^2 2p_{3/2}$  and  $2s^2 2s_{1/2} - 2p^2 2p_{1/2}$ ) and 237.8 Å line belonging Cl XIV ( $(2s^2) 1s_0 - (2s2p) 1p_1$ ). Some lines may be attributed to hydrogen-like transitions of highly ionized chlorine ions and a few new lines seem to be observed. But further identification should be suspended until we will measure the line intensities at higher beam energies than 80 MeV and with thicker target foils than  $15 \mu\text{g}/\text{cm}^2$ .

Figures 2(a) and 2(b) show typical decay curves of intensities of a wavelength-selected line as a function of distance between foil and viewing position of spectrometer for 384 Å Cl XV line and 415.6 Å Cl XV line, respectively, measured at 80 MeV ion energy. The decay curves for  $2p^2 2p_{3/2}$  level and  $2p^2 2p_{1/2}$  level were fitted one exponential function as cascading and the line blending with 380.4 Å Cl XIV line ( $n=5-6$ ) and 419.5 Å Cl XIII line ( $(2s2p) 1p_1 - (2p)^2 1p_2$ ) are expected to be negligible. The measured life times are 0.74 nsec and 1.02 nsec for  $2p^2 2p_{3/2}$  and  $2p^2 2p_{1/2}$  levels, respectively. The measured life times are in good agreement with experimental results measured by Ishii et al.<sup>2)</sup> and Forester et al.<sup>3)</sup>.

#### References

- 1) M.Sataka, K.Ozawa, K.Kawatsura, K.Ishii, A.Ootuka, K.Komaki, F.Fujimoto, A.Kikuchi and T.Kitahara: "JAERI TANDEM Annual Report 1983", JAERI-M 84-129(1984)20.
- 2) K.Ishii, E.Alvarez, R.Hallin, J.Lindskog, A.Marelines, J.Phil, R.Sjödin, B.Denne, L.Engström, S.Huldt and I.Martinson: Physica Scripta 18(1978)57.
- 3) J.P.Forester, D.J.Pegg, P.M.Griffin, G.D.Alton, S.B.Elston, H.C.Hayden, R.S.Thoe, C.R.Vane and J.J.Wright: Phys.Rev. A18(1978)1476.
- 4) B.C.Fawcett: J.Phys. B: At.Mol.Phys. 3(1970)1152.
- 5) P.L.Kelly: ORNL-5922(1982).



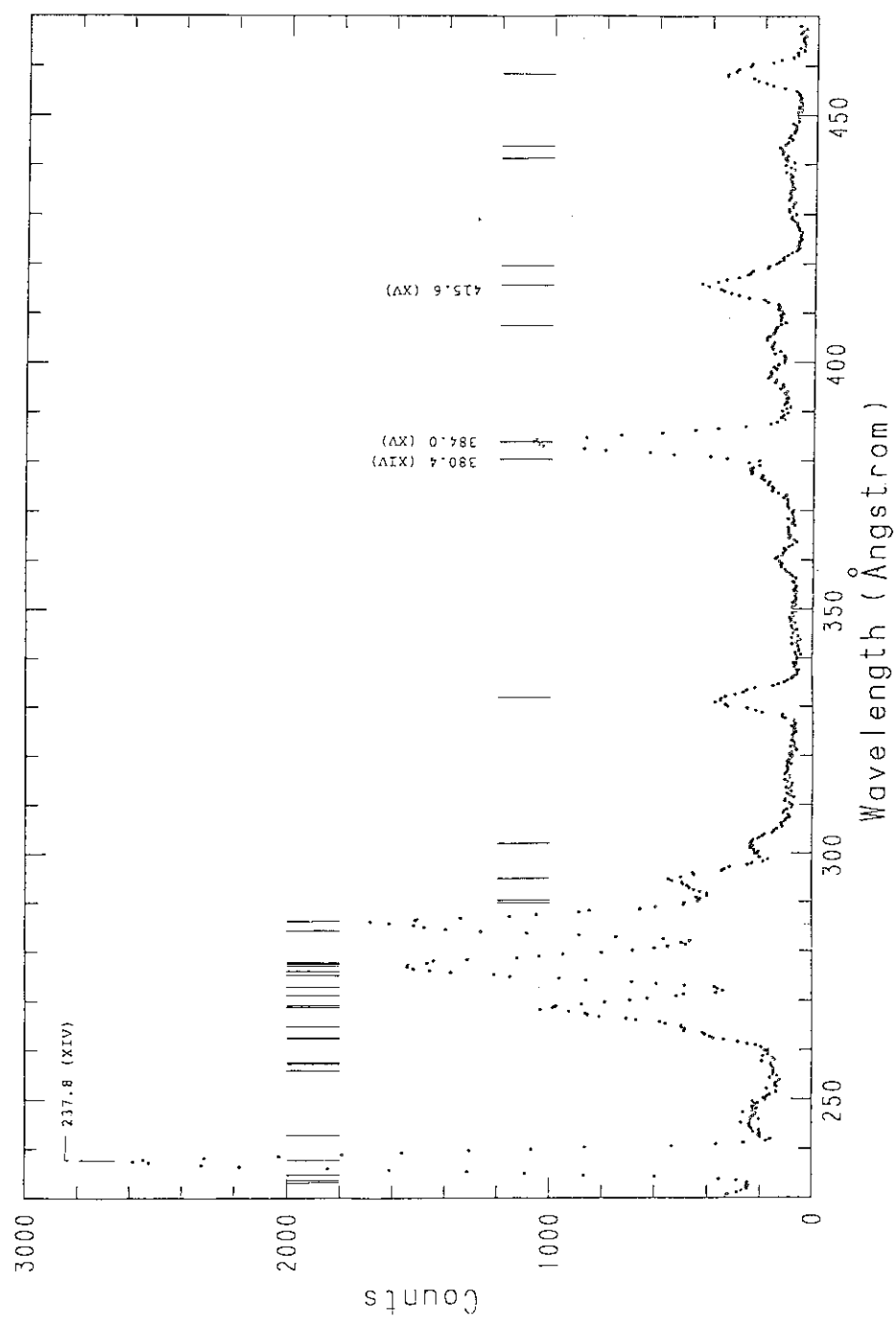


Fig. 1 Spectrum of foil-excited chlorine ions of incident energy 80 MeV.

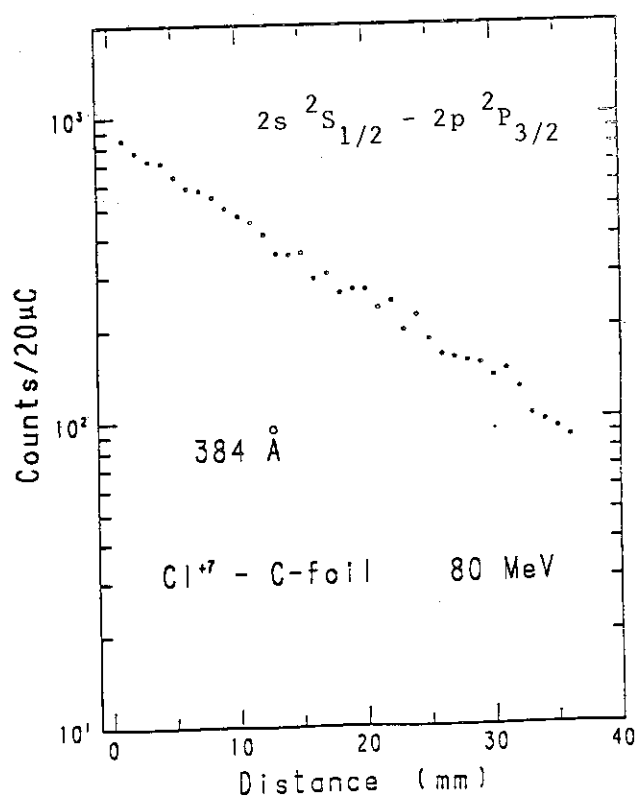


Fig. 2(a) Intensity decay curve for 384 Å line in Cl XV measured at 80 MeV.

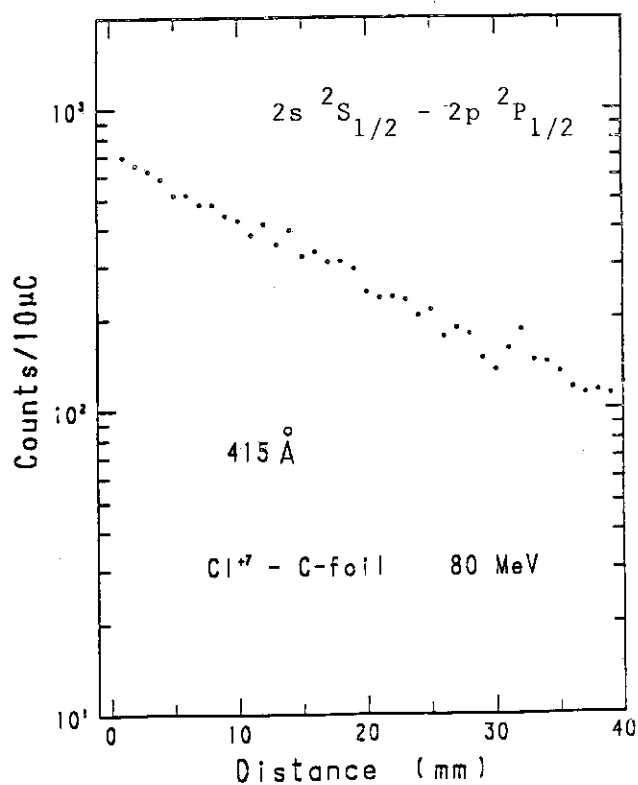


Fig. 2(b) Intensity decay curve for 415 Å line in Cl XV measured at 80 MeV.

## 2.2 ION BEAM ANALYSIS ON Nb-Mo ALLOY WITH ENERGETIC HEAVY IONS

Hiroshi NARAMOTO, Kunio OZAWA, Kiyoshi KAWATSURA,  
Masao SATAKA, Sadae YAMAGUCHI\* and Kuniaki MASAI<sup>+</sup>

Department of Physics, JAERI, \*Faculty of Engineering,  
Tohoku University

1. Introduction

The interaction of energetic heavy ions with atoms can be characterized by the following three processes: (1)nuclear reactions, (2)elastic recoiling and (3)ionization of inner shell electrons. The excited probe nuclei are introduced in a specimen through process (1) and the  $\gamma$ -ray spectroscopy can be realized employing perturbed angular correlation and/or recoilless emission of  $\gamma$ -rays. Process (2) makes forward recoiling more probable for low Z elements in solid, and the depth distribution of the elements can be determined with the energy analysis of recoils. Through process (3), selective identification of high Z elements can be performed detecting induced characteristic X-rays even in high Z matrix where the backscattering analysis is not effective.

The lattice location of hydrogens dissolved in Va bcc metals has drawn considerable attention from the viewpoint of hydrogen diffusion<sup>1)</sup>. The introduction of VIa solute atoms in the periodic table may influence the behavior of hydrogen atoms through the change of electronic structure. Nb-Mo alloy is chosen for this purpose and crystallographic investigation is made in a virgin specimen before hydrogen introduction. This report describes the results of preliminary experiment obtained through process (3) using high energy heavy ions.

2. Experimental Procedure

Nb-Mo alloys were grown by the Pedestal method, and disc specimens were sliced out from a grown block. A specially designed vacuum chamber was prepared for the heavy ion beam analysis of atomic elements in solid. Alloy specimen was bombarded with 80 MeV  $^{35}\text{Cl}^{7+}$  ions from a tandem-type Van de Graaff accelerator in JAERI. The beam intensity was about 5 npA.

---

<sup>+</sup>Present address: Institute of Plasma Physics, Nagoya University

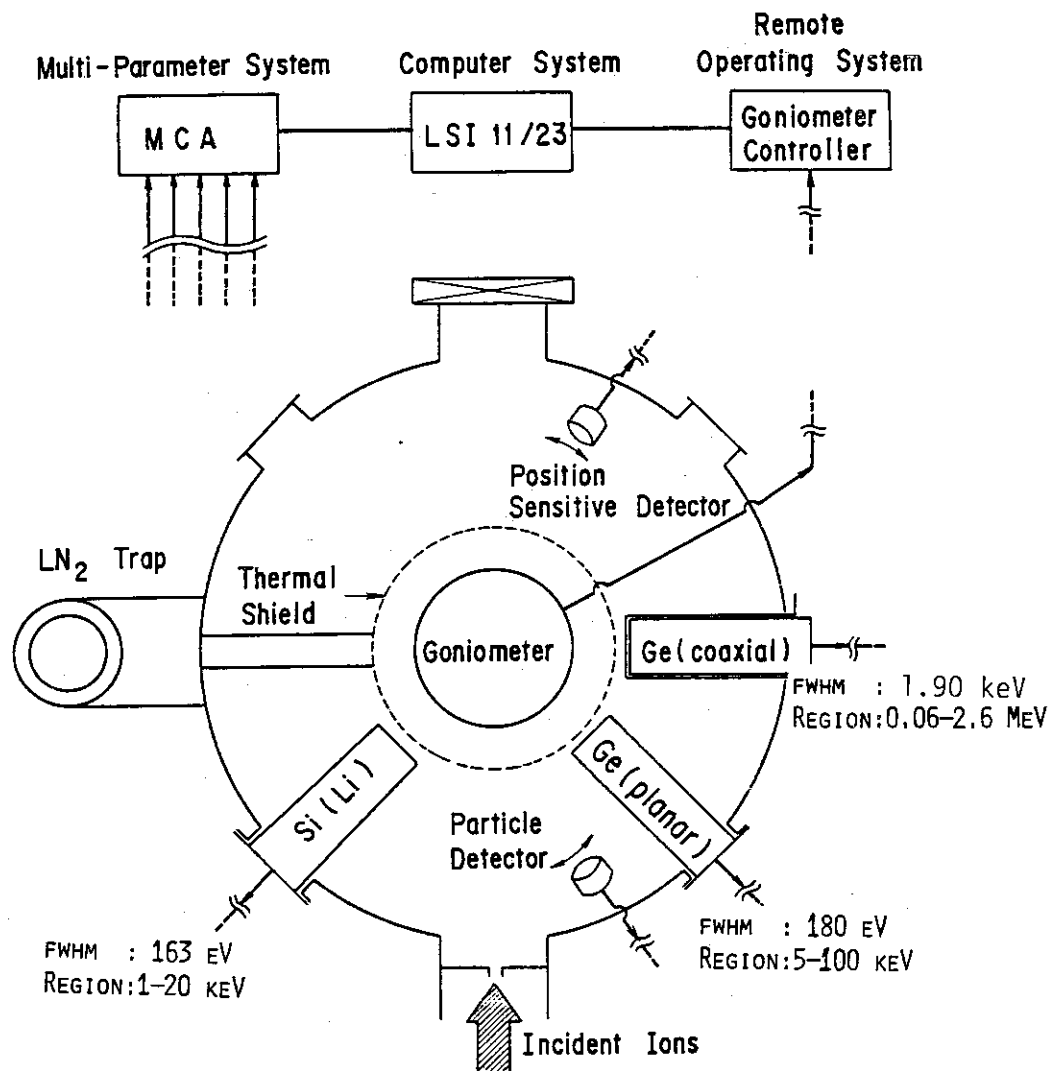


Fig. 1 Setup for heavy ion beam analysis on atomic elements in solids.

An experimental arrangement of this chamber is illustrated schematically in Fig. 1. One can detect photons with the energies ranging from 1 keV to 2.6 MeV. A Si(Li) detector is used for X-ray region, a planar Ge detector for soft  $\gamma$ -ray region, and a coaxial Ge detector for  $\gamma$ -ray region. The crystallographic orientation was made with a goniometer system equipped with the mechanisms of three axial rotations and a translational motion. This goniometer was purchased from Panmure Instruments Ltd. In the above system, it is possible to organize the methods mentioned in the previous section, and one can perform easily both the crystallographic and the spectroscopic studies which are complementary in nature.

### 3. Results and Discussion

Figure 2 shows X-ray spectra from Nb-Mo alloy induced by 80 MeV

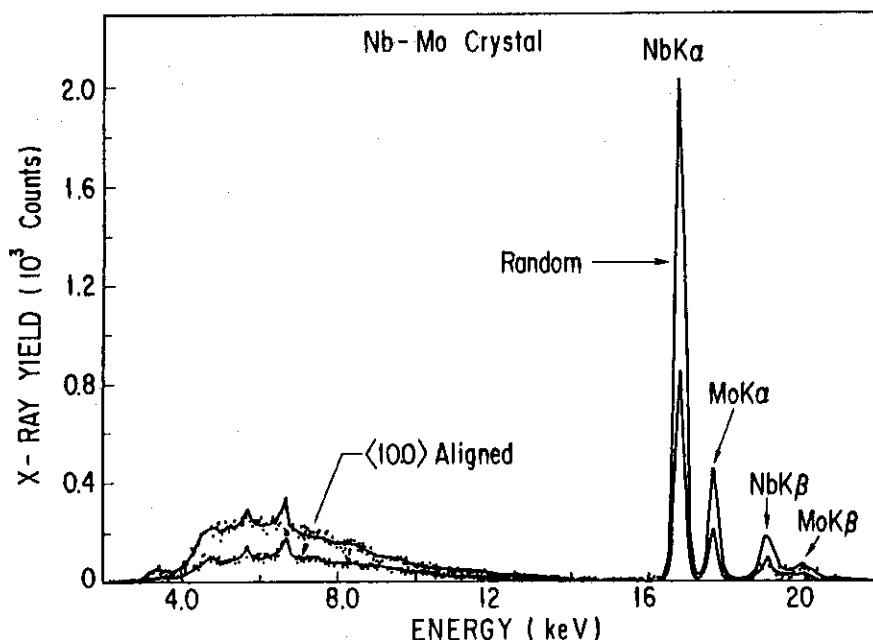


Fig. 2 Induced X-ray spectra in Nb-Mo alloy crystal bombarded with 80 MeV  $^{35}\text{Cl}^{7+}$  ions. Lower yield is obtained when a crystal is aligned around the  $\langle 100 \rangle$  axis.

$^{35}\text{Cl}^{7+}$  bombardments. X-rays were detected with a Si(Li) detector. The resolution of this detector is 163 eV in FWHM for Mn K $\alpha$  X-rays (5.9 keV). The X-ray yield in lower energy region was reduced employing Al filter with thickness of 51  $\mu\text{m}$  to avoid the influence of pile-up in the spectra because the yield of L X-rays from matrix elements is high in the lower energy region. In this figure, it is seen that when the incident beam is aligned around the  $\langle 100 \rangle$  axis, the X-ray intensity is lowered reflecting the channeling effect. The spectra show good separation between K $\alpha$  components of Nb and Mo and the angular dependence of these X-ray intensities can be obtained without any erroneous data-processing. As a result of multiple ionization by heavy ion bombardment, some shift of 100 eV toward the high energy side is seen for the peak energies of Nb and Mo K $\alpha$  X-rays. The solute content of Mo was determined to be about 20 %, which is far from the initial charge of 50 % Mo atoms in Nb matrix. The reduction of Mo could be explained by high vapour pressure of Mo metal.

Figure 3 indicates the results of angular scans around the  $\langle 100 \rangle$  axis for K $\alpha$  X-rays from Mo and Nb elements in alloy and pure Nb crystals. The full widths at the half maximum in the channeling dip curves are the same within the experimental error for Mo and Nb elements of alloy, and these are much smaller than that in pure Nb crystal shown with a solid curve

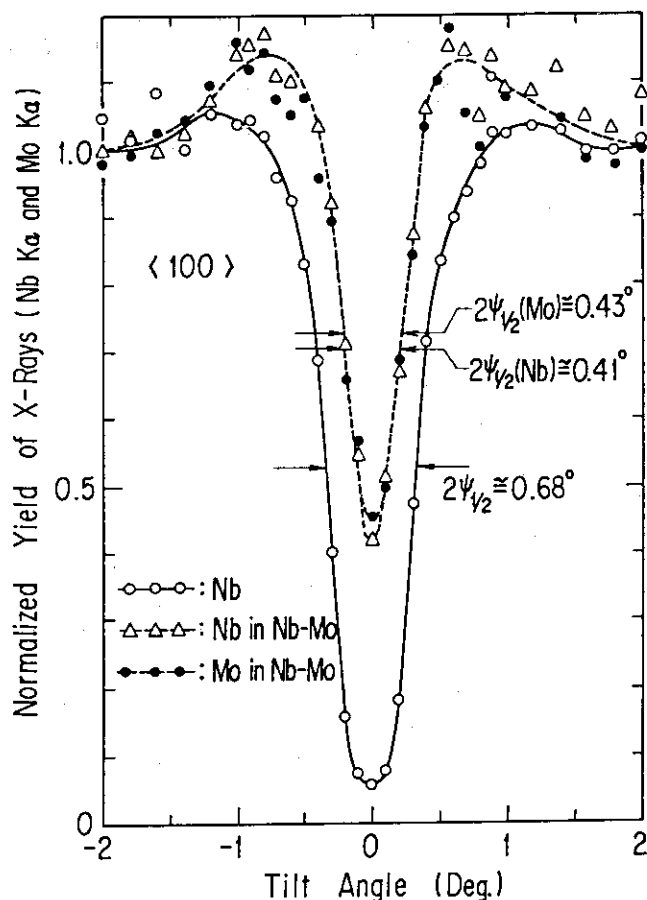


Fig. 3 Angular dependence of K $\alpha$  X-ray yield around the  $\langle 100 \rangle$  axis in Nb-Mo alloy and pure Nb crystal.

( $2\psi_{1/2}(\text{Nb}) = 0.68$ ). The large  $\chi_{\min}$  may be attributed to the lattice imperfection incorporated through alloying process. In this energy region investigated, the cross-section of Rutherford scattering is decreased to about 2 % of that for 2 MeV  $^4\text{He}^+$  ions, and the ion beam analysis of backscattered  $^{35}\text{Cl}^{7+}$  ions is not effective. Complementary experiment was performed using 1.1 MeV  $^{14}\text{N}^+$  ions from 2 MV Van de Graaff accelerator. The  $\langle 100 \rangle$  axial half angle for scattered  $^{14}\text{N}^+$  ions in the same Nb-Mo alloy is very close to the calculated value without any distinguishing treatment of mass difference between Nb and Mo atoms. In the present study, notable difference is not observed between Mo and Nb atoms, but it should be remarked that the heavy ion beam analysis like the method employed here will become an unreplaceable way to analyse an alloy composed of high Z elements.

#### Reference

- 1) S. Yamaguchi, O. Yoshinari, J. Takahashi, Y. Fujino, K. Ozawa, H. Naramoto, M. Koiwa and M. Hirabayashi: Proc. JIMIS-2, Hydrogen in Metals(1980) p.249.

## 2.3 DEFECT PRODUCTION AND RECOVERY IN COPPER IRRADIATED WITH ENERGETIC IONS

Akihiro IWASE, Shigemi SASAKI, Tadao IWATA and  
Takeshi NIHIRA\*

Department of Physics, Japan Atomic Energy Research  
Institute, \* Faculty of Engineering, Ibaraki University

### §1. Introduction

Many studies of damage in metals irradiated with energetic ions have been performed recently because cascade damage by energetic ions can simulate the effects of fusion neutron damage. In order to accomplish the meaningful simulation work, it is very important to determine the initial defect concentration and the defect structure induced by energetic ions.

In the present experiment, the defect production cross sections in copper, which is the candidate for the stabilizer of a superconducting magnet in a fusion reactor, have been obtained for several ion=

irradiations by means of electrical resistivity measurements at liquid helium temperatures. The defect production cross section is the number of the displaced atoms for unit fluence of incident ions. After irradiations, the annealing treatments have been performed up to 300 K in order to obtain the defect recovery curves. From the recovery spectra, we can get useful information about the defect structure.

### §2. Experimental procedure

The specimens were thin Cu foils about 0.2 $\mu$ m thick which were grown on the Al<sub>2</sub>O<sub>3</sub> substrates by vapor depositions at a pressure below 3x10<sup>-7</sup> Torr. The irradiations were performed with 0.54-1.80 MeV H, He, N and Ar ions from a 2MV Van de Graaff accelerator and with 100-140 MeV Cl, Br and I ions from the JAERI tandem accelerator. The thickness of the specimens is much smaller than the ranges of ions, thus ions pass completely through the specimens. After irradiations, the defect recoveries were measured at a constant heating rate of 1.5 deg/min.

### §3. Results and discussion

Figure 1 shows the experimental results on the irradiation induced resistivity change per unit fluence  $d(\Delta\rho)/d\Phi$  against the resistivity

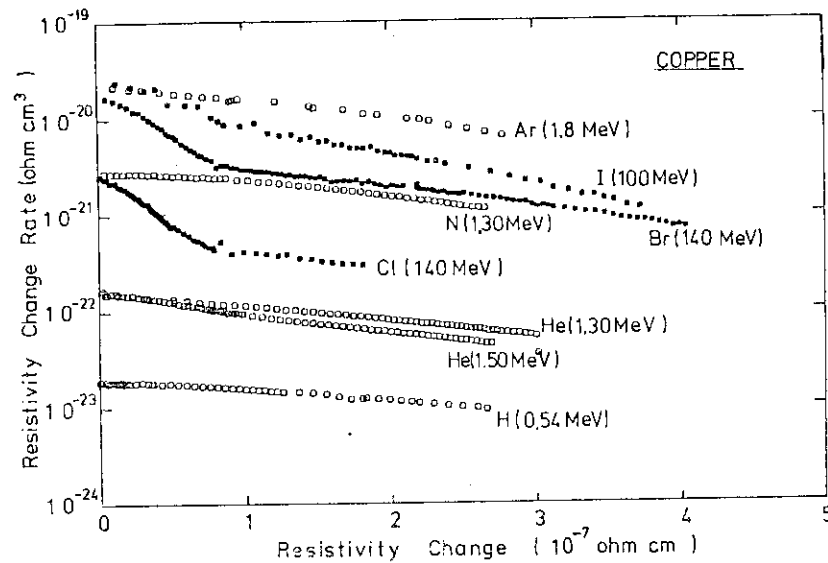


Fig. 1 The irradiation induced resistivity change per unit fluence (resistivity change rate) against the resistivity change.

change  $\Delta\rho$ . From the initial value of  $d(\Delta\rho)/d\Phi$ , the defect production cross section  $\sigma_d$  can be determined experimentally. In Table I, the initial ion energy  $E_0$ , the mean energy of ion in the specimen  $\bar{E}$ , the resistivity change rate  $d(\Delta\rho)/d\Phi$  and the defect production cross section  $\sigma_d$  are shown for several ion-irradiations.

Table I Defect production cross section, damage efficiency and percentage of stage I recovery.

Ion	Initial Energy $E_0$ (MeV)	Mean Energy $\bar{E}$ (MeV)	Resistivity Change Rate $d(\Delta\rho)/d\Phi$ ( $\Omega\text{cm}^3$ )	Defect Production Cross Section $\sigma_d(E)$ ( $\text{cm}^2$ )	PKA Median Energy $T_{1/2}$ (keV)	Damage Efficiency $\xi$	Stage I Recovery (%)
$^1\text{H}$	0.54	0.524	$1.91 \times 10^{-23}$	$9.54 \times 10^{-20}$	0.64	0.71	43
$^1\text{H}$	1.01	1.00	-	-	0.81	-	42
$^4\text{He}$	1.30	1.23	$1.63 \times 10^{-22}$	$8.13 \times 10^{-19}$	1.89	0.77	35
$^4\text{He}$	1.50	1.44	$1.49 \times 10^{-22}$	$7.43 \times 10^{-19}$	1.94	0.81	33
$^{14}\text{N}$	1.30	1.12	$3.02 \times 10^{-21}$	$1.51 \times 10^{-17}$	7.39	0.40	26
$^{40}\text{Ar}$	1.80	1.48	$2.20 \times 10^{-20}$	$1.10 \times 10^{-16}$	29.5	0.30	21
$^{35}\text{Cl}$	140	139.2	$5.66 \times 10^{-22}$	$2.83 \times 10^{-18}$	6.49	0.45	-
$^{81}\text{Br}$	140	137.5	$4.00 \times 10^{-21}$	$2.00 \times 10^{-17}$	16.5	0.41	19
$^{127}\text{I}$	100	96.3	$1.20 \times 10^{-20}$	$5.98 \times 10^{-17}$	36.7	0.31	10



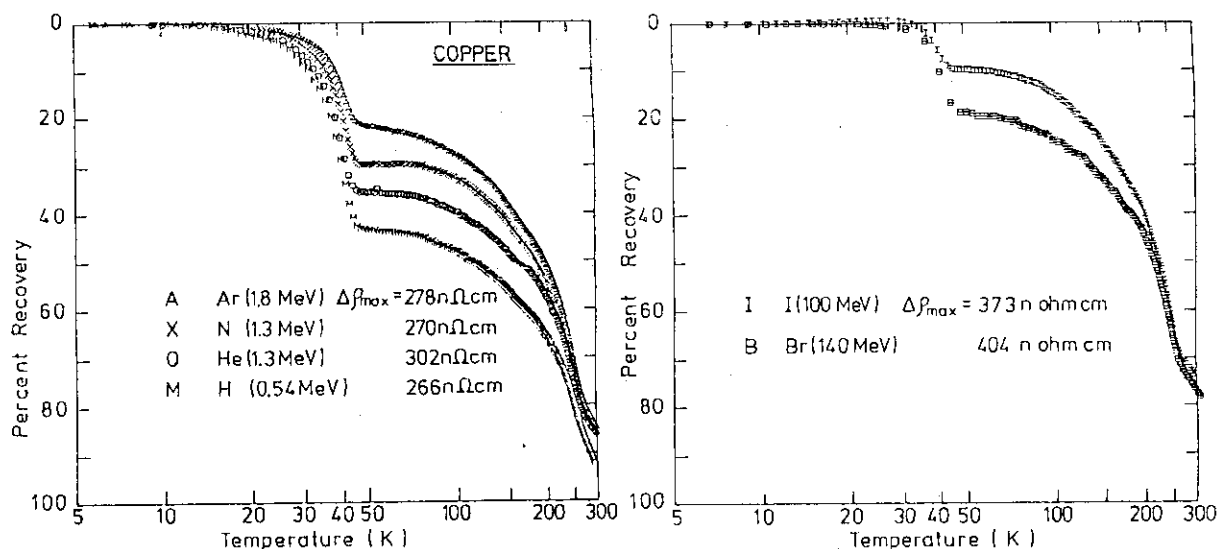


Fig. 2 Percent recovery of the resistivity of Cu as a function of temperature.

Figure 2 shows the percent recovery of the resistivity of Cu as a function of temperature. The value  $\Delta \rho_{\max}$  is the irradiation induced resistivity increment, that is proportional to the initial defect concentration in the specimen.

Figure 3 shows the damage efficiency, i.e., the ratio of the experimental defect production cross section to the calculated one, as a function of the PKA median energy  $T_{1/2}$ . The PKA median energy is one of the parameters which characterize the PKA energy spectrum.<sup>1)</sup> The method of the

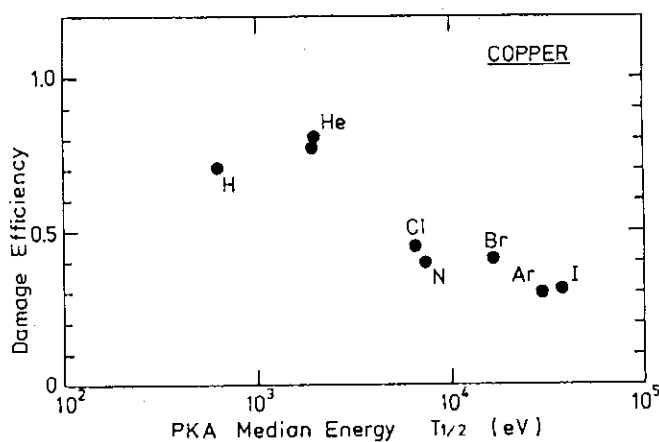


Fig. 3 Damage efficiency for Cu as a function of the PKA median energy  $T_{1/2}$ .

calculation has been described elsewhere<sup>2)</sup>. Except for the case of He ion irradiation, the damage efficiencies decrease with increasing the PKA median energy. The damage efficiency for the He ion irradiation is higher than that for the H ion irradiation. In the case of Al target, the damage efficiencies decrease monotonically with increasing the PKA median energy<sup>2,3)</sup>. The cause of the too high value of the damage efficiency for the He irradiation remains uncertain.

The percentage of the stage I recovery is shown in the last column of Table I and in Fig. 4 as a function of the PKA median energy. Figures 2 and 4 show that the percentage of the stage I recovery decrease with increasing the PKA median energy, and that the stage I recovery begins at

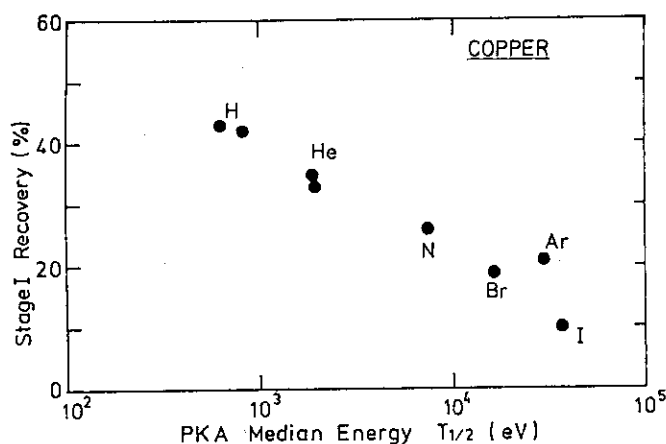


Fig. 4 Percentage of the stage I recovery as a function of PKA median energy.

the higher temperature for irradiation with the higher PKA energy.

From the dependence of the damage efficiency and the recovery of stage I on the PKA energy, it is concluded that as the PKA energy increases the spontaneous recombinations of Frenkel pairs during irradiation occur more frequently, and the structure of the resultant defects become more complex.

#### References

- 1) R. S. Averback, R. Benedek and K. L. Merkle: Phys. Rev. B18, (1978) 4156.
- 2) A. Iwase, S. Sasaki, T. Iwata and T. Nihira: J. Nucl. Mater. 133&134 (1985) in press.
- 3) A. Iwase, S. Sasaki, T. Iwata and T. Nihira: "JAERI TANDEM Annual Report 1983", JAERI-M 84-129 (1984) 22.

## 2.4 TRANSMISSION SPUTTERINGS OF MOLYBDENUM AND SILVER BY HIGH-ENERGY HEAVY IONS

Teikichi A.SASAKI, Yuji BABA and Kiichi HOJOU

Department of Chemistry, Japan Atomic Energy Research Institute

### 1. Introduction

Transmission sputtering is considered to provide very useful information about the depth profile of energy deposition in solid. Thus several works on the sputtering have been recently published.<sup>1-4)</sup> In the case of incident ion with an energy of  $\sim 100$  MeV, it has been revealed that the sputtering occurs only at the depth of the projected range of the ion.<sup>5)</sup> Furthermore, it has been pointed out that depth profiles of the sputtered atoms trapped in a catcher foil should be examined for the quantitative evaluation of the sputtering yield.

In the present work, the transmission sputterings of Mo/Ag system by  $F^{7+}$  ions and Ag/Nb system by  $C^{5+}$  ions were investigated by means of the stack-foil method. Auger electron spectroscopy(AES) was employed to obtain information on the depth profile of the sputtered atoms and on the sputtering yield.

### 2. Experimental

Target materials were metallic foils of Mo and Ag. The thick foils were mechanically polished into mirrorlike plane. The thickness was determined by means of a gravimetric method within an accuracy of  $\pm 0.2$   $\mu m$ . The foils stacked were set in a target holder made of copper together with catcher foils for the sputtered atoms. To reduce the carbon- and/or oxygen-containing adsorbates, the catcher foils were chemically cleaned by heating at  $350$   $^{\circ}C$  for 3 hours under a pressure of  $\sim 10^{-7}$  Pa and then exposed to a faint beam of 8-keV  $Ar^{+}$ -ions.

Bombardments were performed by means of a heavy-ion accelerator at JAERI. A uniform beam with a diameter of  $\sim 10$  mm $\phi$  was obtained using a magnetic beam-scanner. The other details on the bombardments were previously reported.<sup>5)</sup>

Ion etching for the depth profile of the sputtered atoms trapped in

the catcher foil was carried out by 8-keV  $\text{Ar}^+$ -ions from a PIG gun. The ion current during the etching was ca.  $4 \mu\text{A}/\text{cm}^2$ , determined by use of a small Faraday cup in a chamber of the electron spectrometer. The sputtering yields were estimated from the relative intensity of the Mo(LMM, 186 eV), Ag(LMM, 358 eV) and Nb(LMM, 167 eV) Auger-lines.

### 3. Results and discussion

Fig. 1 shows changes in the AES spectra observed for the Mo target. It is clearly seen that the transmission sputtering on to the Ag catcher-foil occurs at the definite thickness of the target, viz.  $31 \sim 32.5 \mu\text{m}$  for 117-MeV  $\text{F}^{7+}$  ions.

Etching profile of the Ag catcher-foil by  $\text{Ar}^+$  ion is shown in Fig. 2. Since the etching rate in the present experiment was  $\sim 40 \text{ \AA}$  for a fluence of  $2 \times 10^{16} \text{ ions}/\text{cm}^2$ , the deposited layer of the sputtered atoms is estimated to be within 10  $\text{\AA}$  from the top surface. Almost the same results were observed for the etching profile of the near surface of the Nb

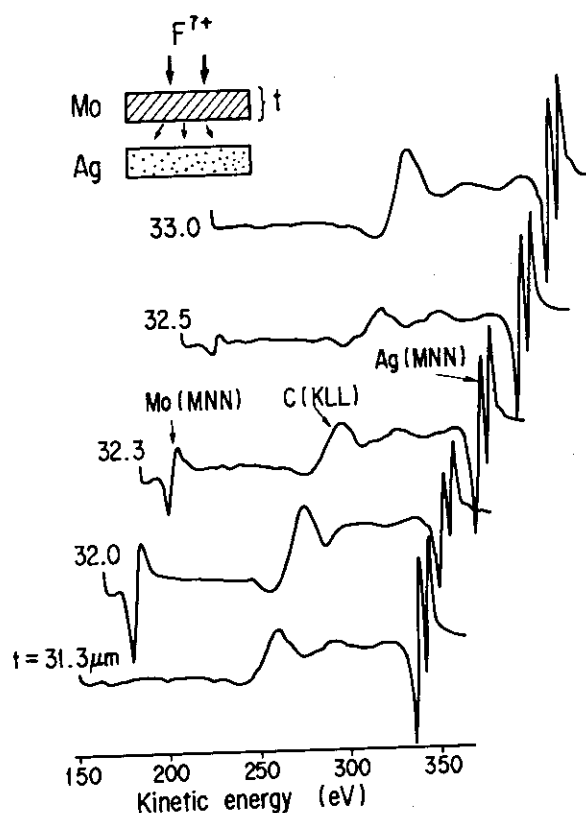


Fig. 1 Changes in the AES spectra of the Ag catcher-foils as a function of the Mo target-thickness.

foil. These observations lead to a conclusion that the AES method is available for the semiquantitative estimation of the sputtering yield.

Figs. 3 and 4 show relative yields of the sputtering as a function of the target thickness. Compared with the solid curves for energy-deposition profiles by the EDEP-1 code<sup>6)</sup> modified for high-energy ions, the peak positions of the experimental curves obtained locate by 1 % shallower than the predicted one. Furthermore, the sputtering scarcely occurs in the region where the target thicknesses are by  $\sim 3 \mu\text{m}$  less than the mean projected ranges, though considerable amount of the energy is deposited in a form of the nuclear stopping.

Taking the depth profiles of the

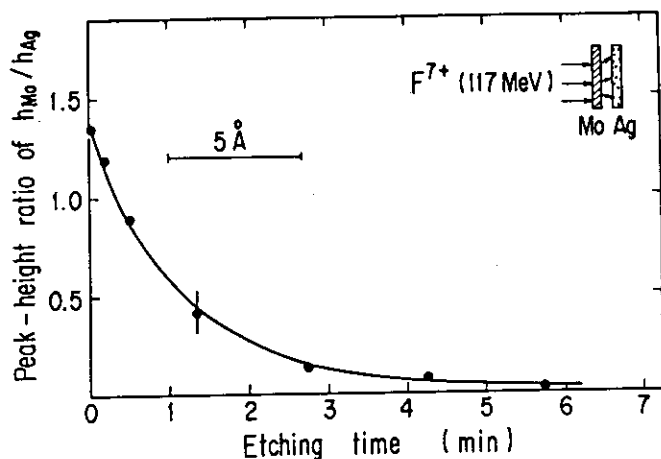


Fig.2 Etching profile of the sputtered Mo atoms deposited on near surface of the Ag catcher-foil.

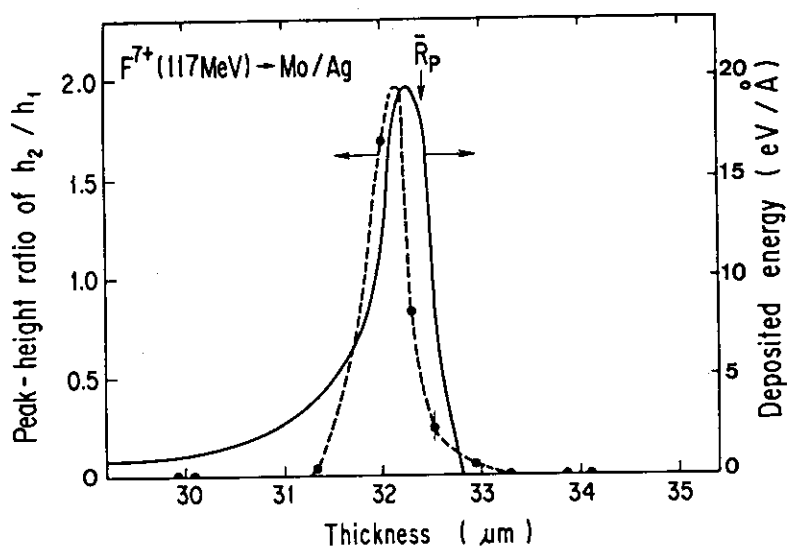


Fig.3 AES peak ratio(Mo/Ag) as a function of the target thickness. Total fluence was  $3.8 \times 10^{15}$  ions/cm<sup>2</sup>. ----: experimental, —: energy-deposition profile calculated by the EDEP-1 code.

$$Y(t) \approx \frac{C_c h_t S_c}{N_f h_c S_t} n_\lambda,$$

where  $S_t$  and  $S_c$  are the elemental sensitivity factors of the AES signals from the target and catcher foils, respectively. Consequently, maximum

sputtered atoms into account, the sputtering yield at thickness  $t$ ,  $Y(t)$ , is estimated as

$$Y(t) = \frac{C_t \cdot n_\lambda}{N_f} \quad (1)$$

where  $C_t$  and  $N_f$  are the concentration of sputtered atoms in the atomic layer and the fluence of heavy ions respectively, and  $n_\lambda$  the number of the atomic layers where the sputtered atoms are implanted. Although  $C_t \times n_\lambda$  depends upon energy spectrum of the sputtered atoms, it is evident from Fig.2 that  $n_\lambda$  is in the range of 2 ~ 3. Furthermore, the AES peak-ratio  $h_{Mo}/h_{Ag}$  or more generally  $h_t/h_c$  determined is correlated with  $C_t$  and the atomic concentration of the catcher foil  $C_c$  as<sup>7)</sup>

$$\frac{h_t}{h_c} \approx \frac{S_t C_t}{S_c C_c} \quad (2)$$

Then eq.(1) can be written as

$$(3)$$

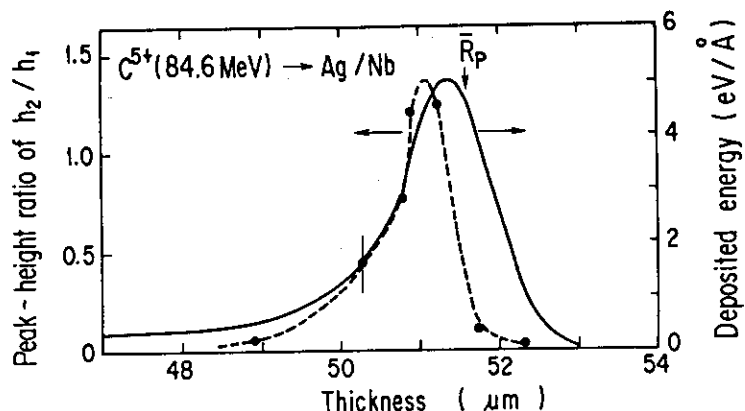


Fig.4 AES peak ratio(Ag/Nb) as a function of the target thickness. Total fluence was  $3.5 \times 10^{15}$  ions/cm<sup>2</sup>. ----: experimental, —: energy-deposition profile calculated by the EDEP-1 code.

values of the sputtering yield estimated from eq.(3) are  $0.90 n_d$  for the  $F^{7+}(114 \text{ MeV}) \rightarrow \text{Mo}$  system and  $0.33 n_d$  for the  $C^{5+}(84.6 \text{ MeV}) \rightarrow \text{Ag}$  system. Considering that  $n_d$  is in the range of  $2 \sim 3$ , the values of  $Y(t=32.3 \text{ μm})$  for the Mo target and of  $Y(t=51.2 \text{ μm})$  for the Ag target are estimated to be  $1.8 \sim 2.7$  and  $0.66 \sim 1.0$ , respectively.

Nuclear stopping calculations by the EDEP-1 code with the surface binding energy taken to be 5.9 eV for the  $F^{7+}(117 \text{ MeV}) \rightarrow \text{Mo}$  system and 2.7 eV for the  $C^{5+}(84.6 \text{ MeV}) \rightarrow \text{Ag}$  system give the maximum sputtering-yields of 2.1 and 1.4, respectively. The experimental values determined is in reasonable agreement with the calculated one. Thus, the stack-foil method combined with AES seems to be a promising technique for the determination of the transmission-sputtering yield by high-energy heavy ions.

#### References

- 1) H.L.Bay, H.H.Andersen, W.O.Hofer and O.Nielsen: Appl. Phys. 11(1976)289.
- 2) A.D.Marwick: Nucl. Instrum. Methods 132(1976)313.
- 3) K.H.Ecker and K.L.Merkle: Phys. Rev. B18(1978)1020.
- 4) G.Ayrault and D.N.Seidman: J. Appl. Phys. 53(1982)6968.
- 5) T.A.Sasaki, Y.Baba, K.Hojou and T.Aruga: J. Nucl. Mater. 132(1985) in press.
- 6) I.Manning and G.P.Mueller: Computer Phys. Commun. 7(1974)85.
- 7) L.E.Davis, N.C.MacDonald, P.W.Palmberg, G.E.Riach and R.E.Weber: Handbook of Auger Electron Spectroscopy (Physical Electronics Inc., Minnesota, 1976).

## 2.5 THE PRELIMINARY STUDY WITH THE LIGHT SCATTERING EQUIPMENT

Yukio KAZUMATA

Department of Physics, JAERI.

The equipment for the study of irradiation effects with a light scattering method was fabricated with the budget of 1982-1983 fiscal years. In this report, the preliminary results with this equipment are described. The equipment is comprised of three instruments ; a chamber for high energy irradiation, a Raman and a Brillouin spectrometer. At first, the outline of these instruments will be described and then several results obtained will be shown.

1. The chamber for the irradiation: The chamber used for high energy ion irradiations is installed at the beam line H-1 on the heavy ion target room no.2 in the Tandem accelerator building. The vacuum of this chamber is below  $1.3 \times 10^{-6}$  Pa at room temperature (RT). The irradiation temperature can be adjusted variably at a temperature from 80 to 800 K. Six specimens can be exchanged during the irradiation by the rotation being controlled from the operating room apart about 100 m from the target room. The shape of irradiating beam is monitored by the viewer attached just in front of the specimen and the uniform irradiation to the specimen is obtained by means of a beam scanner. After the irradiation, the specimen is detached from the chamber at RT and then the effects by the irradiation are measured by the optical scattering method described below.

2. Raman scattering : A Raman spectrometer is purchased from Japan spectroscopic Co., Ltd. Besides the measurements of conventional Raman scattering, this instrument provides the microscopic information to the accuracy of 1  $\mu$ m by the use of micro-Raman system. Further, for the study of the characteristics of the polarization in solids, two polarizers are attached at the back of an illuminating lens and just in front of an entrance slit. In addition to these special devices, a diode array detector is equipped at an exit slit. This detector has the great advantage to the measurements of a rapid phenomenon and to setting up the

specimen correctly. The data from the detector transfers to the multichannel analysis system, TN-1710, obtained from Tracor Northan.

The results for glassy carbon are shown in Fig.1 together with these by esr. Two lines associated with defects and  $E_{2g}$  mode in graphite are clearly seen at  $1360$  and  $1580\text{ cm}^{-1}$ , respectively. In the esr spectrum, only a single line is observed, which is associated with conduction carriers. By the bombardment of  $350\text{ keV Ne}^+$  ions, both of the lines in the Raman spectrum increase their widths with fluence and at an ultimate fluence of  $10^{16}\text{ Ne}^+/\text{cm}^2$  a broad band which indicates the transformation to amorphous carbon is observed. By esr, two lines are observed after the irradiation and one of them at higher magnetic field is attributed to be due to localized spins. From these facts, the Raman line at  $1360\text{ cm}^{-1}$  is concluded to be in no correlation with paramagnetic defects.

3.Brillouin scattering : Brillouin spectroscopy studies the scattering of light from the long-wave length thermal acoustic modes in contrast to Raman spectroscopy being concerned with optical modes. A Brillouin spectrometer is not just purchased as a complete unit. It has to be assembled from various optical parts. In Fig.2 the experimental set-up of the spectrometer is shown. A single frequency laser line of the argon-ion line of  $\lambda=514.5\text{ nm}$  is focused by means of the illuminating lens, (8) in the Fig., into the specimen and the scattered light is led to a Fabry-Perot interferometer through the pinhole (12) and the collecting lens (13). The plane Farby-Perot interferometer, model RC-110, obtained from Burleigh Instrument has the minimum mirror separation of  $0.1\text{ mm}$  which corresponds to a  $100\text{ cm}^{-1}$  free specrtal range. The DAS-1 system from the above manufacture is used for the Fabry-Perot stabilization and data aquisition system.

The results for benzene and a  $\text{BaTiO}_3$  single crystal are shown in Fig.3 and 4, respectively. The observed Brillouin frequency shifts  $\Delta\nu$  are related to the sound velocity  $V$  through  $\Delta\nu = 2nV/c\lambda$ , where  $c$  is the velocity of light,  $\lambda$  the wave legth of the incident radiation  $514.5\text{ nm}$ , and  $n$  is the refractive index. For benzene, the sound velocity is calculated to be  $1077\text{ m/sec}$  with  $n=1.51$ . This value is somewhat smaller than the ordinary value of  $1324\text{ m/sec}$ , but it will be tolerated from the rough estimation of the free spectral range.



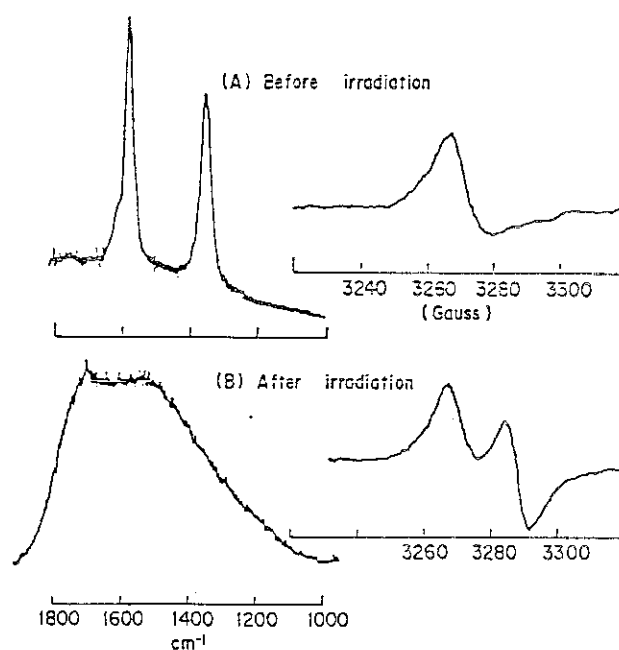


Fig.1 Raman and esr spectrum of glassy carbon.

(A) Before irradiation.

(B) After the bombardment of 350 keV  $\text{Ne}^+$  ions  
at the fluence of  $10^{16} \text{ Ne}^+/\text{cm}^2$ .

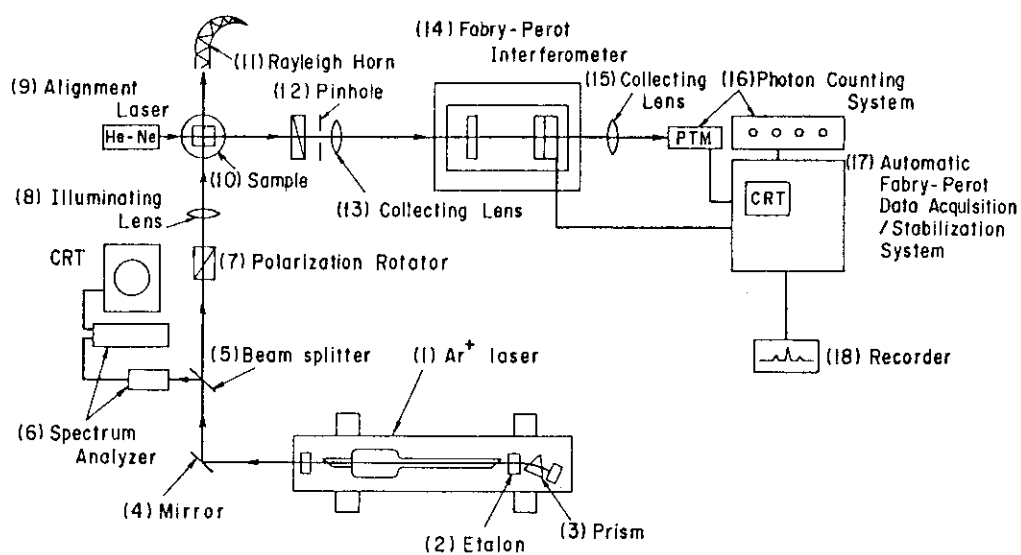


Fig.2 The experimental set-up for the measurement of Brillouin-scattered light.

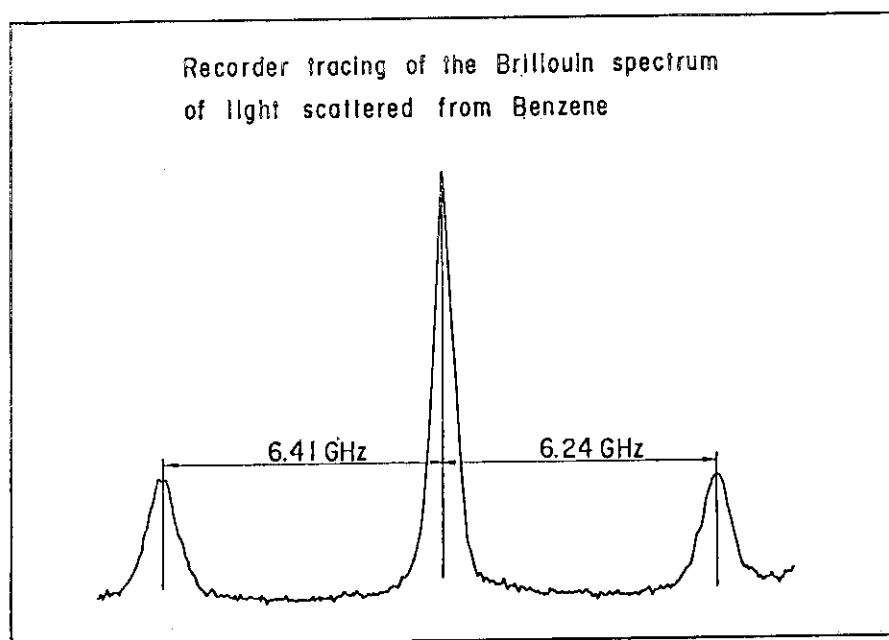


Fig.3 Brillouin spectrum of Benzene. The large peak is due to Rayleigh scattering.

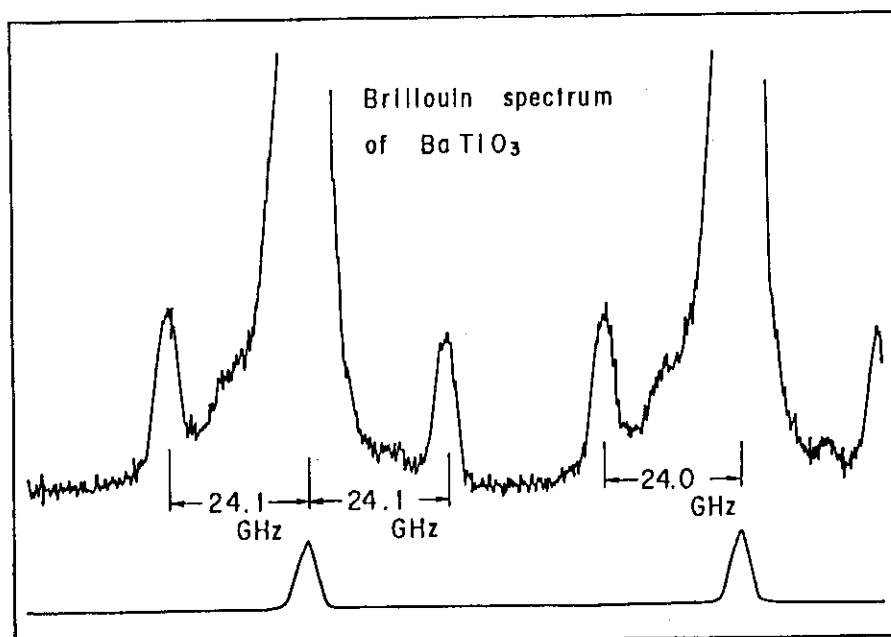


Fig.4 Brillouin spectrum of a  $\text{BaTiO}_3$  single crystal.

## 2.6 MEASUREMENT OF MEAN PROJECTED RANGES OF HIGH ENERGY IONS

Shozo HAMADA, Tomotsugu SAWAI, Katsumaro FUKAI and Kensuke SHIRAISHI\*

Department of Fuels and Materials Research and \*Radioisotope and Nuclear Engineering School, JAERI

The heavy-ion irradiation experiments have been performed to simulate the neutron irradiation damage in fusion reactor materials. The amount of displacement damage produced by ions has a steep gradient exhibiting the highly damaged region around the mean projected range of the incident ions. Then, precise estimation of the mean projected range is required for microstructural observation of the radiation damage. The measurement of the mean projected range of He-ions in Type 316 stainless steel<sup>1)</sup> has been reported, which employs optical microscopy on the cross-sectional plane of the specimen chemically etched. In this paper, the mean projected ranges for various ions injected into Type 316 stainless steel and pure nickel are measured by optical microscopy and compared with the calculations by the extended E-DEP-1 code using Ziegler's stopping powers<sup>2)</sup>.

The plates of type 316 stainless steel ( $2.5 \text{ mm}^w \times 12 \text{ mm}^l \times 0.2 \text{ mm}^t$ ) and pure nickel ( $0.2 \text{ mm}^t \times 10 \text{ mm}^\phi$ ) were solution annealed for 30 min at 1373 K and for 1 hr at 1273 K in vacuum of  $10^{-3}$  Pa, respectively. The annealed plates were polished using diamond paste to clean the surface. The ion energies used were 24 MeV for He-ions, 40, 60, 80 and 90 MeV for C-ions, 86.2 MeV for N-ions, 130 MeV for Cl-ions, 45.7 MeV for Ar-ions and 190 MeV for Ni-ions. Both the He- and N- ion irradiations were performed in the cyclotron of the Institute of Physical and Chemical Research (Riken). The Riken Heavy Ion Linac was used for the Ar-ion irradiation experiment. The C-, Cl- and Ni-ion irradiations were carried out in the JAERI tandem accelerator. After the irradiation, the sample was electroplated with nickel on both the irradiated and back surface to a thickness of about 1.5 mm, and then sliced in a plane normal to the irradiated surface with a low-speed diamond saw. The sliced sample was mechanically polished and etched by a saturated solution of CuCl in aqua regia. The optical microscopy was used for the observation of the etched surface. The specimens were then electropolished for transmission

electron microscopy. A JEM-200A electron microscope operating at 200 kV was used for TEM examination.

The optical micrograph of the specimen irradiated with 40 MeV C-ions is shown in Fig. 1. An etched band is seen at a distance of 18-19  $\mu\text{m}$  from the ion-incident surface. Figure 2(b) shows the calculated distributions of injected ions and displacement damage for 40 MeV C-ion irradiation to amorphous iron, using the extended E-DEP-1 computer code<sup>3)</sup> with Ziegler's electronic stopping power<sup>2)</sup>; the injected ion and damage distributions peak at depths of 18.7 and 18.6  $\mu\text{m}$ , respectively. This implies that the mean projected range of 40 MeV C-ions in the steel is closely approximated by the peak position of the displacement damage curve. A typical damage structure in the region containing the etched band shown in Fig. 1 is shown in Fig. 2(a) with the depth distribution of the number density of the defect clusters. The number density of the dislocation loops peaks to be  $4 \times 10^{22} \text{ m}^{-3}$  at a depth of 18.5  $\mu\text{m}$ . The average loop diameters were about 30 nm, and the loop sizes were little changed throughout the damage region. Then, the loop number density could approximate to the depth distribution of the displacement damage produced by C-ion irradiation. The depth histogram of the number density is fairly in good agreement with the calculated displacement damage profile in the depth from 18.1 to 18.7  $\mu\text{m}$  (Fig. 2(b)). It is, therefore, concluded that the center of the etched band seen in Fig. 1 is corresponding to the mean projected range, and that the calculation give a good approximation for this case.

The mean projected ranges of N-, Ar- and Ni-ion in Type 316 stainless steel and of Cl-ion in nickel were measured by the similar method. The measured values are given in Table 1 with the calculated ones. The table shows that both are in good agreement within the accuracy of 5% except for the Ar-ion irradiation. Energies of each projectiles but Ar-ion belong to the high energy region. In this region, the stopping power is well approximated by the modified Bethe-Bloch equations, which have been reported to be in good agreement with experiments. On the other hand, at the intermediate energy region around the maximum in the stopping power versus energy curve (Fig. 3), the estimations of the stopping power have not yet been well established. The low value of the calculated mean projected range for Ar-ion irradiation is caused by overestimation in the stopping power. Then, another calculation has been made with the stopping power of Northcliffe and Schilling<sup>4)</sup>, whose value for nickel target,  $S_{\text{Ni}}^{\text{NS}}$ ,

has been converted to that of iron target,  $S_{Fe}$ , by the following equation;

$$S_{Fe} = S_{Ni}^{NS} \times (S_{Fe}^{Zig} / S_{Ni}^{Zig})$$

where  $S_{Fe}^{Zig}$  and  $S_{Ni}^{Zig}$  are the stopping powers of Fe and Ni target by Ziegler, respectively. This value is plotted in Fig. 3 with the values of both Ziegler and Lindhard at lower energy region. The mean projected range calculated with the stopping power of Northcliffe and Schilling gives better agreement rather than that of Ziegler as shown in Fig. 4.

In summary, the mean projected ranges were measured for He-, C-, N-, Ar- and Ni-ions injected into Type 316 stainless steel and Cl-ion into nickel by the optical microscopy on the cross-sectional surface chemically etched. The calculations of the mean projected ranges using the extended E-DEP-1 with Ziegler's stopping powers give fairly good agreement with the measurement except for Ar-ion irradiation. In the case of Ar-ion with the intermediate energy, a marked discrepancy arises between the measured and calculated mean projected ranges. The fact suggests that improvements are required for the evaluation of the stopping power at the intermediate energy region.

#### References

- 1) K. Shiraishi and K. Fukai: J. Nucl. Mater. 117 (1983) 134.
- 2) J. F. Ziegler: Handbook of Stopping Cross-Sections for Energetic Ion in All Elements (pergamon Press, New York, 1980).
- 3) I. Manning and G. P. Mueller: Comp. Phys. Comm. 7 (1974) 85.
- 4) L. C. Northcliffe and R. F. Schilling: Nucl. Data Tables, Sec. A7 (1970) 233.

Table 1 Measured and calculated mean projected ranges

Ion	Energy (MeV)	Target	$\bar{R}_p$ ( $\mu m$ )	
			exp.	cal.
He	24	SUS316	107.3	108
C	40	SUS316	18	18.7
	60	SUS316	31	32.7
	80	SUS316	47	49.5
	90	SUS316	57	59.2
N	86.2	SUS316	40	39.8
Cl	130	Ni	12.5	13.0
Ar	45.7	SUS316	6	5.2
Ni	190	SUS316	12.2	12.8

Irradiated surface Etched line

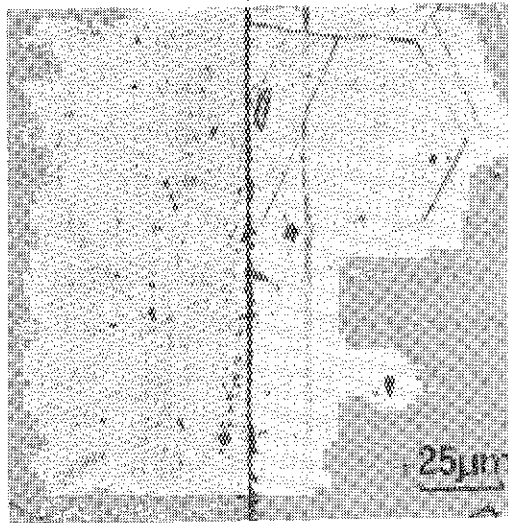


Fig.1 Microstructure view from etched surface of Type 316 stainless steel irradiated with 40 MeV C-ion.

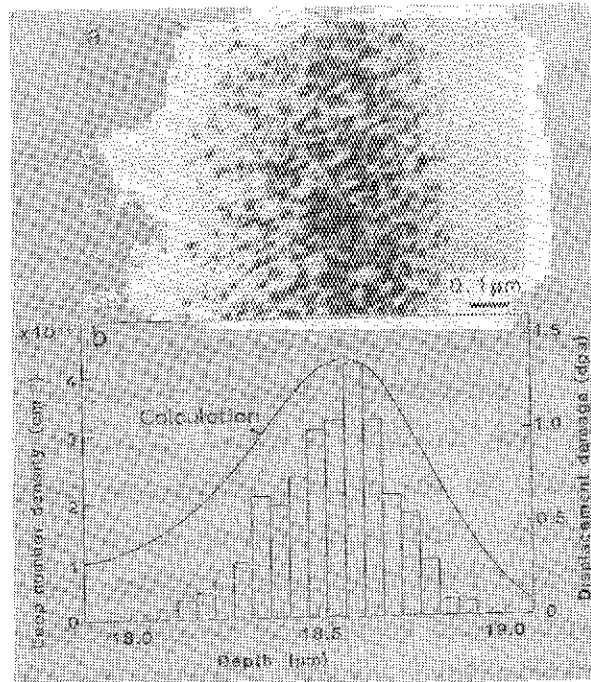


Fig.2 a: Transmission electron micrograph of damage region, b: Number density of dislocation loops in relevant region.

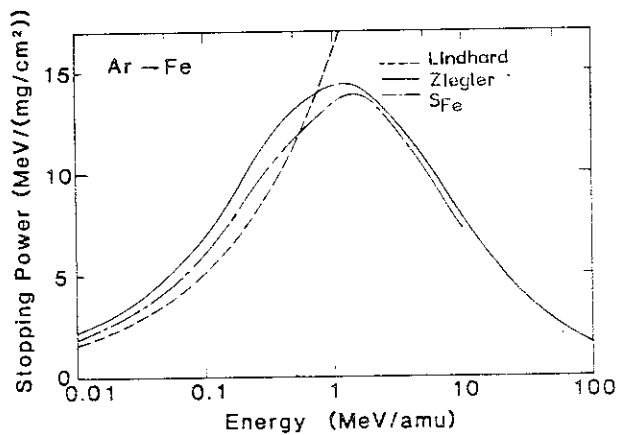


Fig.3 Stopping power as a function of the energy.

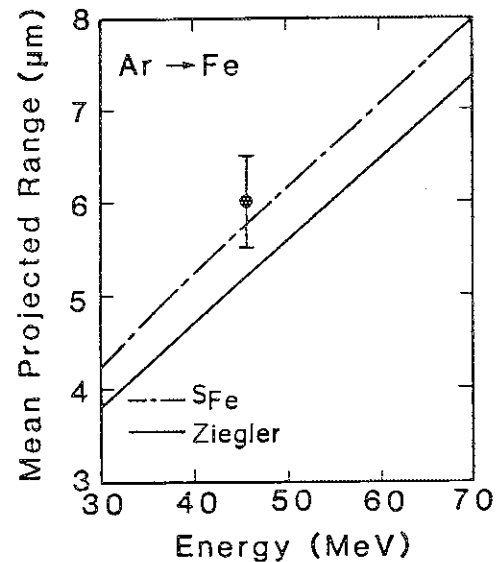


Fig.4 Comparison of the measured (close circle) with the calculated (solid and dash lines) in the mean projected ranges.

## 2.7 MOLECULAR EFFECT OF O AND Al K $\alpha$ X-RAY YIELDS FROM Al<sub>2</sub>O<sub>3</sub> FILMS FOR H<sup>+</sup> AND H<sub>2</sub><sup>+</sup> IONS

Kiyoshi KAWATSURA, Kunio OZAWA, Akio OOTUKA\*, Ken-ichiro KOMAKI\*, Fuminori FUJIMOTO\* and Mititaka TERASAWA\*\*

Department of Physics, JAERI, \* College of General Education,  
University of Tokyo, \*\* Nuclear Engineering Laboratory,  
Toshiba Corporation

### Introduction

Inner-shell vacancy production by light ions is approximately proportional to the square of the ion charge. Hence the clustered ions might be expected to show the same enhanced effect in x-ray or Auger electron production as they do in their energy loss. Chen et al.<sup>1)</sup> have measured Al K $\alpha$  x-ray yields from a thick Al target by H<sup>+</sup>, H<sub>2</sub><sup>+</sup> and H<sub>3</sub><sup>+</sup> ions. They found the x-ray yields produced by the clustered protons are lower than those produced by protons, which could be explained by the increased stopping powers of the molecular projectiles. Lurio et al.<sup>2)</sup> have measured Al K $\alpha$  x-ray yields from thin Al targets (123 Å and 370 Å) for H<sup>+</sup> and H<sub>2</sub><sup>+</sup> ions at the energy of 1.0 MeV/amu. They found that the KL<sup>1</sup>/KL<sup>0</sup> ratio by the clustered protons is slightly smaller than that by the protons.

In the present work, we report on the observations of spectra of the O<sup>0</sup> and Al K $\alpha$  x rays from thin aluminum oxide films with the thickness of 100 Å and 300 Å for H<sup>+</sup> and H<sub>2</sub><sup>+</sup> ions (0.8~0.95 MeV/amu) incident by a Bragg crystal spectrometer.<sup>3)</sup> The K $\alpha$  x-ray spectra of oxygen and aluminum for light ion consist of the main KL<sup>0</sup> peak and a satellite KL<sup>1</sup> one. The intensity ratio of the KL<sup>1</sup> line to the KL<sup>0</sup> one, I(KL<sup>1</sup>)/I(KL<sup>0</sup>), for He ion incident was reported to be much larger than that for H<sup>+</sup> one.<sup>2)</sup> We studied the molecular effect by comparing the intensity ratio, I(KL<sup>1</sup>)/I(KL<sup>0</sup>), for H<sup>+</sup> and H<sub>2</sub><sup>+</sup> ions with the same velocity, as Lurio et al.<sup>2)</sup> have carried out for aluminum foil.

### Experimental

The aluminum oxide films were deposited on thick silicon crystal plates by dip-coating from alcoholic solution of Al(NO<sub>3</sub>)<sub>3</sub> and then heating at a temperature higher than 500°C. The film thickness was controlled by

the speed of lifting the sample from the organic solution. Ion beams of  $H^+$  and  $H_2^+$  ions from the 2 MV Van de Graaff accelerator of JAERI were bombarded on the target normal to the surface. The target was surrounded by a cold trap to avoid contamination. The x rays radiated to  $45^\circ$  direction to the normal of the surface were measured by a flat crystal Bragg spectrometer. Bragg crystals of RbAP (2d spacing=26.12Å) and PET (2d spacing=8.76Å) were used for analyzing O K $\alpha$  x rays and Al K $\alpha$  x rays, respectively. The x-ray detector was a gas-flow proportional counter with a 1.0  $\mu$ m thick polypropylene window. The vacuum was  $2 \times 10^{-7}$  Torr and the beam intensity was about 100 nA. The spectra were obtained by repeating the energy scanning several times. The experimental arrangement has been described in a previous paper.<sup>4)</sup>

### Result and Discussion

Observed spectra of Al K $\alpha$  x rays from the film with the thickness of 100 Å for 0.95 MeV/amu  $H^+$  and  $H_2^+$  ions are shown in Fig.1, where the intensities of spectra are normalized by the integrated intensity of KL<sup>0</sup> line. We can see that the intensity of the KL<sup>1</sup> line for  $H_2^+$  ion is larger than that for  $H^+$  one. The intensity ratios,  $I(KL^1)/I(KL^0)$ , were obtained from the peak area of the Gaussian distribution best fitted for each peak. The result is shown in Fig.2, where  $\delta$  is defined as  $\delta = R_s(H_2)/R_s(H) - 1$  and  $R_s(H_2)$  and  $R_s(H)$  are the intensity ratios,  $I(KL^1)/I(KL^0)$ , for  $H_2^+$  and  $H^+$  ions, respectively, with the same velocity. This figure shows the enhancement of the intensity of the KL<sup>1</sup> line by  $H_2^+$  ion beam in the aluminum oxide case, on the contrary to the case of pure aluminum<sup>2)</sup>. The enhancement decreases with the film thickness.

Basbas and Ritchie<sup>5)</sup> have theoretically discussed the vicinage effects in the inner-shell ionization and estimated value of  $\delta$  as a function of the internuclear distance,  $R$ . Because the internuclear distance increases while the cluster ion travels in the film, we must calculate the average values of  $\delta$  for 100 Å and 300 Å films. By using the expression of the internuclear distance by Brandt and Ritchie<sup>6)</sup>, we obtained the values of  $\delta$  for Al atoms being 0.040 and 0.030 for 100 Å and 300 Å films, respectively, in the case of 1.8 MeV  $H_2^+$  ion bombardment. This value is roughly a half of the observed one for 100 Å oxide films and is slightly smaller than that for 300 Å ones. The calculated values for O atoms are 0.850 and 0.700, respectively. These values are only in qualitative agreement with the



experimental ones.

Yamazaki et al.<sup>7)</sup> have considered an effect of the projectile electron from the molecular ion as a reason of the enhancement. In the present case, x rays are emitted from deep part of film where ions do not accompany the electron, unlike the case of Auger electrons. Therefore, this effect is very small. Any enhancement effect of 2p shell ionization for the metallic Al target bombarded with molecular ions has never been found by x-ray production<sup>1,2)</sup> neither Auger electron production<sup>7)</sup>. Any theoretical prediction cannot explain the experimental difference between Al and  $\text{Al}_2\text{O}_3$ . However, the experimental results show that the molecular effect for the 2p shell ionization in Al atoms is correlated with the chemical state of the target atoms.

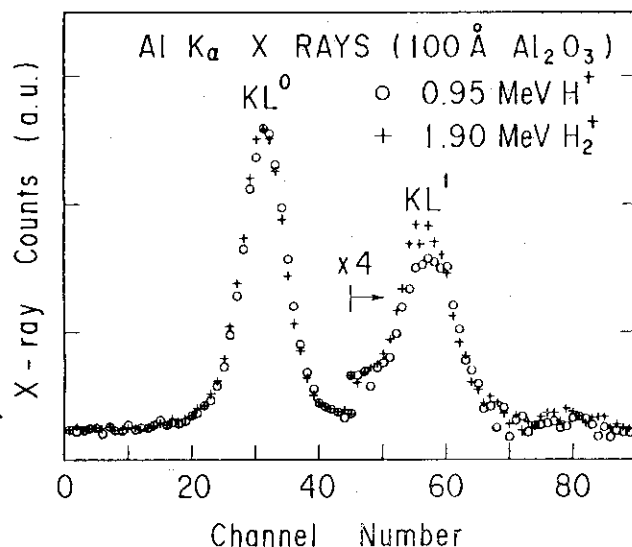


Fig. 1 Al K $\alpha$  x-ray spectra for 0.95 MeV/amu  $\text{H}^+$  and  $\text{H}_2^+$  ion bombardments.

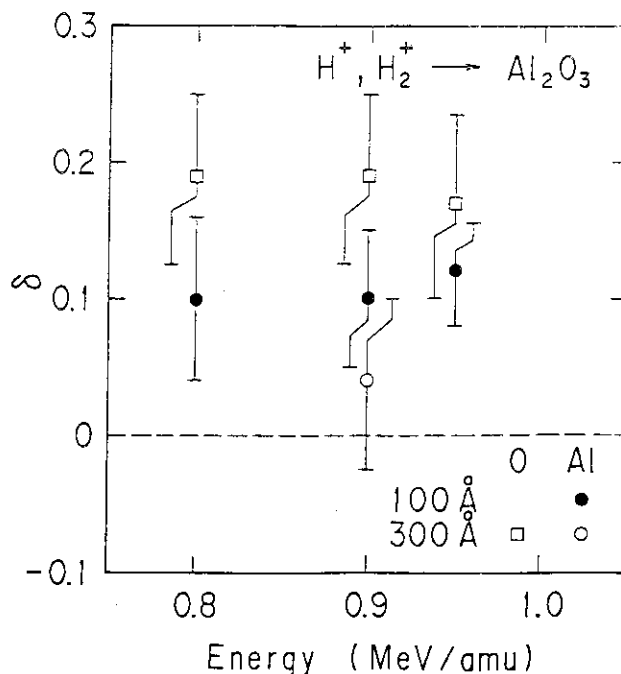


Fig. 2 Molecular effect for O and Al K $\alpha$  x-ray production cross sections.

References

- 1) F. K. Chen, R. Laubert and W. Brandt: Phys. Rev. A15 (1977) 2227.
- 2) A. Lurio, H. H. Andersen and L. C. Feldman: Phys. Rev. A17 (1978) 90.
- 3) A. Ootuka, F. Fujimoto, K. Komaki, K. Kawatsura, K. Ozawa and M. Terasawa: Phys. Lett. A97 (1983) 191.
- 4) K. Ozawa, K. Kawatsura, F. Fujimoto and M. Terasawa: Nucl. Instrum. & Methods 132 (1976) 517.
- 5) G. Basbas and R. H. Ritchie: Phys. Rev. A25 (1982) 1943.
- 6) W. Brandt and R. H. Ritchie: Nucl. Instrum. & Methods 132 (1976) 43.
- 7) Y. Yamazaki, A. Yasaka and N. Oda: Phys. Rev. A28 (1983) 1873.

## 2.8 DEUTERIUM RETENTION IN TiC CRYSTALS PREPARED BY ZONE MELTING METHODS

Sadae YAMAGUCHI, Kentaro SATO\*, Hiroshi NARAMOTO\*\* and  
Kunio OZAWA\*\*

Department of Nuclear Engineering, Tohoku University,  
\*Miyagi National College of Technology, \*\*Department of  
Physics, JAERI

### 1. Introduction

Hydrogen isotopes implanted into the first walls of fusion plasma devices affect both the material involved and the plasma itself through hydrogen recycling. Current problems are understanding of hydrogen trapping and recycling at first wall surfaces, and minimization of contamination of plasma from impurities emitted from surfaces, such as limiters. Because the potentially large radiation losses, caused by the contamination of plasma, strongly depend on the atomic number, low-Z refractory materials with good thermal shock resistance are desirable for limiters or other first wall elements. The above requirements make TiC be receiving much attention as candidates for the first wall materials. Consequently hydrogen trapping in TiC and re-emission from it during implantation of energetic hydrogen have so far been investigated by several workers<sup>1-4)</sup>, but some discrepancies remain. According to the measurements by Doyle et al.<sup>1,2)</sup>, TiC formed by chemical vapor deposition shows a saturation behavior at an ion fluence below  $10^{18}$  H/cm<sup>2</sup>, and the saturation concentration is measured to be 0.26 H/host-atom at room temperature by using the  $D(^3\text{He}, p)^4\text{He}$  nuclear reaction analysis. On the other hand, Erents<sup>3)</sup> showed that TiC prepared by co-sputtering of titanium and carbon traps the majority (90% at 2 keV  $D_2^+$ ) of incident deuterons up to a fluence of  $10^{18}$  D/cm<sup>2</sup>.

As is well known, TiC has a wide nonstoichiometric composition range from  $\text{TiC}_{0.55}$  to  $\text{TiC}_{1.0}$ <sup>5)</sup>. Therefore, it is interesting to measure the deuterium retention properties on the samples with different compositions and on those prepared by different methods. In the present work, deuterium accumulation data at the near surface are compared for several types of TiC samples prepared by CVD and grown by a floating-zone (FZ) method.

In addition, the effect of radiation damage on deuterium retention and the thermal release of deuterium during isochronal annealing up to 800°C are investigated.

## 2. Experimentals

Five types of TiC samples were studied in this investigation: (1) TiC<sub>0.96</sub> single crystal (abbreviated as TiC<sub>0.96</sub><sup>(FZ)</sup>); (2) TiC<sub>0.83</sub> single crystal (TiC<sub>0.83</sub><sup>(FZ)</sup>); (3) TiC<sub>0.77</sub>O<sub>0.006</sub>N<sub>0.003</sub> (TiC<sub>0.77</sub>O<sub>0.006</sub>N<sub>0.003</sub><sup>(FZ)</sup>); (4) polycrystal deposited on carbon substrate (TiC(CVD)); (5) TiC<sub>0.96</sub> bombarded with 350 keV C<sup>+</sup> ions at fluence of  $5 \times 10^{15}$  ions/cm<sup>2</sup> (predamaged TiC). The compositions of these samples were determined by chemical analysis.

In the ion beam analysis, two types of experiments were performed. The first one is the measurement of deuterium accumulation at the near surface. 5 keV D<sub>2</sub><sup>+</sup> ions were irradiated to the samples and simultaneously the amount of them retained near the surface was measured by elastic recoil detection (ERD) technique with 2.8 MeV <sup>4</sup>He beam.

In the second experiments, 15 or 44 keV deuterons from an electromagnetic isotope separator were implanted with  $2 \times 10^{16}$  ions/cm<sup>2</sup> or  $10^{17}$  ions/cm<sup>2</sup> into the specimen at room temperature. ERD technique was also used to determine the total amount of implanted deuteriums.

## 3. Results and discussion

The amount of deuterium trapped within the top surface of 0.2 μm thick is plotted in Fig. 1 as a function of implantation fluence for TiC<sub>0.96</sub>, TiC<sub>0.83</sub>, TiC<sub>0.77</sub>O<sub>0.006</sub>N<sub>0.003</sub> and TiC(CVD) samples. All the curves show a linear increase with the implantation fluence up to  $7 \times 10^{17}$  D/cm<sup>2</sup>, but no saturation behavior. We note that the trapping efficiency decreases in the order of TiC<sub>0.77</sub>O<sub>0.006</sub>N<sub>0.003</sub> - TiC(CVD) - TiC<sub>0.83</sub> - TiC<sub>0.96</sub>, being considerably lower

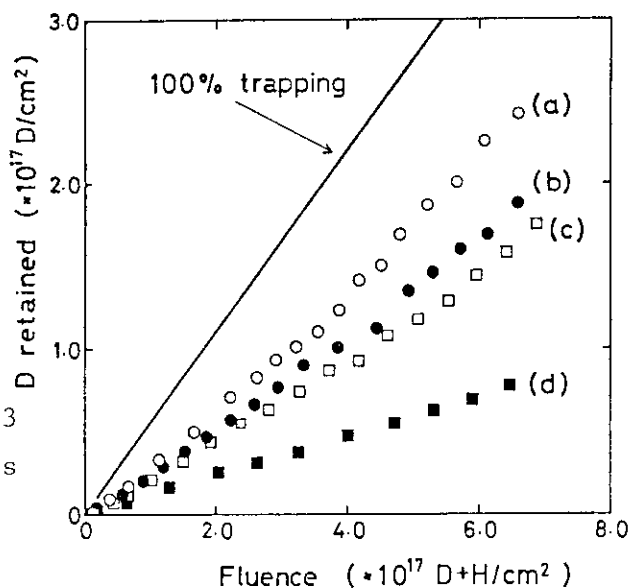


Fig. 1 D build-up of (a) TiC<sub>0.77</sub>O<sub>0.006</sub>N<sub>0.003</sub>, (b) TiC(CVD), (c) TiC<sub>0.83</sub> and (d) TiC<sub>0.96</sub>. The solid line represents 100% trapping.

than 100% in all cases. The trapping coefficients deduced from Fig. 1 are shown in Fig. 2. Remarkable differences are noticed between the present results and both results taken from the re-emission measurements of 2 keV  $D_2^+$  by Erents<sup>3)</sup> and from the retention measurements of 1.5 keV  $D_2^+$  by Doyle et al.<sup>1)</sup>.

The present results suggest a fairly high rate of diffusion of deuterium in TiC during implantation, because only 20–70% of the implanted ions are retained within the range of the ions in specimens. For the 5 keV  $D_2^+$  ions, kinetic backscattering is insignificant ( $\sim 10\%$ )<sup>6)</sup>, and sputtering yield of  $10^{-2}$  atoms/ion<sup>7)</sup>, a surface layer 10 Å thick is sputtered by an incident fluence of  $10^{18}$  ions/cm<sup>2</sup>, which is thinner than the ion range of more than 350 Å. The present results and results by Erents contradict with the results by Doyle et al., since the retention curves do not show any saturation behavior at fluences below  $10^{18}$  H(D)/cm<sup>2</sup>. The reason for the discrepancies is not yet clear. We suggest, however, that the difference in hydrogen(deuterium) diffusivity in the samples studied may be an origin; the diffusion rate is sensitive to the concentration and the preparation method of the samples, but release rate from the surface i.e. surface recombination coefficient is insensitive to the characteristics of bulk samples. From this result, we may conclude that the majority of deuterium atoms implanted in TiC samples diffuse readily away from the near-surface region

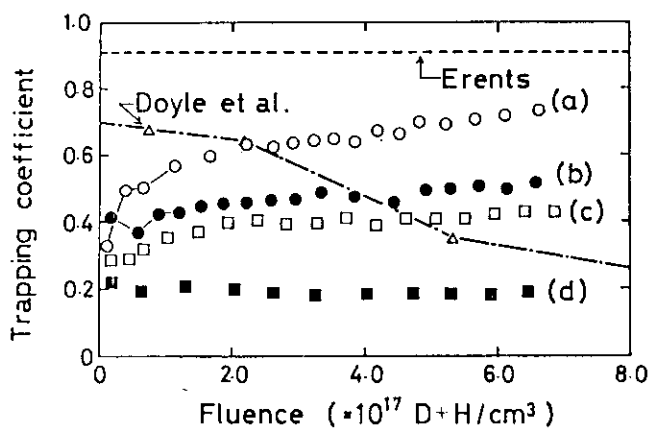


Fig. 2 Trapping coefficient versus fluence for (a)  $TiC_{0.77}O_{0.006}N_{0.003}$ , (b)  $TiC(CVD)$ , (c)  $TiC_{0.83}$ , (d)  $TiC_{0.96}$ . The results by Erents and Doyle et al. are also shown.

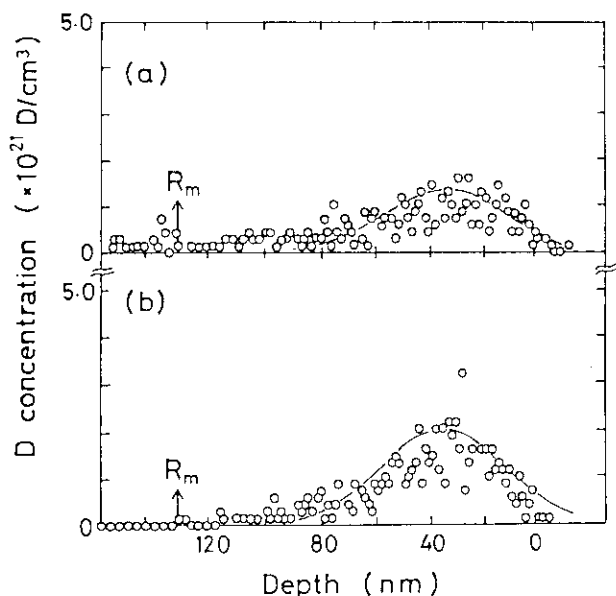


Fig. 3 Depth profile of 5 keV  $D_2^+$  implanted in (a)  $TiC_{0.96}$  and (b)  $TiC_{0.77}O_{0.006}N_{0.003}$ . The solid curves show the calculated range profiles.  $R_m$ : total path length.

to the interior beyond the probing depth of ERD technique.

This fact is also supported by the depth profile measurements shown in Figs. 3 and 4. Figure 3 shows depth distributions of 5 keV  $D_2^+$  in  $TiC_{0.96}$  and  $TiC_{0.77}O_{0.006}N_{0.003}$  at the fluence of  $6 \times 10^{16}$  D/cm<sup>2</sup> in comparison with theoretical range profiles<sup>8)</sup>. The theoretical curves are normalized at the peak of the experimental distributions. It is shown that the near-surface slope of the observed distributions agree well with those of the calculated curves, whereas the inner sides have a long tail towards larger depth. The tailing beyond the total path length is greater for  $TiC_{0.96}$  than for  $TiC_{0.77}O_{0.006}N_{0.003}$ . This result is consistent with the conclusion described above; the diffusion rate of deuterium in  $TiC_{0.96}$  is higher than that in  $TiC_{0.77}O_{0.006}N_{0.003}$ , and the interstitial impurities and the vacancies associated with nonstoichiometry act as a trap for the diffusing deuterium atoms.

In Fig. 4 depth distributions of 5 keV  $D_2^+$  implanted in  $TiC_{0.83}$  at the fluences of  $6.8 \times 10^{16}$  to  $6.4 \times 10^{17}$  D/cm<sup>2</sup> are shown. At the beginning of implantation, the deuterium accumulates near the ion range. As the fluence increases, an increase of deuterium concentration is observed in the inner side beyond the total path length of implanted ions. This indicates again the movement of deuterium towards the interior.

The detailed mechanisms involved in the trapping of deuterium in  $TiC$  are not known, but we suggest that the formation of either deuterides or bubbles is responsible for the accumulation of large amount of deuterium beyond the ion range; the strain field around the deuterides or bubbles traps the diffusing atoms further, and successive accumulation may cause the formation of deuterides or bubbles at larger depth.

Depth profiles for 15 keV and

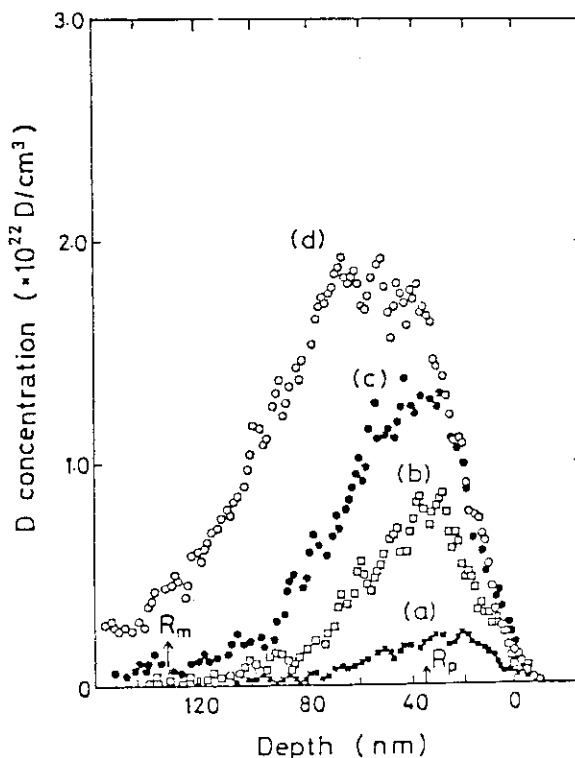


Fig. 4 Depth profiles of 5 keV  $D_2^+$  implanted in  $TiC_{0.83}$  at the fluence of (a)  $6.8 \times 10^{16}$ , (b)  $2.0 \times 10^{17}$ , (c)  $3.7 \times 10^{17}$ , (d)  $6.4 \times 10^{17}$  D/cm<sup>2</sup>.

44 keV deuterons implanted into TiC samples at room temperature were also examined. In the case of FZ-TiC, it is found that a considerable amount of deuterium is lost from the near surface region during the ageing for one week at room temperature, because of the fast diffusion rate. Contrarily, deuteriums implanted into predamaged TiC are retained near its projected range; the deuteriums are trapped by defects induced by  $C^+$  bombardment. This is consistent with the deuterium accumulation described above; the existence of defects or impurities affects strongly the retention properties in TiC samples.

As described above, deuteriums trapped by the radiation induced defects are not released by ageing at room temperature. In order to evaluate the binding energy of deuterium with defect in TiC, the D retention in predamaged TiC is measured after isochronal annealing for 10 minutes at temperatures from 30 to 800°C. The deuterium content decrease dramatically at about 600°C, and are released completely at 800°C as seen in Fig. 5. From this result, the binding energy was evaluated as  $2.8 \pm 0.5$  eV.

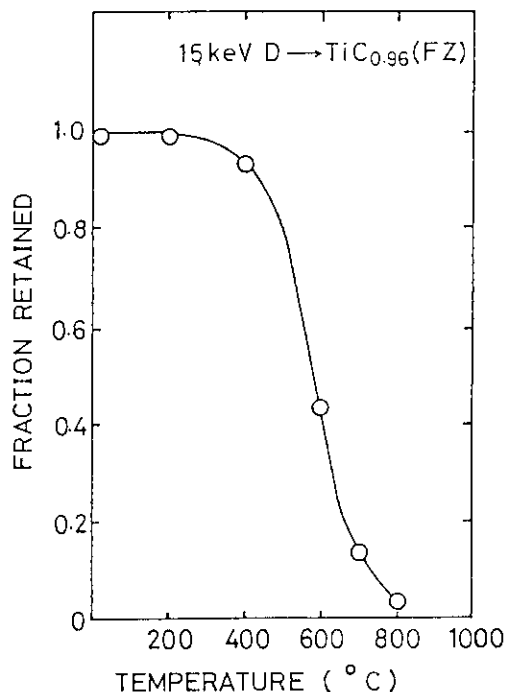


Fig. 5 Retained D fraction versus annealing temperature for damaged TiC implanted with 15 keV D of  $2 \times 10^{16}/\text{cm}^2$ .

#### References

- 1) B. L. Doyle et al.: J. Nucl. Mater. 93 & 94 (1980) 551.
- 2) B. L. Doyle et al.: J. Nucl. Mater. 103 & 104 (1981) 513.
- 3) S. K. Erents: J. Nucl. Mater. 111 & 112 (1982) 590.
- 4) K. L. Wilson and A. E. Pontau: J. Nucl. Mater. 93 & 94 (1980) 569.
- 5) E. K. Storms: Transition Metal Carbide and Nitrides, ed L. E. Toth (Academic Press, New York, 1971) p. 72.
- 6) J. Bohdanský et al.: J. Nucl. Mater. 63 (1976) 115.
- 7) J. Roth, J. Bohdanský and H. E. Martinelli: Rad. Effects 48 (1980) 213.
- 8) J. Lindhard et al.: Mat. Fys. Medd. Dan. Vid. Selsk. 33 (1963) 1.

2.9 ION BEAM ANALYSIS ON  $\alpha$ -SiC CRYSTAL IRRADIATED WITH Ar IONS

Hiroshi NARAMOTO and Kunio OZAWA

Department of Physics, JAERI

1. Introduction

The ion beam processing such as ion implantation and ion beam mixing has been increasingly employed to modify the near surface properties of various kinds of materials<sup>1)</sup>. In the processing of ceramics, the resultant lattice disorder is complicated because ceramics are composed of more than two elements. In order to understand the entire process of ion beam processing, it is necessary to investigate the ion irradiation effect separately from the effect of impurity introduction. Among the recent promising ceramics,  $\alpha$ -SiC is expected to be used at high temperatures as the structural and the electronic materials, but the studies of the ion beam processing are limited. In this report, the results of the ion beam analysis are shown on the irradiation effect by inert  $^{40}\text{Ar}^+$  ions.

2. Experimental Procedure

Various kinds of  $\alpha$ -SiC single crystals with the (0001) surface were purchased from Pacific Rundum Co., Ltd. A part of a specimen was irradiated with 200 keV  $^{40}\text{Ar}^+$  ions from 2 MV Van de Graaff accelerator to a dose of  $2 \times 10^{16} / \text{cm}^2$ , and a comparison was made between the results from the irradiated and the as-prepared regions of the same specimen. In order to obtain the information of lattice defects and compositional change in the near surface region, the ion scattering/channeling experiment was performed using 1.8 MeV  $^4\text{He}^+$  ions and 1.25 MeV  $\text{d}^+$  ions. Deuterium ions were used to analyse the carbon sublattice of  $\alpha$ -SiC crystal selectively through the nuclear reactions of  $^{12}\text{C}(\text{d}, \text{p})^{13}\text{C}$ .

3. Results and Discussion

Figure 1 shows backscattering spectra of 1.8 MeV  $^4\text{He}^+$  ions from a virgin  $\alpha$ -SiC crystal. A spectrum with higher yield (denoted by R) was obtained under the random condition, and two distinct steps are formed resulting from collisions with Si and C atoms. Under the  $\langle 0001 \rangle$  channelled condition, the scattered intensity (denoted by A) is decreased to



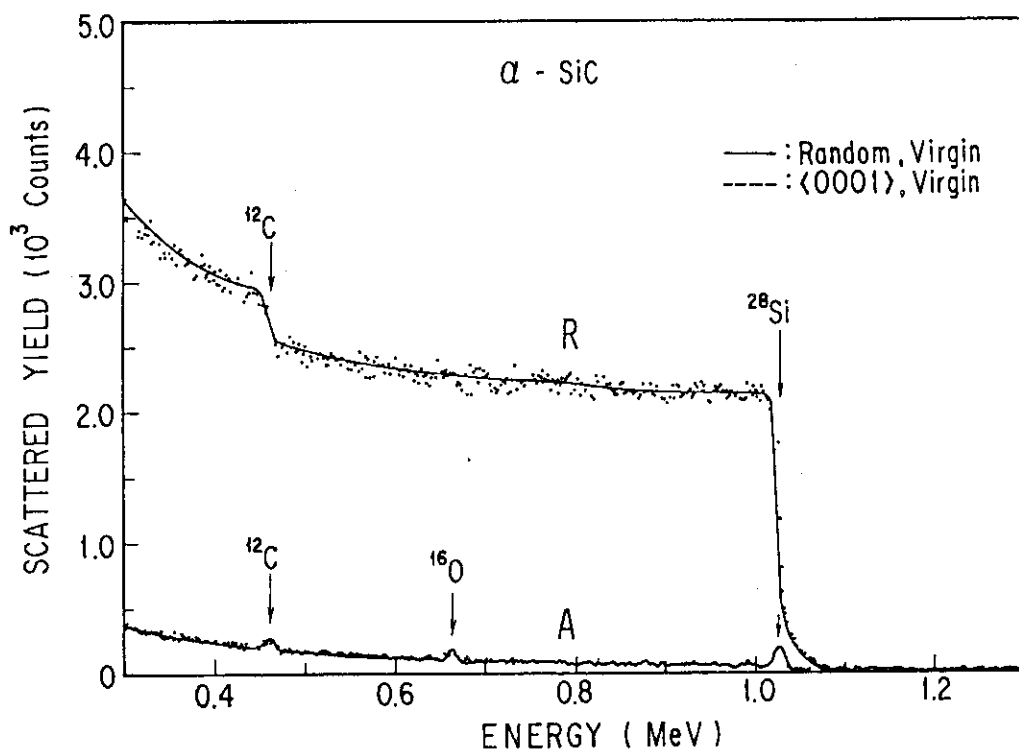


Fig. 1 1.8 MeV  $^4\text{He}^+$  ion backscattering spectra from virgin  $\alpha$ -SiC crystal under the random (marked R) and the  $\langle 0001 \rangle$  aligned (marked A) conditions.

7 % in the surface region, and mainly three peaks are observed. The first and the third peaks reflect the surface disorder of Si and C sublattices within a few atomic layers in the near surface region, respectively. The third peak observed in the mid-energy region results from oxygen impurities. These oxygen atoms are considered to be localized in the near surface region because any evidence of step formation by oxygen atoms is not detected in the random spectrum. In the higher energy region than the Si leading edge, any traces from heavier elements are not detected.

As observed already in Fig. 1, the scattered yield from C sublattice is overlapped with that from Si sublattice in lower energy region, and it is very erroneous to extract the carbon component with the linear extrapolation of scattering yield from Si sublattice. The use of the nuclear reactions  $^{12}\text{C}(d, p)^{13}\text{C}$  can avoid this difficulty. Figure 2 shows three kinds of spectra from  $\alpha$ -SiC crystal irradiated with 200 keV  $^{40}\text{Ar}^+$  ions to a dose of  $2 \times 10^{16} / \text{cm}^2$ . The spectra with a solid and a dotted lines correspond to random and aligned ones, respectively. The  $\langle 0001 \rangle$  aligned spectrum from virgin region is shown for a comparison. The spectra in lower energy region result from the backscattering, and those in higher energy region come from the nuclear reactions of  $^{12}\text{C}(d, p)^{13}\text{C}$ .

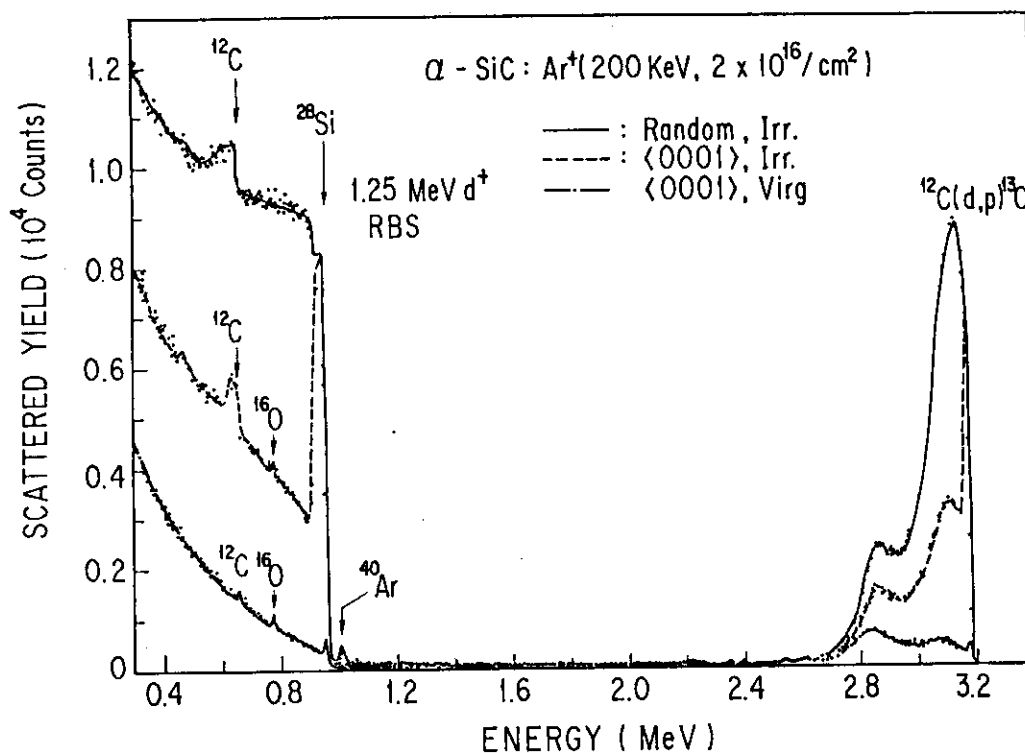
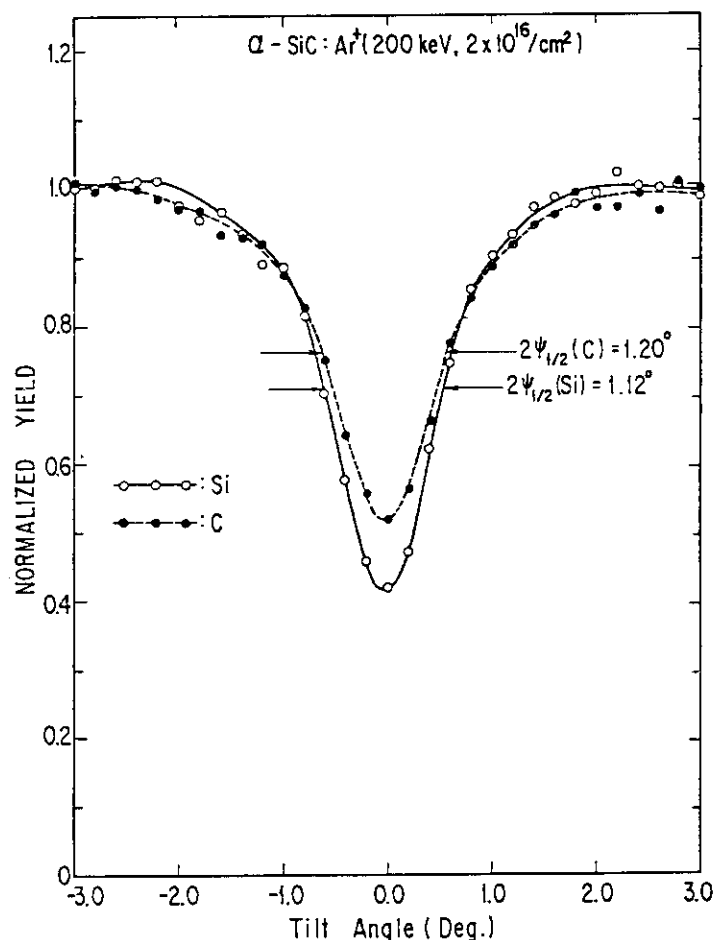


Fig. 2 Energy spectra for 1.25 MeV  $d^+$  ions incident on  $\alpha$ -SiC crystal irradiated with  $Ar^+$  ions ( $200 \text{ keV}$ ,  $2 \times 10^{16} / \text{cm}^2$ ). Spectra in lower energy region result from backscattering and that in higher energy region results from nuclear reactions  $^{12}\text{C}(d, p)^{13}\text{C}$ .

In the backscattering spectra, an isolated peak of implanted Ar atoms is observed, and any difference between random and aligned spectra is not observed, which means the random incorporation of Ar atoms in the  $\alpha$ -SiC crystal lattice. Implanted quantity of Ar atoms was calculated to be about  $2 \times 10^{16} / \text{cm}^2$ . After  $^{40}\text{Ar}^+$  ion irradiation, the aligned yield amounts to the random value in the near surface region in backscattering spectra, which shows the amorphization of Si sublattice by ion irradiation. In the nuclear reaction spectra, the complicated structure of proton yield reflects energy dependence of the employed nuclear reactions. At the higher energy region corresponding to the surface layer, the amorphization of C sublattice is also observed. At the amorphous layer, the number density of Si atoms is assumed to be decreased judging from the result of the lowered yield in the random spectrum after irradiation.

Figure 3 shows angular scans across the  $\langle 0001 \rangle$  axis for 1.25 MeV  $d^+$  incident on  $\alpha$ -SiC irradiated with  $200 \text{ keV } ^{40}\text{Ar}^+$  ions to a dose of  $2 \times 10^{16}$

Fig. 3 The  $\langle 0001 \rangle$  axial angular scans for 1.25 MeV  $d^+$  ions incident on  $\alpha$ -SiC crystal irradiated with  $Ar^+$  ions (200 keV,  $2 \times 10^{16}/cm^2$ ). Backscattering (for Si) and nuclear reactions (for C) yields are normalized to the value under random condition.



$/cm^2$ . The energy window was set just below the amorphous layer, and channeling effect in both Si and C sublattices is observed. Angles labelled  $2\psi_{1/2}$  refer to the full width at the half maximum of the channeling dip curves. The amorphous layer induced by ion irradiation increases the channeling critical angles for both Si and C atoms by 20 % and 35 %, respectively, which reflects the spreading of incident beam while passing through the amorphous layer. The channeling critical angle for C atoms is rather smaller than that for Si atoms in virgin crystal, but after ion irradiation, it has become larger than that for Si atoms in addition to the decrease of channeling dip. These results are not contradictory with the interpretation that C sublattice is compressed along the  $\langle 0001 \rangle$  direction in the interfacial region adjacent to the amorphous layer.

#### Reference

- 1) B. R. Appleton, H. Naramoto, C. W. White, O. W. Holland, C. J. Mchargue G. C. Farlow, J. Narayan and J. M. Williams: Nucl. Inst. and Meth. B1 (1984) 167.

## 2.10 COMPUTER SIMULATION STUDY OF LOW ENERGY RADIATION DAMAGE IN MOLYBDENUM

Terufumi YOKOTA, Yukichi TAJI, and Tadao IWATA

Department of Physics, JAERI

Low energy radiation damage in copper and  $\alpha$ -iron was intensively studied, and importance of the focusing collisions in creating a Frenkel pair was pointed out.<sup>1)</sup> There exists "simple" and "complex" directions in the threshold initial velocity of primary knock-on atoms (PKAs) for creating a Frenkel pair.<sup>2)</sup> In the "simple" direction, displacement of atoms occurs in a single sequence of collisions along low index directions. These includes focusing collisions. On the other hand, in the "complex" direction, the kinetic energy of PKAs is transferred to various directions. We deal with molybdenum and study the anisotropy in the threshold energy by the molecular dynamic method.

The interaction among ions is assumed to be two-body central force. We adopt the interatomic potential of Johnson and Wilson<sup>3)</sup> approximated by the Born-Mayer potential for  $r < 1.7 \text{ \AA}$ . The size of the crystal used in these computations is finite, so we must add some artificial surface forces. Constant, spring, and viscous forces act on the surface atoms. The number of atoms in these calculations is more than 1000.

Main results are represented in figures collectively. In Fig.1, the threshold initial kinetic energy of PKAs to create a Frenkel pair is shown. All directions of PKAs are included in this "triangle", which has the corners corresponding to [100], [110], and [111] axial directions of the crystal. We carried out the computations every 5 degrees within this "triangle". The contour lines are drawn only for the eyeguide. The "simple" directional regions exist around [100] and [111] but not [110]. Threshold energy is almost constant in a "simple" directional region because a single sequence of the focusing collisions is important to form a Frenkel pair in these directions. We also notice that the corresponding figure of the threshold energy for  $\alpha$ -iron<sup>1)</sup> looks rather different. There is a "simple" directional region around [100] for  $\alpha$ -iron but not for molybdenum although they have the same b.c.c. structure. In "complex" directions, the number of Frenkel pairs is not always a monotonously

increasing function of the initial energy of the PKAs. In Fig.2, two examples are shown corresponding to the directions of A and B in Fig.1. In the "complex" directional region, not a single sequence of focusing collisions is important but complex collisions are dominate to create Frenkel pairs. As the initial kinetic energy of PKA increases, focusing becomes more difficult to occur and "simple" directions can change to "complex". Fig.3 shows focusing parameter  $\Lambda$  as a function of initial kinetic energy of PKA at the point C in Fig.1. If we measure angles between the focusing axis and the direction of the maximum velocity of atoms, focusing parameter is defined as a ratio of the two angles of neighbouring atoms in the collision chain. If  $\Lambda$  is smaller than 1.0, focusing occurs. Even if  $\Lambda$  is greater than 1.0 at first, the collisions can sometimes become focusing ones as the maximum kinetic energy of the atoms in a collision chain decreases. In Fig 2(C), the number of Frenkel pairs as a function of the initial kinetic energy of PKA are shown for the direction C in Fig.1. As is seen from this example, the energy region in which one Frenkel pair is created is large in "simple" directions in the threshold energy.

In conclusion, we have obtained the threshold energy of PKAs to create a Frenkel pair for all directions of the initial velocity. The existence of the "simple" and "complex" directions in the threshold initial velocity of PKA is confirmed. There are some difficult problems in these simulations. One problem is the correctness of the interatomic potential which can affects not only the values of the threshold energy but also the final form of the stable positions and directions of defects. Another problem is the treatment of the surface, which comes from the finiteness of the crystal used in these simulations. Because of this limitation, we cannot treat correctly the energy loss at the surface, which is important for the cooling stage of radiation damage events. Also, finite temperature effects, which are not included here, may affect the results.

#### References

- 1) J.B. Gibson, A.N. Goland, M. Milgram, and G.H. Vineyard:  
Phys. Rev. 120 (1960) 1229.  
C.Erginsoy, G.H. Vineyard, and A. Englert: Phys. Rev. 133 (1964) A595.

- 2) J.O.Schiffgens and R.D.Bourquin: J. Nucl. Mater. 69 & 70 (1978) 790.  
W.E. King and R. Benedek: Phys. Rev. B23 (1981) 6335.
- 3) R.A. Jhonson and W.D. Wilson: in Interatomic Potentials and Simulation of Lattice Defects, ed. by P.C. Gehlen et al. (Plenum, 1972).

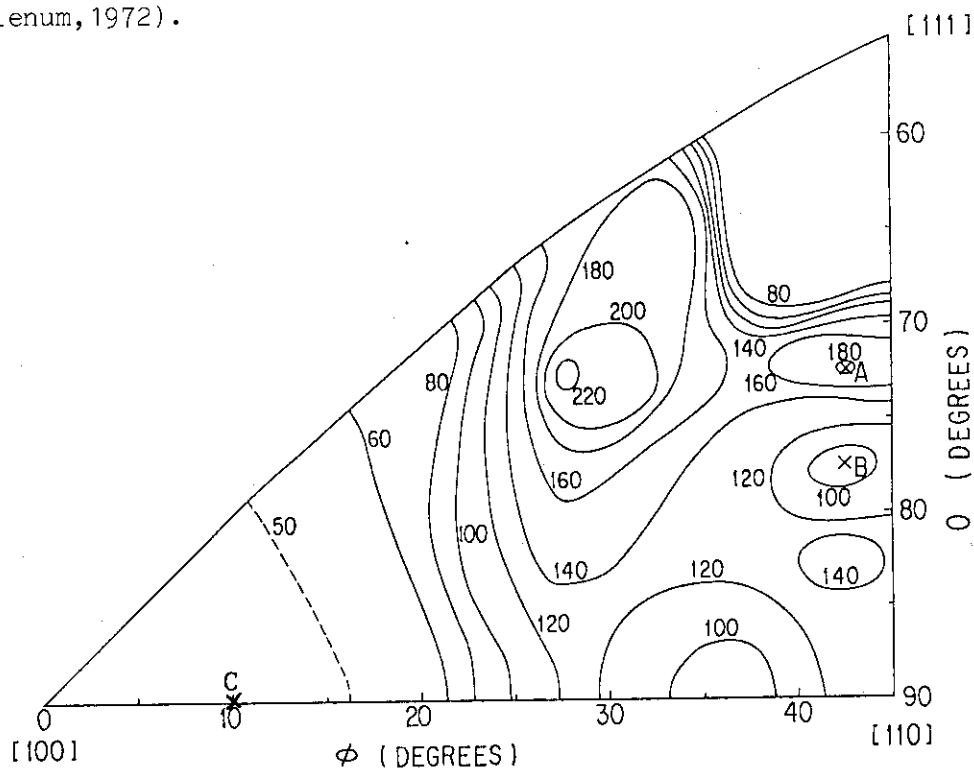


Fig.1 The threshold initial kinetic energy of PKAs to create a Frenkel pair.

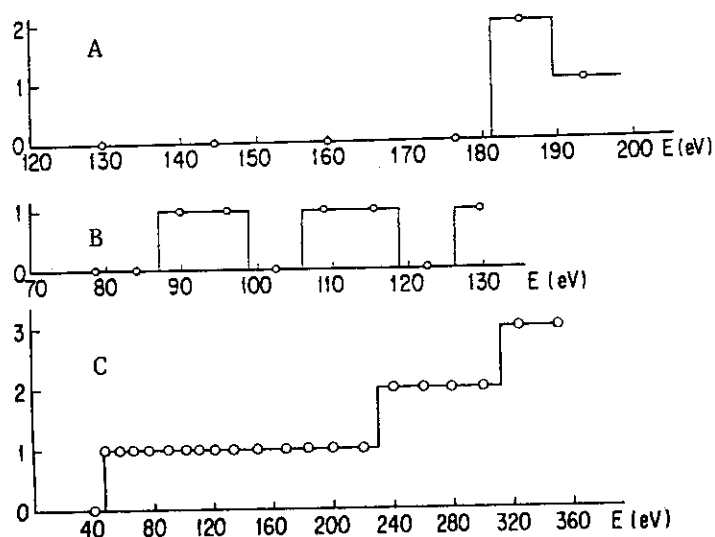


Fig.2 Number of Frenkel pairs as a function of initial kinetic energy of PKAs. Three examples are corresponding to the directions of A, B, and C in Fig.1 respectively.

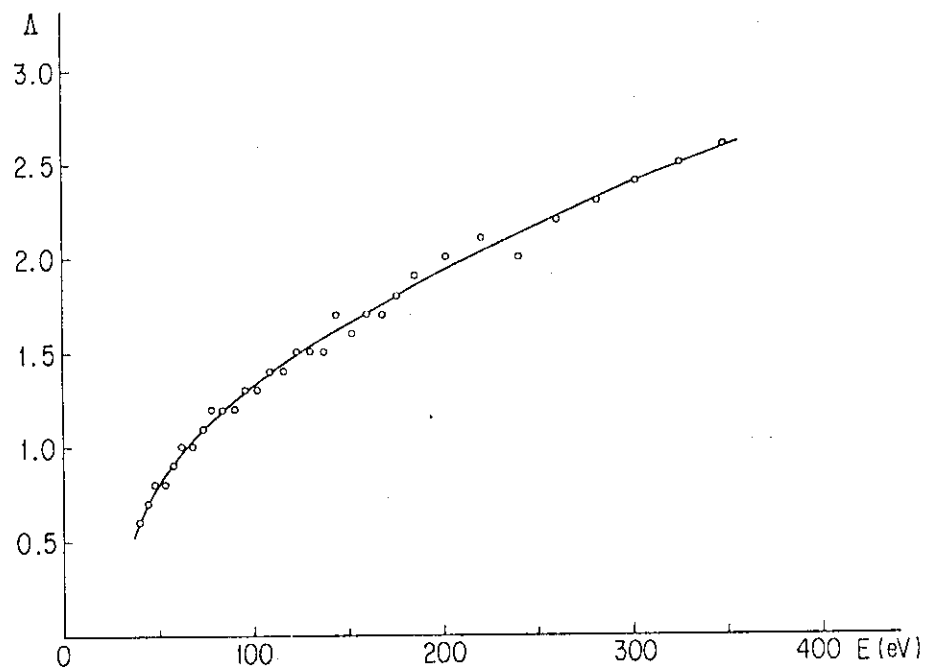


Fig.3 Focusing parameter  $\Lambda$  as a function of initial kinetic energy of PKA at the point C in Fig.1.

## 2.11 ELECTRON CAPTURE AND LOSS CROSS SECTIONS FOR 300 keV TO 1.5 MeV CARBON ATOMS IN COLLISIONS WITH HELIUM

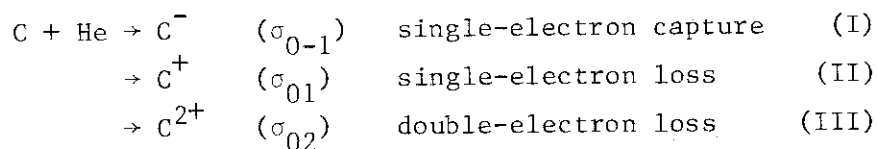
Yohta NAKAI, Masao SATAKA and Akira KIKUCHI\*

Department of Physics, JAERI, \*Faculty of Engineering,  
Ibaraki University

### 1. Introduction

Ions or atoms of carbon, nitrogen and oxygen are common impurities in controlled thermonuclear fusion devices. A knowledge of the cross sections for electron capture and loss in collisions involving such species with helium is directly relevant to the neutral beam probe diagnostics and to the understanding of the mechanisms of energy and particle loss in magnetically confined plasmas.

In the present work we have measured the electron capture and loss cross sections for the processes of



in the energy range 300 keV to 1.5 MeV (25 to 125 keV/amu).

### 2. Experimental approach

The apparatus and the experimental procedure will be described briefly.  $\text{C}^+$  ions produced from carbon monoxide gas in a PIG ion source were accelerated by means of the 2 MV Van de Graaff. The monoenergetic  $\text{C}^+$  beam was introduced into the differentially pumped first collision cell for the production of a neutral carbon beam, which was formed by electron capture of the incident  $\text{C}^+$  from the gas in the cell. Following the first collision cell, the charged components of the beams were removed by a pair of electrostatic deflection plates. The neutral carbon beam was then introduced into the second collision cell, target cell, of 15 cm length. The pressure of target gas was varied by a fine leak valve between  $10^{-6}$  and  $10^{-4}$  Torr during the measurements. The pressure measurement was made with an ionization gauge calibrated against a capacitance manometer (MKS Baratron). The carbon beams emerging from the second collision cell were separated into their charge components by the second pair of electrostatic deflection plates.  $\text{C}^-$ ,  $\text{C}^+$  and  $\text{C}^{2+}$  components were counted with solid-state



detectors as well as the primary neutral component.

The cross sections for electron capture and loss were deduced from the growth rate of the corresponding charge components with the increase of target density, under the assumption that the single-collision is satisfied. The uncertainties in the measured cross sections arise mainly from the following factors; the pressure measurements of the target gas, the deviation from the single-collision condition, the measurements of beam intensities, and the neglect of the excited species possibly included in the incident neutral carbon beam. The resulting uncertainties from above effects are estimated to be within 13% for processes (I), and 10% for (II) and (III).

### 3. Experimental results

Measured cross sections for processes (I), (II) and (III) are given in Table 1, and plotted in Figs. 1 to 3 with results of previous measurements<sup>1,2)</sup>.

Table 1. Electron capture and loss cross sections for C in He

C energy (MeV)	Electron capture		Electron loss	
	$\sigma_{0-1}$ ( $10^{-18} \text{ cm}^2$ )	$\sigma_{01}$ ( $10^{-16} \text{ cm}^2$ )	$\sigma_{02}$ ( $10^{-17} \text{ cm}^2$ )	
0.3	23.5	2.38	4.61	
0.4	23.4	2.38	4.77	
0.5	22.7	2.40	4.47	
0.6	19.0	2.19	4.13	
0.7	16.9	2.17	4.20	
0.8	14.2	2.18	3.88	
0.9	12.5	2.09	3.85	
1.0	11.4	2.02	3.62	
1.1	9.16	1.98	3.42	
1.2	8.55	1.90	3.40	
1.3	7.21	1.88	3.09	
1.4	6.82	1.82	3.07	
1.5	5.75	1.77	2.99	

For process (I), as shown in Fig. 1, the results of Fogel et al.<sup>1)</sup> for low-energy cross sections join more smoothly to the present data than that of Dmitriev et al.<sup>2)</sup>. Our results attain peak value at the energy of about 400 keV beyond the high-energy limit of Fogel et al.

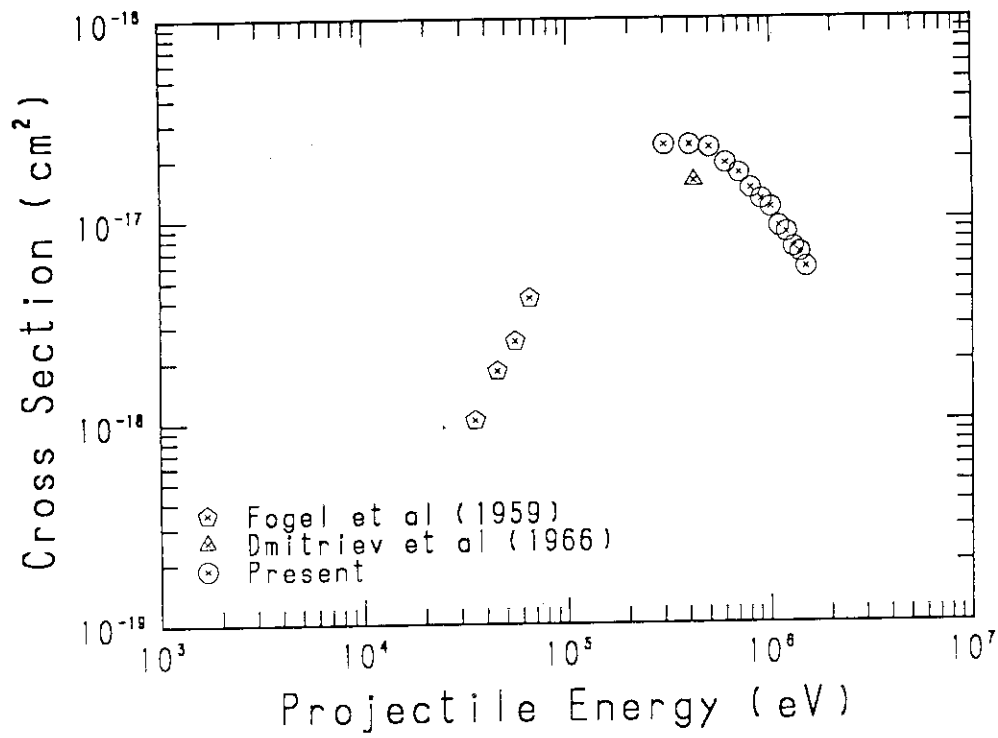


Fig. 1. Single-electron capture cross sections for C in He.

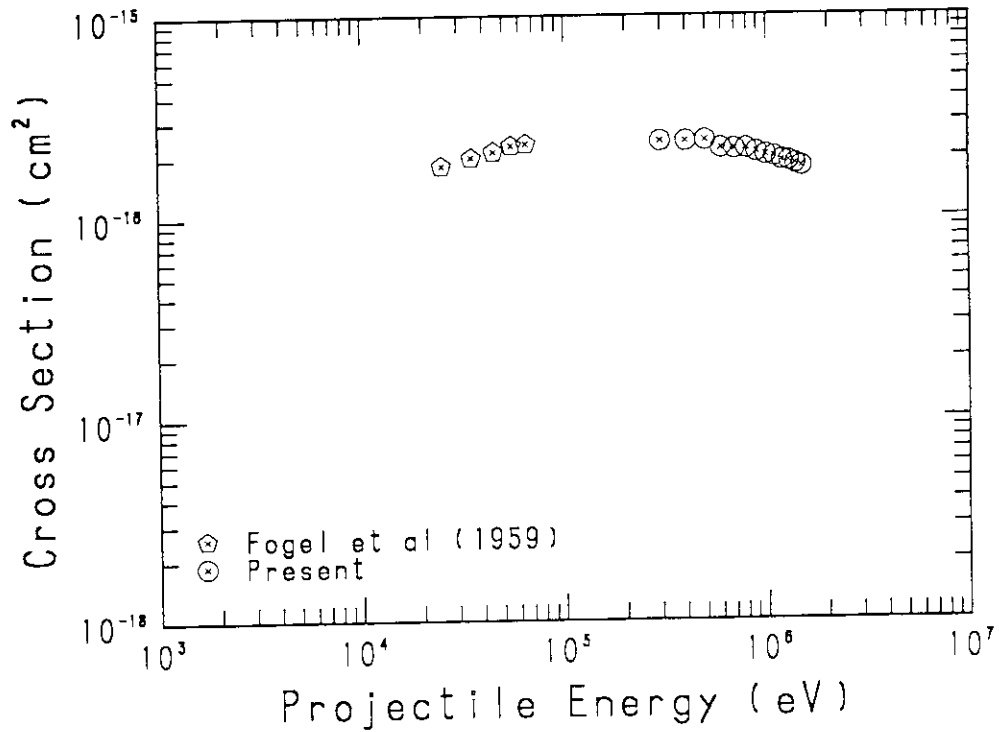


Fig. 2. Single-electron loss cross sections for C in He.

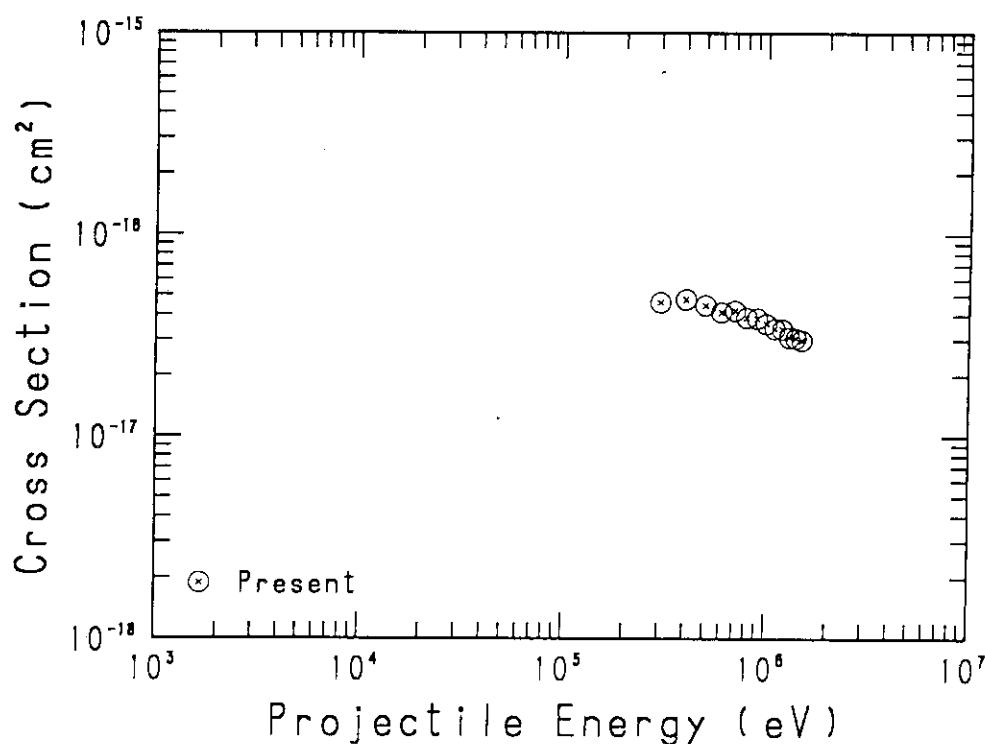


Fig. 3. Double-electron loss cross sections for C in He.

Fig. 2, for process (II), shows that the present results also seem to be consistent with those of Fogel et al<sup>1)</sup>. These results give general shape of the whole curve of one-electron loss cross sections for neutral heavy atoms in the wide range of energy for the first time.

For process (III), as shown in Fig. 3, our results are only the available data at present.

Up to the present day, there has been no theoretical study dealing with above three processes to compare with our experimental results in this energy range.

#### References

- 1) Ya. M. Fogel, V. A. Ankudinov and D. V. Pilipenko: Sov. Phys. JETP 8 (1959) 601.
- 2) I. S. Dmitriev, V. S. Nikolaev, Ya. A. Teplova, B. B. Popov and L. I. Vinogradova: Sov. Phys. JETP 23 (1966) 832.

## 2.12 CHARACTERISTICS OF GAS STRIPPER CELL FOR PRODUCTION OF MULTI-CHARGED IONS

Masao SATAKA, Kiyoshi KAWATSURA and Kunio OZAWA

Department of Physics, JAERI

Collision processes of multi-charged ion impacts on atoms and molecules are of importance not only in basic atomic physics but in many other fields such as plasma physics, astrophysics and laser physics etc.. Nevertheless, studies on this process have been performed only recently, because of the difficulties of production of the multi-charged ions.

Experimental apparatus for production of multi-charged ions has been constructed at 2 MV Van de Graaff accelerator of JAERI. This apparatus can be used to investigate the collision processes through measurements of charge states of ions, X-ray spectra and electron spectra, etc.. Though the multi-charged ions are produced in the RF ion source or the PIG ion source of 2 MV Van de Graaff accelerator, the fraction of multi-charged ions to singly charged ions is so small. Then multi-charged ions must be produced with use of charge changing collisions. The collision targets are to be selected from gases or thin foils. We have selected the gas target because we have found in preliminary experiment that the effective production with gas target are larger than that with thin foil targets.

A general schematic view of the apparatus is shown in Figure 1. The apparatus consists of two parts, namely, the gas cell and the charge selector, each of which is differentially pumped with three independent diffusion pump systems. The singly charged ions produced in the ion source are extracted, accelerated (0.3 - 1.8 MeV) and, after energy analyzed, focused in this apparatus. In this apparatus the ions are electron stripped by the collision of atoms in the gas cell and are magnetically charge selected in the charge selector.

In Figure 2 shown is a block diagram of the pumping system. The main parts of this system are made of Type 304 stainless steel and sealed with use of copper gaskets. The base pressures  $2 \times 10^{-5}$ ,  $1.5 \times 10^{-7}$ ,  $4 \times 10^{-8}$  and  $2 \times 10^{-8}$  Torr in the gas cell, chamber A, B and C, respectively, can be easily attained. A target gas is fed into the gas cell and the gas

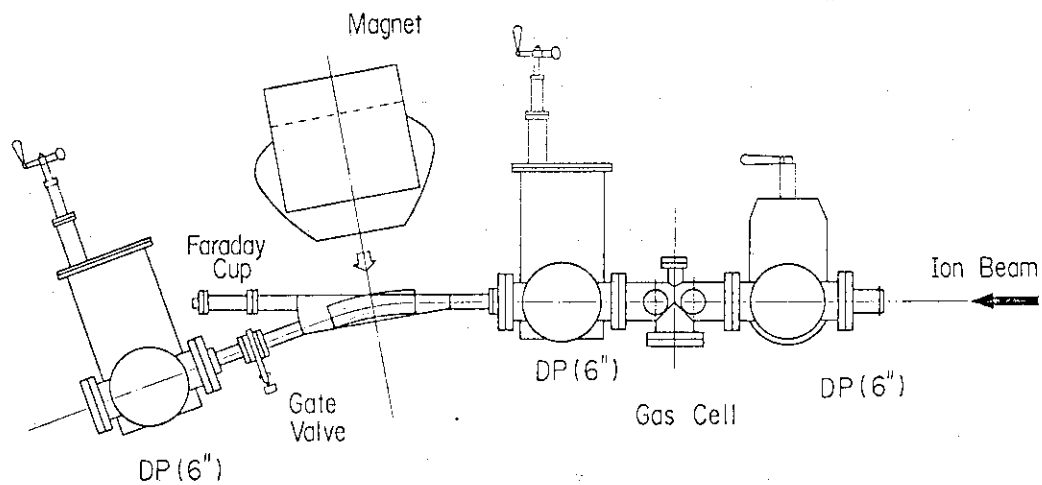


Fig. 1 Schematic view of the apparatus.

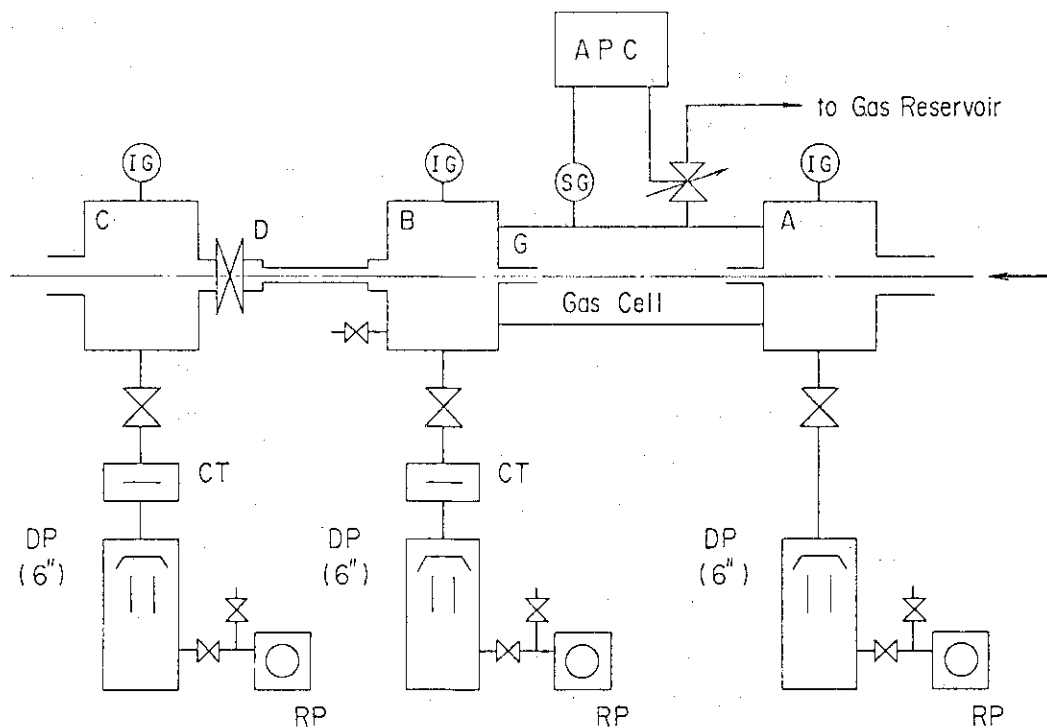


Fig. 2 Schematic view of the pumping system: IG; ion gauge, CT; cold trap, DP; diffusion pump, RP; rotary pump, APC; automatic pressure controller, SG; Schulz gauge.

pressure is controlled automatically. The design principle is that no charge exchange process significantly contributes to the magnetically selected ion beams, even when the gas is fed into the gas cell. Therefore gas effused from the gas cell is pumped by two 6" diffusion pump systems through 5 mm diameter and 100 mm long conduit tubes. In Figure 3 shown is the gas pressures of chamber A, B and C assigned as a function of gas pressure in the gas cell. From the figure, it is found that the pressure differential of 1000 was obtained between gas cell and both chamber A and B.

A magnet is used for the charge selector. Radius of central orbit of the magnet is 650 mm and the deflection angle is  $20^\circ$ . The mass energy product of the magnet is 18 MeV.amu same as the magnets equipped at 2 MV Van de Graaff accelerator of JAERI. Then, the magnet has a capability of analyzing the ions which is introduced from the 2 MV Van de Graaff accelerator. No slit is used because the fine resolution is not required but the large transmission is.

Using the apparatus, we have performed the measurements of charge state fractions of helium ions in the energy region between 0.3 and 1.5 MeV passing through the argon gas, as a function of target pressure. Ion beams were introduced to the gas cell in which the ion beams were charge-changed by argon gas and then charge-selected by the magnet. The target pressure was measured by means of a Schulz gauge and an ionization gauge. The ion beam currents were measured by a Faraday cup. In Figure 4 shown are the charge fractions of  $\text{He}^0$ ,  $\text{He}^+$  and  $\text{He}^{++}$  in the ion energy 1.0 MeV. The charge fractions show the equilibrium at the gas cell pressure higher than  $5 \times 10^{-2}$  Torr. Then the pressure of the chamber C is about  $9 \times 10^{-7}$  Torr, the charge exchange processes contributed to the magnetically selected ion beams is estimated to be negligibly small. The figure also shows that 66% of  $\text{He}^+$  beam is changed to  $\text{He}^{++}$  beam in this apparatus and the apparatus works well as expected.

Ion beams of C, N, O, Ne and Ar atoms are now accelerated at 2 MV V.d.G. of JAERI. It is also expected that the highly ionized ions of such atoms are obtainable in the MeV energy range. We intend to measure the electron and X-ray spectra ejected by multi-charged ion impacts on atoms and molecules.

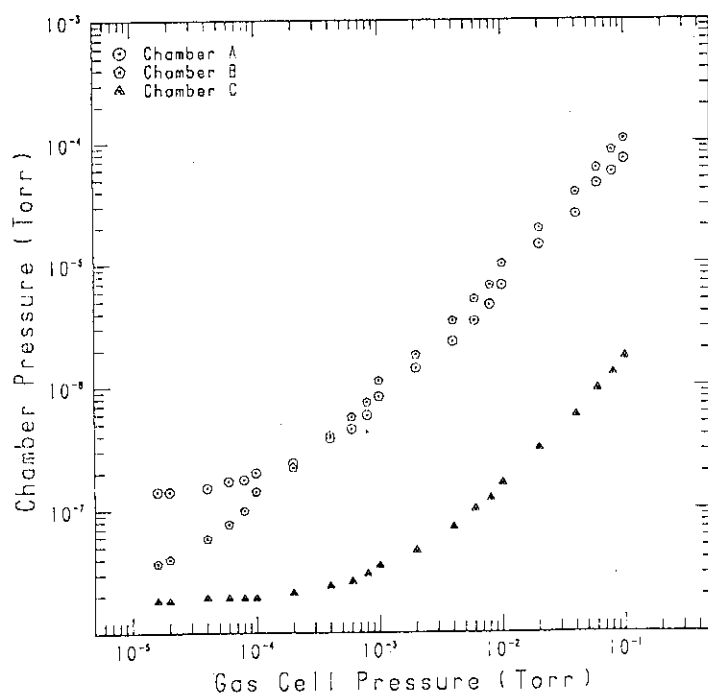


Fig. 3 The gas pressure of chambers A, B and C, assigned in Fig. 2, as a function of gas cell pressure.

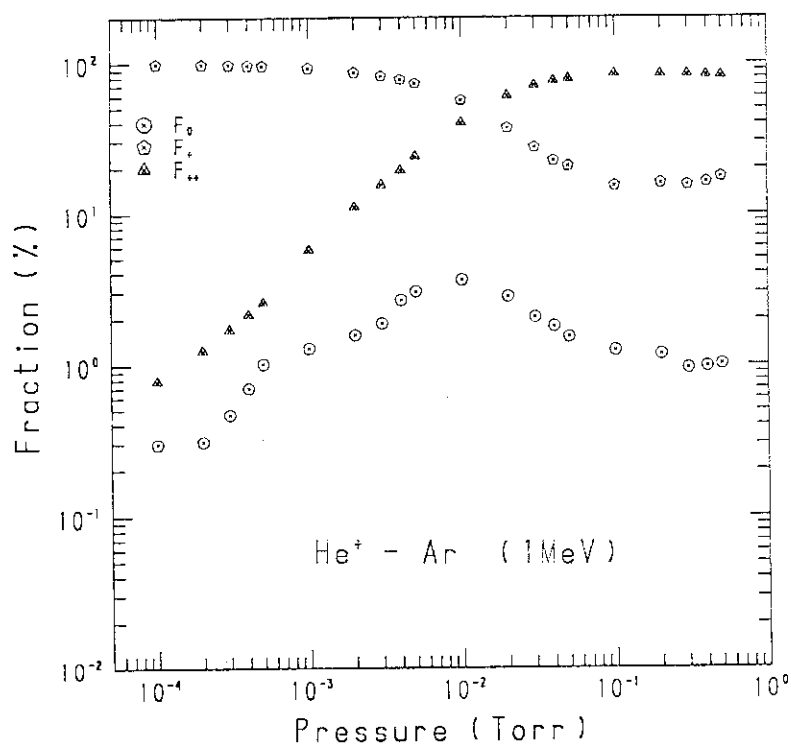


Fig. 4 Charge fraction of helium ions with energy 1.0 MeV in argon.

### III RADIATION EFFECTS IN MATERIALS



## 3.1 IRRADIATION EFFECTS WITH HEAVY IONS ON ALKALI HALIDES (II)

Akira KIKUCHI\*, Hiroshi NARAMOTO\*\* and Kunio OZAWA\*\*

\*Faculty of Engineering, Ibaraki University and \*\*Department of Physics, Japan Atomic Energy Research Institute

The use of high-energy heavy ions has been increasingly interested in the study of radiation damage for the high efficiency of defect production. The interaction between high-energy heavy ions and solid atoms introduces radiation damage into insulators along the track of the ions, mainly by dense electronic excitation process. This process can be visualized especially in alkali halides because they sustain radiation damage primarily by the process and the defects produced spread in the irradiated area on a large scale, although the spread is limited to the range of incident ions. Heavy ions penetrating into alkali halides are reasonably expected to leave their tracks and the density of the defects along the tracks varies as a function of the penetration depth of the ions from the surface<sup>1)</sup>. The distribution of defects along the ion tracks can give important information on the defect production process and can be connected with the energy loss processes of the incident ions.

In the previous report<sup>2)</sup> the results were given on the direct measurement of the depth profile of color centers in LiF and NaF crystals irradiated with 180 MeV  $^{63}\text{Cu}^{11+}$  ions. The results indicated that the depth of the damaged layer was somewhat longer than the mean projected range and that the region where Li metallic colloids precipitated, closely related to the depth of the maximum in the electronic energy loss.

In the present report are presented the experimental results on the depth-dependent distribution of defects obtained from the irradiation by 100 MeV  $^{12}\text{C}^{5+}$  ions in the same crystals. In addition to a microscopic approach, micro-hardness was measured as the indication of the radiation damage. A theoretical deposited energy curve calculated by the modified E-DEP-1 code<sup>3)</sup> was employed for the comparison of the experimental data on the depth distribution of the radiation-induced defects.

LiF and NaF crystals obtained from the Harshaw Chemical Co. were cleaved on {100} into platelets of dimensions approximately  $10 \times 8 \times 1 \text{ mm}^3$ .

Specimens were irradiated at liquid nitrogen temperature with 100 MeV  $^{12}\text{C}^{5+}$  ions from the JAERI tandem accelerator and received the total dose of  $7.0 \times 10^{12}$  ions/cm<sup>2</sup>. The temperature of the specimens was estimated to be near 100 K. Irradiation experiments by 1.8 MeV protons were also carried out at room temperature (RT) using a 2 MV Van de Graaff accelerator to facilitate the identification of defects in an atomic level. Optical absorption measurements were made at RT in the wavelength region 240 - 700 nm with an Olympus MMSP-TU system at the measuring spot of 2  $\mu\text{m}$  in diameter. Micro-hardness measurements in the Knoop test were performed at RT with an Akashi micro-hardness tester at the applied load of 10g and the period of indentation time was taken to be 30s after the full load was applied.

Fig. 1 shows optical absorption spectra taken at a position of 5, 110 and 140  $\mu\text{m}$  from the irradiated surface in the LiF crystal. Absorption bands

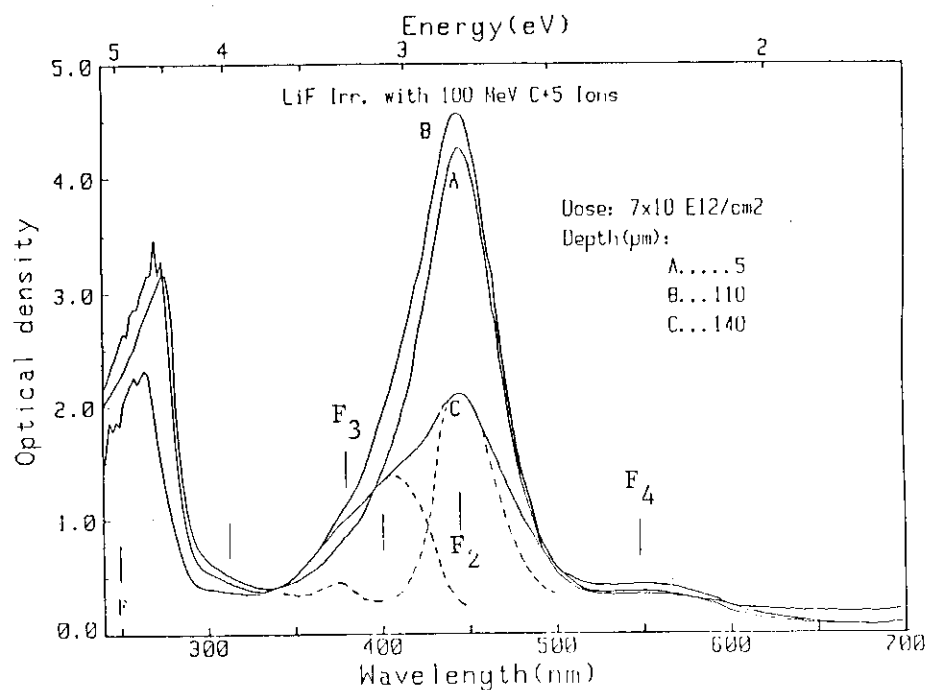


Fig. 1 Depth variation of optical absorptin spectra of LiF crystals irradiated with carbon ions.

are observed at 250, 380, 444 and 548 nm, which are attributed to F, F<sub>3</sub>, F<sub>2</sub> and F<sub>4</sub> centers, respectively. A broad absorption with half-width of ca. 0.38 eV can be discernible at about 400 nm, as is seen from the curve taken at the depth of 140  $\mu\text{m}$ , being due to Li metallic colloids.

In Fig. 2 are shown both the depth-dependent distribution of radiation-induced defects responsible for the F, F<sub>2</sub>, F<sub>3</sub>, F<sub>4</sub>, 380 nm and 400 nm bands

in optical density (solid lines) and the depth distribution in micro-hardness (open circles). A broken line shows a deposited energy curve for 100 MeV carbon ions vs. path length.

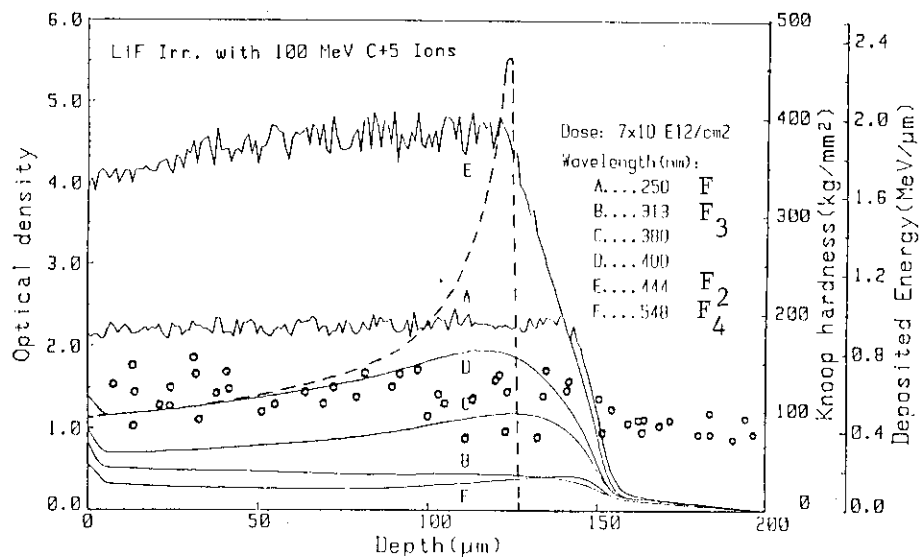


Fig. 2 Depth-dependent distribution of carbon ion damage in optical density and micro-hardness in LiF crystals.

The depth profile of both the F<sub>2</sub> and the center due to the Li colloids attain their maxima at the depth of ca. 120 μm. In comparison with the absorption spectrum taken at 140 μm, it can be surmised that the precipitate region of metallic colloids nearly coincides with the depth where the incident ions deposit their maximum energies in the electronic excitation process. The concentrations of F and F<sub>2</sub> centers are deep-distributed across the projected range of 124 μm and the depth of the damaged layer is ca. 20% longer than the calculated range. This suggests some of the subtleties of the last stage of energy loss. It can be concluded that secondary radiation causes radiation damage beyond the penetration depth.

The depth-dependent distribution of Knoop hardness seems to be similar to that of optical density of the 400 nm band, suggesting that the defects associated with the band is due to a precursor of the colloid production. The change in relative hardness is ca. 1.29, being small. It can be considered that the recovery process of radiation-induced defects due to the rise in temperature during irradiation possibly decreases the hardening events by colloid nucleation.

In NaF crystals, unlike LiF, some of differences are found in the de-

tails of the depth-dependent distribution of the radiation-induced damage but no colloidal band is observed. The damage feature is described by the non-uniform damage distribution, and the damage level decreases with depth from the surface. The damage distribution curves yield the penetration depth of ca. 150  $\mu\text{m}$  which agrees well with the calculated value of 147  $\mu\text{m}$ . The relative increment in hardness is ca. 1.24. Especially in the surface layer within the depth of about 20  $\mu\text{m}$ , the hardness decreases from that of about 55  $\text{kg/mm}^2$  in the unirradiated area.

#### References

- 1) J. M. Loman and R. B. Murray: Radiation Effects 52 (1980) 1.
- 2) H. Naramoto, A. Kikuchi and K. Ozawa: "JAERI TANDEM Annual Report 1983" JAERI-M 84-129 (1984).
- 3) T. Aruga: JAERI-M 83-226 (1983).

### 3.2 IRRADIATION DAMAGE IN LITHIUM OXIDE

Kenji NODA, Yoshinobu ISHII, Hisayuki MATSUI\*, Mikio HORIKI\*,  
Naomi OBATA\*, Masanobu ARAI\* and Hitoshi WATANABE

Department of Fuels and Materials Research, JAERI, \*Faculty  
of Engineering, Nagoya University

#### 1. Introduction

Lithium oxide ( $\text{Li}_2\text{O}$ ) is a prime candidate of tritium breeding blanket materials of an experimental fusion reactor designed at Japan Atomic Energy Research Institute (JAERI)<sup>1)</sup>. During operation of the fusion reactor, severe irradiation damage will be introduced in  $\text{Li}_2\text{O}$  by neutrons with energies up to 14 MeV, tritons (2.7 MeV) and helium ions (2.1 MeV) produced by  ${}^6\text{Li}(\text{n},\alpha){}^3\text{H}$  reactions. Recently, the swelling of  $\text{Li}_2\text{O}$  sintered pellets has been observed in a fast-neutron irradiation test using EBR-II (fast breeder reactor)<sup>2)</sup>, although the neutron spectrum of EBR-II is different from that of the fusion reactor. So, knowledge of irradiation defects is required to evaluate the irradiation integrity such as swelling under the irradiation condition of fusion reactor. In order to understand the irradiation defects in  $\text{Li}_2\text{O}$ , the defects have been studied using thermal-neutron irradiation and oxygen-ion irradiation<sup>3-6)</sup>.

In the production of irradiation defects in  $\text{Li}_2\text{O}$  as a tritium breeding blanket material of the fusion reactor, oxygen atoms are displaced as one kind of primary knock-on atoms (PKA) by the fast neutrons, tritons and helium ions due to  ${}^6\text{Li}(\text{n},\alpha){}^3\text{H}$  reactions. By this PKA many irradiation defects are introduced. Consequently, oxygen-ion irradiation is essential to investigate the production of defects. In this study, the production process and the fundamental properties of the irradiation defects in  $\text{Li}_2\text{O}$ , irradiated directly with oxygen ions as one kind of PKA, were investigated by the optical absorption method.

#### 2. Experimental

Specimens used were  $\text{Li}_2\text{O}$  single crystals. The single crystals were grown from  $\text{Li}_2\text{O}$  sintered rods by the floating zone method, using an infrared imaging furnace in an argon atmosphere. The detailed procedure was described elsewhere<sup>7)</sup>. The single crystals were cleaved on a  $\{111\}$  plane or cut with

a diamond cutter into disk specimens (about  $0.5 \text{ mm} \times 6 \text{ mm}\phi$ ) for optical absorption measurement. These specimens were heated at 1270 K for 5 to 10 h in a vacuum better than  $1 \times 10^{-3} \text{ Pa}$  to decompose  $\text{LiOH}$  and  $\text{Li}_2\text{CO}_3$  at the surface of the specimens and to remove the residual strain.

Oxygen-ion irradiation was carried out using a tandem accelerator or a 2 MV Van de Graaff (VDG) accelerator at JAERI. In case of the tandem accelerator irradiation, the specimens were irradiated to a fluence from  $10^{18}$  to  $10^{20} \text{ ions/m}^2$  at an ion energy of 100 MeV. In case of the VDG accelerator irradiation, the irradiation was done to a fluence in the range from  $7 \times 10^{20}$  to  $1.9 \times 10^{21} \text{ ions/m}^2$  at energies from 0.5 to 1.25 MeV. After the irradiation, the optical absorption measurement was made at room temperature with Cary model 14 R.

### 3. Results and discussion

Fig. 1 shows optical absorption spectra of  $\text{Li}_2\text{O}$  single crystals irradiated to  $3 \times 10^{19}$  and  $4 \times 10^{18} \text{ ions/m}^2$  by oxygen ions with an energy of 100 MeV. A remarkable absorption band was observed at about 310 nm in wave length, in addition to the fundamental optical absorption edge below 250 nm. The intensity of the 310 nm band increased with the ion fluence in the examined fluence range. Besides the 310 nm band, relatively weak bands at 375 and 570 nm were observed at the high fluence. These three bands were also observed for  $\text{Li}_2\text{O}$  single crystals and the sintered pellets irradiated from  $10^{19}$  to  $10^{22} \text{ thermal neutrons/m}^2$  in JRR-2 or  $-4^3$ ). The 310 nm band was determined to be  $\text{F}^+$ -centers (an oxygen-ion vacancy trapping an electron) from the following experimental result. The isochronal annealing behavior of this band is quite similar to that of  $\text{F}^+$ -centers observed with ESR method for  $\text{Li}_2\text{O}$  irradiated by

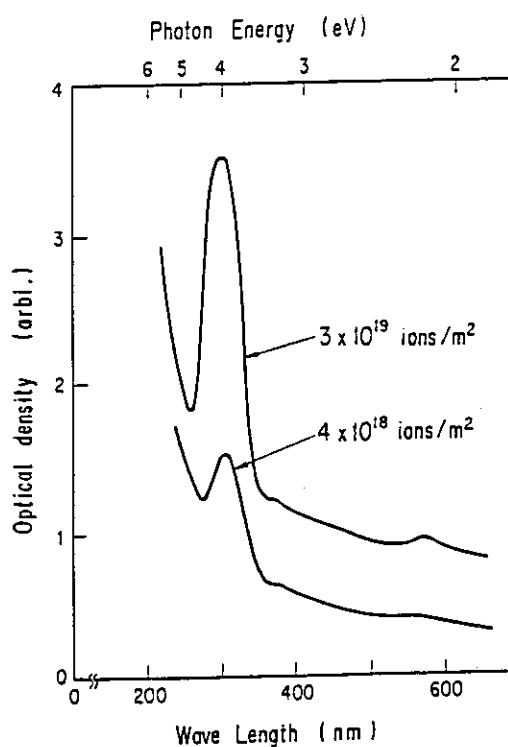


Fig.1 Optical absorption spectra of  $\text{Li}_2\text{O}$  irradiated to  $3 \times 10^{19}$  and  $4 \times 10^{18} \text{ ions/m}^2$  by oxygen ions with an energy of 100 MeV.

thermal neutrons<sup>5)</sup> and by oxygen ions, as shown in Fig. 5.

In case of oxygen-ion irradiation using the VDG accelerator, the 310 nm band was also observed for the specimens irradiated to a fluence from  $7 \times 10^{20}$  to  $1.9 \times 10^{21}$  ions/m<sup>2</sup> at the ion energy range from 0.5 to 1.25 MeV. At the high fluence, the weak 570 nm band was observable in addition to the 310 nm band.

Fig. 2 shows the relationship between the intensity of the 310 nm band and the incident ion energies at various fluences. In this figure, typical examples of the intensity of 310 nm band for the specimens irradiated by the tandem accelerator are shown as well as the data obtained with the VDG irradiation. The intensity increased considerably with the incident ion energy. From such a large energy dependence of the intensity, a large number of the  $F^+$ -centers can be conjectured to be introduced not only by displacement due to nuclear collision but also by a certain mechanism associated with the electronic excitation process due to the incident oxygen ions, as described below. Fig. 3

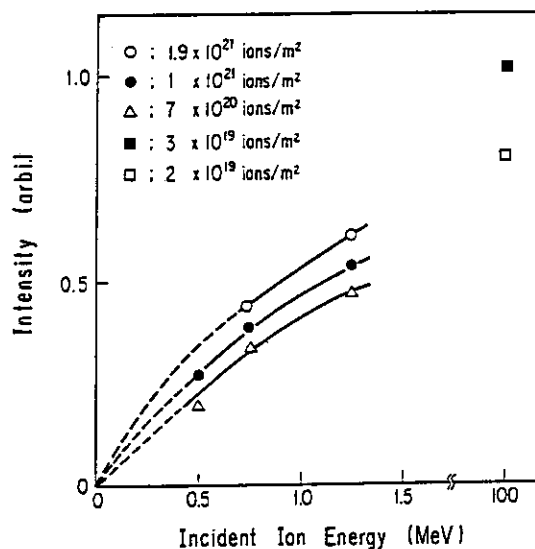


Fig. 2 Intensity of the 310 nm band as a function of the ion energies.

shows electronic and nuclear energy losses as a function of oxygen ion energies. The electronic energy loss increases considerably with the energy, while the nuclear energy loss increases very slightly. This suggests that displacement per atom (dpa) due to the nuclear energy loss (nuclear collision) in  $\text{Li}_2\text{O}$  irradiated with oxygen ions does not so change with the incident ion energy. Fig. 4 shows dpa as a function of the depth from the surface of the specimen along the incident ion beam, which was calculated by E-DEP-81 code<sup>8)</sup> on the assumption that displacement of atoms in  $\text{Li}_2\text{O}$  during the oxygen-ion irradiation was attributed only to the nuclear collision. Although the projected range increases considerably with the incident ion energy, the integrated dpa from the surface to the projected range increases very slightly. The ratio between the integrated dpa at 1.25 MeV and that at 0.5 MeV

is about 1.1, and even the integrated dpa at 100 MeV is only 1.8 times as large as that at 0.5 MeV. By such a slight increase with the energy, it is difficult to explain the large energy dependence of the intensity in Fig. 2. On the other hand, the electronic energy loss increases considerably with the incident ion energy, as shown in Fig. 3. When the  $F^+$ -centers are assumed to be introduced by a certain mechanism associated with the electronic excitation process, the large energy dependence in Fig. 2 can be explained easily. Especially, it can be well understood that the number of  $F^+$ -centers in  $Li_2O$  irradiated to only  $2 \times 10^{19}$  ions/m<sup>2</sup> at the incident energy of 100 MeV is larger than that irradiated to  $1.9 \times 10^{21}$  ions/m<sup>2</sup> at 1.25 MeV. Thus, the electronic excitation process is considered to play an important role in the production of irradiation defects in  $Li_2O$  irradiated by oxygen ions.

On the other hand, for  $Li_2O$  irradiated to  $2.4 \times 10^4$  C/kg ( $10^8$  R) by  $^{60}Co$   $\gamma$ -ray, the 310 nm band and the ESR spectra of  $F^+$ -centers were not observed<sup>3,5)</sup>. This implies that the defect production due to the electronic excitation process hardly occurs during  $\gamma$ -ray irradiation as in alkaline-earth oxides<sup>9)</sup>, in contrast with the case of the oxygen-ion irradiation. To clarify the production mechanism of irradiation defects in  $Li_2O$ , further investigation is required.

The recovery behavior of the 310 nm band ( $F^+$ -centers) and the 570 nm band was investigated by the isochronal and the isothermal annealing methods.

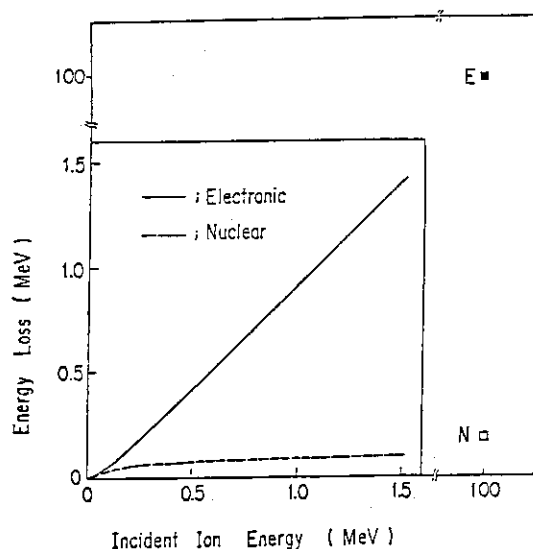


Fig. 3 Electronic and nuclear energy losses as a function of the oxygen ion energies.

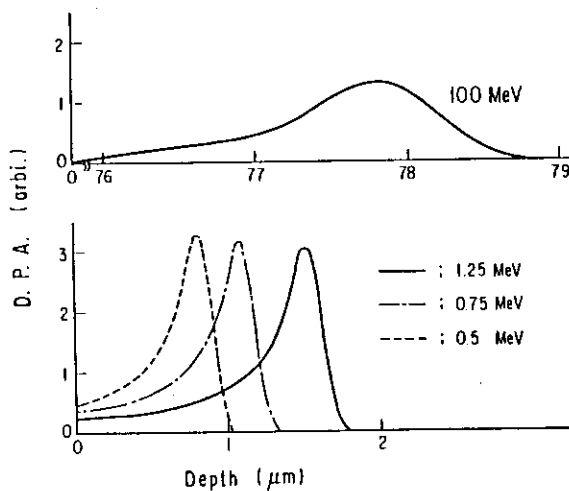


Fig. 4 Relationship between dpa due to nuclear collision and depth.



In the isochronal annealing experiments, the specimens, irradiated to  $7 \times 10^{18}$ ,  $3 \times 10^{19}$  and  $1.5 \times 10^{20}$  ions/m<sup>2</sup> at an ion energy of 100 MeV, were heated at each annealing temperature for 1800 s and the temperature was raised stepwise to 670 K at intervals of about 50 K. The defects in the former two specimens were observed with the optical absorption method, while the F<sup>+</sup>-centers in the latter specimen were detected by the ESR method. Fig. 5 shows the intensity of the 310 nm band, the 570 nm band and the ESR spectra of F<sup>+</sup>-centers normalized to those before the annealing as a function of annealing temperature. Both the 310 nm band and the ESR spectra of F<sup>+</sup>-centers began to decrease at about 520 K and almost disappeared at about 670 K. On the other hand, the 570 nm band increased once around 420 K and vanished at about 670 K.

In Fig. 6 the above results are compared with those in case of the specimens irradiated to  $4 \times 10^{20}$  and  $2.2 \times 10^{21}$  thermal neutrons/m<sup>2</sup> <sup>3)</sup>. The temperature at which the recovery occurred shifts to the high temperature side in case of the specimens irradiated by oxygen ions in the present study. The concentration of the F<sup>+</sup>-centers in Li<sub>2</sub>O irradiated to a fluence from  $7 \times 10^{18}$  to  $1.5 \times 10^{20}$  ions/m<sup>2</sup> by oxygen ions with an energy of 100 MeV can be estimated to be higher than those irradiated to the above thermal-neutron fluences <sup>6)</sup>. The recovery of high concentrated

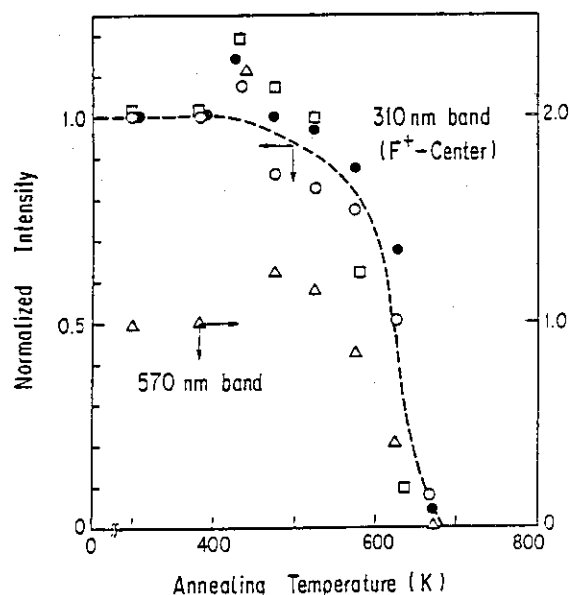


Fig. 5 Behavior of the 310 nm band (F<sup>+</sup>-centers) and the 570 nm band in isochronal annealing experiments. ○, △;  $3 \times 10^{19}$  ions/m<sup>2</sup>, ●;  $7 \times 10^{18}$  ions/m<sup>2</sup>, □;  $1.5 \times 10^{20}$  ions/m<sup>2</sup>.

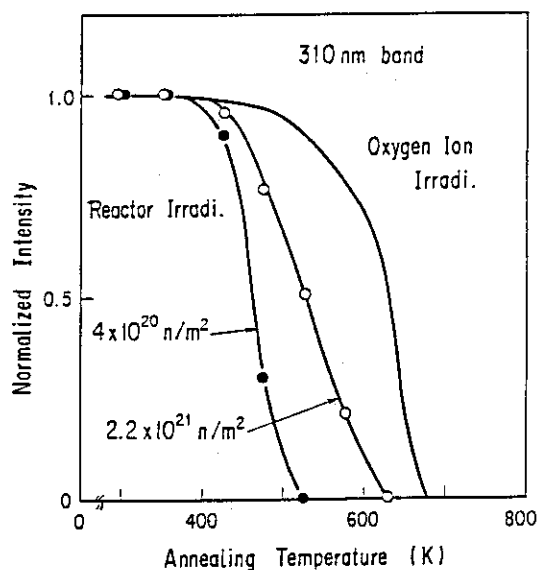


Fig. 6 Comparison between isochronal annealing behavior of the 310 nm band in oxygen-ion irradiated specimens and that in thermal-neutron irradiated specimens.

$F^+$ -centers is delayed in comparison with that of low concentration. From this consideration, decrease in the  $F^+$ -centers during the annealing seems to be attributed not to the formation of F aggregate centers by gathering the  $F^+$ -centers but to the annihilation of the  $F^+$ -centers by migration of oxygen interstitial atoms from the surrounding.

Fig. 7 shows the behavior of the 310 nm band in the isothermal annealing experiments at 578, 600 and 628 K for the specimens irradiated to  $3.8 \times 10^{19}$  ions/m<sup>2</sup> by oxygen ions with an energy of 100 MeV. In the experiments, the activation energy for recovery of the  $F^+$ -centers was determined to be 135 kJ/mol. This value is in very good agreement with the activation energy for recovery of the  $F^+$ -centers in Li<sub>2</sub>O irradiated by thermal neutrons<sup>5)</sup>.

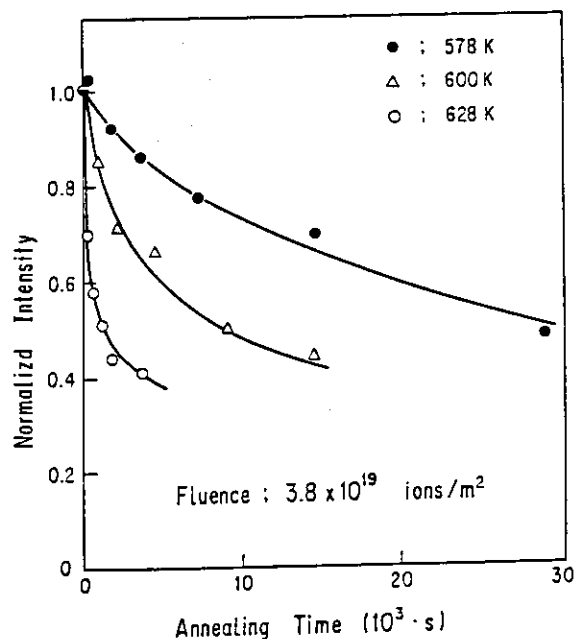


Fig. 7 Behavior of the 310 nm band in isothermal annealing experiments.

#### References

- 1) T. Tone, N. Fujisawa, Y. Seki, H. Iida, K. Tachikawa, M. Sugihara, A. Minato, S. Nishio, T. Yamamoto, K. Kitamura, K. Ueda, S. Saito, R. Shimada, Y. Matsuda, Y. Naruse, S. Shimamoto, S. Tamura, M. Yoshikawa and K. Tomabechi: Nuclear Technology/Fusion 4 (1983) 573.
- 2) G. W. Hollenberg: J. Nucl. Mater. 122 & 123 (1984) 896.
- 3) K. Uchida, K. Noda, T. Tanifuji, S. Nasu, T. Kirihara and A. Kikuchi: phys. stat. sol. (a) 58 (1980) 557.
- 4) K. Noda, K. Uchida, T. Tanifuji and S. Nasu: J. Nucl. Mater. 91 (1980) 234.
- 5) K. Noda, K. Uchida, T. Tanifuji and S. Nasu: Phys. Rev. B 24 (1981) 3736.
- 6) K. Noda, T. Tanifuji, Y. Ishii, H. Matsui, N. Masaki, S. Nasu and H. Watanabe: J. Nucl. Mater. 122 & 123 (1984) 908.
- 7) I. Shindo, S. Kimura, K. Noda, T. Kurasawa and S. Nasu: J. Nucl. Mater. 79 (1979) 418.
- 8) T. Aruga: JAERI-M 83-226 (1983).
- 9) B. Henderson and J. E. Wertz: Advances in Physics 17 (1968) 749.

### 3.3 IR, UV, and ESR Studies on Polyvinylidene Fluoride Irradiated with Heavy Ions.

Yoshihide KOMAKI\*, Shinichi OHNO\*, Norio MORISHITA\*\*, Tadao SEGUCHI\*\*

\*Department of Chemistry and \*\*Takasaki Radiation Research Establishment, JAERI.

#### Introduction

In the polymeric track detectors, the products along the trajectories of heavy ions have been left vague, although there has been a few of discussion about polycarbonate and polymethylmethacrylate.<sup>1)</sup> The examination is indispensable for the production of heavy ion track microfilter. Effects of heavy ions irradiation on polyvinylidene fluoride (PVDF) were studied by IR, UV, and ESR measurements in comparison with that of  $\gamma$ -ray irradiation.

#### Experimental

Samples were the commercial PVDF films of 9 and 100  $\mu\text{m}$  in thickness. The 9 and 100  $\mu\text{m}$  thick films were irradiated with the  $\text{Au}^{13+}$  ions (200 MeV) and with the  $\text{Ni}^{10+}$  ions (150 MeV), respectively.

#### Results and Discussion

The IR spectra of irradiated PVDF are shown in Fig. 1. The absorption at  $1710\text{ cm}^{-1}$  increases by  $\text{Au}^{13+}$  irradiation in vacuo, and the absorption at  $1750\text{ cm}^{-1}$  increases by  $\text{Au}^{13+}$  and  $\gamma$ -ray irradiation in the presence of oxygen. Though the former absorption had been already assigned to the double bond formed in the molecular chains,<sup>2)</sup> this was also confirmed from the decrease of the absorption by the reaction of double bonds with bromine and the exposure to UV in oxygen. On the other hand, the absorption at  $1750\text{ cm}^{-1}$  was assigned to a carbonyl group, because it increased by the irradiation in oxygen and decreased by the etching with alkaline solution.

The UV spectra are shown in Fig. 2. The spectrum on the  $\text{Au}^{13+}$  irradiated sample is rather smooth but with a shoulder at 225 nm as compared with that of  $\gamma$ -ray. Several peaks owing to the conjugated double bonds such as diene, triene, and so on, were clearly perceptible in the range 200–400 nm on a low dose of  $\gamma$ -ray irradiation, but they smeared out at a high dose. This smearing effect was caused by the decrease of crystallinity. Therefore, the smooth

spectrum in the  $\text{Au}^{13+}$  irradiated sample would be reflecting the conjugated double bonds trapped in the defected crystallites.

The ESR spectrum of  $\text{Ni}^{10+}$  irradiated PVDF is shown in Fig. 3. This resembles to the spectrum of high dose of  $\gamma$ -ray,<sup>3)</sup> but it was difficult to compare precisely to each other because the temperature of  $\text{Ni}^{10+}$  irradiation was higher than that of  $\gamma$ -ray. The spectrum means that the radicals are trapped in the conjugated double bonds.

In tentative conclusion from IR, UV, and ESR measurements, the heavy ion irradiation induced many double bonds in a heavy ion track by the formation of conjugated double bonds and by the decrease of the crystallinity as seen

in PVDF received high doses of  $\gamma$ -ray. The free radicals trapped in the conjugated double bonds react with oxygen in the presence of oxygen, and the oxidized products can be easily dissolved in the alkaline solution.

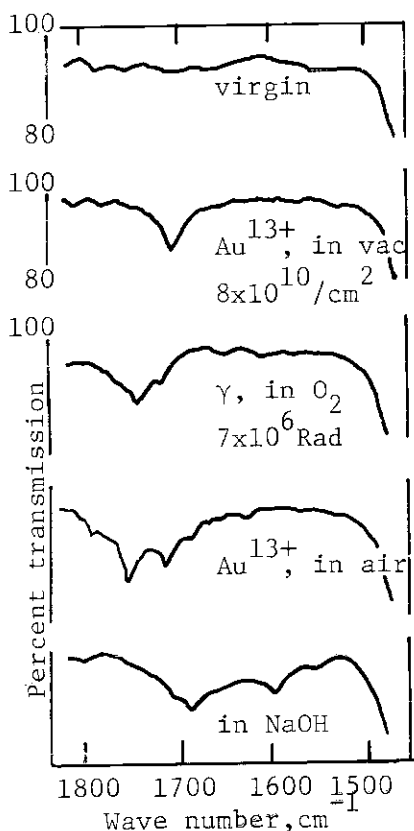


Fig. 1 IR Spectra of PVDF.

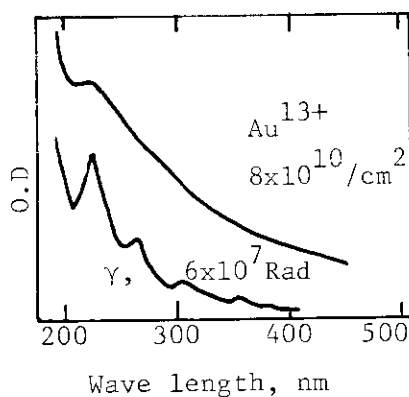


Fig. 2 UV Spectra of PVDF irradiated with the  $\text{Au}^{13+}$  ions and  $\gamma$  ray.

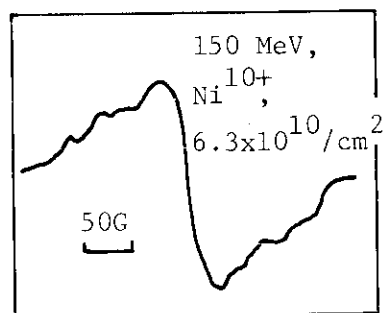


Fig. 3 ESR Spectrum at 77K of PVDF irradiated with the  $\text{Ni}^{10+}$  ions.

#### References

- 1) A. Chambaudet and J. Roncin: Solid State Nuclear Track Detectors, 11th Conf, Bristol, 1981, pp. 15-21.
- 2) M. Hagiwara, G. Ellinhorst, and D.O. Hummel: Makromol.Chem, 178, 2913 (1977).
- 3) T. Seguchi, K. Makuuchi, T. Suwa, N. Tamura, T. Abe, and M. Takehisa: Nippon Kagaku Kaishi. 1974, 1309 (1974).

### 3.4 RESIDUAL RADIOACTIVITIES IN SILICON AND GERMANIUM IRRADIATED WITH VARIOUS HIGH-ENERGY HEAVY-IONS

Eiji SAKAI and Hideo NAKATANI\*

Department of Reactor Engineering, JAERI,

\*Faculty of Engineering, Toyama University

Semiconductor detectors are known to be sensitive to radiation damage which might be annealed by heating at an elevated temperature. In high-energy heavy-ion detection with semiconductor detectors, nuclear reactions can be expected in the semiconductor materials themselves to increase background counting rates due to long-life radioactivities produced and these radioactivities can not be annealed by heating. In order to evaluate the amount of background-counting-rate increase in semiconductor heavy-ion detectors, we started to measure high-purity Ge gamma-ray spectra obtained from the semiconductor wafers (25 mm diameter, 0.3 to 1 mm thickness) which had been taken out of an irradiation chamber after a heavy-ion irradiation at 77 K. The spectra were analyzed to identify the induced gamma-ray emitting nuclides and to calculate their radioactivities, their numbers of atoms at the end of the irradiation and also the numbers of atoms per incident ion.

We had already made the irradiations with 50 MeV  $^{11}\text{B}^{3+}$ , 100 MeV  $^{12}\text{C}^{5+}$ , 100 MeV  $^{16}\text{O}^{8+}$ , 150 MeV  $^{35}\text{Cl}^{9+}$ , 150 MeV  $^{58}\text{Ni}^{9+}$ , 180 MeV  $^{63}\text{Cu}^{11+}$ , 150 MeV  $^{115}\text{In}^{10+}$  and 80 MeV  $^{127}\text{I}^{7+}$ . Some of the results were reported<sup>1)</sup>.

In this fiscal year (1984), the irradiations with 120 MeV  $^{16}\text{O}^{7+}$  (August 30, 1984), 170 MeV  $^{179}\text{Au}^{13+}$  (September 19, 1984), 70 MeV  $^{10}\text{B}^{4+}$  (November 28, 1984), 150 MeV  $^{28}\text{Si}^{9+}$  (January 10, 1985) and 195 MeV  $^{209}\text{Bi}^{14+}$  (January 24, 1985) were carried out. Some of the results obtained on Si, Ge and Cu are summarized in Tables 1 and 2. The results on Cu were obtained from the mounting plates which placed Si or Ge wafers onto the cold finger. Long-life radioactive nuclides such as  $^{22}\text{Na}$  (2.602 y) in Si,  $^{75}\text{Se}$  (118.45 d) and  $^{88}\text{Y}$  (106.61 d) in Ge were observed. These radioactive nuclides will increase background counting rates of the semiconductor detectors and will make it difficult to use the detectors thereafter even after an annealing operation has been performed. An only method to remove these radioactive nuclides is etching. The production of radioactive nuclides is also important to manu-

facture buried layers deep into semiconductor materials by the ion implantation. The depths of the buried layers from the surface will be limited in order to avoid any radioactivity production by keeping the energies of implant ions below the threshold energies for compound nucleus formation.

### Reference

- 1) E. Sakai: IEEE Trans. Nucl. Sci. NS-31 (1984) 316.

Table 1 Residual gamma-emitting nuclides induced in materials irradiated with heavy ions, their radioactivities at the end of irradiation, corresponding numbers of atoms, numbers of atoms per incident ion and resultant stable daughter nuclides observed.

Heavy ions (Range)	Numbers of particles	Irradiated material	Residual nuclide	Radioacti- vity(nCi)	Number of atoms	Number of atoms per particle	Stable daughter nuclide	Note
$^{10}\text{B}$ 70MeV (155 $\mu\text{m}$ )	$8.13\text{E}13^*$ /0.77cm <sup>2</sup>	Si	Re-7(53.29d) Na-22(2.602y)	3.83 0.094	9.43E8 4.12E8	1.16E-5 5.07E-6	Li-7 Ne-22	$E_{\text{th}}=17.03\text{MeV}^{**}$ Strong $\beta$
$^{10}\text{B}$ 70MeV (97.2 $\mu\text{m}$ )	$7.49\text{E}14$ /3.14cm <sup>2</sup>	Ge	Ga-67(78.3h) As-71(61h) As-72(26.0h) As-73(80.30h) As-74(17.79d) Se-72(8.40d) Se-75(118.45d) Br-77(57.04h) Kr-79(35.04h) Rb-83(86.2d)	23.2 418 42.9 65.6 32.2 42.7 2810 3420 2.9	3.49E8 4.90E9 1.82E10 5.38E9 1.25E9 2.33E10 3.08E10 2.30E10 1.17E9	4.77E-7 6.74E-6 2.43E-5 7.22E-6 1.67E-6 3.11E-5 4.11E-5 3.24E-5 1.56E-6	Zn-67 Ga-71 Ge-72 Ge-73 Ge-74, Se-74 Ge-72 As-75 Se-77 Br-79 Kr-83	$E_{\text{th}}=27.97\text{MeV}$ Se-72 $\rightarrow$ As-72
$^{10}\text{B}$ 70MeV (55.9 $\mu\text{m}$ )	$3.37\text{E}14$ /1.77cm <sup>2</sup>	Cu	Zn-65(244.0d) Ga-67(78.26h) Ge-69(39.05h) As-71(61h) As-72(26.0h) Se-72(8.40d)	5.84 820 2010 740 50.7	6.57E9 1.24E10 1.50E10 8.73E9 1.96E9	1.95E-5 3.67E-5 4.46E-5 2.59E-5 5.87E-6	Cu-65 Zn-67 Ga-69 Ga-71 Ge-72 Ge-72	$E_{\text{th}}=26.01\text{MeV}$ Se-72 $\rightarrow$ As-72

\*  $8.13\text{E}13 = 8.13 \times 10^{13}$

\*\*  $E_{\text{th}}$  = threshold energy for compound nucleus formation

Table 2 Summary of residual gamma-emitting nuclides observed in materials irradiated with high-energy heavy ions

Heavy ions	Range (μm)	Number of particles on area of material	Irradiated material	Residual nuclide(half-life)	Threshold energy** (MeV)
$^{10}_5\text{B}^{4+}$ 70MeV	155	$8.13 \times 10^{15} / 0.77 \text{cm}^2$	Si	Be-7(53.29d), Na-22(2.602y)	17.03
$^{10}_5\text{B}^{4+}$ 70MeV	97.2	$7.49 \times 10^{14} / 3.14 \text{cm}^2$	Ge	Ga-67(78.3h), As-71(61h), As-72(26.0h), As-73(80.30h), As-74(17.79d), Se-72(8.40d), Se-75(118.45d), Br-77(57.04h), Kr-79(35.04h), Rb-83(86.2d)	27.20
$^{10}_5\text{B}^{4+}$ 70MeV	55.9	$3.37 \times 10^{14} / 1.77 \text{cm}^2$	Cu	Zn-65(244.0d), Ga-67(78.26h), Ge-69(39.05h), As-71(61h), As-72(26.0h), Se-72(8.40d)	26.01
$^{16}_8\text{O}^{7+}$ 120MeV	129.2	$6.75 \times 10^{14} / 0.982 \text{cm}^2$	Si	Be-7(53.3d), Na-22(2.602y), Sc-44m(2.442d), Sc-44(3.93h)	29.30
$^{16}_8\text{O}^{7+}$ 120MeV	80.6	$3.015 \times 10^{15} / 3.14 \text{cm}^2$	Ge	Ga-67(78.26h), Ge-69(39.05h), As-71(61h), As-72(26.0h), As-73(80.30d), As-74(17.79d), Se-72(8.40d), Se-75(118.45d), Br-77(57.04h), Kr-79(35.04h), Rb-83(86.2d), Rb-84(32.77d), Sr-82(25.0d), Sr-83(32.4h), Sr-87m(2.805h), Y-86(14.74h), Y-87(80.3h), Y-88(106.61d), Zr-88(83.4d), Zr-89(78.43h)	44.04
$^{16}_8\text{O}^{7+}$ 120MeV	45.8	$1.70 \times 10^{15} / 1.77 \text{cm}^2$	Cu	Zn-65(244.0d), Ga-67(78.26h), Ge-69(39.05h), As-71(61h), As-72(26.0h), As-73(80.30d), As-74(17.79d), Se-72(8.40d), Se-75(118.45d), Br-77(57.04h), Kr-79(35.04h), Rb-83(86.2d), Sr-83(32.4h), Zr-88(83.4d)	42.43
$^{28}_{14}\text{Si}^{9+}$ 150MeV	60	$1.02 \times 10^{14} / 0.86 \text{cm}^2$	Si	Sc-44m(2.44d), Sc-44(3.93h), V-48(15.976d), Cr-48(21.56h), Cr-51(27.70d), Mn-52(5.59d), Fe-52(8.27h)	59.21
$^{28}_{14}\text{Si}^{9+}$ 150MeV	37.5	$2.54 \times 10^{14} / 3.14 \text{cm}^2$	Ge	Ga-67(78.3h), Ge-73m(0.449s), Ge-69(39.05h), As-71(61h), As-72(26.0h), As-73(80.3d), As-74(17.78d), As-76(26.3h), Se-72(8.4d), Se-73(7.1h), Se-75(118.5d), Sr-87m(2.80h), Y-86(14.74h), Y-87m(13h), Y-87(80.3h), Y-88(106.61d), Zr-86(16.5h), Zr-88(83.4d), Zr-89(78.4h), Nb-90(14.6h), Nb-94(29.3min), Mo-90(5.67h), Mo-93m(6.9h), Tc-95m(61d), Tc-95(20.0h), Tc-96(4.3d), Ru-97(2.88d), Rh-99m(4.7h), Rh-99(15.0d), Rh-100(20.8h), Rh-101m(4.34d), Pd-100(3.6d)	80.93

(Table 2 continued)

150MeV $^{28}_{14}\text{Si}^{9+}$	22.3	1.43E14/1.77cm <sup>2</sup>	Cu	Zn-65(244.0d), Ga-67(78.3h), As-71(61h), Br-76(16.1h), Kr-79(35.7h), Rb-82(1.25min), Rh-83(86.2d), Sr-82(25.0d), Sr-83(32.4h), Sr-85(64.85d), Sr-87m(2.80h), Y-86(14.74h), Y-87m(13h), Y-87(80.3h), Zr-86(16.5h), Zr-88(83.4d), Zr-89(78.4h), Nb-90(14.6h)	79.02
170MeV $^{197}_{79}\text{Au}^{13+}$		8.33E13/0.97cm <sup>2</sup>	Si	None	900.08
170MeV $^{197}_{79}\text{Au}^{13+}$	14	1.63E14/3.14cm <sup>2</sup>	Ge	None	867.04
170MeV $^{197}_{79}\text{Au}^{13+}$		9.15E14/1.77cm <sup>2</sup>	Cu	None	900.98
195MeV $^{209}_{83}\text{Bi}^{14+}$	15	4.55E12/3.14cm <sup>2</sup>	Ge	None	940.15
195MeV $^{209}_{83}\text{Bi}^{14+}$		2.56E12/1.77cm <sup>2</sup>	Cu	None	978.44
* 8.13 x 10 <sup>13</sup> ** Threshold energy for compound nucleus formation					



### 3.5 X-RAY DIFFRACTION TOPOGRAPHIC OBSERVATION OF SILICON SINGLE CRYSTALS IRRADIATED WITH ENERGETIC HEAVY IONS

Hiroshi TOMIMITSU, Yukio KAZUMATA and Eiji SAKAI\*

Department of Physics; \*Department of Reactor Engineering, JAERI

#### 1. Introduction

The lattice disorder induced by ion-bombardments has been studied by X-ray diffraction topography (XDT), which detects sensitively the feature of the imperfections caused by the irradiation and records the difference between the damaged and the undisturbed parts within the specimen crystal through the interference effects. Schwuttke et al.<sup>1)</sup> have shown that the disorder concentrates at the very thin layer within the stragglings of the ranges of projectiles on the bombardment of Si crystals by 2 MeV N, B or P ions (dose: more than  $10^{15}$  ions/cm<sup>2</sup>), while the upper and lower parts of the specimen crystal separated by the very thin layer remain perfect. Further study by Bonse, Hart and Schwuttke<sup>2)</sup> finds the interference fringes arising from the two perfect regions separated by the very thin layer.

One of the present authors(HT)<sup>3)</sup> has also reported the following results by the conventional XDT-observation in Si single crystals irradiated with 150 MeV Ni<sup>9+</sup> and Cl<sup>9+</sup> ions; 1)the specimens were macroscopically deformed as a whole; 2)they sustained heavy strains which were concentrated at the irradiation boundaries, and 3)two kinds of characteristic and systematic fringes were seen in the irradiated areas. However, the nature of the systematic fringes seemed to be quite different from that reported by the previous authors<sup>2)</sup>. One of the present authors(HT)<sup>4)</sup> subsequently reported that the Si wafers irradiated with 58 MeV B<sup>3+</sup> and 100 MeV C<sup>5+</sup> ions showed only the marginal strains concentrated at the irradiation boundaries, without macroscopic deformation or systematic fringe.

We have made further measurements on the specimens irradiated with 70 MeV B<sup>4+</sup>, 120 MeV O<sup>7+</sup>, 150 MeV Si<sup>9+</sup> and 169 MeV Au<sup>13+</sup> ions in the last fiscal year(1984). The present article briefly summarizes the results of the XDT-observation on those heavy-ion-irradiated Si single crystals.

## 2. Experimental Procedure

The silicon single crystals used in this experiment were grown by Cz. method along the [001] direction. The crystals had the resistivities of 11~25  $\Omega\cdot\text{cm}$  by doping B. They were sliced parallel to the (001) plane, then chemically etched and mechanically polished into "mirrors", the resultant thicknesses being 0.3~0.4 mm. The Si wafers were then cut into rectangular pieces of about 3x3 cm<sup>2</sup>. The X-ray diffraction topographs of these original Si wafers showed no significant contrast, and indicated that they are very perfect. The present authors are much indebted to Dr.T.Masui of the Shin-Etsu Handotai Co. Ltd., for his kind offering of the silicon wafer used in this experiment.

The ion-irradiations were carried out with the tandem accelerator operated around 15 MV, on which ions were accelerated up to 100 MeV and more. The irradiation conditions are summarized in Table 1, which includes the irradiations made in the last fiscal year 1984 as well as in the past. The Si wafers were partially covered with specially designed Al- or Mo-masks to obtain the definite analysis. They were mounted on a Cu-supporter cooled with liquid nitrogen during the irradiation.

Table 1. Irradiation Conditions

	Names of Ions	Energy (MeV)	Current (nA)	Period (hrs)	Dose $\times 10^{13}$ ions/cm <sup>2</sup>
	<sup>11</sup> B <sup>4+</sup>	58	25	4.5	10
*	<sup>10</sup> B <sup>4+</sup>	70	30	4	11
	<sup>12</sup> C <sup>5+</sup>	100	165	3.5	50
*	<sup>16</sup> O <sup>7+</sup>	120	140	7	70
*	<sup>28</sup> Si <sup>9+</sup>	150	50	5.5	12
	<sup>35</sup> Cl <sup>9+</sup>	150	450	2.5	57
	<sup>58</sup> Ni <sup>9+</sup>	150	20	3.5	5
*	<sup>169</sup> Au <sup>13+</sup>	169	50	4	9

\* The irradiation was made during the fiscal year 1984.

Since the ranges of such high energy ions are as long as several tens of  $\mu\text{m}$  or more, one could expect to observe the irradiation-induced changes in the specimens more easily using conventional XDT-observation. The XDT was carried out with a fine focus X-ray generator having the effective

focus size of  $0.1 \times 0.1 \text{ mm}^2$ , which was operated at 50 kV with 1.3 mA by the use of Cu or Mo target.

### 3. Summary of Results

As already described in section 1, two different types of irradiation-effects have been revealed by one of the present author (HT)<sup>3,4)</sup> through XDT-observation. The very faint, black-and-white contrasts, indicating the lattice strains, were observed at the irradiation boundaries in the case of the irradiation with B and C ions. Besides this characteristic contrasts, by the bombardment with Ni and Cl ions, the systematic fringes in the irradiated areas and the macroscopic deformation of the specimen crystal were detected.

On the basis of these results, some Si wafers under various irradiation conditions shown in Table 1 were surveyed to see which type the irradiation-effect belong to, by the conventional XDT. The results are summarized in Table 2, where the mark "O" means the detection of the image, and "X" undetection.

Table 2. Summary of the XDT-Observation

	Ions	Energy (MeV)	Dose $\times 10^{13}$ ions/cm <sup>2</sup>	Results		
				Marginal-Strain	Deformation	Fringe
	<sup>11</sup> B <sup>4+</sup>	58	10	X	X	X
*	<sup>10</sup> B <sup>4+</sup>	70	11	X	X	X
	<sup>12</sup> C <sup>5+</sup>	100	50	O	X	X
*	<sup>16</sup> O <sup>7+</sup>	120	70	O	X	X
*	<sup>28</sup> Si <sup>9+</sup>	150	12	O	X	X
	<sup>35</sup> Cl <sup>9+</sup>	150	57	O	O	O
	<sup>58</sup> Ni <sup>9+</sup>	150	5	O	O	O
*	<sup>179</sup> Au <sup>13+</sup>	169	9	O	O	O

\* The irradiation was made during the present fiscal year 1984.

From Table 2 the followings are clearly seen;

- 1) The irradiation with lighter ions gives no characteristic image (B<sup>4+</sup> case) or only the faint black-and-white contrasts at the irradiation boundaries, a typical example being shown in Fig.1.
- 2) On the other hand, the systematic fringes within the irradiated areas

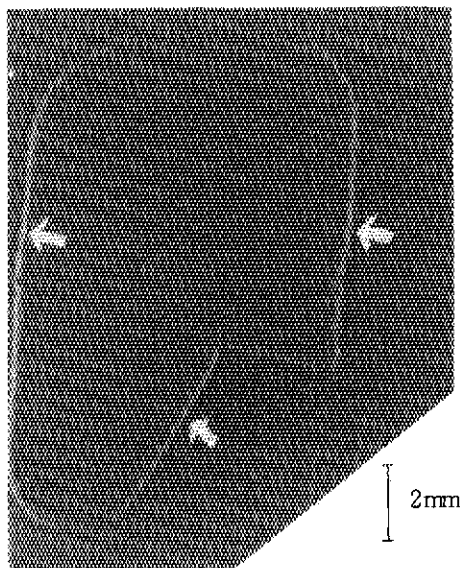


Fig.1 Example of X-ray diffraction topograph of Si wafer irradiated with  $\text{Si}^{9+}$  ions of 150 MeV and the dose of  $12 \times 10^{13}$  ions/cm<sup>2</sup>. Only the faint black-and-white contrasts are visible at the irradiation boundary, indicated by arrows. Mo-K $\alpha$  radiation with 220 reflection was used.

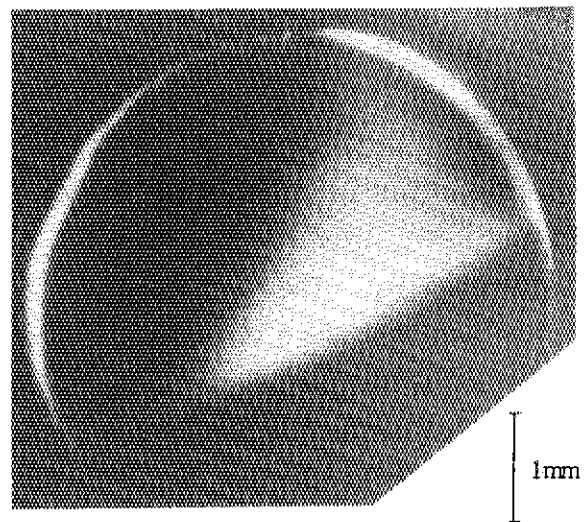


Fig.2 Example of systematic fringes within the irradiated area observed in the topograph of the Si wafer irradiated with 169 MeV  $\text{Au}^{13+}$  ions of the dose of  $5 \times 10^{13}$  ions/cm<sup>2</sup>. Mo-K $\alpha$  radiation with 440 reflection were used.

and the macroscopic crystal deformation appear in the case of the irradiation with heavier ions, in addition to the black-and-white contrasts, as typically shown in Fig.2.

Further investigation is in progress with respect to the effects of the dose, the ion range and so-called "dpa".

#### References

- 1) G.H.Schwuttke, K.Brack, E.E.Gardner and H.M.DeAngelis: Proc.Santa Fe Conf.Radiation Effects in Semiconductors, ed. F.Vook, (Plenum Press, N.Y., 1968) pp.406.
- 2) U.Bonse, M.Hart and G.H.Schwuttke: Phys.Stat.Solidi 33(1969) 361.
- 3) H.Tomimitsu: Jpn.Appl.Phys.22(1983) L674.
- 4) H.Tomimitsu: JAERI-M 84-129(1984) pp.47.

### 3.6 RADIATION DAMAGE OF MATERIALS ION-IRRADIATED AT LOW TEMPERATURE

Saburo TAKAMURA\*, Hiroshi MAETA\* and Mamoru KOBIYAMA\*\*

\* Department of Physics, JAERI

\*\* Faculty of Engineering, Ibaraki University

#### 1. Introduction

A low temperature ion-irradiation cryostat was constructed. The objective of irradiation experiments using the cryostat is to investigate the behavior of radiation induced defects in materials after ion-irradiation at low temperature. The ion-irradiation, in comparison with neutron and electron irradiations, can induce the point defects of high concentration in materials.

Since the interstitial, which is a kind of the elementary defects in radiation induced defects, migrates at very low temperature, the investigations of point defects in irradiated materials need to be performed at low temperature.

The following experiments will be performed using the low temperature ion-irradiation cryostat:

- 1) The properties of point defects induced by high energy ion-irradiation.
- 2) The recovery processes for radiation induced defects of high concentration.
- 3) The depth profile of defects produced by ion-irradiation and the annealing effect of the depth profile.
- 4) The mechanical properties of ion-irradiated materials at low temperature.
- 5) The structure of implanted materials and a change in the structure due to annealing processes.

In this paper, the construction and test of the cryostat are described.

#### 2. Experimental apparatus

Figure shows a general lay-out of the low temperature ion-irradiation cryostat. A small chamber in the cryostat is cooled by liquid helium which is supplied through a flexible tube from a liquid helium vessel. The sample holder with hexagonal pillar fits on the small chamber by means of a pin. The samples are set on five planes on the sample holder. The

irradiation cryostat was constructed to allow five samples to be irradiated sequentially at low temperature. The rotation of the sample holder is operated by a motor. For the ion-irradiation, the first sample is positioned to the irradiation place and, after the first sample is irradiated, the small chamber rotates to bring the next sample into the irradiation place. By removing the pin, the sample holder with samples drops from cryostat into a transporting liquid helium vessel connected to the ion-irradiation cryostat. A small vacuum-insulated metal bucket is set into the transporting vessel and, after transporting the vessel to the experimental room, the bucket is lifted up in the box in an atmosphere of helium gas and then it is hung down into the liquid helium of the measuring Dewar. In the Dewar, the samples are removed from the sample holder and the measurements are performed.

### 3. Irradiation experiment

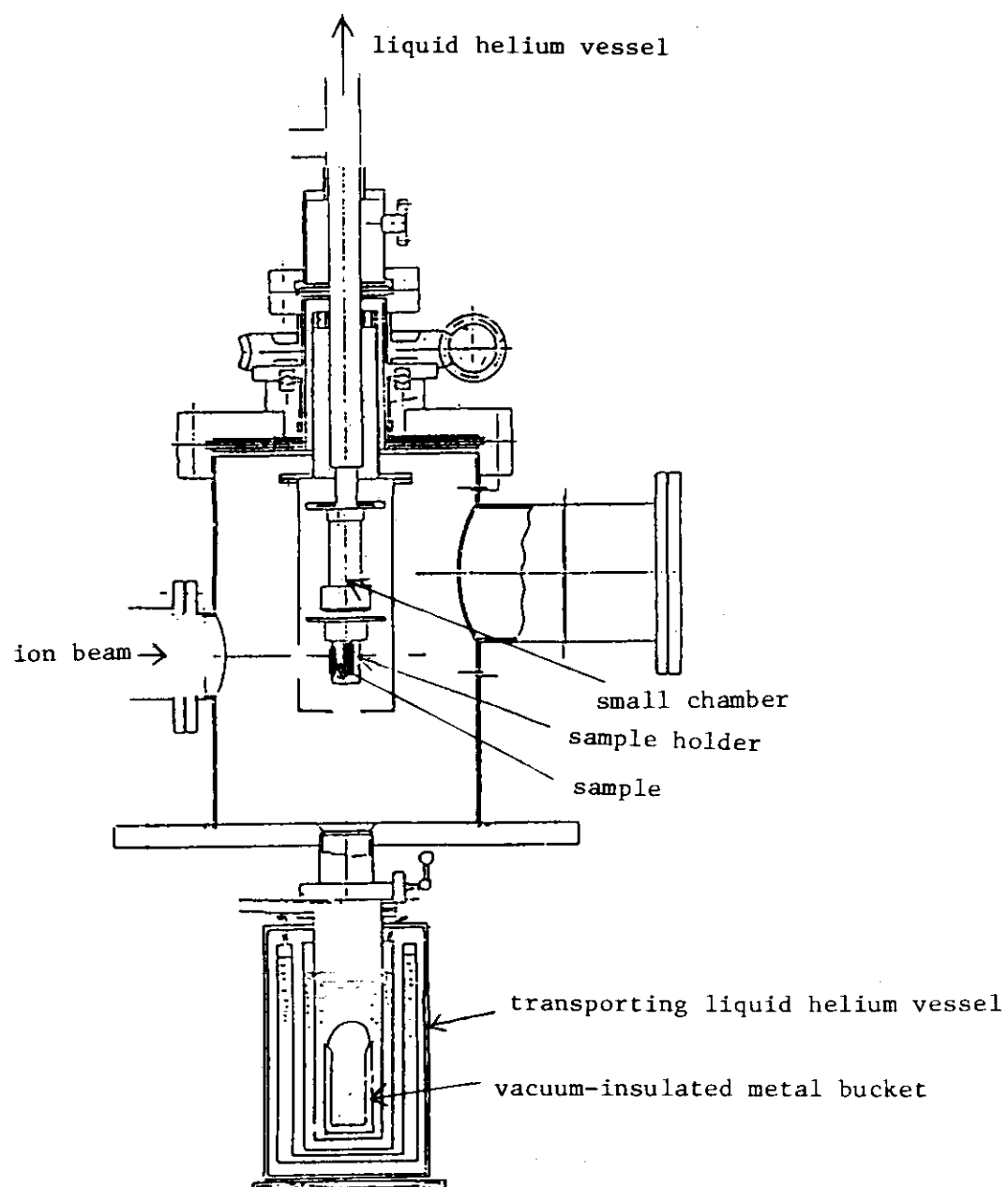
The preliminary experiment was performed by using the irradiation of 90 MeV  $C^{6+}$  ions. The following experiments were made; the measurement of the ion beam current, the rotation of sample holder to irradiate several samples, and taking out the sample holder with samples without warm-up after irradiation.

So far as we know, this is the first cryostat from which the samples set in vacuum can be taken out without warm-up.

The content of experiment in radiation damage using the irradiation cryostat is as follows:

- 1) Internal friction measurement in Al alloy (by Takamura and Kobiyama).
- 2) Lattice parameter measurement by X rays in Al crystal (by Maeta).
- 3) ESR measurement of NaF crystal (by Kazumata).
- 4) Structure change of polyvinylidene film (by Komaki).

These experiments after ion-irradiation are in progress.



low temperature ion-irradiation cryostat

### 3.7 TRACK FORMATION IN EVAPORATED FILMS OF GERMANIUM, SILICON AND TITANIUM

Shigemi FURUNO, Kazuhiko IZUI and Hitoshi OTSU

Department of Chemistry, Japan Atomic Energy  
Research Institute

High energy ions dissipate most of their energies in electron excitations. Through this electron excitation process these ions produce their tracks in some insulating or semiconducting materials. The observations of the structure of tracks are important from the fundamental standpoint to elucidate the mechanism of track formation. In this report, the tracks of ions in the evaporated films of titanium, silicon and germanium are shown and mechanism for track formation is investigated.

Thin films of titanium, silicon and germanium of 50 Å in thickness were prepared by vacuum evaporation. These specimens were set on the low temperature stage cooled by liquid nitrogen. Irradiation was performed with 207 MeV  $\text{Au}^{13+}$  ions with the incident angle of about  $10^\circ$  to the surface of the specimens. After irradiation the specimens were observed at room temperature with an electron microscope of JEM-100C type operating at 100 kV.

In titanium and silicon, the tracks of 207 MeV  $\text{Au}^{13+}$  ions are observed as shown in figures 1(a) and (b). Corresponding energy depositions ( $dE/dx$ ) are 2,600 eV/Å for titanium and 1,700 eV/Å for silicon. For energy depositions smaller than the above mentioned values, no track was observed as reported already<sup>1)</sup>. In germanium, there are also observed the tracks of 207 MeV  $\text{Au}^{13+}$  ions of 230 Å in width. The experimental results are summarized in table 1 together with the previous data<sup>1,2)</sup>. These results clearly show the effect of energy depositions on the track formation. The track width increases with increasing the energy depositions.

In the case of germanium, it was reported that the tracks consisted of small crystallites of about 100 Å in diameter, and this recrystallization along the tracks was considered to arise from the thermal spike effect due to the energy dissipated in electron excitations<sup>2)</sup>. In this report, mechanism for track formation is discussed



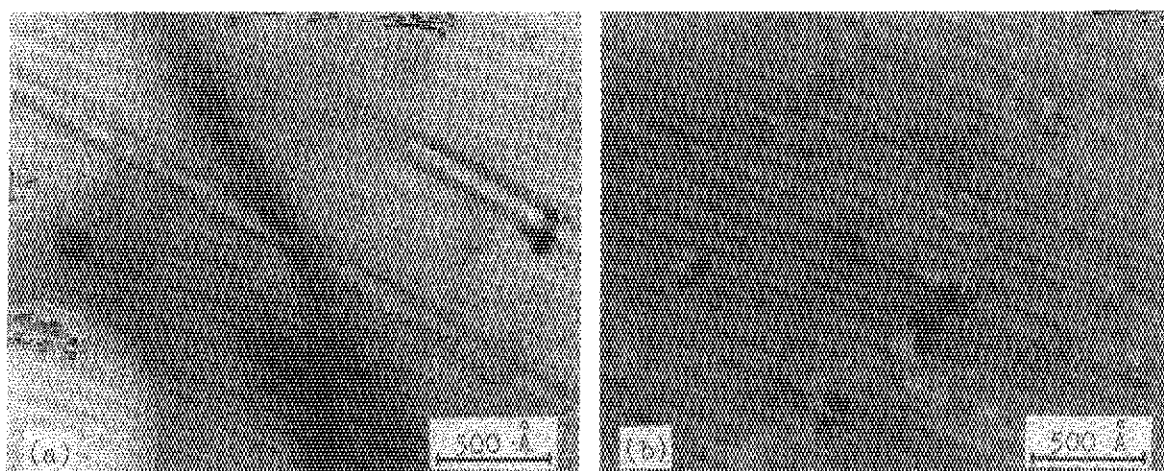


Fig. 1 Tracks of 207 MeV Au<sup>13+</sup>. (a): tracks in titanium and (b): tracks in silicon.

Table 1 Ions and specimens used in the irradiation experiments, some parameters and experimental results.

Ions	Specimens	Melting points of specimens(°C)	dE/dx (eV/Å)	Widths of tracks(Å)	References
150 MeV In	Ti	1,820	1,900	invisible	(2)
207 MeV Au	"	"	2,600	100	
150 MeV In	Si	1,415	1,200	no track	(2)
207 MeV Au	"	"	1,700	70	
100 MeV O	Ge	958	130	no track	
128 MeV Cl	"	"	530	80	(1)
143 MeV Ni	"	"	1,100	100	(2)
150 MeV In	"	"	1,800	170	(2)
207 MeV Au	"	"	2,600	230	

in terms of a time dependent line source model<sup>3)</sup> which was proposed by considering energy distribution of secondary electrons excited by an ion, various collision processes of these electrons and relaxation time in energy transfer from electrons to the lattice. If electrons release their energies to the lattice at the rate,  $Q(t)$ , then the temperature  $T(r,t)$  at a normal distance  $r$  from the line source at the time  $t$  is given by

$$T(r,t) = \frac{1}{4K} \int_0^t \frac{Q(t')}{t-t'} \exp \left\{ -\frac{1}{4D(t-t')} \right\} dt' \quad (1)$$

$$Q(t) = -n \frac{d\varepsilon}{dt} = nA \left( \frac{A}{2} t + \varepsilon_0^{-1/2} \right)^{-3} \quad (2)$$

where  $K$  is the thermal conductivity,  $D$  is the thermal diffusion coefficient,  $A$  is a constant characteristic of the materials<sup>3)</sup>,  $d\varepsilon/dt$  is the energy loss rate of an electron due to electron-phonon collisions<sup>4)</sup>,  $\varepsilon_0$  is the initial energy which an electron receives from incident ion and  $n$  is the number of electrons contributing to the thermal spike per unit length along this line source and these electrons are assumed to have the same initial energy.

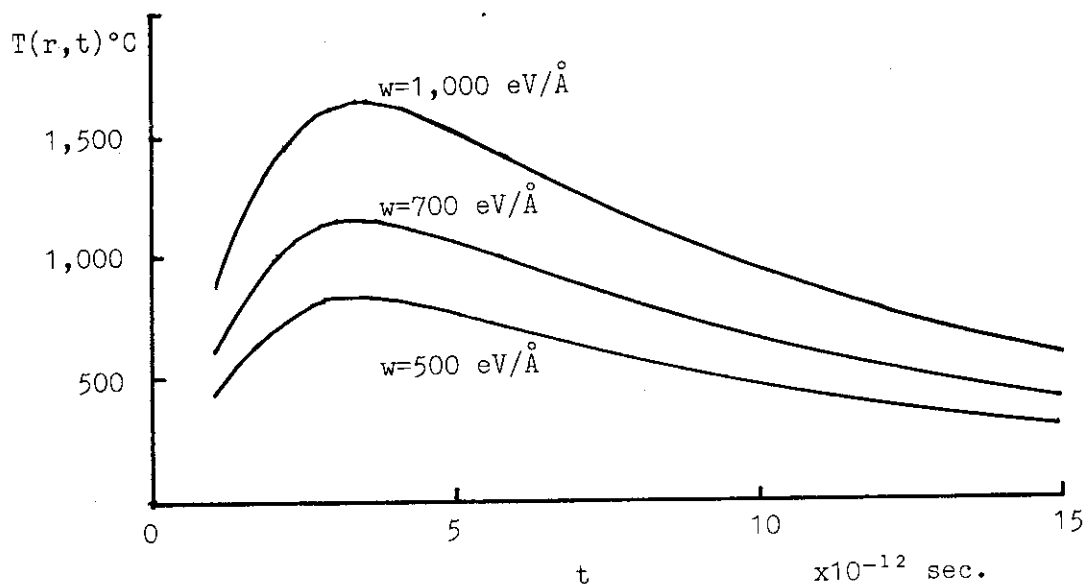


Fig. 2 Temperature variations at distance of 50 Å from a heat source with  $w=500, 700$  and  $1,000$  eV/Å.

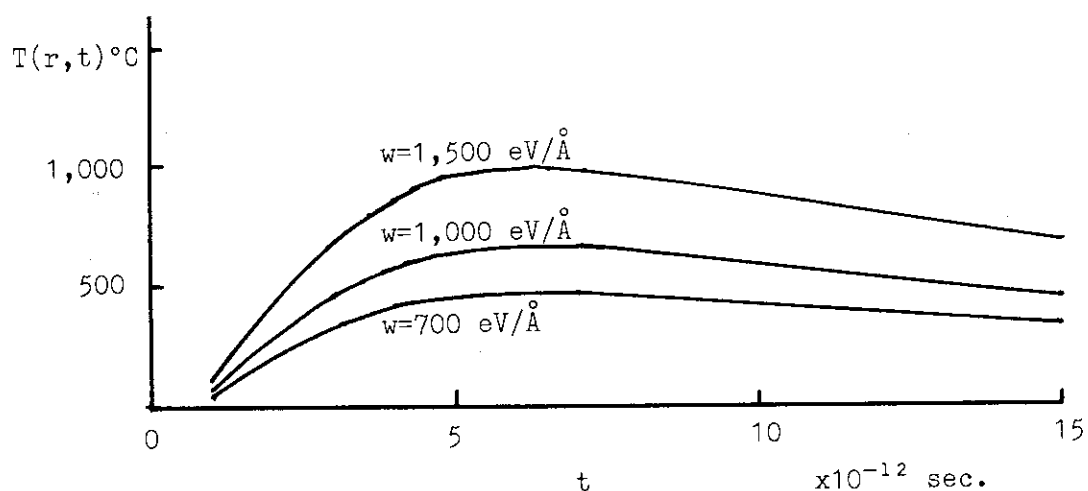


Fig. 3 Temperature variations at distance of 100 Å from a heat source with  $w=700, 1,000$  and  $1,500$  eV/Å.

Applying this model to the case of germanium, temperature  $T$  were calculated as a function of time  $t$ . In this calculation  $r$  and  $w$  were taken as parameters, where  $w=n\epsilon_0$  is total energies of electrons which contribute effectively to the heat source. The calculated results for the cases of  $r=50$  and  $100 \text{ \AA}$  are shown in figures 2 and 3 respectively, where  $w$ 's take the values of 500, 700 and  $1,000 \text{ eV/\AA}$  for  $r=50 \text{ \AA}$  and 700, 1,000 and  $1,500 \text{ eV/\AA}$  for  $r=100 \text{ \AA}$ . Recently picosecond laser pulse irradiation experiments have proved that melting or consequent recrystallization occurs within several picosecond<sup>5)</sup>. The melting point of evaporated films is considered to be lower by a few ten percent than that of crystalline<sup>6)</sup>. From these facts, the time of duration necessary for melting is considered to be  $5 \times 10^{-12}$  second and the melting point is assumed to be  $700^\circ\text{C}$ . Then it is deduced from the calculated results that the energies of 550 and  $1,200 \text{ eV/\AA}$  are necessary to raise the temperature above the melting point within the cylindrical regions with the radii of 50 and  $100 \text{ \AA}$  respectively.

On the other hand, the experimental results show that the energy depositions necessary for the formation of the tracks with the width of 100 and  $200 \text{ \AA}$  are  $1,100$  and  $2,200 \text{ eV/\AA}$  respectively. In this case the values of  $200 \text{ \AA}$  in diameter and  $2,200 \text{ eV/\AA}$  are estimated from the interpolation between the data of the irradiations with  $150 \text{ MeV In}^{10+}$  ions and  $207 \text{ MeV Au}^{13+}$  ions. From the comparison between the estimated values for  $w$ 's and the experimental values for  $dE/dx$  in the case of the tracks of 100 and  $200 \text{ \AA}$  in width, it can be concluded that about half of the energy dissipated into electron excitations contribute to the thermal spike.

#### References

- (1) S. Furuno, K. Izui and H. Otsu: "JAERI TANDEM Annual Report 1983", JAERI-M 84-129 (1984) 44.
- (2) S. Furuno, H. Otsu and K. Izui: "JAERI TANDEM Annual Report 1982", JAERI-M 83-095 (1983) 43.
- (3) K. Izui: J. Phys. Soc. Jpn. 20 (1965) 915.
- (4) F. Seitz: Phys. Rev. 76 (1949) 1376.
- (5) G. A. Rozgonyi, H. Baumgart, F. Phillipp, R. Uebbing and H. Oppolzer : Laser and Electron-Beam Interactions with Solids (North-Holland, New York, 1982) 177.
- (6) M. Blackman and A. E. Curzon: Structure and Properties of Thin Films, (John Wiley and Sons Inc., New York, 1959) 217.

## 3.8 TEM Observation of Cascade Damage Structure in Pure Nickel

Shiori ISHINO, Hiroshi KAWANISHI, Naoto SEKIMURA,  
Shozo HAMADA\* and Tomotsugu SAWAI\*

Department of Nuclear Engineering, University of Tokyo  
and \*Department of Fuels and Materials Research, JAERI

It has been pointed out that radiation damage in the first wall materials is one of the critical problems in developing fusion reactors. Characteristic features of radiation effects by 14 MeV neutrons can be divided into two points, i.e. (1) nuclear transmutation, and (2) atomic displacement with high energy cascade. In the present study, cascade damage in pure nickel has been examined by utilizing 150 MeV self ions from JAERI tandem accelerator. This enables us to observe the defect structure free from the effect of specimen surface.

The material used is Marz Grade pure nickel (99.995 %). The samples are annealed at 1023 K for 30 min in a high vacuum followed by the irradiation with 150 MeV  $\text{Ni}^{10+}$  ions at ambient temperature. The calculation by the extended E-DEP-1 code shows that the peak of the displacement damage is situated at the depth of about 10  $\mu\text{m}$  from the specimen surface, in which stopping power data given by Northcliffe and Schilling are used. Specimens for TEM are prepared by the cross-section method to observe the depth dependent change of the microstructure directly.

Detailed observation of the microstructure by TEM has been carried out only on the specimens irradiated up to the fluence of  $5.2 \times 10^{12}$  particles/ $\text{cm}^2$ , which produces 0.011 dpa at the damage peak. No radiation-induced defects are detected from the surface to the calculated damage peak. However, stacking fault tetrahedra (SFT) images of about 5 nm are observed at the depths of 11.7, 11.8 and 12.4  $\mu\text{m}$ . It may be said from these results that the stopping power data given by Northcliffe and Schilling are overestimated, even if one takes into account the error in the estimation of the depth from the ion indident surface. Some images consist of the aggregation of several SFT's, which indicates the sub-cascade formation. The density of SFT is found to be very low compared with the results obtained from 14 MeV neutron irradiated nickel up to 0.01 dpa. This can be attributed to the difference in the PKA energy spectrum.

### 3.9 Irradiation Induced Defects of Dual Phase (Austenite and Ferrite, Duplex) Stainless Steel

Naohiro IGATA, Kazuya MIYAHARA, Shinji SATO, Shozo HAMADA\* and Tomotsugu SAWAI\*

Department of Materials Science, University of Tokyo  
and \*Department of Fuels and Materials Research, JAERI

The microstructural evolution of the irradiated steel is affected by its crystallographic structure. It is, therefore, important as a fundamental research for developing fusion reactor materials to investigate the effects of the crystallographic structure on the cascade and/or secondary defect formation and on other microstructural evolution of the materials irradiated with high energy particle. Duplex steel has austenitic phase (fcc phase) and ferritic phase (bcc phase) of almost same chemical composition. So, in the present work, it is intended to investigate the effects of the crystallographic structure on the defect structure of the duplex steel irradiated with heavy ions in JAERI tandem accelerator, using electron microscope and positron annihilation measurement technique. As a preliminary experiment which is associated with this research, the both phases of the duplex steel was irradiated and examined in HVEM. The void swelling peak temperatures of the austenitic phase and ferritic phase are 873 and 623 K, respectively. And the peak void swelling of the austenitic phase and ferritic phase are 6 % and 3 % at 20 dpa irradiation, respectively. Furthermore, the steel was irradiated with 190 MeV Ni-ion and 60 MeV C-ion using JAERI tandem accelerator and the specimens for TEM were prepared by the cross-section method. The specimens are now being analyzed.

3.10 NEAR SURFACE MODIFICATION OF  $\alpha$ -Al<sub>2</sub>O<sub>3</sub> BY Nb IMPLANTATION

Hiroshi NARAMOTO, Clark W. WHITE\*, James M. WILLIAMS\*,  
 Carl J. McHARGUE\*\*, Kunio OZAWA and Bill R. APPLETON\*

Department of Physics, JAERI, \*Solid State Division and  
 \*\*Metals & Ceramics Division, ORNL

1. Introduction

The ion implantation is well described by the nonequilibrium process associated with the high density production of defects and the squeezing of impurities in crystal lattice. This process has been employed to alter the near surface properties of materials by controlling the depth and the atomic quantity of implants precisely. In the modification of ceramics, the ion implantation is made so as to obtain a new atomic structure, and necessary is the high concentration of implants which amounts to 1 - 20 at. %. Thus, the implantation damage in ceramics is severe and complicated. To study such a system, the Rutherford backscattering analysis combined with the channeling effect is very effective. In this report, some typical results of the ion beam analysis after thermal annealing are shown in  $\alpha$ -Al<sub>2</sub>O<sub>3</sub> crystal implanted with <sup>93</sup>Nb<sup>+</sup> ions.

2. Experimental Procedure

Platelet specimens with specific orientation were cut from  $\alpha$ -Al<sub>2</sub>O<sub>3</sub> single crystal purchased from Union Carbide Corp. The specimens were polished and annealed at 1200 °C in air for 120 hours to remove the surface strain. Implantation of <sup>93</sup>Nb<sup>+</sup> ions was made at 7° off the <0001> crystal axis at ambient temperature with 220 keV to a dose of  $4 \times 10^{16}$  /cm<sup>2</sup>. A part of each specimen was masked during implantation to preserve a virgin region which could be examined subsequent to each annealing cycle. Thermal annealing in air was carried out for 1 hour in the temperature range from 600 °C to 1600 °C. The effect of implantation and thermal annealing on structure was evaluated using 1.8 MeV <sup>4</sup>He<sup>+</sup> ions from 2 MV Van de Graaff accelerator to determine the depth profile of implanted Nb atoms, the depth distribution of induced damage and the lattice location of implants. A scattering angle of 160° was used for the energy analysis of scattered ions, resulting in a depth resolution of 200 Å.

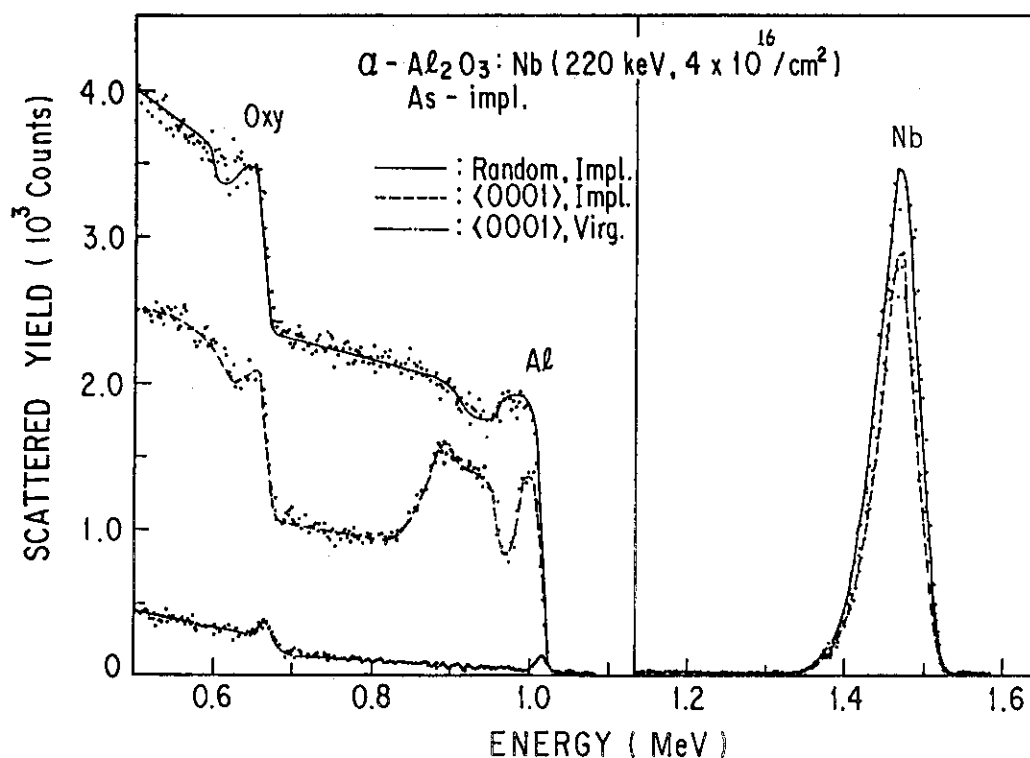


Fig. 1 1.8 MeV  $^4\text{He}^+$  ion backscattering spectra from  $\alpha\text{-Al}_2\text{O}_3$  single crystal implanted with  $^{93}\text{Nb}^+$  ions (220 keV,  $4 \times 10^{16} / \text{cm}^2$ ). The random and the  $\langle 0001 \rangle$  aligned spectra from implanted region are compared with the  $\langle 0001 \rangle$  aligned spectrum from virgin region.

### 3. Results and Discussion

Figure 1 shows typical backscattering spectra of 1.8 MeV  $^4\text{He}^+$  ion from the  $\langle 0001 \rangle$   $\alpha\text{-Al}_2\text{O}_3$  crystal implanted with 220 keV  $^{93}\text{Nb}^+$  ions to a dose of  $4 \times 10^{16} / \text{cm}^2$ . Due to large mass difference among Nb, Al and O atoms, the kinetics of Rutherford scattering produce characteristic steps in the yields of particles scattered from the matrix elements (Al and O) as well as an isolated peak for scattering from the implanted Nb atoms. Some Nb atoms occupy the substitutional sites even if just after the implantation. Comparing the  $\langle 0001 \rangle$  aligned yields from implanted and virgin regions, substantial disorder is recognized in both Al and O sublattices. However, the amorphization in the near surface region is not observed after the implantation, which indicates the existence of reordering process.

The definite recovery of the lattice damage begins in both Al and O

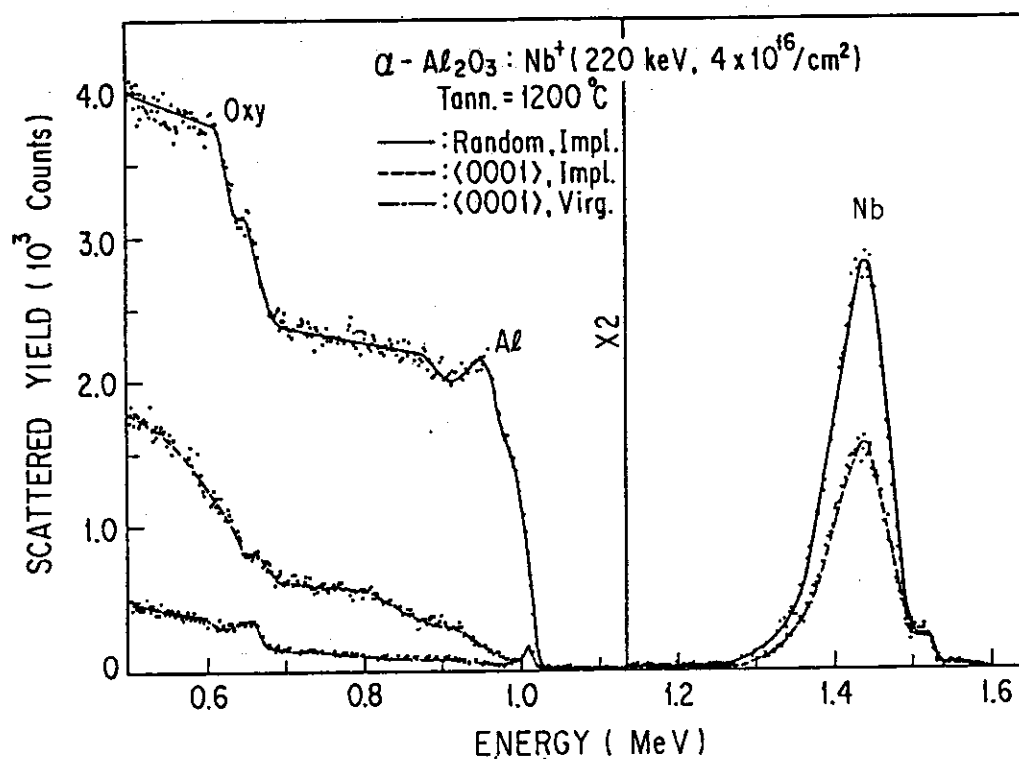


Fig. 2 Typical change of 1.8 MeV  $^4\text{He}^+$  ion backscattering spectra from Nb implanted  $\alpha\text{-Al}_2\text{O}_3$  crystal after thermal annealing at 1200 °C in air.

sublattices after annealing at 1000 °C. In Fig. 2, it is observed that after annealing at 1200 °C, the  $\langle 0001 \rangle$  aligned spectrum decreases its scattered yield and additional humps are formed at the leading edges of Nb, Al and O atoms. This result is explained by the formation of ternary compound like  $\text{Nb}_x\text{Al}_y\text{O}_z$  in the near surface region of  $\alpha\text{-Al}_2\text{O}_3$  crystal in competition with the damage recovery. The process of compound formation could be attributed to the Nb pile up at the surface by diffusion and the oxygen incorporation from annealing circumstance because the depth profile of implanted Nb is broadened with holding the peak position. A comparison between the aligned and the random spectra also shows that in this compound the implanted Nb atoms are accommodated in a random manner, and Al and O atoms occupy the crystal lattice well conformed to the corundum structure along the  $\langle 0001 \rangle$  crystallographic direction. This is a typical result of the nonequilibrium material processing by ion implantation. Some Nb atoms isolated in the inner region of specimen occupy the substitutional sites of Al sublattice, and the substitutionality defined by  $(1 - x_m(\text{Nb})) / (1 - x_m(\text{Al}))$  amounts to 50 %, where the value  $x_m$  is the ratio of the  $\langle 0001 \rangle$  aligned to the random yields.



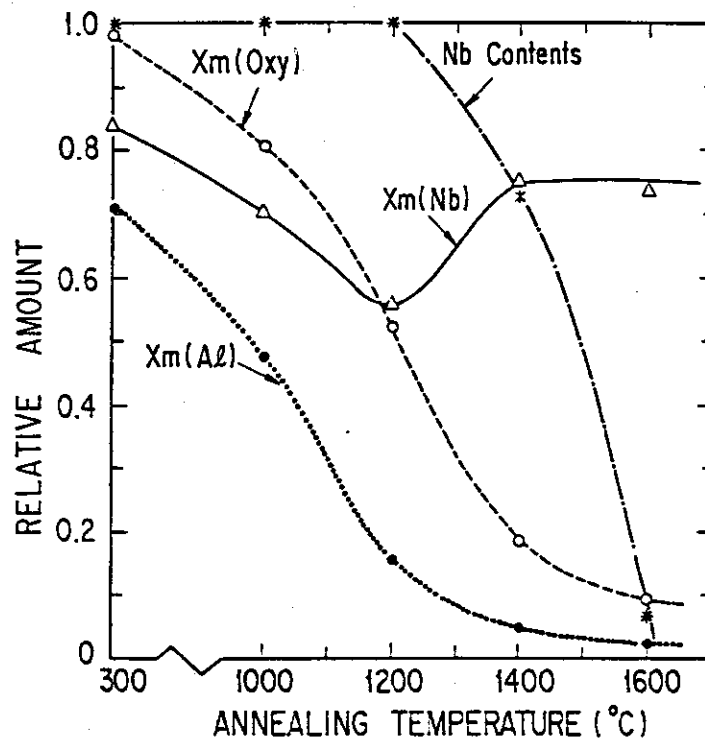


Fig. 3 Summary of thermal annealing results for crystal quality levels of Al sublattice, O sublattice, implanted Nb and total Nb concentration.

In order to show the entire thermal annealing behavior, the relative changes with temperatures are illustrated in Fig. 3 for  $x_m(\text{Al})$  the damage level in Al sublattice,  $x_m(\text{O})$  damage level in O sublattice,  $x_m(\text{Nb})$  the fraction of implanted Nb accommodated to the random sites and the total Nb content, respectively. In this figure, both Al and O sublattices recover in a similar manner with being different from Cr, Ti and Zr implantations<sup>1)</sup>. The recovery curve of implanted Nb has the minimum at 1200 °C, and  $x_m(\text{Nb})$  increases again above 1200 °C. In the same temperature region, total Nb content starts to decrease with diffusing inward and outward. After annealing at 1600 °C, only detectable amount of Nb atoms is left in the substrate. In this study, it is clear that the annealing circumstance influences the structure of implanted specimen, and a comparison is scheduled in a specimen annealed in reducing atmosphere.

#### Reference

- 1) H. Naramoto, C. W. White, J. M. Williams, C. J. Mchargue, O. W. Holland, M. M. Abraham and B. R. Appleton: J. Appl. Phys. 54 (1983) 683.

### 3.11 TEMPERATURE DEPENDENCE OF DAMAGE PROFILE IN HELIUM IRRADIATED STAINLESS STEEL

Shozo HAMADA, Kenji SUZUKI, Tomotsugu SAWAI and Kensuke  
SHIRAISHI\*

Department of Fuels and Materials Research and \* Radioisotope  
and Nuclear Engineering School, JAERI

Helium ion irradiation has been used for studying the helium effects on microstructural development and swelling of fusion reactor materials, in which a much amount of helium is produced by the high energy neutron spectrum. Ion irradiation, however, makes the concentrated damage around the mean projected range unlike neutron irradiation. In order to observe the damage structure induced by ion irradiation using transmission electron microscope, the mean projected range must be exactly known. In addition, the damage profile would be changed with irradiation temperature as a result of point defects diffusion. So, the effect of irradiation temperature should be considered on the profile of the damage profile. This paper reports the effects of the irradiation temperature on depth distribution of damage structure produced in Type 316 stainless steel during helium ion irradiation.

The specimens used in this study were 3 x 0.2 mm thick discs of Type 316 stainless steel, which were solution annealed in vacuum for 1 h at 1323 K. The discs were slightly polished by diamond-paste to clean the surface. The irradiations were carried out at R.T., 673, 773 and 873 K using 2 MV Van de Graaff accelerator with 1.0 MeV He ions upto 2000 appm at the peak. Specimens were prepared by the cross-section method for optical and transmission electron microscopies, which would be described in detail elsewhere<sup>1)</sup>. Several specimens of 873 K irradiation, prepared by the back-thinning method, were observed in the direction normal to the irradiated surface.

The cross-sectional optical micrographs of specimens irradiated at the temperatures of R.T., 673, 773 and 873 K are shown in Fig. 1. The parallel lines to the incident surface were observed in all specimens. As the irradiation temperature increases, the etched lines becomes darker. The center of each lines was identified at the same position, and its

distance from the incident surface was measured to be  $1.6\ \mu\text{m}$ . A typical damage structure of R.T. irradiation in the region around the etched band in Fig. 1(a) is presented in Fig. 2(a) and 2(c). In Fig. 2(c), the specimen contains 10000 ppm He at the peak. Defect clusters are seen as black- and white-dots with the average diameters of 5 to 10 nm for both defect clusters. The depth dependence of the defect number densities are given in Fig. 2(b), together with displacement damage and helium distribution curves. The damage and helium distribution curves were calculated using the extended E-DEP-1 computer code<sup>2)</sup>. The depth histograms for black- and white-dots are in good agreement with the displacement damage and helium distribution curves, respectively.

At 673 K irradiation, the band structure of  $0.2\ \mu\text{m}$  width is observed at depth of  $1.6\ \mu\text{m}$  similarly to R.T. irradiation (Fig. 3(a) and (c)). The band also consists of two sizes of black-dots; the average diameter of larger ones is 20 nm and that of smaller ones 5 nm. Tangled dislocation lines were observed (Fig. 3(b)) in the region shallower than the mean projected range.

Figure 4 shows the microstructures produced by 873 K irradiation. Tangled dislocation lines and large dislocation loops with and without stacking faults were broadly observed over a range of depth from  $1.5\ \mu\text{m}$  to  $2.3\ \mu\text{m}$ , and the dislocation loops were also observed at the depth of  $2.8\ \mu\text{m}$ , which is located deeper than the mean projected range. The reason of presence of these dislocation loops can not be easily explained, and further experimental and theoretical studies are required. The damage structures observed in the direction normal to the irradiated surface are given in Figs. 4(b) to 4(d). These structures are consisted of (a) dislocation loops with stacking fault, (b) dislocation lines, (c) dislocation loops with a black dot at the center and (d) helium bubbles at the grain boundary.

In summary, the depth distributions of damage structure in Type 316 stainless steel, which was irradiated with 1.0 MeV He-ion at R.T., 673 and 873 K, were observed by transmission electron microscopy. The damage structure bands consisted of black-dots were observed around the mean projected range at R.T. and 673 K irradiation. At 873 K irradiation, dislocation lines and larger dislocation loops with and without stacking fault were dominant around the mean projected range and a few dislocation loops were observed at the depth of  $2.8\ \mu\text{m}$ , which is located deeper than

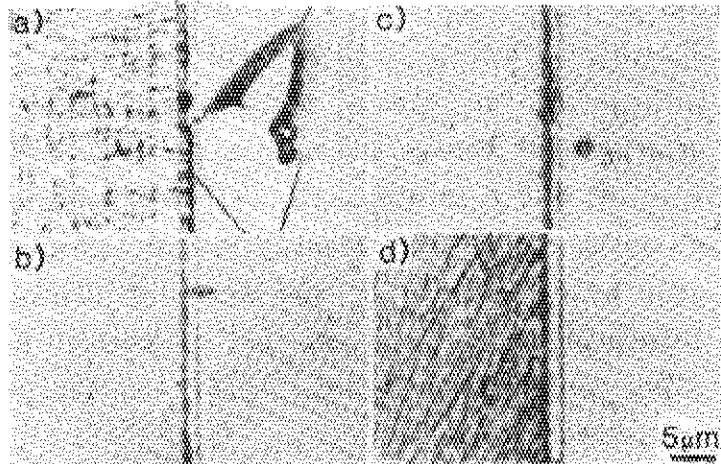
the mean projected range, from the irradiated surface.

### References

- 1) S. Hamada, T. Sawai, K. Fukai and K. Shiraishi: "Measurement of Mean Projected Range in Ion Irradiation", this Tandem Annual Report.
- 2) I. Manning and G. P. Mueller: Comp. Phys. Comm. 7 (1974) 85.

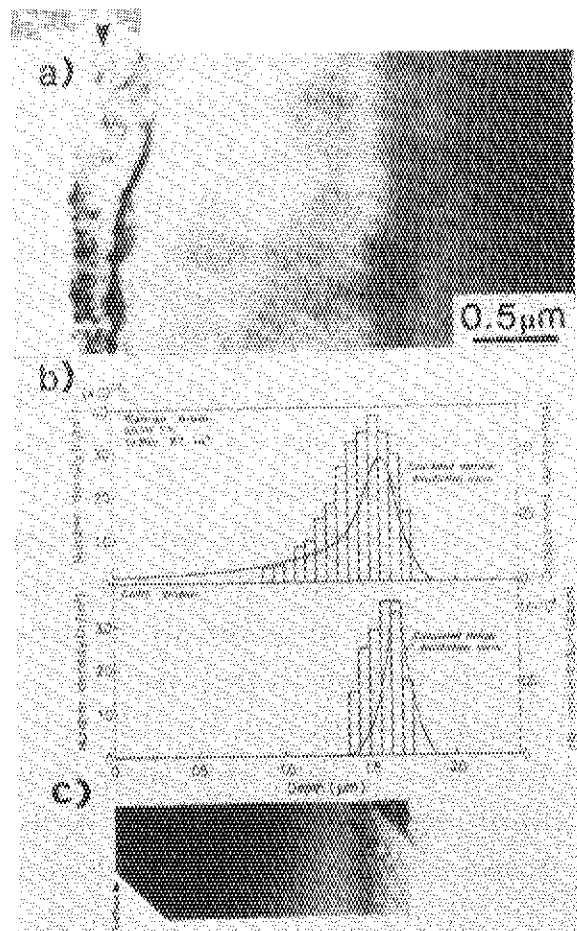
Irradiated surface    Etched line

Fig.1 Optical micrographs of the irradiated stainless steel cross-section specimen  
a) R.T. b) 673 c) 773 and d) 873 K.



Irradiated surface

Fig.2 Damage structures observed in the specimen irradiated at R.T. a) He content 2000appm b) and c) are size distribution of damage clusters and TEM micrograph in containing 10000appm He, respectively.



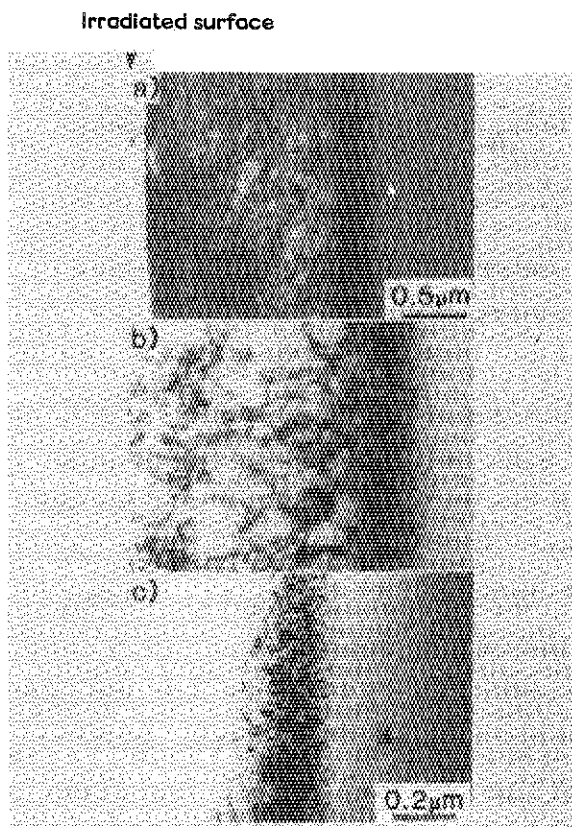


Fig.3 Damage structure observed in the specimen irradiated at 673 K.

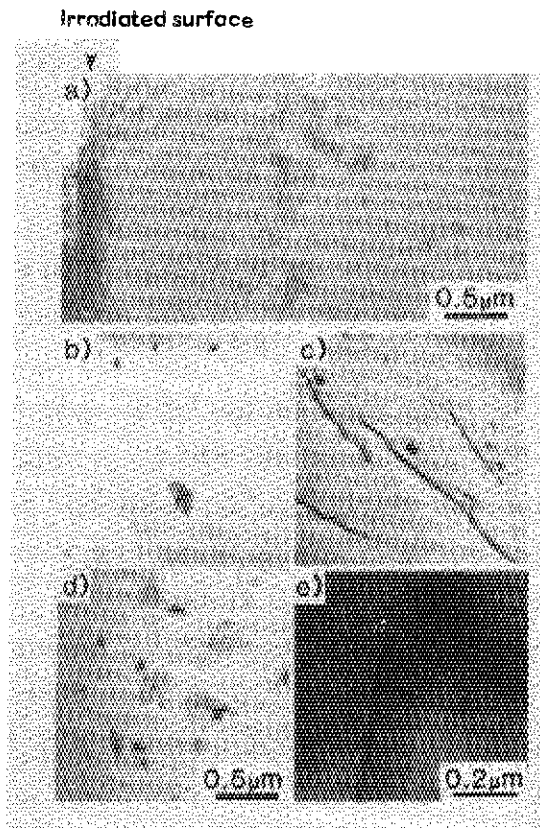


Fig.4 Damage structures observed in the specimen irradiated at 873 K.

### 3.12 EFFECT OF SOLUTE CARBON CONTENT ON THE DISTRIBUTION OF HELIUM BUBBLE AND DISLOCATION LOOP IN Ti-MODIFIED TYPE 316 STAINLESS STEELS IRRADIATED WITH HELIUM IONS

Kenji SUZUKI, Yoshio KATANO, Takeo ARUGA, Shozo HAMADA and Kensuke SHIRAISHI\*

Department of Fuels and Materials Research and \*Radio-isotope and Nuclear Engineering School, JAERI

The observation of helium bubbles and dislocations in Ti-modified Type 316 stainless steels irradiated with helium ions were made with an electron microscope in order to clarify the governing factor and mechanism for microstructure evolution. In this report, the effect of solute contents on the distributions of bubbles and dislocation loops is investigated in Ti-modified Type 316 stainless steels.

The materials used in this study were Ti-modified Type 316 stainless steel with 0.06 wt% carbon (PCA) and steels containing carbon up to 0.15 wt% (T-0, T-1, T-2). Chemical composition of the samples are given in Table 1; the base composition of Fe, Cr, Ni and Ti is selected to be equivalent to that of PCA. Samples of 3 mm diameter and 0.2 mm in thickness were solution annealed for 0.5 h at 1373 K in a vacuum of  $1 \times 10^{-4}$  Pa. The samples were irradiated for 1 h at 350 or 1023 K with 1.0 MeV He-ions using 2MV Van de Graaff accelerator<sup>1)</sup> to a dose of  $5 \times 10^{19}$  He/m<sup>2</sup> at a current density of 2 mA/m<sup>2</sup>. The injection produced a maximum concentration of  $2 \times 10^3$  appm and displacement damage of 0.08 dpa. Calculation with the E-DEP-81 code<sup>2)</sup> shows that the injected helium is distributed in the range from 1.4 to 1.9  $\mu$ m from the ion-incident surface of the specimen. Some samples irradiated at 350 K were annealed for 1 h at 1023 K in vacuum. All the samples were carefully electropolished so as to remove about 1.6  $\mu$ m from the front surface of the specimen, and then back-thinned to perforation. The radiation-produced microstructure was examined with a JEM-200A electron microscope operating at 200 kV. The foil thickness in the observed area was estimated to be 0.2-0.3  $\mu$ m by counting the number of equal thickness fringes at the edge of the specimen or the grainboundary. Distributions of helium bubbles were analyzed with a Zeiss TGZ particle size analyzer.

Typical microstructures produced by irradiation with 1.0 MeV He-ions to a dose of  $5 \times 10^{19}$  He/m<sup>2</sup> are shown in Fig. 1; symbols from a to d and from a' to d' denote the results obtained from specimens irradiated at 1023 K and post-irradiation annealed for 1 h at 1023 K, respectively. In the case of the specimen irradiated at 1023 K, helium bubbles are seen within the grain. Some helium bubbles are associated with fine precipitates in the T-0 and T-1 specimens (Fig. 1 a and b); the crystallographic structure of the precipitate could not be identified by selected area electron diffraction. Note that the precipitates were not observed in unirradiated specimens of T-0 and T-1, both having a thermal history similar to the irradiated specimens (Fig. 1 a-d). Many dislocation loops having same tendency of the distribution were observed together with helium bubbles in the specimen annealed for 1 h at 1023 K after irradiation at 350 K (Fig. 1 a'-d'). These observation indicate that the distribution of the dislocation loops were less affected by carbon content.

The correlation between the titanium and carbon contents in the austenitic steel is given in Fig. 2 in terms of the solubility relationship and stoichiometric composition for titanium carbide. The full curve in the figure indicates the solubility limit of titanium carbide in the matrix at 1373 K and is based on the equation by Padilha et al.<sup>3)</sup>. The solubility curve at 1023 K is approximated by the ordinate and abscissa. The composition of the titanium and carbon in the matrix of the specimens varies along the solid line parallel to the dashed stoichiometric line for titanium carbide. Both titanium and carbon contents in solution decrease to the composition indicated by the open circles when the specimens are solution annealed at 1373 K; undissolved TiC remains in the matrix after the solution annealing. Furthermore, the titanium and carbon in solution approach the composition indicated by the closed square causing the precipitation of titanium carbide during the long term aging at 1023 K.

The average diameter and number density of helium bubbles produced by He-ion irradiation at 1023 K and by post-irradiation annealing is presented in Fig. 3 as a function of the solute carbon content in the specimens solution annealed at 1373 K. The figure indicates that solute carbon in matrix suppresses the growth of helium bubbles within the grains as the result of the increase in the number density. Carbon atoms are considered to trap vacancies and consequently reduce the available

vacancies for diffusion of helium atoms; the diffusion coefficient of helium atoms decreases with an increase in the solute carbon content. The theoretical consideration has proved that the bubble density varies inversely as the square root of the gas atom diffusion coefficient<sup>4)</sup>.

In summary, with an increase in carbon content, the number density increased and the average diameter of helium bubbles decreased, respectively. The observation indicate that the solute carbon in matrix suppresses the growth of helium bubble within the grains as the result of the increase in the number density.

#### Reference

- 1) K. Suzuki, Y. Katano, T. Aruga and K. Shiraishi: JAERI-M 84-181 (1984).
- 2) T. Aruga: JAERI-M 83-226 (1984).
- 3) A.F. Padilha, G. Shanz and K. Anderko: J. Nucl. Mater., 105 (1982) 77.
- 4) J. Gittus: Irradiation Effects in Crystalline Solids (Applied Science Publishers Ltd., London, (1978) 62.

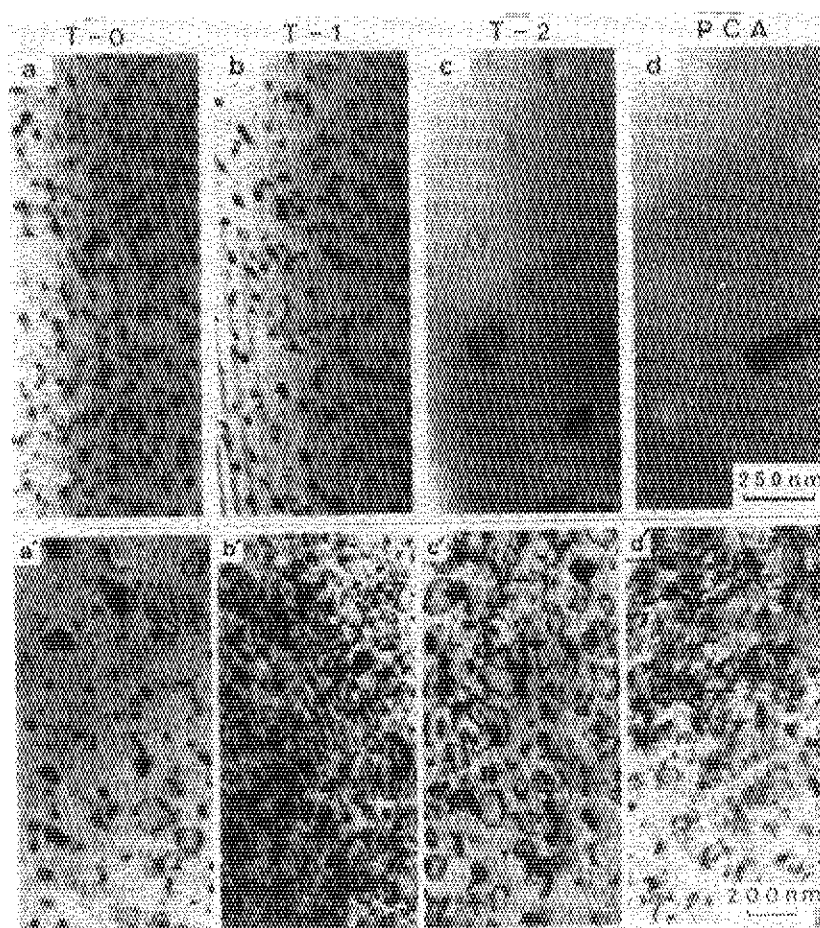


Fig. 1. Bubble, precipitate and dislocation components of the samples irradiated with 1.0 MeV He-ions at 1023 K (a, b, c and d) and post-irradiation annealed for 1h at 1023 K (a', b', c' and d').



Table 1 Chemical composition of Ti-modified type 316 stainless steel (wt %)

	Ni	Cr	Mo	Si	Mn	Ti	C	P	B	S	Nb	Fe
T-0	16.69	15.28	-	<0.01	0.07	0.31	<0.01	<0.003	0.0004	0.014	<0.01	Bal.
T-1	16.11	15.00	-	0.05	0.06	0.30	0.055	0.002	0.0004	0.010	<0.05	Bal.
T-2	16.70	14.71	-	0.09	0.22	0.27	0.15	0.003	0.0004	0.015	<0.05	Bal.
PCA	16.22	14.51	2.37	0.53	1.79	0.24	0.06	0.027	0.0035	-	-	Bal.

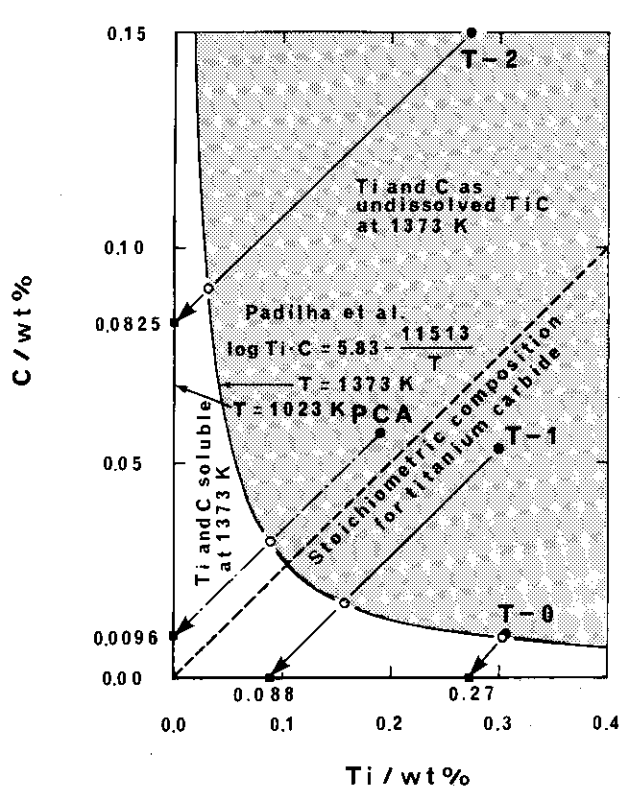


Fig. 2. The correlation between titanium and carbon content in the austenitic steel with respect to the solubility relationship and stoichiometric composition for titanium carbide.

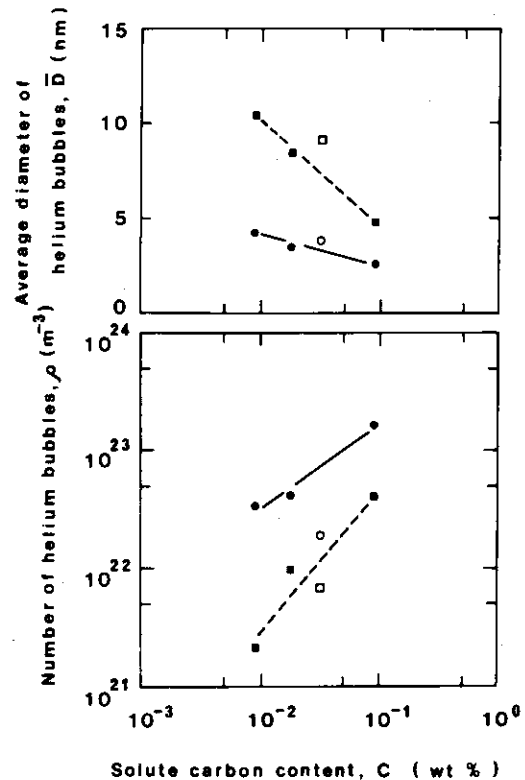


Fig. 3. Density and average diameter of helium bubbles in the Ti-modified steels irradiated at 1023 K (dashed line) and post-irradiation annealed (solid line).

## 3.13 MICROSTRUCTURAL EVOLUTION IN N-ION IRRADIATED STAINLESS STEEL

Takeo ARUGA, Yoshio KATANO and Kensuke SHIRAIISHI

Department of Fuels and Materials Research, JAERI

1. Introduction

Ion irradiation has been in use as a tool to study radiation damage in metals. The radiation damage produced by ions has a strong gradient and the implanted ions affect the microstructural evolution during the irradiation. However, sophisticated examination of the ion-produced microstructures with the predicted damage energy and implanted-ion profiles provides data useful for understanding the fundamental mechanisms of the radiation damage. As well as implanted helium<sup>1)</sup>, nitrogen and carbon ions are reported to modify the radiation-produced microstructure of Type 316 stainless steel<sup>2,3)</sup>.

This report describes the microstructural observation of Type 316 stainless steel irradiated by N-ions with a 2MV Van de Graaff.

2. Precipitates produced in N-ion irradiated stainless steel

Samples of solution-annealed Type 316 stainless steel were irradiated at 803 K with 1.1 MeV N-ions up to a dose of 60 dpa at a damage peak. The damage profile calculated by the E-DEP-1 computer code<sup>4)</sup> with displacement energy of 40 eV shows that the peak damage position occurs at a depth of 0.77  $\mu\text{m}$  from the specimen surface. The rates of damage and nitrogen-ion injection are estimated to be about  $1 \times 10^{-3}$  dpa/s and 2.8 appm/s, respectively, at their peaks. The irradiated samples were electropolished carefully so as to remove the front surface of the specimen by about 0.7  $\mu\text{m}$ , and then back-thinned to perforation. The microstructure produced was examined with a JEM-1000D electron microscope operating at 1000 kV. The compositions of the precipitates were analyzed using the technique of X-ray EDS with a JEM-200CX.

The microstructure produced by the irradiation to a peak dose of 20 dpa is characterized by fine precipitates formed at the radiation-produced Frank loops. The EDS analysis reveals that Si and Ni are enriched at the precipitate. Furthermore, weak superlattice spots appear between the strong matrix spots in the selected area diffraction (SAD) pattern. Thus, the fine precipitate is deduced to be the ordered  $\gamma'$ -phase of nominally  $\text{Ni}_3\text{Si}$ <sup>5)</sup>. In

the specimen irradiated to a peak dose of 60 dpa, the precipitates with diameter of 9 to 56 nm are observed in the number density of  $7.5 \times 10^{21}/\text{m}^3$ . The microstructure and the EDS spectrum for the specimen irradiated 60 dpa are given in Fig. 1. The EDS analysis shows that Cr is enriched to be 26-42 wt% in the precipitate. The diffraction spots in SAD pattern indicate that the precipitate is CrN phase; a NaCl-type structure with a lattice parameter of 0.4141 nm.

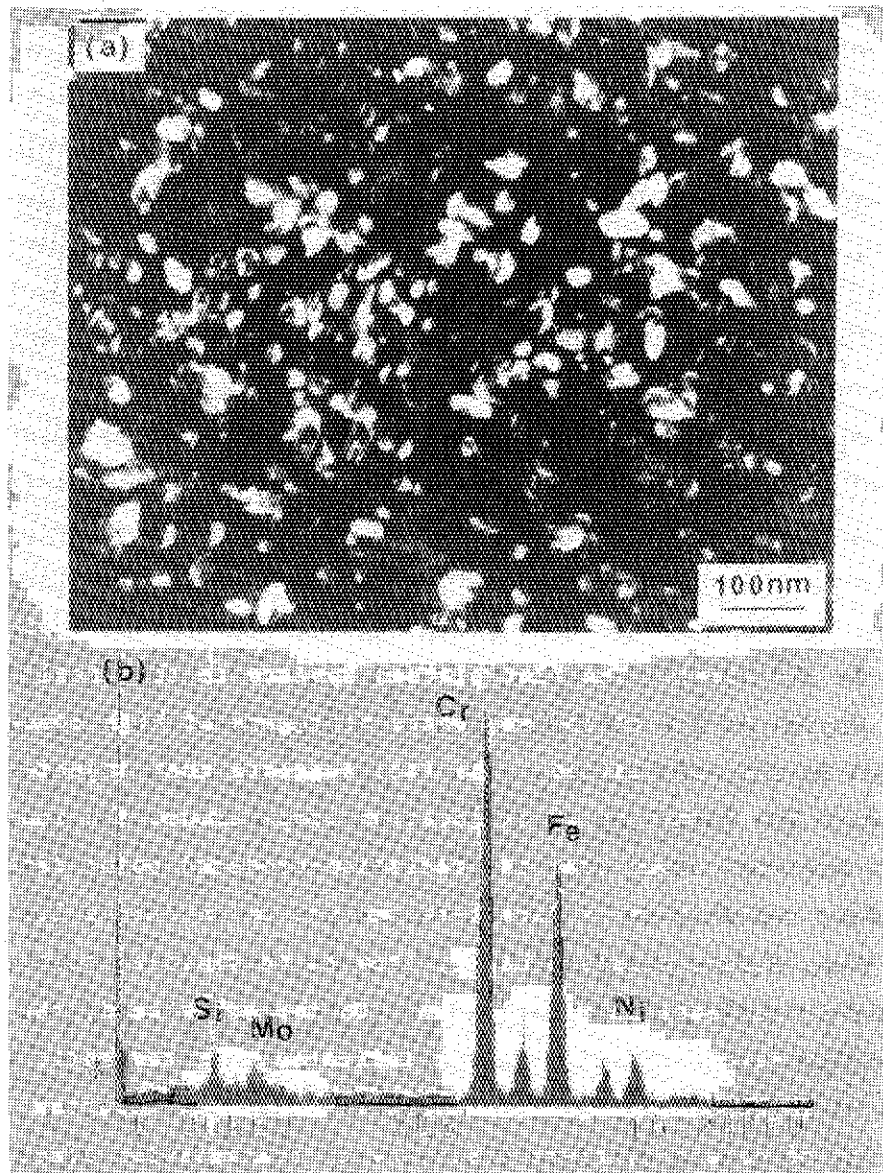


Fig. 1 The dark-field micrograph (a) and EDS spectrum (b) for the precipitate in Type 316 stainless steel irradiated with 1.1 MeV N-ions to 60 dpa at 803 K.

The injected nitrogen atoms segregate to stabilize the radiation-produced Frank loops in an early stage of irradiation. Then, Si and Ni binding with radiation-produced interstitials migrate to the Frank loops to form the precipitate of the  $\gamma'$ -phase. When the irradiation proceeds to 60 dpa, injected nitrogen precipitates as CrN phase. The radiation-produced precipitates of  $\gamma'$  are swallowed up by the nitride.

### 3. Depth profile of loop formation in N-ion irradiated stainless steel

Wedge-shaped specimens in a disk of 3 mm in diameter for transmission microscope observation were prepared from solution-annealed Type 316 stainless steel. The specimens were irradiated with 0.3 MeV N-ions at 723 K to a peak dose of 0.6 dpa. The irradiation corresponds to injected nitrogen concentration of 0.046 wt% at peak. The projected range and peak damage depths are 0.30 and 0.24  $\mu\text{m}$  in the calculation with E-DEP-1 code, respectively. The microstructure of the irradiated specimen was examined with a JEM-200A electron microscope and the areal loop number density was measured as a function of distance from the foil edge.

Small dislocation loops of interstitial type with 3 to 50 nm in size are observed to form in the foil region where the thickness is larger than about 100 nm. The region thinner than 100 nm is denuded of loops. The areal loop number density increases to be  $1.2 \times 10^{15}/\text{m}^2$  with the foil thickness up to 400 nm which corresponds to the penetration depth for 0.3 MeV N-ions in the steel. The flat plateau appears in the areal loop number density at depths of 250 to 350 nm, where nitrogens of high concentration are injected in the calculation. The fact suggests that injected nitrogen atoms suppress the formation of dislocation loops around the ion-end-of-range. The nitrogen atoms trap the radiation-produced point defects and enhance defect annihilation by direct-recombination to reduce local defect density. Then, defect clusters hardly grow to be visible loops even if defect clusters nucleate in this region. On the other hand, the increase of loop density beyond the flat region indicates that the ratio of displacement atoms to injected nitrogen concentration plays an important role for the formation of defect clusters visible with transmission electron microscopy.

### 4. Summary

The irradiation of Type 316 steel with 1.1 MeV N-ions at 803 K to 20

dpa at peak induces precipitation of  $\gamma'$ -phase, nominally  $\text{Ni}_3\text{Si}$ , and precipitates are replaced by CrN phase during the irradiation to 60 dpa. Suppression of dislocation loop formation around the ion-end-of-range is also observed in Type 316 steel irradiated with 0.3 MeV N-ions at 723 K to a low dose of 0.6 dpa.

#### References

- 1) K. Farrell: Radiat. Eff. 53 (1980) 175.
- 2) K. Shiraishi, T. Aruga and Y. Katano: J. Nucl. Mater. 103&104 (1981) 1053.
- 3) T. Aruga, Y. Katano and K. Shiraishi: J. Nucl. Mater. 122&123 (1984) 191.
- 4) I. Manning and G. P. Mueller: Computer Phys. Commun. 7 (1974) 85.
- 5) Y. Katano, T. Aruga and K. Shiraishi: J. Nucl. Mater. in press.

3.14 DAMAGE STRUCTURE IN ION-IRRADIATED  $\text{Si}_3\text{N}_4$ 

Kenji NODA, Yoshinobu ISHII, Kotaro KURODA\*, Hiroyasu SAKA\*,  
Yoshinobu NAKATA\*, Masayuki ARITA\*, Toru IMURA\* and  
Hitoshi WATANABE

Department of Fuels and Materials Research, JAERI, \*Faculty  
of Engineering, Nagoya University

Refractory low-Z materials as surface materials of the first wall of fusion reactors will be subjected to not only surface erosion but also irradiation damage due to 14 MeV neutrons. In this study, microstructure of ion-irradiated  $\text{Si}_3\text{N}_4$  was observed by transmission electron microscope (TEM), to understand the irradiation damage in  $\text{Si}_3\text{N}_4$  as one of candidate of the low-Z materials.

Sintered  $\text{Si}_3\text{N}_4$  including 8 %  $\text{Y}_2\text{O}_3$  as a binder was thinned by ion beam milling, to make TEM specimens. The specimens were irradiated to  $2.2 \times 10^{21}$  ions/ $\text{m}^2$  at an ambient temperature by He or Ar ions with an energy of 400 keV. Before and after the irradiation, microstructure of the specimens was observed with 200 kV TEM.

Before irradiation, the specimens consisted of  $\text{Si}_3\text{N}_4$ , SiC, WC and Y-containing phase ( $\text{Y}_{10}(\text{SiO}_4)_6\text{N}_2$ ), and all of them were crystalline. Fig. 1 (a) shows the microstructure after the Ar-ion irradiation. The small grain denoted by X was identified as crystalline  $\text{Si}_3\text{N}_4$  by the diffraction pattern and it was surrounded with amorphous materials denoted by A. In Fig. 1 (b) the diffraction halos due to the amorphous material A are shown. The interface between the crystalline  $\text{Si}_3\text{N}_4$  and the amorphous material appears white. Fig. 2 shows the interface at high magnification. In the amorphous area adjacent to the crystalline  $\text{Si}_3\text{N}_4$ , many white spots are observed. These spots were found to be voids or bubbles by defocusing experiments. Fig. 3 shows the amorphous materials in some regions other than  $\text{Si}_3\text{N}_4$  grains, the diffraction halos and white parts of the interface between the  $\text{Si}_3\text{N}_4$  grain and the amorphous materials (many voids or bubbles) in He-ion irradiated specimens. In case of the He-ion irradiation, the irradiation damage was not so severe in comparison with the case of Ar-ion irradiation, although microstructures are similar in both cases. This may be attributed to displacement per atom by the Ar-ion irradiation which is larger than that by the He-ion irradiation.

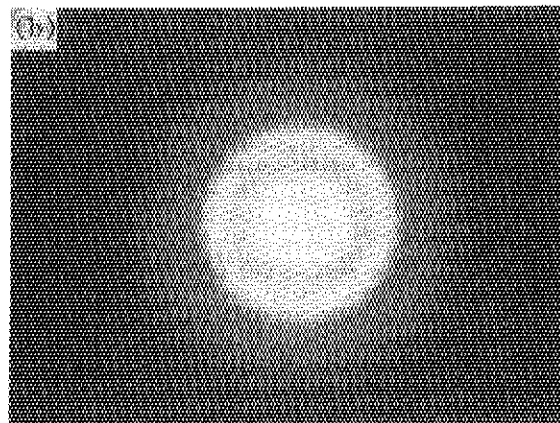
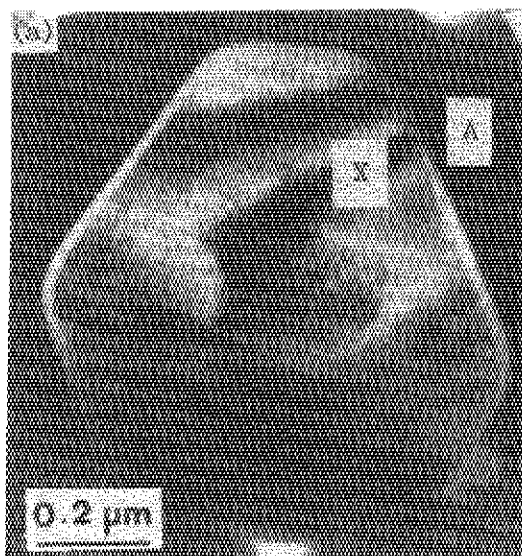


Fig. 1 (a) Microstructure of Ar-ion irradiated  $\text{Si}_3\text{N}_4$ , (b) diffraction halos from the amorphous material A.

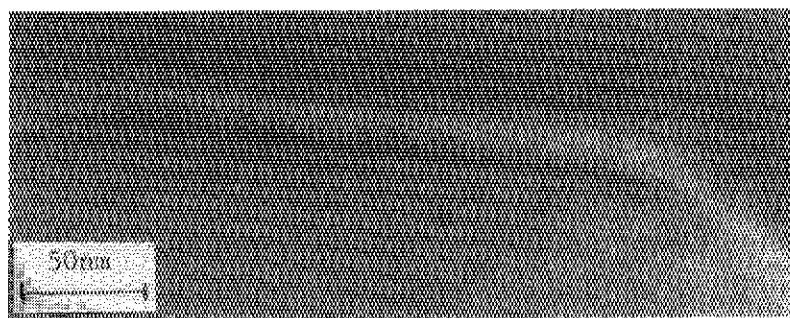
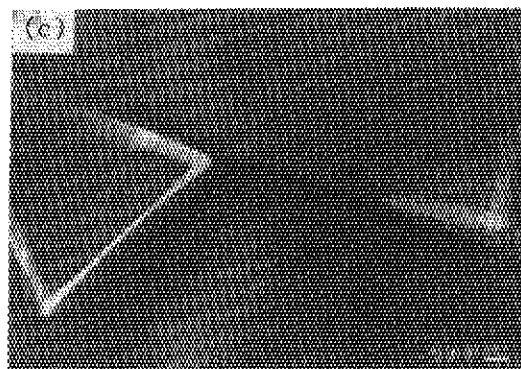
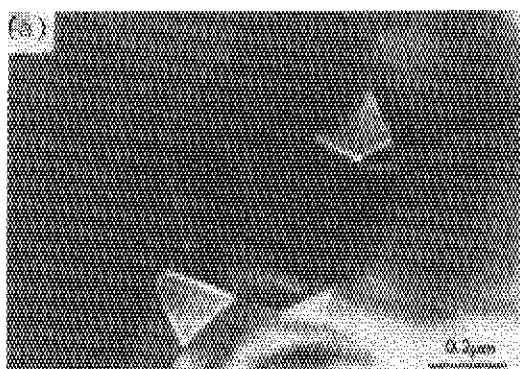


Fig. 2 Interface between the amorphous material and the  $\text{Si}_3\text{N}_4$  grain.



(b)

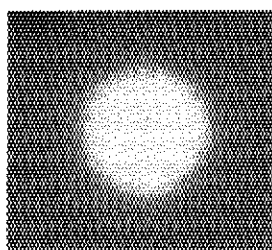


Fig. 3 (a) Microstructure of He-ion irradiated  $\text{Si}_3\text{N}_4$ , (b) the halo pattern, (c) the interface between the amorphous material and the  $\text{Si}_3\text{N}_4$  grain (white parts).

### 3.15 IRRADIATION EFFECT WITH LIGHT IONS ON SOME CERAMICS AND GLASSES

Hideo OHNO, Takanori NAGASAKI and Hiroji KATSUTA

Department of Nuclear Fuels and Materials Research,  
Japan Atomic Energy Research Institute

It is one of the important research items to investigate the nature of neutron- and ion-irradiated materials for the development of heavy-duty special purpose materials such as ceramics and glasses in nuclear fusion reactor.

Our research is concentrated to reveal the relation between the irradiation damage and bond character of these non-metallic inorganic materials. The PbO-SiO<sub>2</sub> glass is selected for research.

The structure of non-irradiated PbO-SiO<sub>2</sub> glasses was investigated by X-ray diffraction analysis and Raman spectroscopy. The Pb-O bond has the ionic character in the SiO<sub>2</sub>-rich region and has more of the covalent character with increasing PbO concentration.

Fig.1(a) shows Raman spectra of non-irradiated PbO-SiO<sub>2</sub> glasses of various composition. They are characterized by some peaks due to the Pb-O vibrational mode in a frequency region of less than  $2 \times 10^4 \text{ m}^{-1}$  and also by a large broad band due to Si-O stretching in the frequency region of  $8 \times 10^4$  to  $12 \times 10^4 \text{ m}^{-1}$ . It is deduced that the broad band due to Si-O stretching consists of five peaks near  $8.9 \times 10^4$ ,  $9.2 \times 10^4$ ,  $9.6 \times 10^4$ ,  $10.3 \times 10^4$  and  $11.5 \times 10^4 \text{ m}^{-1}$  as shown in Fig.1(b). Comparison with the Raman and infrared absorption spectra suggests that these five peaks will arise from the SiO<sub>4</sub> tetrahedron with four, three, two, one non-bridged oxygens and with four bridged oxygens, respectively.

The distributions of three kinds of oxygen, i.e. bridged oxygen(O<sup>0</sup>), non-bridged oxygen(O<sup>-</sup>) and free oxygen(O<sup>2-</sup>), have been calculated from the analysis of area intensities of these five peaks. The results are shown in Fig.2.

The irradiation of neutron or ion will affect the distribution of three kind of oxygen. The preliminary experiment for PbO-SiO<sub>2</sub> glasses with 1MeV H<sup>+</sup> ion was carried out. The analysis of Raman spectroscopy and a comparison with neutron irradiation are underway.



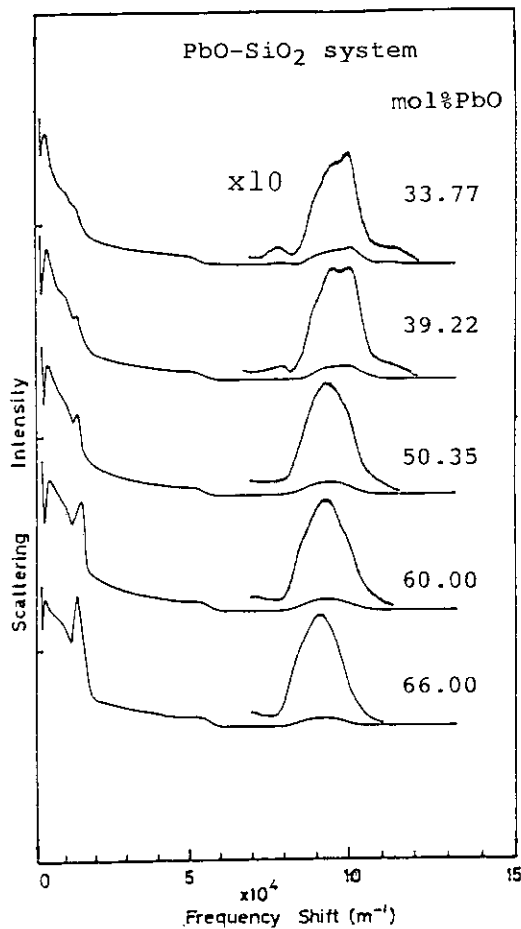


Fig.1(a) Raman spectra of PbO-SiO<sub>2</sub> glasses.

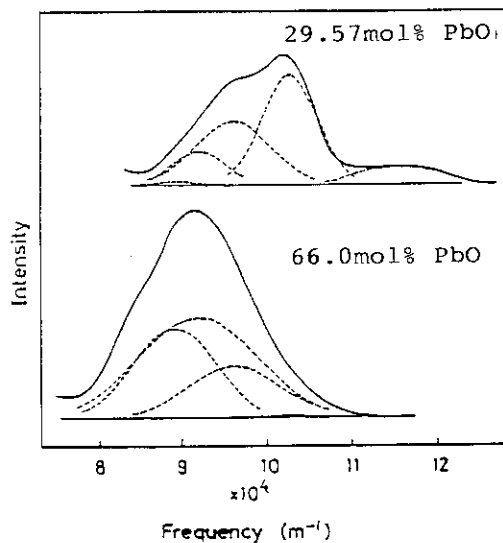


Fig.1(b) Raman spectra of PbO-SiO<sub>2</sub> glasses separated into five Gaussian bands.

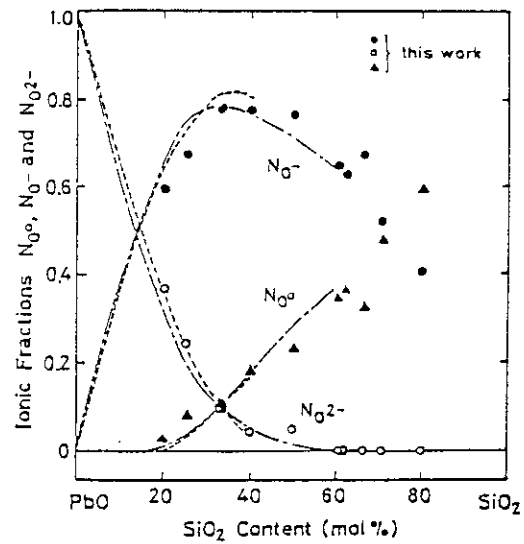


Fig.2 Distribution of  $O^0$ ,  $O^-$  and  $O^{2-}$  calculated from analysis of Raman spectra depending on the composition of PbO-SiO<sub>2</sub> glasses. --- and --- are the calculated values thermodynamically.

## IV      NUCLEAR CHEMISTRY

## 4.1 NUCLEAR CHEMISTRY OF ACTINIDS

III.  $^{16}\text{O} + ^{238}\text{U}$  AND  $^{12}\text{C} + ^{242}\text{Pu}$  REACTIONS

Nobuo SHINOHARA, Shigekazu USUDA, Shin-ichi ICHIKAWA,  
 Toshio SUZUKI, Hiroshi OKASHITA, Hideki YOSHIKAWA\*,  
 Yousei IWATA\*\*, Takayoshi HORIGUCHI\*\*, Yasukazu YOSHIKAWA\*\*,  
 Seiichi SHIBATA\*\*\* and Ichiro FUJIWARA\*\*\*\*

Department of Chemistry, JAERI, \* Department of Chemistry,  
 Tokyo Metropolitan University, \*\* Department of Physics,  
 Hiroshima University, \*\*\* Institute for Nuclear Study,  
 University of Tokyo and \*\*\*\* Institute of Atomic Energy,  
 Kyoto University

The production of actinoids from the reaction of  $^{16}\text{O}$  with  $^{238}\text{U}$  target has been studied<sup>1,2)</sup> and seventeen nuclides were identified for this reaction. To investigate the production mechanism of actinoids from heavy-ion bombardment of actinoid targets, we started the experiment of an alternative reaction system in which  $^{242}\text{Pu}$  target is irradiated by  $^{12}\text{C}$  ions. The reaction forms the same compound nucleus of  $^{254}\text{Fm}$  by complete fusion reaction as that in the  $^{16}\text{O} + ^{238}\text{U}$  reaction system. It was found so far that the isotopes of  $^{250}\text{Fm}$ ,  $^{244,245,246}\text{Cf}$  and  $^{242}\text{Cm}$  were also produced in the  $^{12}\text{C} + ^{242}\text{Pu}$  reaction as well as in the  $^{16}\text{O} + ^{238}\text{U}$  reaction.

Experimental

The  $^{238}\text{U}$  target arrangement, the irradiation of  $^{16}\text{O}$  ions, the chemical separations and the measurements of radioactivity were similar to those described in the previous reports<sup>1,2)</sup>.

The  $^{242}\text{Pu}$  target containing  $0.1 \text{ mg/cm}^2$  (99.8 %  $^{242}\text{Pu}$ ) was prepared by electrodeposition onto 7- $\mu\text{m}$  thick Al foil. The target was bombarded by  $^{12}\text{C}$  ions with energy 75 to 95 MeV and the beam intensity was up to 200 pA. The chemical separation was performed so far only for the Al catcher foil which collected the recoil nuclei. The measurements of radioactivity were carried out as described earlier<sup>1,2)</sup>.

## Results and discussion

 $^{16}\text{O} + ^{238}\text{U}$  reaction

In the previous paper<sup>1)</sup>, it was reported that nine actinoids such as  $^{250}\text{Fm}$ ,  $^{244,245,246}\text{Cf}$ ,  $^{242}\text{Cm}$ ,  $^{238,239}\text{Np}$  and  $^{237,239}\text{U}$  were identified in this reaction and their excitation functions were obtained at  $^{16}\text{O}$  ion energy from 85 to 110 MeV.

When the projectile energy increased to 110-130 MeV, formation of the Fm, Cf and Cm nuclides was diminished and production of Th, Ac and Ra nuclides was came into observation. After measuring the alpha-activities

and the half-lives and examining the chemical nature, various nuclides

such as  $^{225,226,227,228}\text{Th}$ ,  $^{224,225}\text{Ac}$  and  $^{223,224}\text{Ra}$  were

identified. The nuclides of the Th, Ac and Ra seem to be formed by picking up 2 to 4 protons and 8 to 11 neutrons from the  $^{238}\text{U}$  target;

He, Li, or Be fragments of various masses could be transferred to the projectile. Figure

1 gives the

formation cross sections of these nuclides as a function of the number of neutrons and protons picked up from the target

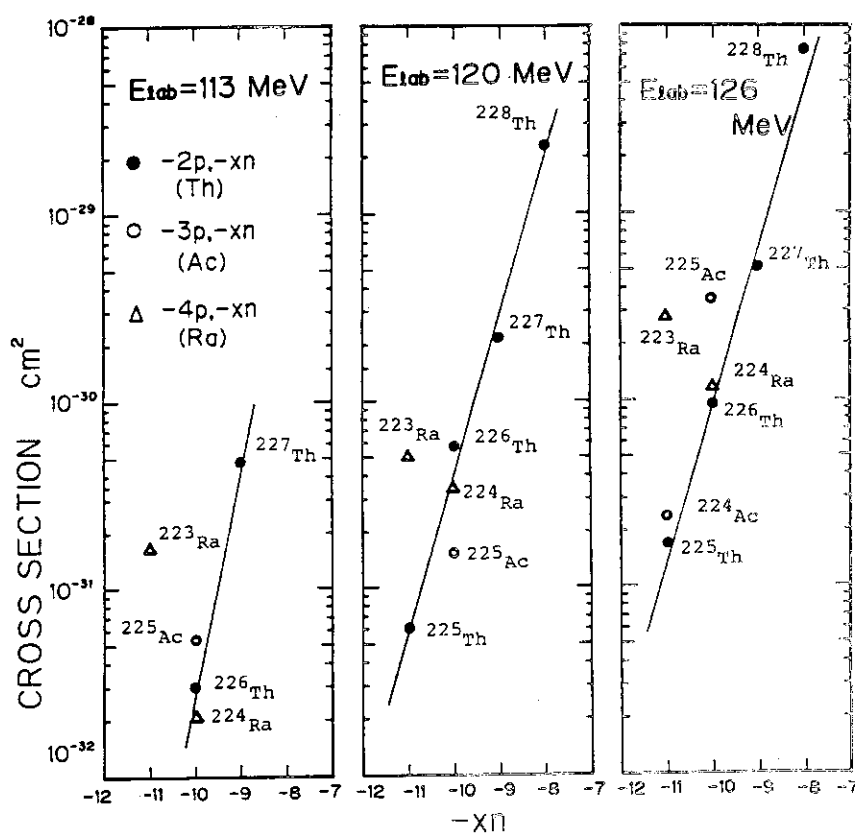


Fig. 1 Formation cross sections of the Th, Ac and Ra nuclides synthesized in the  $^{16}\text{O} + ^{238}\text{U}$  reaction. abscissa: number of the picked up neutrons, ordinate: measured cross section.

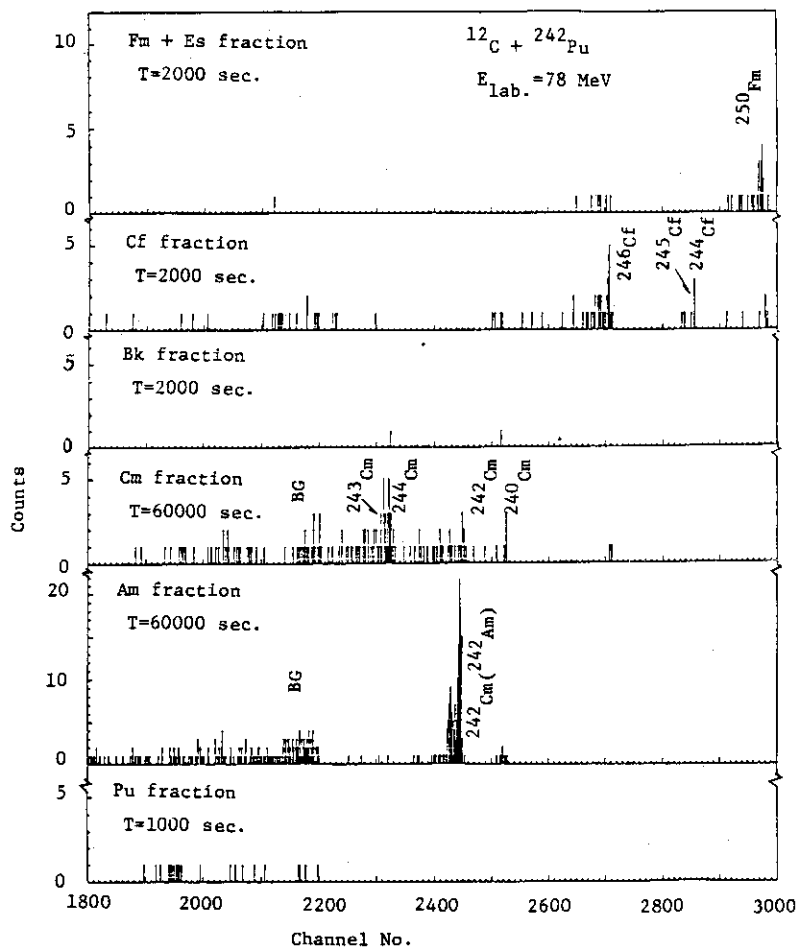


Fig. 2 Alpha-spectra of each actinoid produced in the  $^{12}\text{C} + ^{242}\text{Pu}$  reaction.

T: counting duration.

To clarify the difference between  $^{16}\text{O} + ^{238}\text{U}$  and  $^{12}\text{C} + ^{242}\text{Pu}$  reactions, further measurements of the formation cross sections of  $^{250}\text{Fm}$ ,  $^{244-246}\text{Cf}$  and  $^{242}\text{Cm}$  are in progress.

#### References

- 1) N. Shinohara et al.: "JAERI TANDEM Annual Report 1983", JAERI-M 84-129 (1984) pp. 57-59.
- 2) N. Shinohara et al.: Proceedings of the 1984 International Chemical Congress of Pacific Basin Societies, in press, D.Reidel Publishing Company (1985).

nucleus.

#### $^{12}\text{C} + ^{242}\text{Pu}$ reaction

The actinoid nuclides such as  $^{250}\text{Fm}$ ,  $^{244,245,246}\text{Cf}$  and  $^{242}\text{Cm}$  were expected to be synthesized in  $^{12}\text{C} + ^{242}\text{Pu}$  reaction. The chemical behaviors, the alpha-energies and half-lives observed indicated the formation of  $^{250}\text{Fm}$ ,  $^{244-246}\text{Cf}$  and  $^{242}\text{Cm}$  nuclides. The alpha-spectra of each actinoid fraction after ion-exchange separation are shown in Fig. 2.

#### 4.2 DECAY OF THE COMPOUND NUCLEI PRODUCED IN THE REACTIONS OF $^{197}\text{Au}$ INDUCED BY $^{16}\text{O}$ AND $^{12}\text{C}$

Sumiko BABA\*, Kentaro HATA\*, Toshiaki SEKINE\*, Yuichiro NAGAME\*, Shin-ichi ICHIKAWA\*\*, Nobuo SHINOHARA\*\*, Hiroshi BABA\*\*\*, Tadashi SAITO\*\*\*, Akihiko YOKOYAMA\*\*\*, Naruto TAKAHASHI\*\*\*, Masahide SHOJI\*\*\*, Ichiro FUJIWARA\*\*\*\*

\*Department of Radioisotopes, \*\*Department of Chemistry, JAERI, \*\*\*Osaka University, \*\*\*\*Kyoto University

The radiochemical study of nuclear reactions of  $^{197}\text{Au}$  with  $^{16}\text{O}$  and  $^{12}\text{C}$  ions has been continued. In this work, the neutron evaporation of the compound nuclei produced in the reaction of  $^{197}\text{Au}$  with  $^{16}\text{O}$  or  $^{12}\text{C}$  was investigated to discuss the competition between evaporation and fission.

Table 1 lists the decay properties of Fr isotopes which are produced after neutron evaporation of the compound nucleus in the  $^{197}\text{Au} + ^{16}\text{O}$  reactions. All the Fr isotopes are short-lived and some of them compose pairs of nuclides possessing similar half lives and therefore similar  $\alpha$ -ray energies to one another. Therefore we used the following three types of measuring instruments; an isotope separator on-line (ISOL), a rapid  $\alpha$ -emitter-detection (RAED) system, and conventional  $\gamma$ -ray spectrometer. An appropriate combination of the results of these three types of experiments made it possible to deduce the absolute cross section of

Table 1. Decay properties of Fr isotopes<sup>†</sup>

Isotope	Half life	$E_{\alpha}$ (MeV)	$\alpha$ /total	Daughters
$^{210}\text{Fr}$	3.18 m	6.572	1.00 <sup>††</sup>	$^{206}\text{At}$
$^{209}\text{Fr}$	50 s	6.646	0.89	$^{205}\text{At}$ , $^{209}\text{Rn}$
$^{208}\text{Fr}$	58 s	6.636	0.74	$^{204}\text{At}$ , $^{208}\text{Rn}$
$^{207}\text{Fr}$	14.8 s	6.761	0.93	$^{203}\text{At}$ , $^{207}\text{Rn}$
$^{206}\text{Fr}$	16.0 s	6.785	0.85	$^{202}\text{At}$ , $^{206}\text{Rn}$

<sup>†</sup> P. Hornshøj et al. (ref. 6)

<sup>††</sup> tentative

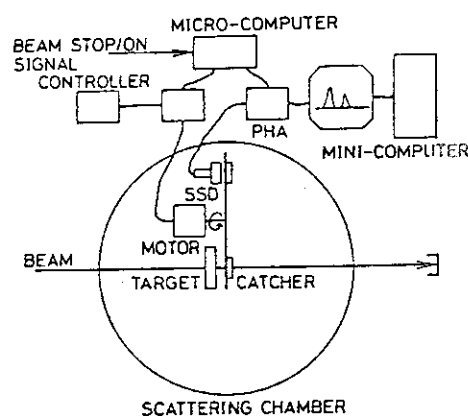


Fig. 1 Experimental setup for  $\alpha$ -ray measurement of catcher foil with the rapid  $\alpha$ -emitter-detection system.

Fr isotopes for the first time. Namely, we measured relative yields of Fr isotopes by ISOL, the equipments of which was previously described elsewhere<sup>1)</sup>, while relative yields of Fr isotopes and At isotopes were obtained by  $\alpha$ -ray measurement of catcher foil with the RAED system (shown in Fig.1). Furthermore,  $\gamma$ -ray measurements with Ge(Li) detector were carried out to determine the cumulative absolute cross sections.

The evaporation cross section data of the  $^{197}\text{Au} + ^{12}\text{C}$  reaction published up to date disagree with each other. The present work was performed to find the data by Bimbot et al.<sup>2)</sup> are most reliable. We determined cross sections of At isotopes in the  $^{197}\text{Au} + ^{12}\text{C}$  reaction by means of  $\gamma$ -ray spectrometry. The results of experiment are shown in Fig.2 and Fig.3.

A new trend of the angular-momentum dependence of the fission barrier  $B_f$  was empirically derived as

$$B_f(L) = B_f(0) (1 - kL/A^{1/3})^3 \quad 3)$$

with  $k = 0.069 \pm 0.003 \text{ n}^{-1}$ , where  $L$  is the angular momentum and  $A$  is the mass number. Fig.4 shows how well observed fission barriers (open

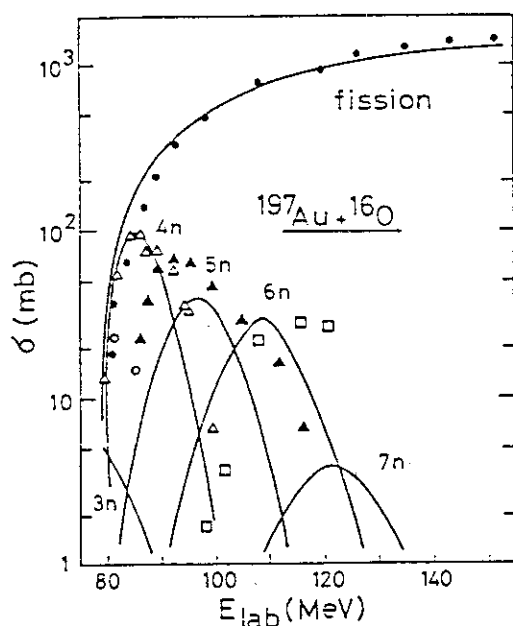


Fig.2 Excitation functions for the  $^{197}\text{Au}(^{16}\text{O}, xn)$  reactions and the fission process compared with the values calculated by ALICE code (solid line).

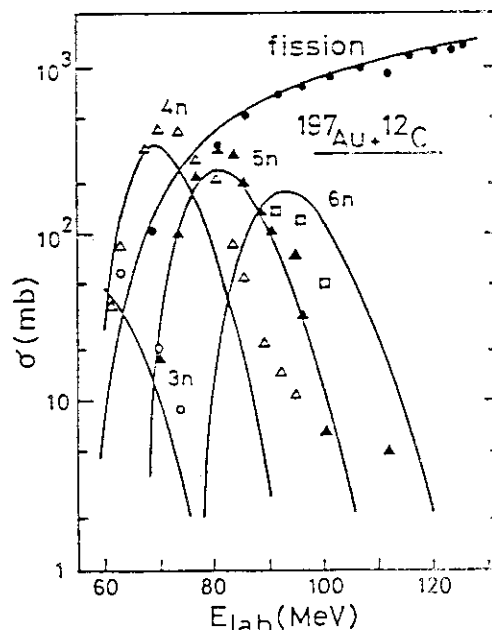


Fig.3 Same as Fig.2, but for the  $^{197}\text{Au}(^{12}\text{C}, xn)$  reactions and the fission process.

circles) are reproduced by the above equation (solid line). Applying the fission barrier deduced from the above formula to the  $^{16}\text{O}$ -induced and  $^{12}\text{C}$ -induced reactions, statistical calculation of evaporation and fission cross sections was done with ALICE code<sup>4)</sup>. The results are compared with the data of this work and the previously published experimental data for fission in Fig.2 and 3<sup>5)</sup>. The calculated values and the experimental ones agree well with each other in the evaporation residue cross sections and they agree excellently with each other in the fission cross sections.

#### References

- 1) S. Ichikawa et al.: JAERI-M 84-129 (1984) 60.
- 2) R. Bimbot et al.: J. Phys. 29 (1968) 563.
- 3) H. Baba and S. Baba: to be published.
- 4) F. Plasil et al.: Phys. Rev. C11 (1975) 508.
- 5) T. Sikkeland: Phys. Rev. 135B (1964) 669, G. E. Gordon et al.: Phys. Rev. 120 (1960) 1341.
- 6) P. Hornshøj et al.: Nucl. Phys. A230 (1974) 380.

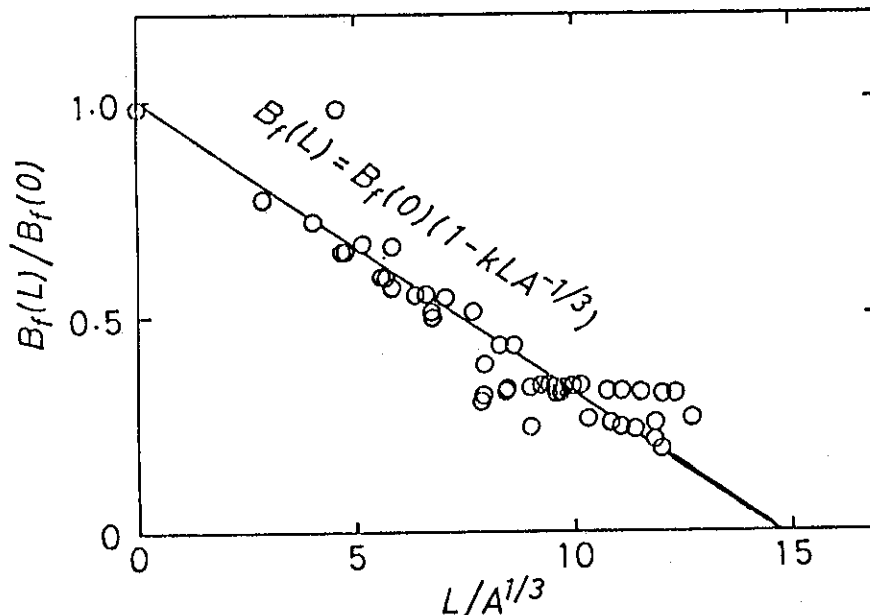


Fig.4 The fission barriers as a function of the angular momentum  $L$ .



## 4.3 NUCLEON TRANSFER REACTION OF GOLD INDUCED BY HEAVY IONS

Kentaro HATA, Yuichiro NAGAME, Sumiko BABA, Toshiaki SEKINE, Shin-ichi ICHIKAWA\*, Hiroshi BABA\*\*, Tadashi SAITO\*\*, Akihiko YOKOYAMA\*\*, Masahide SHOJI\*\* and Nobutsugu IMANISHI\*\*\*

Department of Radioisotopes, \*Department of Chemistry, JAERI, \*\*Osaka University, \*\*\*Kyoto University

Introduction

In experiments with light projectiles and heavy target nuclei at bombarding energies of the order of 10 MeV/u, one usually observes two distinct types of interaction: quasielastic transfer (QET) and deep-inelastic transfer (DIT) reactions. The QET reaction is distinguished from the DIT reaction by differences in the amount of energy dumping and in the characteristics of the angular distribution besides the degree of mass transfer and the tendency towards the charge equilibration. The purposes of the present work are to find some characteristics of those two types of transfer reaction and to deduce the precise interaction distance in the QET reaction. We have chosen very asymmetric systems composed of light projectiles and gold as a target, in which the DIT reaction is less important.

Experimental

We performed two types of experiments. One is an experiment to detect target-like products of the reaction induced by  $^{16}\text{O}$  and  $^{12}\text{C}$ , radiochemically. The details of this experiment were described elsewhere<sup>1)</sup>. In addition an experiment was carried out to detect projectile-like fragments in the 105 MeV- $^{16}\text{O}$  induced reaction using  $\Delta E$ -E counter telescope technique.

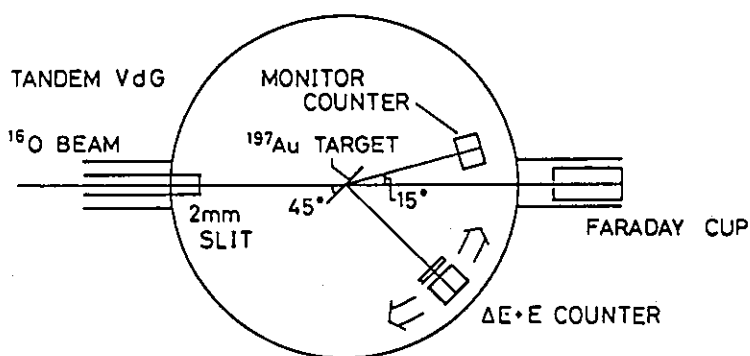


Fig.1 Experimental setup of the counter experiment of the  $^{197}\text{Au} + ^{16}\text{O}$  reaction.

Used detectors were a 50 $\mu$ m-thick( $\Delta E$ ), a 2 mm-thick(E), and a 100 $\mu$ m-thick Si semiconductor detectors(monitor). The experimental setup is shown in Fig.1.

### Results and discussion

Fig.2 gives the excitation functions of target-like products of the oxygen induced reaction. All the excitation functions exhibit the features of direct reaction. Fig.3 shows the angular distribution of projectile-like fragments ranging between 2 and 8 in atomic number. The spectra of  $^{17}\text{O}$ ,  $^{18}\text{O}$  and N are found to have a narrow peak. As the number of transferred nucleons increases, the maximum width becomes broader, and the position is displaced toward

smaller angles. These characters of the spectra show that a continuous transition from QET to DIT reaction occurs as the inelasticity of the process increases. Fig.4 shows the energy spectra of the oxygen component of the projectile-like products. The solid arrows show the product energy assuming QET mechanism producing  $^{17}\text{O}$  or  $^{18}\text{O}$ . At an angle of  $71^\circ$  the spectrum has two peaks: an elastic and an inelastic peak. On the contrary there are few counts except elastic  $^{16}\text{O}$  at  $40^\circ$ . The inelastic peak which lies near the grazing angle( $83.9^\circ$ ) is assigned to be QET process. Fig.5 shows the distribution of production cross sections of gold isotopes which form the counterparts of oxygen isotopes. All these distributions are found to be similarity reproduced with two gaussian distributions<sup>2)</sup>. Of the two gaussians, one closer to the

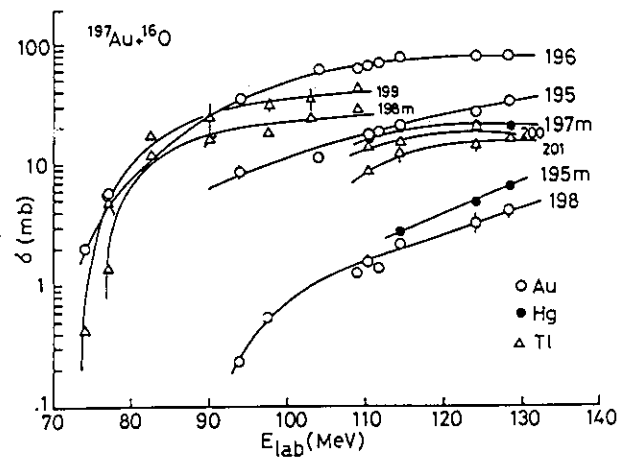


Fig.2 Excitation functions of target-like products in the  $^{197}\text{Au} + ^{16}\text{O}$ .

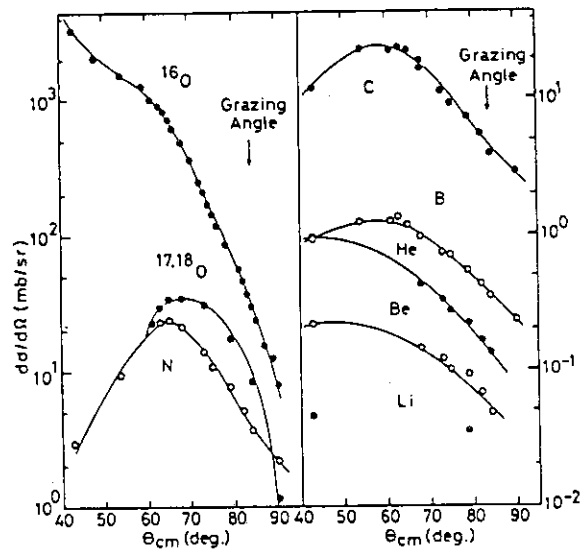


Fig.3 The angular distribution of projectile-like products ranging from O to N(left) and from C to Li(right).

target mass number is characterized by a narrower width, and the other has a wider distribution composed of both isotopes far from target and high spin metastable isotopes near the target mass. The peak positions of wider distributions all lie near the  $N/Z$  value of the compound system. This shows accomplishment of the charge equilibration found as one of the features of the DIT reaction. On the other hand, narrower peak represents the contribution of the QET reaction which is consistent with the general concept in the case of a few nucleon transfer reactions. We found that both width and peak position of the QET reaction are nearly independent of incident energy in the energy region of our experiment. On the contrary, the peak positions of the DIT reaction have a tendency of shifting to a lower mass number as the incident energy increases. This is an consequence of increasing of interaction time in the DIT reaction. In Fig.6 we assumed the expression of tunneling penetration applied to neutron transfer reaction below Coulomb barrier, and the interaction distances of one neutron transfer reaction were derived. In the expression,  $V_n$  is the neutron separation energy,  $E_n$  the excitation energy of a

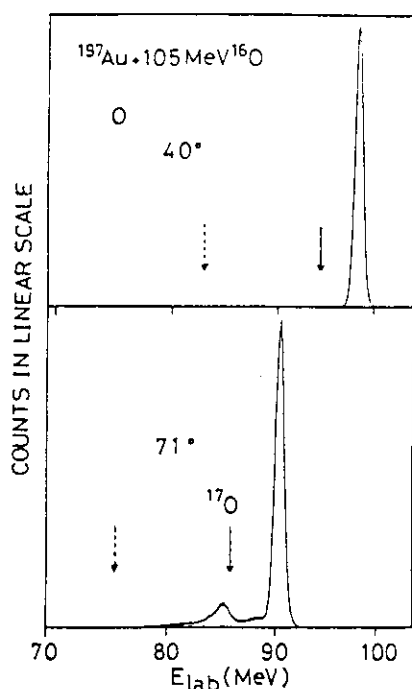


Fig.4 The energy spectra at 40° and 71° in lab. angle. Arrows indicate product energy assuming QET (solid one) or DIT mechanism (dashed one).

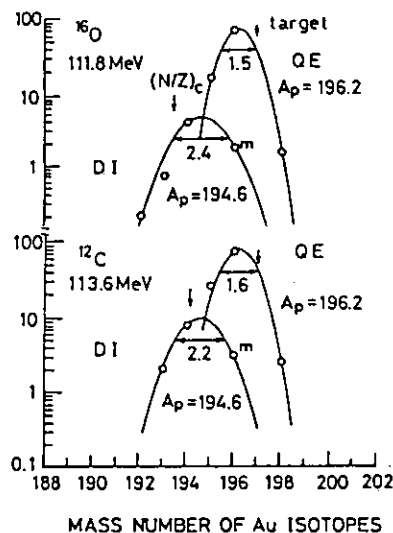


Fig.5 The formation cross sections of gold isotopes as a function of mass number of the products.

neutron in the nuclear potential well and  $L$  the width of the barrier or the separation between the surfaces. We assumed that the interacting configuration should be rather indifferent to the kind of projectile and consequently the  $L$  value is expected to be nearly the same among two projectiles we studied. Then we concluded that  $E_n$  should be 7 to 8 MeV close to the top of the potential well for the gold nucleus so as to assure the above postulate. In Fig.6 open circles represent the interaction distances derived from thus obtained  $L$ , while closed circles represent the interaction distances derived from the range data that we reported last year<sup>1)</sup>. The open circles are in good agreement with the closed one. This shows that with increasing incident energy the distance of closest approach decreases slowly in the one neutron transfer reaction.

#### References

- 1) S. Baba et al.: JAERI TANDEM ANNUAL REPORT 1983 (1984) 63.
- 2) J.V. Kratz et al.: Nucl. Phys. A357 (1981) 437.
- 3) G. Breit and M.E. Ebel: Phys. Rev. 103 (1956) 679,  
G. Breit and M.E. Ebel: Phys. Rev. 104 (1956) 1030.

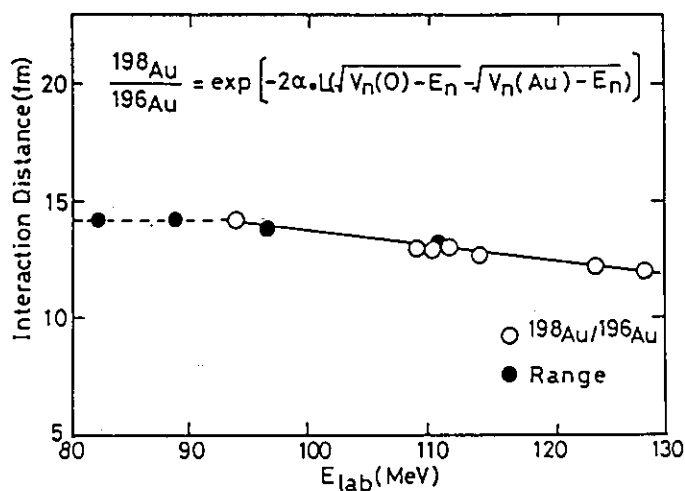


Fig.6 Dependence of the interaction distance on incident energy for one neutron transfer reaction in the  $^{197}\text{Au} + ^{16}\text{O}$  reaction. A solid line is drawn to guide the eyes for the observed data.

4.4 A STUDY OF THE DECAY OF  $^{121}\text{Ba}$ 

Shin-ichi ICHIKAWA, Toshiaki SEKINE\*, Kentaro HATA\*,  
Nobuo SHINOHARA and Naruto TAKAHASHI\*\*

Department of Chemistry, \*Department of Radioisotopes,  
JAERI, \*\*Osaka University

Introduction

The high-spin states of the  $^{121}\text{Cs}$  nucleus have been investigated by Garg et al. using in-beam gamma-ray spectroscopic method<sup>1)</sup>. The spins, magnetic moments and isotope shifts of Ba isotopes for  $A = 122-146$  have been determined by the ISOLDE collaboration<sup>2)</sup>. These data indicates a systematic change of deformation in this region of nuclides.

With respect to the  $^{121}\text{Ba}$  nucleus, the  $\beta$ -delayed proton emissions have been observed and its half-life was determined<sup>3)</sup>. There is, however, no information of the low-lying level and decay scheme of this nucleus.

The present paper deals with the emitted gamma-rays following decay of  $^{121}\text{Ba}$  nucleus and the tentative low-lying level scheme.

Experimental

The  $^{121}\text{Ba}$  nuclides were produced by the  $^{nat}\text{Mo}(^{32}\text{S}, X)$  reaction with 165-MeV  $^{32}\text{S}$  beam and were separated by the ISOL. The  $A = 121$  pure ions were collected on an aluminum-coated Mylar tape in the tape-transport system and moved in a second to a measuring port. An intrinsic Ge detector having 0.6 keV resolution at 122 keV was applied to the gamma-ray spectroscopy.

The identification of gamma-ray following decay of  $^{121}\text{Ba}$  nucleus was made by the elemental ionization difference of the surface ionization ion-source of ISOL with temperature adjustment. The decays of  $A = 121$  nuclides were traced by gamma-ray spectrometry.

The data were recorded with PDP 11/04 computer and the gamma-ray spectra were analyzed by using the BOB 75 code<sup>4)</sup>.

Results

Figure 1 shows the X- and gamma-ray spectra for the  $A = 121$  fraction when the  $^{nat}\text{Mo}$  target was bombed with  $^{32}\text{S}$  beam. The upper spectrum was measured at a higher temperature condition of the ion-source.

Comparison of these two gamma-ray spectra indicated five new gamma-rays ( 98.2, 99.2, 110.6, 111.6 and 210.8 keV ) appeared in this upper spectrum, which could not be assigned to any of the known isotopes in this mass region. Decays of these gamma-rays were traced as shown in Fig. 2. The 99.2 keV and 111.6 keV gamma-rays had  $30 \pm 2$  sec half-life and were assigned to the decay of  $^{121}\text{Ba}$ .

In the lower spectrum, Cs X-ray is rather weak as compared with the upper one. This gives another evidence for the identification of these gamma-rays to  $^{121}\text{Ba}$  since the supposed electron capture decay of  $^{121}\text{Ba}$  might produced strong Cs X-rays.

The gamma-ray peak at 210.8 keV was obscured by the 210.2 keV gamma-ray from the daughter nuclide ( $^{121}\text{Cs}$ ). The relative intensity of 210.8 keV gamma-ray was corrected for the contribution of  $^{121}\text{Cs}$  decay from the known decay scheme of  $^{121}\text{gCs}$  ( $T_{1/2} = 136$  sec)<sup>5)</sup>.

The energies and relative intensities of  $^{121}\text{Ba}$  gamma-rays were given in Table 1.

The spine and parity of the ground state of  $^{121}\text{Cs}$  was found to be  $3/2^+$ . The first excited state of  $^{121}\text{Cs}$  nucleus was known as an isomer with  $J^\pi = 9/2^+ 1)$ .

On the analogy of the neighbouring odd-mass Ba isotopes, we propose a tentative low-lying level scheme of  $^{121}\text{Ba}$  as shown in Fig. 3. The ground state of  $^{121}\text{Ba}$  is considered to correspond to the Nilsson orbit  $5/2^+ (413)$ .

#### References

- 1) U. Garg, T.P. Sjoreen and D.G. Fossan: Phys. Rev. C19 (1979) 217.
- 2) A.C. Mueller, F. Buchinger, W. Klempt, W.E. Otten, R. Neugart, C. Ekstrom and J. Heinemeier: Nucl. Phys. A403 (1984) 234.
- 3) B.D. Bogdanov, A.V. Demanov, V.A. Karnaukhov, L.A. Petrov and J. Voboril: Nucl. Phys. A303 (1978) 145.
- 4) H. Baba, T. Sekine, S. Baba and H. Okashita: JAERI-report, JAERI-1227 (1973).
- 5) K. Sofia, B.N. Subba Rao and J.E. Cramford: Phys. Rev. C24 (1981) 1615.

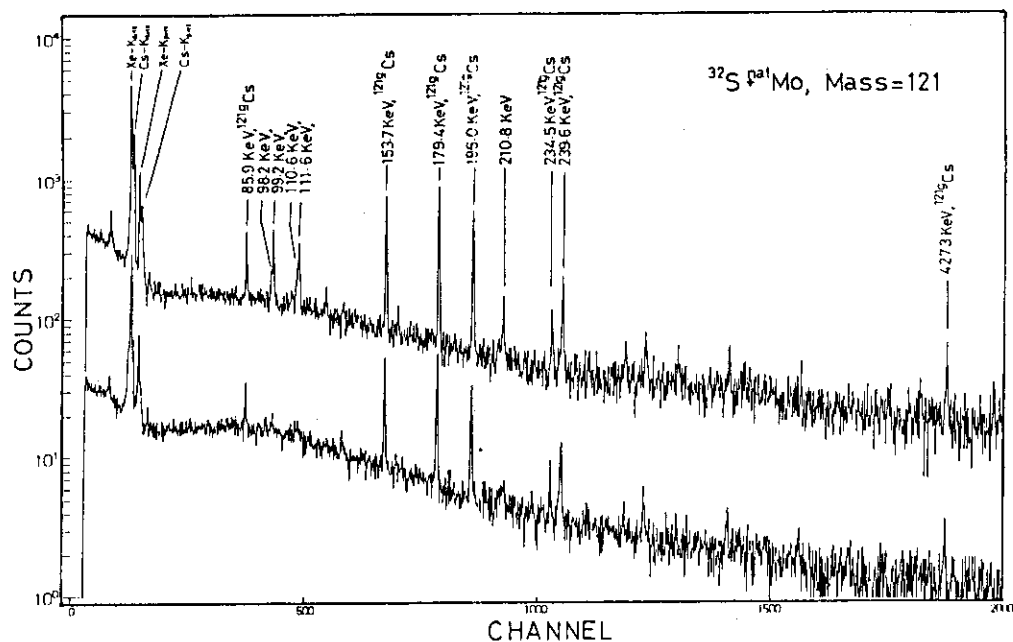


Fig. 1. The X- and  $\gamma$ -ray spectra for isotopes with  $A = 121$  in the bombardment of  $^{nat}\text{Mo}$  with 165-MeV  $^{32}\text{S}$  beam.

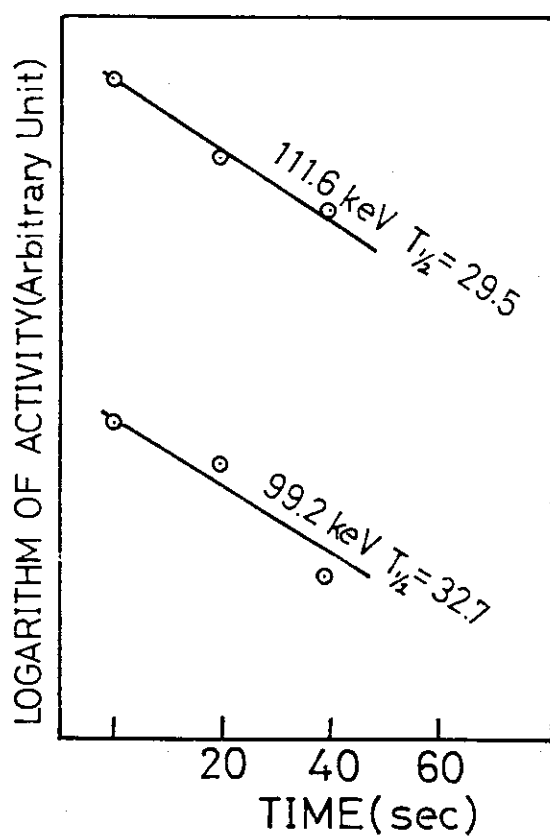


Fig. 2. Decay curves of the  $\gamma$ -rays from  $^{121}\text{Ba}$  nuclei (half-life:  $30 \pm 2$  sec).

Table 1. Energies and relative intensities of  $\gamma$ -rays for the  $^{121}\text{Ba}$  decay.

$E_{\gamma}$ (keV)	$I_{\gamma}$ (relative)
98.2	26.
99.2	86.
110.6	39.
111.6	100.
210.8	61.

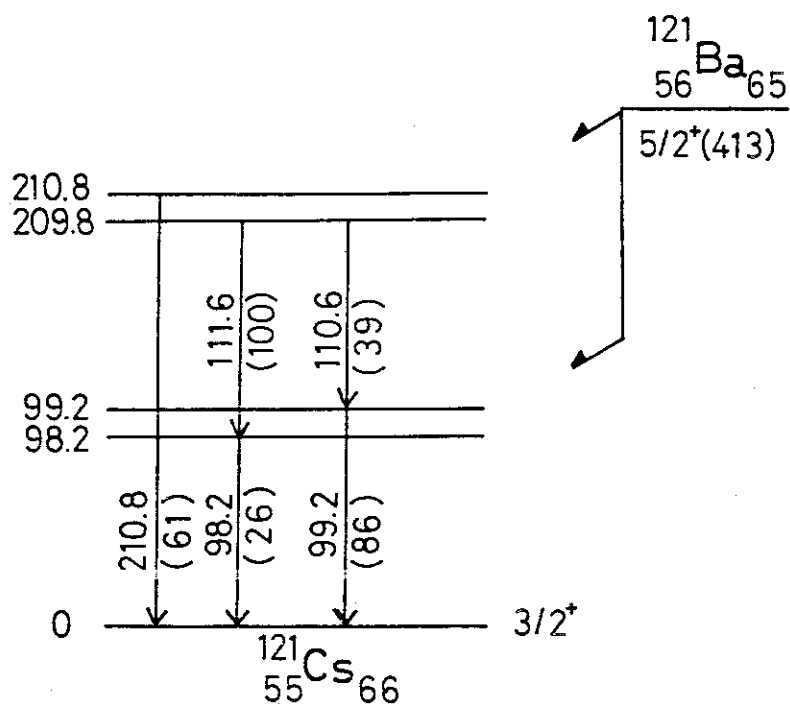


Fig. 3. Tentative level scheme proposed for  $^{121}\text{Ba}$ .



#### 4.5 A STUDY ON THE EXISTENCE OF THE LOW- $\ell$ CUTOFF BY ISOMER-RATIO MEASUREMENTS

Toshiaki SEKINE, Sumiko BABA, Kentaro HATA,  
Shin-ichi ICHIKAWA\* and Nobuo SHINOHARA\*

Department of Radioisotopes and Department of Chemistry,  
JAERI

Yields of various isomeric pairs have been measured in numerous nuclear reactions following the early work of Huizenga and Vandenbosch<sup>1)</sup>. The isomer ratios which were obtained have been analysed with a statistical model in order to deduce the properties of excited nuclei. Isomer ratios also have supplied some information on the initial angular momentum distributions of highly excited nuclei produced in fission or spallation. For heavy-ion nuclear reactions, measurement of isomer ratios offers some hope toward understanding the mechanism of angular momentum transfer between projectile and target.

In order to investigate the possibility of a low- $\ell$  cutoff<sup>2)</sup>, which seems important in the mechanism of angular momentum transfer between heavy ions, we have measured isomer ratios for  $^{99}\text{Rh}$  nuclei produced from  $^{105}\text{Ag}$  compound nuclei formed in two incident channels:  $^{12}\text{C} + ^{93}\text{Nb}$  and  $^{37}\text{Cl} + ^{68}\text{Zn}$ . Here, if the low- $\ell$  cutoff exists, some of the lowest partial waves in the formation of the compound nuclei are cut off in the more symmetrical combination of projectile and target, namely, the  $^{37}\text{Cl} + ^{68}\text{Zn}$  reaction. Isomeric pairs  $^{99\text{m}}\text{Rh}$  ( $9/2^+$ , 4.7 h) and  $^{99\text{g}}\text{Rh}$  ( $1/2^-$ , 15 d) are produced by (HI, $\alpha$ 2n) or (HI,2p4n) reactions: the statistical model<sup>3)</sup> predicts that the (HI, $\alpha$ 2n) reaction occurs for partial waves near a critical value of complete fusion, while the (HI,2p4n) reaction occurs for some of the lowest  $\ell$  waves. Therefore, the (HI,2p4n) component might reflect the low- $\ell$  cutoff in the  $^{37}\text{Cl} + ^{68}\text{Zn}$  reaction.

A part of this work was done in 1983 (4). In 1984 we carried out experiments at higher beam energies. Targets of  $^{93}\text{Nb}$  and  $^{68}\text{Zn}$  described previously<sup>4)</sup> were used. Beam energies incident to the targets were varied from 5.2 to 9.7 MeV/u for  $^{12}\text{C}$  and from 2.7 to 4.1 MeV/u for  $^{37}\text{Cl}$ , covering excitation energies of the compound nuclei from 50 to 100 MeV.

Activities produced in 15-min or 1.5-h irradiation were measured with Ge(Li) detectors connected to standard electronics. From some  $^{68}\text{Zn}$  target,  $^{99}\text{Rh}$  activities were chemically separated to increase the detection sensitivity, since they were accompanied by various activities from activation of the aluminium catcher and energy degrader.

The yields of  $^{99}\text{Rh}$  isomers in each target were determined using published half-lives,  $\gamma$ -ray energies, and branching ratios. Correction for the side feeding from the decay of  $^{99}\text{Pd}$  during and after irradiation was possible using its yield in each sample and its known decay branches to the isomers: 98.6% to  $^{99\text{m}}\text{Rh}$  and 1.4% to  $^{99\text{g}}\text{Rh}$ , respectively.

Cross sections were obtained from the observed yields, integrated beam current and the target thicknesses. The errors attached to the cross-section values were estimated by considering the uncertainties in the target thickness ( $\pm 2\%$  for the Nb target and  $\pm 5\%$  for the  $^{68}\text{Zn}$  target), and in the peak efficiency ( $\pm 2$ -10%) in addition to that of peak area.

In the  $^{12}\text{C} + ^{93}\text{Nb}$  reaction the experimental cross sections of the  $^{99}\text{Rh}$  isomers comprise components of both complete- and incomplete-fusion processes in the  $^{12}\text{C}$  beam energies from 60 to 80 MeV, as described previously<sup>5)</sup>. Modeling the incomplete fusion process, we partitioned the experimental cross sections of each isomer into two components by applying the results of recoil range measurements and obtained isomer ratios for each fusion process. The resulting isomer ratios  $\sigma_{\text{h}}/\sigma_{\text{l}}$  are shown in Fig. 1 as a function of the  $^{12}\text{C}$  beam energy together with the isomer ratios obtained from the experimental cross sections without partition. Here, the suffixes h and l mean a high-spin and a low-spin isomer, respectively. It can be noted from Fig. 1 that the incomplete fusion process suppresses the formation of the high-spin isomer. This result suggests that "breakup"  $\alpha$  particles in incomplete fusion carry away much more angular momenta than evaporation  $\alpha$  particles in complete fusion, provided incomplete fusion is occurring principally for partial wave near or even outside the critical value of complete fusion.

The  $^{99}\text{Rh}$  isomer ratios experimentally obtained from the  $^{37}\text{Cl} + ^{68}\text{Zn}$  reaction are plotted in Fig. 2 as a function of excitation energy  $E^*$  together

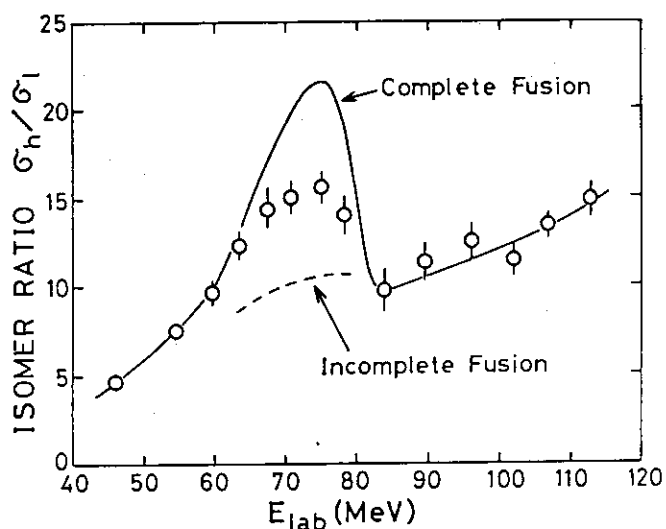


Fig. 1 Isomer ratio of  $^{99}\text{Rh}$  in the  $^{12}\text{C} + ^{93}\text{Nb}$  reaction obtained experimentally and those determined for complete- and incomplete-fusion processes by applying the results of recoil range measurements.

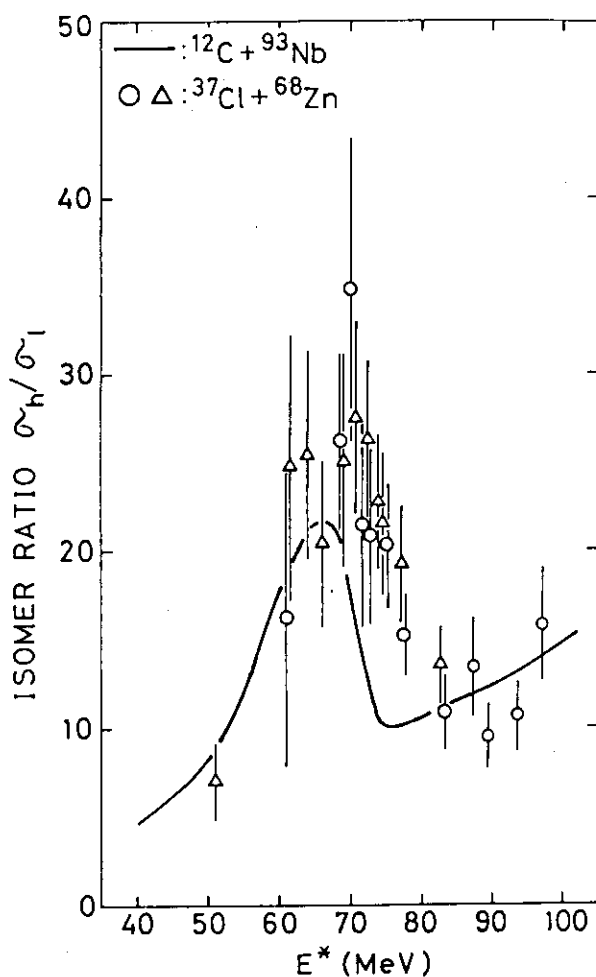


Fig. 2 Isomer ratio of  $^{99}\text{Rh}$  obtained experimentally from the  $^{37}\text{Cl} + ^{68}\text{Zn}$  reaction and determined for complete-fusion process in the  $^{12}\text{C} + ^{93}\text{Nb}$  reaction. The data shown as circles were obtained using chemical separation of rhodium.

with those obtained above for the complete-fusion process, which is comparable with the  $^{37}\text{Cl} + ^{68}\text{Zn}$  reaction, in the  $^{12}\text{C} + ^{93}\text{Nb}$  reaction. The isomer ratios in the two reactions seem to show essentially the same trend. They increase first sharply with  $E^*$ , then decrease, reach minimum values, and again increase rather slowly. This behaviour is expected by the statistical model. The first increase is attributable to the increase of  $\ell_{\text{cr}}$ , since the  $(\text{HI}, \alpha 2n)$  reaction is predominant in this energy range and the formation of the high-spin isomer is favoured. The decrease of the isomer ratios begins as the  $(\text{HI}, 2p4n)$  reaction sets in and the fraction of the low-spin isomers is increasing. The isomer ratio starts decreasing at  $E^* = 65$  MeV in the  $^{12}\text{C} + ^{93}\text{Nb}$  reaction while it is still increasing in the  $^{37}\text{Cl} + ^{68}\text{Zn}$  reaction. This difference reflects the fact that the  $^{37}\text{Cl} + ^{68}\text{Zn}$  reaction has higher values of  $\ell_{\text{cr}}$  above  $E^* \sim 62$  MeV; the same argument on  $\ell_{\text{cr}}$  explains why the isomer ratio in the  $^{37}\text{Cl} + ^{68}\text{Zn}$  reaction reaches a minimum value at much higher energy. The isomer ratio in the  $^{37}\text{Cl} + ^{68}\text{Zn}$  reaction, however, begins to decrease around  $E^* = 70$  MeV, which indicates that a sizable amount of the  $^{99}\text{Rh}$  nuclei is produced in the  $(\text{HI}, 2p4n)$  reaction. These results combined with the statistical model's prediction suggest that even in the  $^{37}\text{Cl} + ^{68}\text{Zn}$  reaction the angular momentum distribution of the compound nuclei extends down to possibly less than  $15 \hbar$ .

Nomura<sup>6)</sup> has reported possible evidence for the existence of a low- $\ell$  cutoff in relatively light heavy-ion reactions. In the foregoing discussion, however, it was not necessary to introduce the low- $\ell$  cutoff. This may be ascribed to the fact that the reaction energies in the present work are still below the critical value for the low- $\ell$  cutoff.

#### References

- 1) J.R. Huizenga and R. Vandenbosch: Phys. Rev. 120 (1960) 1305.
- 2) H. Gaubin, Y. Le Beyec, M. Lefort and R.L. Hahn: Phys. Rev. C10 (1974) 722.
- 3) M. Blann and J. Bisplinghoff: COO-3494-27 (1975).
- 4) T. Sekine, S. Baba, K. Hata, S. Ichikawa and N. Shinohara: "JAERI TANDEM Annual Report 1983", JAERI-M-84 129 (1984) 65.
- 5) T. Sekine: JAERI-M 84-085 (1984) 65.
- 6) T. Nomura: JAERI-M 84-085 (1984) 104.

#### 4.6 PREPARATION OF $^{237}\text{Pu}$ FROM $^{237}\text{Np}$ IRRADIATED WITH DEUTERONS

Sumiko BABA , Kentaro HATA , Toshiaki SEKINE ,  
Mishiroku IZUMO and Ryoza MOTOKI

Department of Radioisotopes, JAERI

The production method of a gamma-ray emitting plutonium isotope  $^{237}\text{Pu}$  by using the  $^{237}\text{Np}(d,2n)^{237}\text{Pu}$  reaction has been investigated. The excitation functions for the formation of Pu in the  $^{237}\text{Np} + d$  reactions were obtained in the previous work<sup>1)</sup> as Fig. 1 shows. From the excitation functions, the thick target yield of  $^{237}\text{Pu}$  was calculated, together with the yields of the radiochemical impurities  $^{236}\text{Pu}$  and  $^{238}\text{Pu}$ . It has been concluded that the relatively large yield of  $^{237}\text{Pu}$  can be expected in the relevant reaction system.

In this work, the test production of  $^{237}\text{Pu}$  was performed by irradiating a thick target of the oxide of  $^{237}\text{Np}$  with deuterons. The particular care was paid for the safety in the bombardment and the chemical processing of a large amount of  $^{237}\text{Np}$ . The yields of Pu isotopes were finally compared with calculation.

About 700 mg of the  $^{237}\text{NpO}_2$  was dissolved in hydrochloric acid solution and purified by an anion exchange method<sup>2)</sup>. The chloride of Np obtained was converted to the oxide and then it was powdered carefully. The resultant powder was mixed with 300 mg of Al powder, and shaped to a thin disc of 15 mm in diameter and 2 mm thick under the pressure of  $2 \text{ ton}\cdot\text{cm}^{-2}$ . The disc gained sufficient hardness for handling after it was heated to  $660^\circ\text{C}$  in the He-gas flow. Though the aluminum powder suppressed the yield of  $^{237}\text{Pu}$ , it had to be added as a bonding material.

The target assembly was irradiated with deuterons for 8 hours. The  $\text{NpO}_2$ -Al target was held between the Al foils of 0.1 mm thick to prevent the R-2 beam line from contamination with Np and F.P. activities, even if it was damaged during the irradiation. The incident energy of the projectile to the target was 20.3 MeV and average ion current was 0.4  $\mu\text{A}$ .

After cooling for about a month, the irradiated  $\text{NpO}_2$ -Al target was dissolved with 12 M  $\text{HNO}_3$  under heating. From the solution, Pu and Np were separated by an anion exchange method<sup>2)</sup>. The sources for gamma-ray and

alpha-ray countings were prepared from the Pu fraction obtained. Neptunium was stored as the solution of  $\text{Np}(\text{NO}_3)_4$  for future utilization.

The overall chemical yield of Pu was 81 %. The amount of Pu isotopes produced at the end of irradiation are given in Table 1. The calculated yield is also listed in the table for comparison. The differences between them are larger than the uncertainties in experimental values. The discrepancies are, however, of the reasonable magnitude, if the uncertainties in the calculation from the possible non-homogeneity of the  $\text{NpO}_2$ -Al target is considered.

#### References

- 1) S.Baba et al., JAERI-M 84-129 (1984) 68.
- 2) H.Natsume et al., J. Nucl. Sci. Tech., 9 (1972) 737.

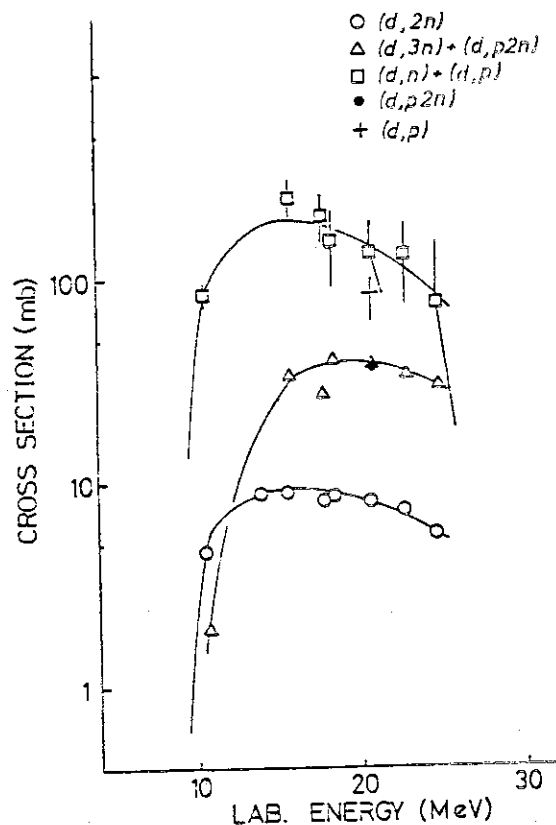


Fig.1 Formation cross sections of plutonium isotopes and neptunium isotopes in the  $^{237}\text{Np} + d$  reactions. Solid lines connect the experimental points to guide the eye.

Table 1 The yields of Pu isotopes at the end of irradiation

Nuclide	Experimental (dps)	Calculated (dps)
$^{237}\text{Pu}$	$(8.2 \pm 1.1) \times 10^4$	$5.9 \times 10^4$
$^{236}\text{Pu}$	$(6.42 \pm 0.13) \times 10^3$	
$^{238}\text{Pu}$	$(1.47 \pm 0.03) \times 10^3$	

V      NUCLEAR PHYSICS

## 5.1 STUDIES OF NUCLEI WITH PROTON AND NEUTRON NUMBERS OF 50 TO 82

Mitsuhiko ISHII, <sup>+</sup>Akiyasu MAKISHIMA, <sup>++</sup>Masakatsu HOSHI,  
<sup>++</sup>Masao OGAWA, <sup>+</sup>Minoru ADACHI and <sup>+</sup>Hiroshi TAKETANI

Department of Physics, <sup>+</sup>Faculty of Science, Tokyo Institute  
of Technology, <sup>++</sup>The Graduate School at Nagatsuda, Tokyo  
Institute of Technology

Collective motion of valence nucleons occupying the  $h_{11/2}^-$  orbital attracts both experimental and theoretical interest. In order to investigate the nuclear deformation in their ground band states, we have studied electromagnetic de-excitation from high spin states in Sm-138, -136 and -134 and Nd-132.

The atomic number of these nuclides has been determined by the use of a charged-particle multiplicity filter "silicon box" <sup>1)</sup>. A few competitive isotopes have been identified by comparison of their yields with the computational results of ALICE <sup>2)</sup>. Additional methods have been applied for isotope identification. One is to compare the relative yields of isotopes involved in two combinations of the target and the projectile nuclides which form compound nuclei different from each other by two in neutron number. Another is to take charged-particle/gamma-ray coincident spectra weighted with neutron multiplicity.

Nuclear reactions exciting the respective nuclides and experiments are summarized as follows:

Sm-138: Ag-107 (Cl-35, xp yn); E(Cl-35) = 165MeV.

2p - gamma- gamma coincidences.

2p - gamma angular distribution.

2p - Doppler shifts.

Sm-136 and Nd-132:

Ag-107 (S-32, xp yn); E(S-32) = 155MeV.

p - gamma - gamma coincidences.

p - gamma angular distribution.

p - Doppler shifts.

xp - gamma - n coincidences for isotope identification.



through reaction Ag-107 or -109 (S-32, xp yn).

Sm-134: Cd-106 (S-32, xp yn);  $E(S-32) = 160$  MeV.

2p - gamma - gamma coincidences.

xp - gamma - n coincidences.

The experimental results have been analyzed on the basis of the IBM-2 <sup>3)</sup>. Fig. 1 shows a comparison of nuclear excitation between the experiments and the calculations. The IBM-2 fails at reproduction of the level scheme above the  $10^+$  state in Sm-138, but the extended IBM-2 which takes into account a residual interaction between two quasi-particles and the bosons improves the situation. On the other hand, the IBM-2 works well for Sm-136 and -134 and Nd-132. This means that nucleus Sm-138 still inherits single-particle aspects from the  $h 11/2^-$  orbital and that the nuclear collectivity grows greater in more neutron-deficient nuclei Sm-136 and -134 and Nd-132.

Lifetime measurements have added support to this fact. Experimental results given in table 1 indicate that the  $10^+$  isomeric state observed in Sm-138 is different in character from those in the other nuclides and that the  $B(E2; 2^+ \rightarrow 0^+)$ 's are enhanced with the decrease of neutron number. Fig. 2 exemplifies the evolution of collectivity in terms of nuclear deformation beta and the ratio of nuclear excitation energies of the  $4^+$  and the  $2^+$  states in samarium isotopes. Details are discussed in reference 3.

#### References

- 1) M.Ishii et. al., JAERI TANDEM ANNUAL REPORT p.73(1983).
- 2) The CODE "ALICE" developed by M.Blann and F.Plasil.  
Refer to F.Plasil and M.Blann, Phys. Rev. C 11, 508(1975).
- 3) A.Makishima, Ph.D. Theses (Tokyo Institute of Technology) May 1985.

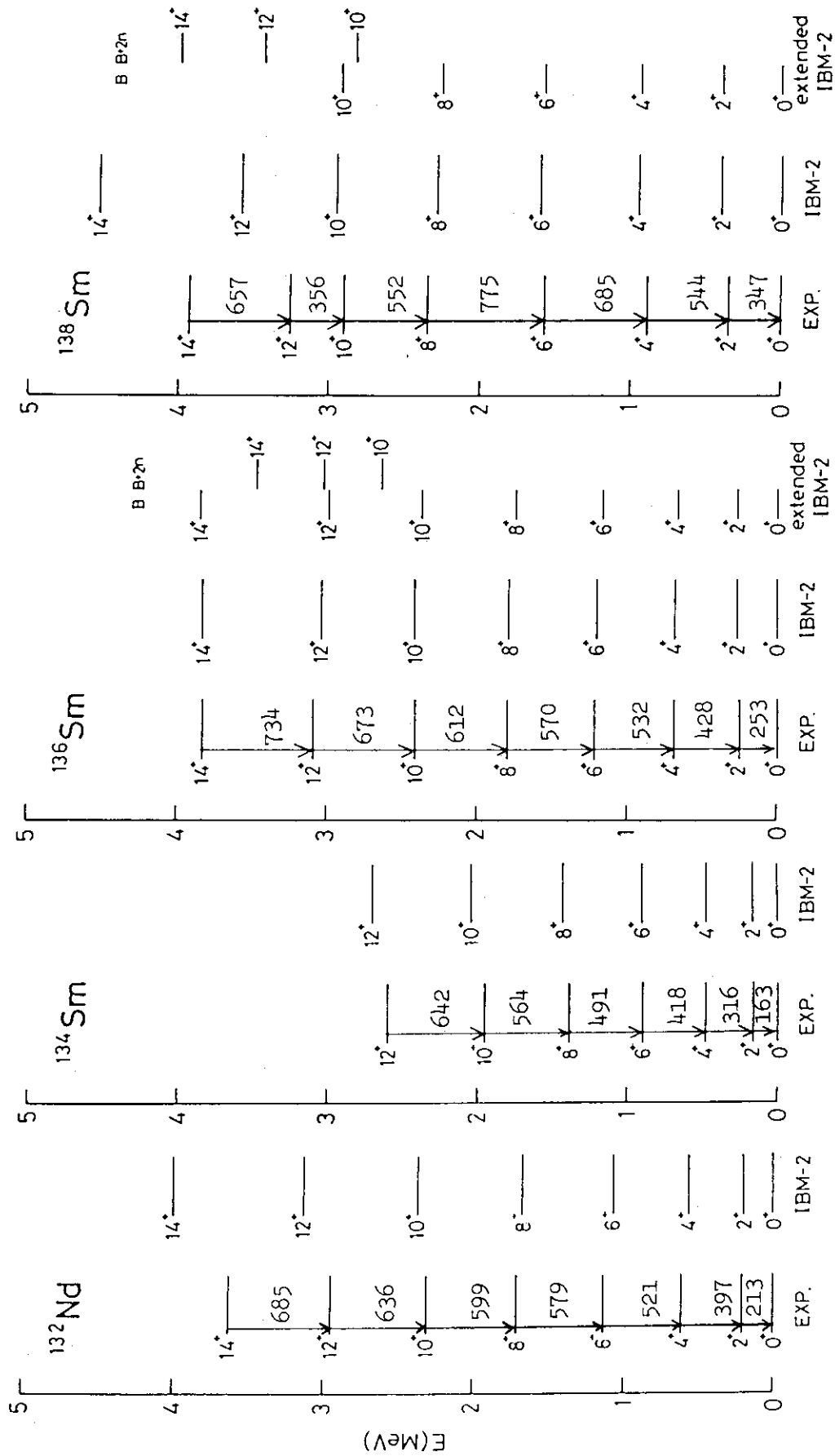


Fig.1 Level schemes of Nd-132 and Sm-134, -136, and -138.

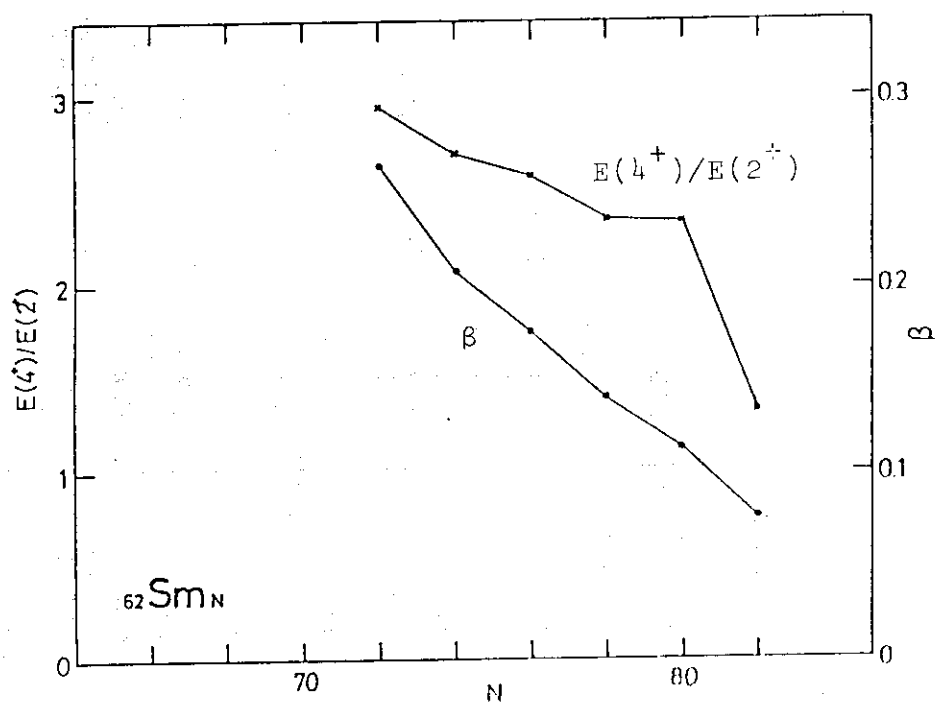


Fig. 2 Evolution of collectivity.  $\beta$  is the nuclear deformation parameter and  $E(4^+)/E(2^+)$  is the ratio of excitation energies of the  $4^+$  and the  $2^+$  states.

Table 1 Half-lifetimes of excited states in Nd-132 and Sm-136/-138.

	$2^+$	$4^+$	$10^+$	$12^+$
Nd-132	$2.2(0.2) \times 10^2$	14 - 19	< a few ps	
Sm-136	$1.3(0.1) \times 10^2$	8 - 13	< a few ps	
Sm-138	45(6)		$5.5(0.2) \times 10^2$	33(2)

Lifetimes in units of ps.

## 5.2 INCLUSIVE AND COINCIDENCE MEASUREMENTS FOR STRONGLY DAMPED REACTIONS IN THE SYSTEM $^{37}\text{Cl} + ^{48}\text{Ti}$

Kazumi IDENO, Watalu YOKOTA\*, Yoshiaki TOMITA,  
Hiroshi IKEZOE, Yasuharu SUGIYAMA, Susumu HANASHIMA,  
Katsunori SUZUKI\*, Mitsuhiro OGIHARA\*, Tetsuro  
KOMATSUBARA\*, S. M. LEE\*, and Takashi MIKUMO\*

Department of Physics, Japan Atomic Energy Research  
Institute, \*Tandem Accelerator Center, University of  
Tsukuba

Above the incident energy of 160 MeV the cross section of fusion evaporations for the system  $^{37}\text{Cl} + ^{48}\text{Ti}$  enters the saturated region.<sup>1)</sup> For this system in the energy region from 160 to 196 MeV we inclusively measured the charges  $Z$  and kinetic energies of strongly damped reaction fragments. Standard ionization chambers were used. The angular distributions and the total kinetic energies (T.K.E.) of the fragments were obtained assuming the binary process. Fig. 1 shows the differential cross sections for the projectile-like and target-like fragments and Fig. 2 the observed most probable T.K.E. for the binary products. Characteristic features about the strongly damped reactions, which were observed for the system  $^{37}\text{Cl} + ^{27}\text{Al}$ ,<sup>2)</sup> appear also for the present system:

1)  $d\sigma/d\theta \propto \text{constant}$  except at forward angles,

2) Observed most probable T.K.E. are constant over a wide range of angles and independent of incident energies.

In the inclusive measurements, however, we cannot know the charge distributions of the binary fragments and the energy losses caused by light particle emissions from the highly excited fragments. In an attempt to eliminate these ambiguities we performed coincidence measurements at 180 and 196 MeV. Fig. 3 shows the angular dependences of the coincident counts, the other counter being fixed at  $\theta_{\text{lab}} = 45$  degrees. It is seen that the coincident events with no proton missed ( $Z_{\text{sum}} = 39$ ) and with one proton missed ( $Z_{\text{sum}} = 38$ ) dominate and that for both cases the angular dependences are very similar. If nucleon emission occurs isotropically, the center posi-

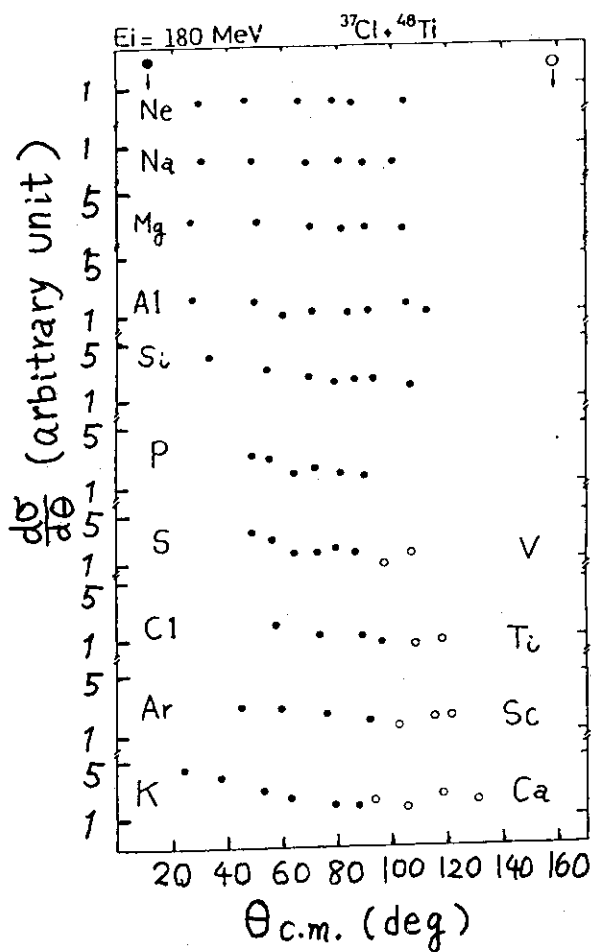


Fig. 1 Differential cross sections for each exit channel at  $E_{inc} = 180$  MeV.

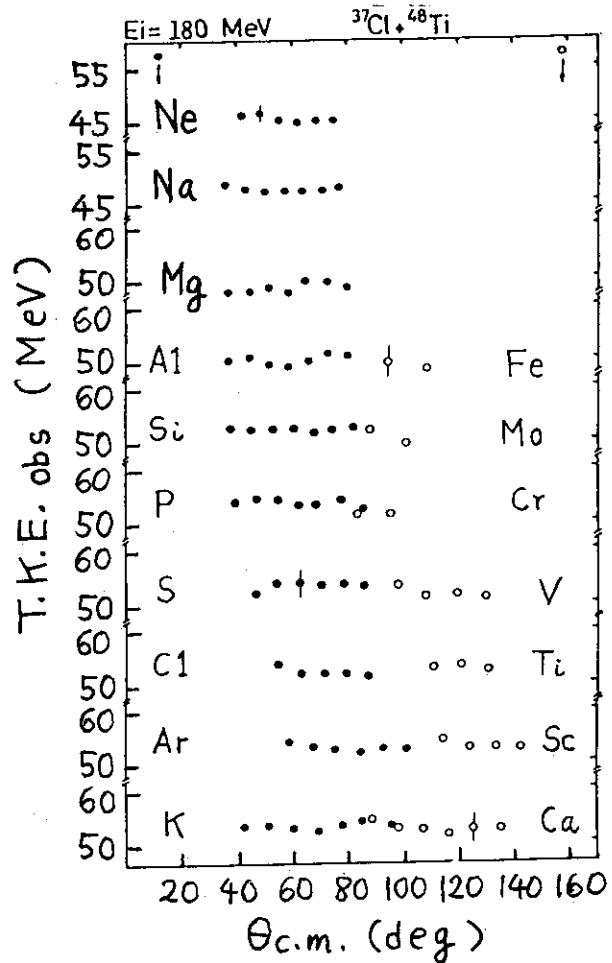


Fig. 2 Angular dependences of observed most probable T.K.E. for each exit channel at  $E_{inc} = 180$  MeV.

tion of the angles into which the fragments are emitted does not change. Then, from the observed coincident angles we can determine the most probable  $Q$ -value and T.K.E., using the two-body kinematics. In Fig. 3 the values of the T.K.E. obtained from the inclusive measurements and from the coincident angles measurements are compared at  $E_{inc} = 180$  MeV. The T.K.E. points from the angle measurements are well reproduced by the Coulomb energies with  $r_0 = 1.2$  fm. The difference between the two values of the T.K.E. around the symmetric fragments amounts to  $\sim 8$  MeV, which corresponds to the energy loss caused by nucleon emissions. We estimate the mass defect  $\Delta M$  for the binary fragments by using the expression:  $\Delta E/E \approx \Delta M/M$ . We obtain  $\Delta M \approx 5$ , which is close to the value extrapolated from the mass

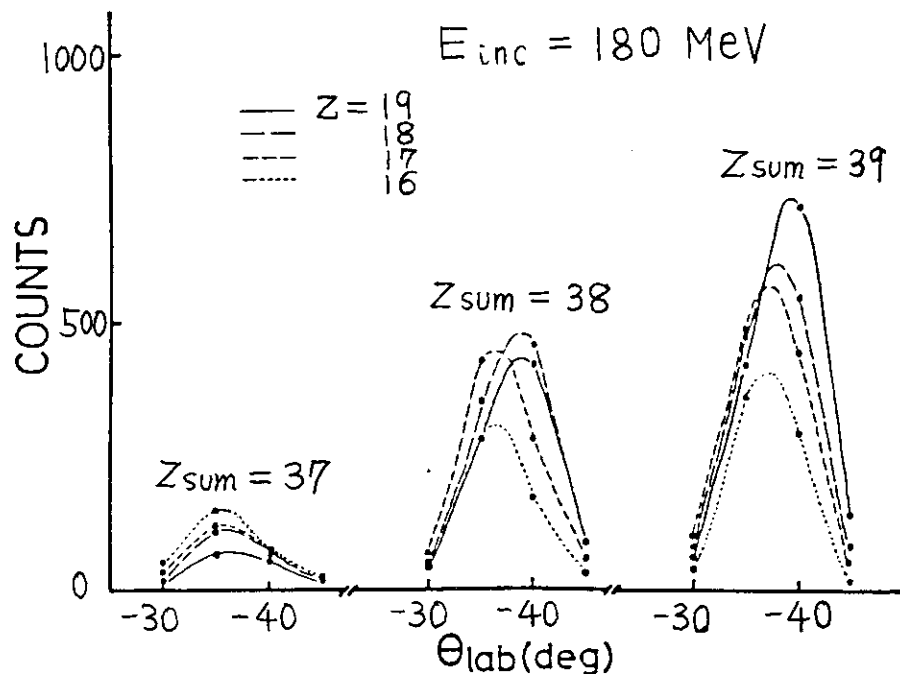


Fig. 3 Angular dependences of the coincident events at  $E_{inc} = 180$  MeV. The other counter was fixed at  $\theta_{lab} = 45$  degrees.

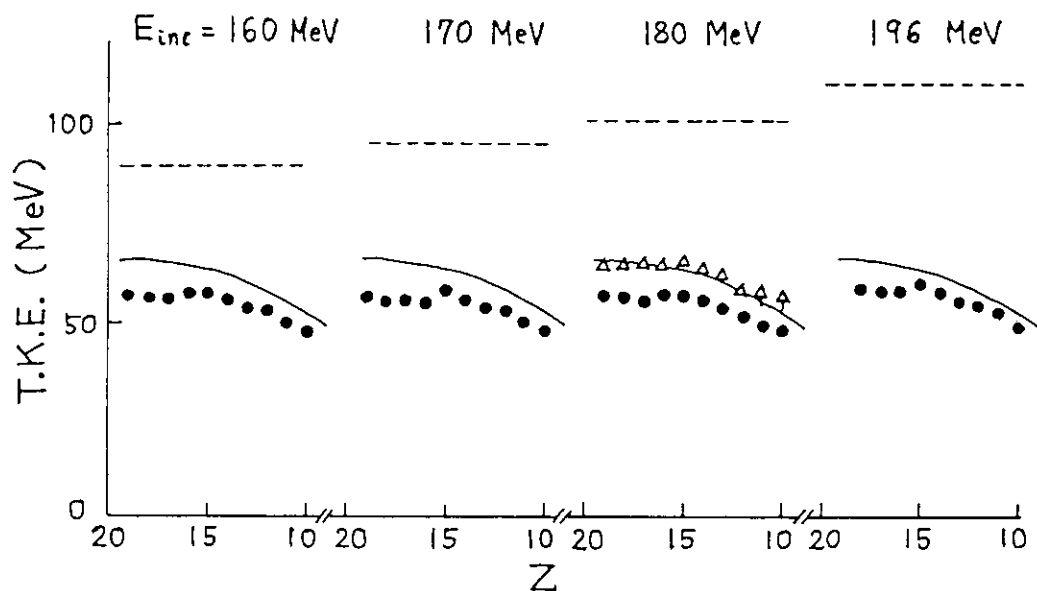


Fig. 4 Dependences of the T.K.E. on the atomic numbers  $Z$  of the fragments. The solid circles represent the values of the T.K.E. obtained from the inclusive measurements, and the open triangles the ones obtained from the coincident angles measurements where the projectile-like fragments were detected at  $\theta_{lab} = 45$  degrees. The solid curves indicate the Coulomb energies calculated with  $r_0 = 1.2$  fm.

defects measured for the system  $^{32}\text{S} + ^{40}\text{Ca}$  at 190 and 225 MeV by Winkler et al.<sup>3)</sup>

Further analyses are in progress.

References

- 1) K. Ideno et al.: JAERI TANDEM Annual Report 1983, p.75.
- 2) T. Mikumo et al.: Nuovo Cimento 81A (1984) 79.
- 3) U. Winkler et al.: Nucl. Phys. A371 (1981) 477.

### 5.3 MAGNETIC SUBSTATE POPULATION IN $^{12}\text{C}+^{12}\text{C}$ INELASTIC SCATTERING

Yasuharu SUGIYAMA, Naomoto SHIKAZONO, Yoshiaki TOMITA,  
Hiroshi IKEZOE, Toshiki TACHIKAWA, Eiko TAKEKOSHI, Shigeru  
KUBONO\* and Masahiko TANAKA\*

Department of Physics, JAERI, \*Institute for Nuclear  
Study, University of Tokyo

In order to clarify the physical processes that underlie the gross structure in the excitation function of the single and mutual  $2^+$  excitations in the  $^{12}\text{C}+^{12}\text{C}$  inelastic scattering, a large amount of experimental and theoretical efforts has been made<sup>1)</sup>. There are various models based on resonant or non-resonant conceptions which can explain this gross structure. As suggested by Tanimura et al.<sup>2)</sup>, however, the predictions of the models are quite different for an energy dependence and angular distribution of the spin alignment.

In the present experiment, the precise angular distributions of the magnetic substate population for the single and mutual  $2^+$  excitations in the  $^{12}\text{C}+^{12}\text{C}$  inelastic scattering have been measured by the  $\gamma$ -ray recoil method<sup>3)</sup>. The quantization axis is chosen to be the direction of the center of mass scattering angle of the outgoing nucleus<sup>4)</sup>. By taking this axis, it becomes possible to extract m-substate populations precisely from the measured line shape<sup>4)</sup>.

Experiments were carried out at JAERI tandem Van de Graaf by using a newly constructed heavy-ion magnetic spectrograph<sup>5)</sup>. The spectrograph has a characteristic feature that a kinematic momentum shift  $k$  is compensated well up to  $k=1.2$ , so that a high momentum resolution is achieved over a wide range of  $k$ . The angular distributions of the m-substate populations for the single and mutual  $2^+$  excitations were measured in a laboratory angle range between  $6.6^\circ$  and  $34.6^\circ$  in a step of  $1^\circ$ . The differential cross sections for these excitations were simultaneously measured. The c.m. energies were chosen to be 19.0, 21.5, 24.25, 25.6, 27.3, 30.0, 33.0, 35.0, 45.0 and 55.0 MeV in order to map over the gross structure. Targets were self-supporting natural carbon foils of 50  $\mu\text{g}/\text{cm}^2$  thickness. Obtained energy resolutions were around 100keV. An



example of measured line shape is shown in Fig.1. Filled circles represent

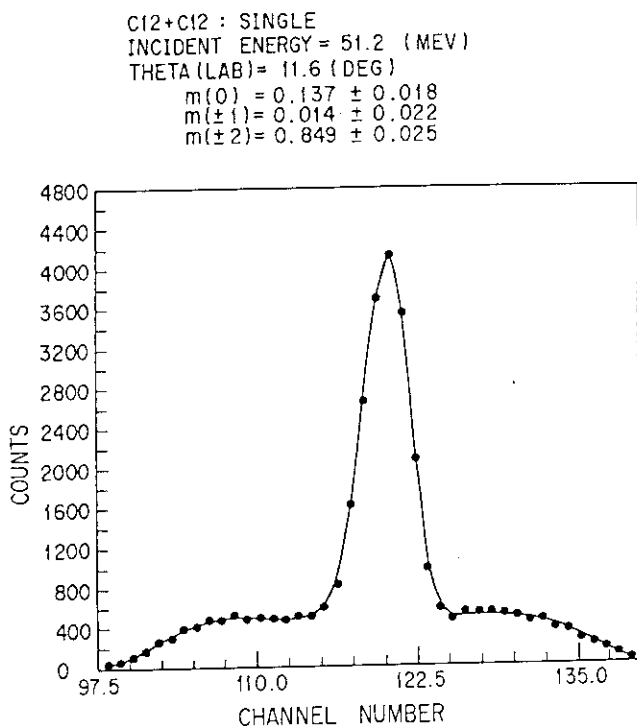


Fig.1 An example of a measured line shape (filled circles) and a fitted curve (solid line). The obtained m-substate population is also shown.

experimental points and the solid line is a least-squares fit to the measured line shape. The obtained m-substate population is also indicated.

The angular distributions of the m-substate population are shown in Fig.2. The population is normalized such that the sum of the populations of  $m=0$ ,  $m=\pm 1$  and  $m=\pm 2$  becomes 1. The errors, which come from the unfolding procedure, are within the filled circles. It is clearly seen that the substate population is characterized by angular oscillations which increase in frequency smoothly with an incident energy. This suggests that partial waves which contribute to the inelastic scattering become getting large smoothly, as the incident energy

increases. Amplitudes of oscillations for each substate, however, change little with an incident energy. The dashed lines in Fig.2 are calculated assuming that only a single partial wave with the aligned coupling to the exit channel contributes to the scattering process at the maxima of the inelastic cross sections whose spins are assigned to be  $J=12, 14, 16$  and  $18$  at  $E_{cm}=19.0, 24.25, 30.0$  and  $35.0$  MeV, respectively. Not only the amplitudes but also the frequencies are seen to be different from the measured ones. Therefore several partial waves with aligned and non-aligned configurations are expected to contribute to the maxima of the inelastic cross sections.

The solid lines indicated in Fig.2 are results<sup>6)</sup> of the DWBA calculations by using the potential parameters of Tanimura et al<sup>7)</sup>. The angular distributions of the substate populations are satisfactorily reproduced except for  $E_{cm}=19$  MeV. This potential parameters have been

shown to reproduce the gross structure and the particle- $\alpha$  angular correlation for the single  $2^+$  excitation and angular distributions for the elastic and inelastic scattering of the  $2^+$  excitation. Therefore phenomena observed in the  $^{12}\text{C}+^{12}\text{C}$  inelastic scattering can be explained by DWBA calculations.

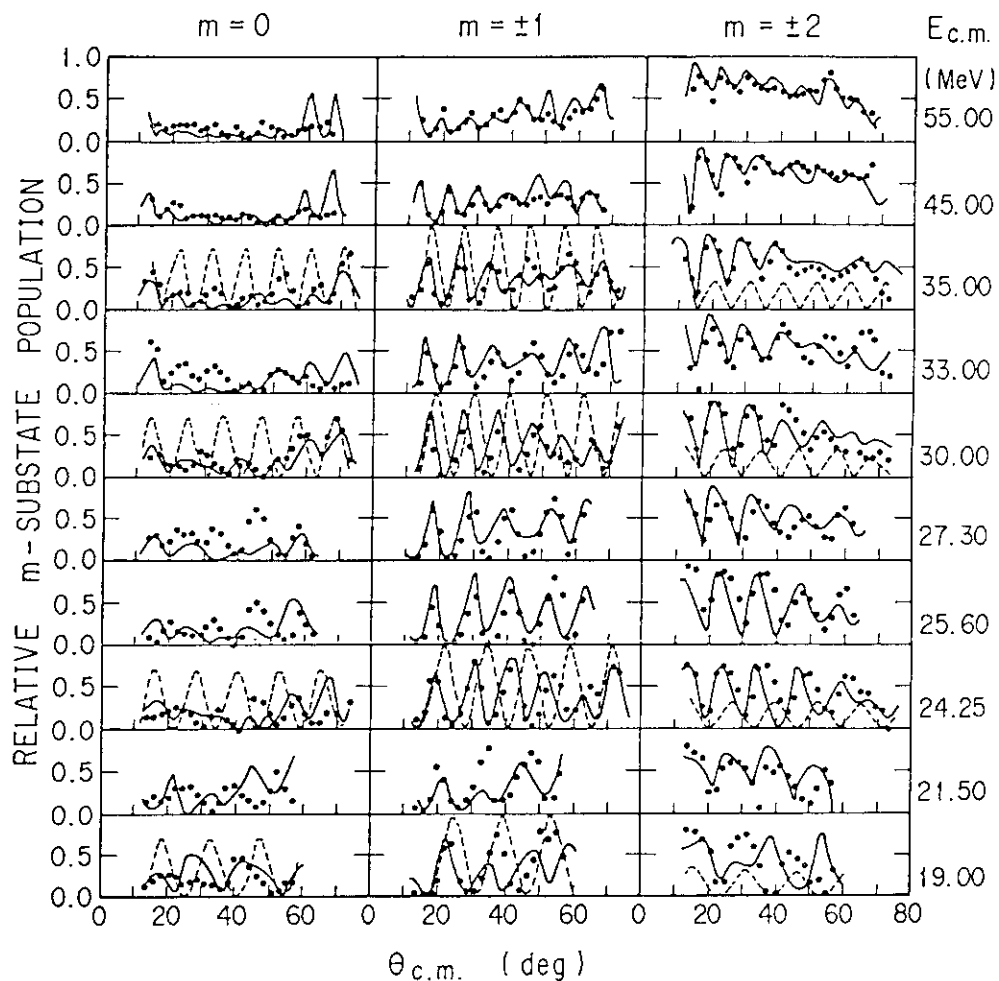


Fig.2 Angular distributions of the m-substate population. Solid lines are the results of the DWBA calculation. Dashed lines are calculated by assuming that only a single partial wave with an aligned coupling to an exit channel contributes to the scattering process.

# References

- 1) See, e.g. K.A.Eberhard, ed., Lecture Notes in Physics, Vol.156 (Springer, Berlin, 1982).
- 2) O.Tanimura and U.Mosel, Phys.Lett. 114B(1982)7.
- 3) H.G.Bohlen et al., Phys.Rev.Lett.37(1976)195; J.R.Beene and R.M.DeVries, Phys.Rev.Lett.37(1976)1027.
- 4) Y.Sugiyama et al., to be published.
- 5) Y.Sugiyama et al., Nucl.Instr. and Meth. 187(1981)25.
- 6) Y.Sugiyama et al., to be published.
- 7) O.Tanimura, R.Wolf and U.Mosel, Phys.Lett.120B(1983)275.

5.4 INCOMPLETE FUSION OF THE  $^{16}\text{O}+^{27}\text{Al}$  REACTION

Hiroshi IKEZOE, Naomoto SHIKAZONO, Yoshiaki TOMITA,  
Kazumi IDENO, Yasuharu SUGIYAMA, and Eiko TAKEKOSHI

Department of Physics, JAERI

It is well known that the complete fusion process is the dominant reaction mechanism at low bombarding energies. At higher bombarding energies ( $E_{\text{inc}} \geq 8 \text{ MeV/u}$ ) the incomplete fusion process contributes significantly where the linear momentum of the entrance channel is not transferred completely to the compound nucleus<sup>1,2)</sup>. In order to investigate the reaction mechanism of the incomplete fusion process, it is important to clarify the role of the entrance channel angular momentum.

A self-supporting  $180 \text{ } \mu\text{g/cm}^2$  Al target was bombarded at two incident energies of 90 MeV and 150 MeV with  $^{16}\text{O}$  beams. The velocity spectra  $V_r^{-2} d^2\sigma/dV_r d\Omega$  of residues for typical mass numbers obtained at 90 MeV are shown in Fig.1, where  $V_r$  is the residue velocity. The solid lines show predictions of a statistical model calculation assuming the complete fusion. Since the statistical model calculation reproduces the velocity spectra very well, there is no evidence of an incomplete fusion component at 90 MeV.

The velocity spectra measured at 150 MeV exhibits the centroids deviated from  $V_c \cos \theta_L$ , where  $V_c$  and  $\theta_L$  are the velocity of the center of mass system and the recoil angle in the laboratory system, respectively. The velocity centroid shifts  $\delta = (\bar{V}_r - V_c \cos \theta_L) / V_c \cos \theta_L$  are plotted (open symbols) in Fig.2. The observed shifts at all measured angles increase as the mass number decreases.

In the following discussion, it is assumed that emission prior to fusion of a single nucleon or a single  $\alpha$  particle with beam velocity is responsible for the observed velocity deficits. The velocity shift  $\delta(Z,A)$  for each residue  $(Z,A)$  is approximated by

$$\delta(Z,A) = \delta_1 F_1(Z,A) + \delta_\alpha F_\alpha(Z,A),$$

where  $F_1(Z,A)$  and  $F_\alpha(Z,A)$  are the fractional yields of the residue  $(Z,A)$  originating from a residual compound nucleus  $^{42}\text{Ca}$  (or  $^{42}\text{Sc}$ ) or  $^{39}\text{K}$ , respectively, with respect to the total yield of the same residue. The velocity shifts due to a single nucleon and a single  $\alpha$ -particle pre-emission are denoted as  $\delta_1$  and  $\delta_\alpha$ , respectively. In order to understand the

trend of the centroid shifts, two different model analyses were performed. One is based on the peripheral collision assumption and the other is based on the angular momentum independent assumption.

In the peripheral collision assumption, the incomplete fusion process takes place within a localized angular momentum window  $\ell_x < \ell < \ell_c$ , where  $\ell_c$  is the critical angular momentum. From this window, nucleon or  $\alpha$ -particle pre-emission takes place with the emission ratio  $\gamma$  of the  $\alpha$ -particle pre-emission to the nucleon pre-emission. The complete fusion process is assumed to occur in the central region  $0 < \ell < \ell_x$ . With given values of  $\gamma$ ,  $F_1(Z,A)$ ,  $F_\alpha(Z,A)$  were calculated by using the statistical model code PACE<sup>3)</sup>. The quantities obtained from this analysis were  $\ell_x = 23-26 \hbar$ ,  $\gamma = 0.4-1$  and  $\beta = 50-60\%$ .  $\beta$  is the ratio of the cross section of the incomplete fusion  $\sigma_{icf}$  to the total cross section of the fusion-like residues ( $\sigma_{icf} + \sigma_{cf}$ ). The calculation (solid symbols in Fig.2) underestimates the shifts for heavier residues ( $A \geq 33$ ).

According to this calculation, the heavy residues ( $A=35,36$ ) are produced only if the  $\alpha$  particle is evaporated with large kinetic energy ( $E_{cm} = 25-30$  MeV) well in excess of beam velocity  $\alpha$  particles. The residual compound nucleus after  $\alpha$ -particle pre-emission with beam velocity still has a high excitation energy, so that many particles can evaporate to produce lighter residues ( $A \leq 34$ ). The nucleon pre-emission is then supposed to be mainly responsible for the velocity shifts of the heavy residues ( $A=35,36,37$ ) but can not induce sufficiently large shift. Therefore, in order to account for the observed larger shifts of heavier residues,  $\ell_x$  should be reduced since these heavier residues are produced favourably from the low angular momentum region of  $^{42}\text{Sc}$  or  $^{42}\text{Ca}$ . On the other hand if  $\ell_x$  is reduced too much, the velocity shifts for lighter residues ( $A \leq 30$ ) would become too large. Hence the range of the optimum value for  $\ell_x$  is limited.

We now discuss the data analysis based on the angular momentum independent assumption, in which the partial cross section for fusion-like residues is simply divided into  $\sigma_{cf}$  and  $\sigma_{icf}$  by the ratio  $\beta/(1-\beta)$  irrespective of the angular momentum. In this analysis, larger velocity shifts for the heavier residues than in the case of the previous analysis can be expected, because even in central collisions incomplete fusion contributes. The results of a calculation with  $\gamma=0.5$  and  $\beta=50\%$  are shown in Fig.3. The agreement with the data is better than in the previous analysis based on the peripheral collision assumption.

The present analyses suggest that the angular momentum independent assumption is more favoured than the peripheral collision assumption to account for the incomplete fusion mechanism. In other words, the incomplete fusion process is not localized in the peripheral region but rather widely distributed in the angular momentum space of the entry states.

#### References

- 1) H.Morgenstern, W.Bohne, K.Grabisch, D.G.Kovar, and H.Lehr, Phys. Letts. 113B (1982) 463.
- 2) H.Morgenstern, W.Bohne, W.Galster, K.Grabisch, and A.Kanowski, Phys. Rev. Letts. 52 (1984) 1104.
- 3) M.Hillman and Y.Eyal, code JULIAN; A.Gavron, modification PACE, Phys. Rev. C21 (1980) 230.

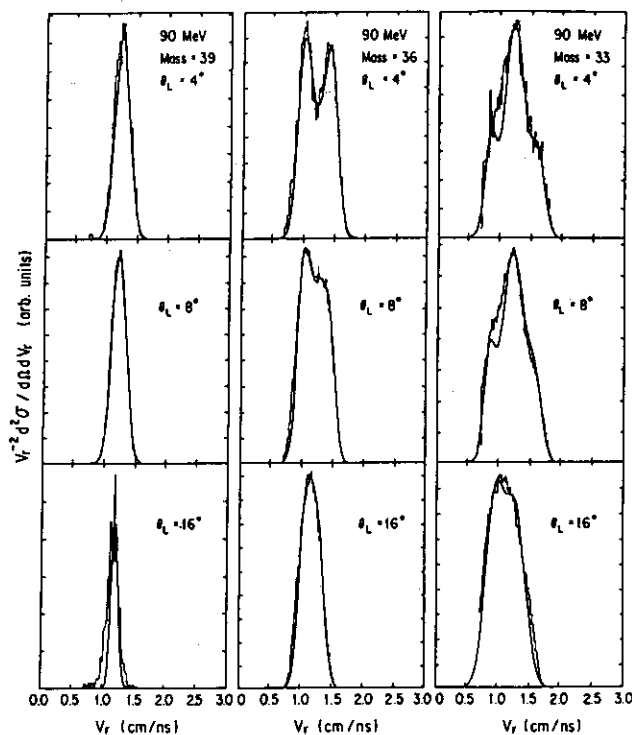


Fig.1 Velocity spectra  $V_r^{-2} d^2 \sigma / dV_r d\Omega$  of evaporation residues at 90 MeV. The mass numbers 39, 36 and 33 mainly correspond to the 2n2p,  $\alpha$ n2p and 2 $\alpha$ np cascades, respectively. The solid lines are the predictions of the statistical model code assuming the complete fusion of the  $^{16}\text{O} + ^{27}\text{Al}$  reaction.

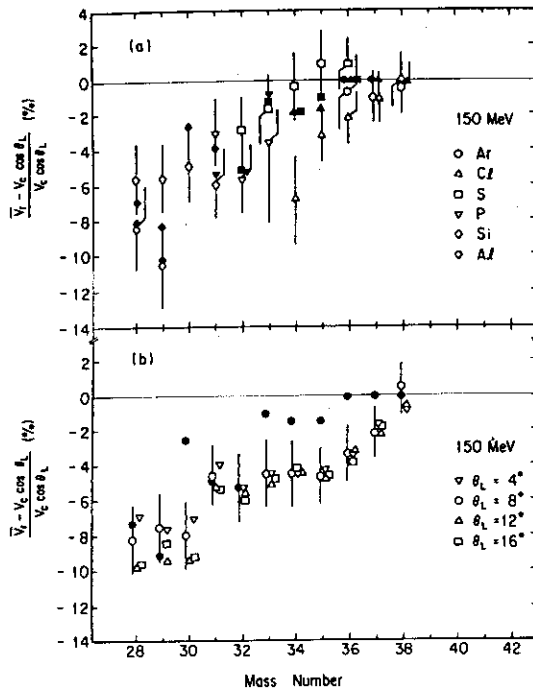


Fig.2 Velocity centroid shifts  $(\bar{V}_r - V_c \cos \theta_L)/V_c \cos \theta_L$  are plotted versus (a) each isotope (b) the mass number at 150 MeV, where  $\bar{V}_r$ ,  $V_c$  and  $\theta_L$  are velocity centroid, center-of-mass velocity and recoil angle, respectively. Prediction by the model calculation based on the peripheral collision assumption is shown by solid symbols.

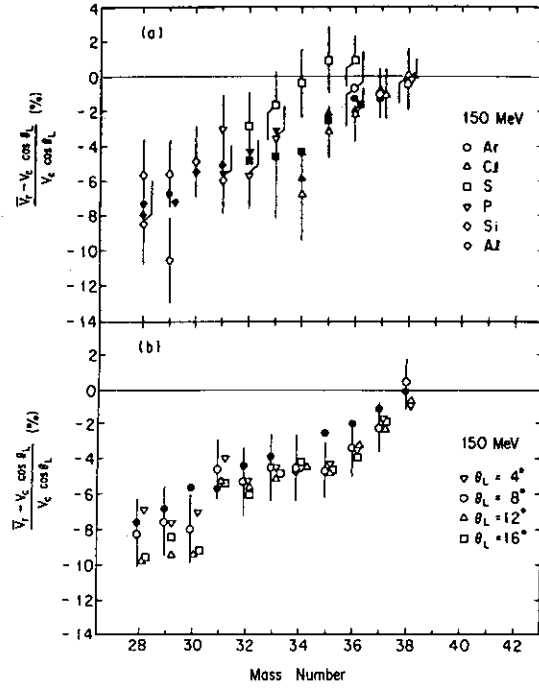


Fig.3 Velocity centroid shifts predicted by the model calculation based on the angular momentum independent assumption (solid symbols) together with data (open symbols).

## 5.5 A STUDY OF LIMITING ANGULAR MOMENTA IN FUSION REACTION

Hiroshi IKEZOE, Naonoto SHIKAZONO, Yoshiaki TOMITA,  
 Yasuharu SUGIYAMA, Kazumi IDENO, Eiko TAKEKOSHI,  
 Toru NOMURA\*, and Toshiki TACHIKAWA\*\*

Department of Physics, JAERI, \*Institute of Nuclear Science,  
 University of Tokyo, \*\*Industrial Machinery Design Department  
 , Sumitomo Heavy Industries LTD.

Time-dependent Hartree-Fock calculation (TDHF)<sup>1,2,3)</sup> for fusion reaction predicts that low partial waves do not contribute to the formation of the compound nucleus at bombarding energies above a certain critical value. In order to investigate the TDHF prediction experimentally, it is essential to measure quantities sensitive to low angular momentum of the entrance channel. It is well known that in the fusion-evaporation process, heavier residues produced by only nucleon evaporations are originated from decays of the compound nucleus with low angular momenta. Taking into account this property of the compound nucleus decay we measured evaporation residues of the  $^{16}\text{O}+^{16}\text{O}$  and  $^{16}\text{O}+^{12}\text{C}$  fusion reactions. The TDHF calculations<sup>1,6)</sup> predict the threshold energy of  $E_{\text{cm}} \simeq 27$  MeV for these systems.

Targets of  $220 \mu\text{g}/\text{cm}^2$  natural carbon and  $310 \mu\text{g}/\text{cm}^2$   $\text{SiO}_2$  were bombarded by  $^{16}\text{O}$  ions ( $E_{\text{Lab}} = 70\text{--}130$  MeV). The evaporation residues (ER) were measured by a time-of-flight telescope (TOF) and an ionization chamber. At each bombarding energy the angular distribution of ER and the elastically scattered  $^{16}\text{O}$  ions were simultaneously measured in a range of  $3^\circ$  to  $25^\circ$  in a step of  $2^\circ$ . The ER cross sections were normalized to the forward elastic scattering.

Each residue cross section is shown in Fig.1. Data were compared with the statistical model calculation CASCADE<sup>4)</sup>. Four channel version of CASCADE was modified so as to include  $^3\text{He}$  evaporation in addition to neutron, proton, deuteron and  $\alpha$ -particle evaporations. Almost the same level density parameters as used in ref.4) were assumed. Known low lying individual levels of all intermediate and final nuclei were used up to excitation energies of 2-5 MeV. Total fusion cross sections measured by Beck et al<sup>5)</sup> were used to estimate the critical angular momentum of the fusion reaction.



The  $^3\text{He}$  evaporation in the CASCADE calculation was important for yields of  $^{24}\text{Na}$  and  $^{21}\text{Ne}$ . Calculated yields of these nuclei were enhanced by including the  $^3\text{He}$  evaporation at the energy region of  $E_{\text{cm}}=30-50$  MeV, so that agreements with data became very well. The ER cross sections of  $^{26}\text{Al}$ ,  $^{25}\text{Al}$ ,  $^{25}\text{Mg}$  and  $^{24}\text{Mg}$ , which are favourably produced from the low angular momentum region of the entrance channel, are reproduced very well by the CASCADE calculation. Fig.2 shows the ER cross sections (dashed lines) calculated assuming the predicted low L cutoff<sup>6)</sup> together with data. This calculation disagrees with data entirely at  $E_{\text{cm}} > 40$  MeV, which means that in the present bombarding energy region ( $E_{\text{cm}}=30-56$  MeV) there is no evidence of the low L cutoff.

Fig.3 shows each ER cross section of the  $^{16}\text{O}$  on  $^{16}\text{O}$  fusion reaction together with the CASCADE calculations. Agreements with data are rather good except  $^{20}\text{Ne}$ . The yield of  $^{20}\text{Ne}$  probably includes contributions from other reaction channel in addition to the fusion reaction. The ER cross sections sensitive to the low angular momentum are those of  $^{28}\text{Si}$  and  $^{28}\text{Al}$  in this fusion reaction. The CASCADE calculations were performed assuming the predicted low L cutoff<sup>1)</sup> and are shown in Fig.4. It is clearly seen that the calculations disagree with data. The measured fusion cross sections of  $Z=14$  and  $A=28$  of the  $^{20}\text{Ne}$  on  $^{12}\text{C}$  fusion reaction<sup>7,8)</sup> were compared with those of the same residues in the  $^{16}\text{O}$  on  $^{16}\text{O}$  fusion reaction. These two systems form the same compound nucleus  $^{32}\text{S}$  but with the different low L cutoffs predicted. There is no difference in the ER cross sections observed in these two systems, that is, no evidence of the low L cutoff in the  $^{16}\text{O}$  on  $^{16}\text{O}$  fusion reaction.

#### References

- 1) P.Bonche, B.Grammaticos, and S.Koonin, Phys. Rev. C17 (1978) 1700.
- 2) P.Bonche, K.T.R.Davies, B.Flanders, H.Flocard, B.Grammaticos, S.E.Koonin, S.J.Krieger, and M.S.Weiss, Phys. Rev. C20 (1979) 20.
- 3) K.R.S.Devi, A.K.Dhar, and M.R.Strayer, Phys. Rev. C23 (1981) 2062.
- 4) F.Pühlhofer, Nucl. Phys. A280 (1976) 267.
- 5) C.Beck, F.Haas, R.M.Freeman, B.Heusch, J.P.Coffin, G.Guillaume, F.Rami, and P.Wagner, Phys. Rev. C29 (1984) 1942.
- 6) C.Y.Wong, Phys. Rev. C25 (1982) 1460.
- 7) F.Saint-Laurent, M.Conjeaud, and S.Harar, Nucl. Phys. A327 (1979) 517.
- 8) S.Kox, R.Ost, and A.J.Cole, Phys. Letts. 119B (1982) 303.

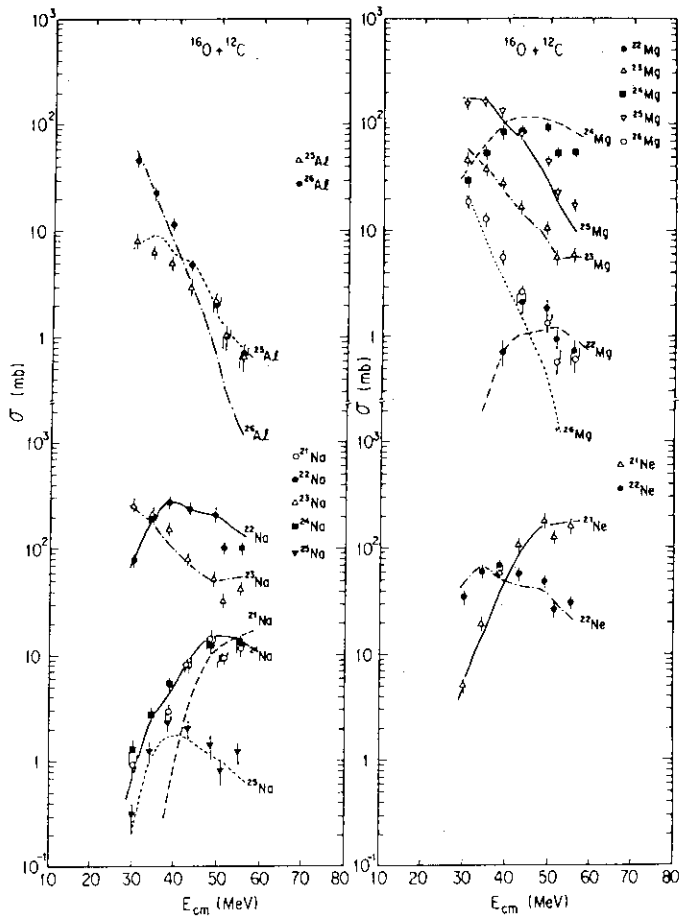


Fig.1 Evaporation residues cross sections produced in the  $^{16}\text{O}$  on  $^{12}\text{C}$  fusion reaction. Solid and dashed lines are the statistical model calculations by CASCADE.

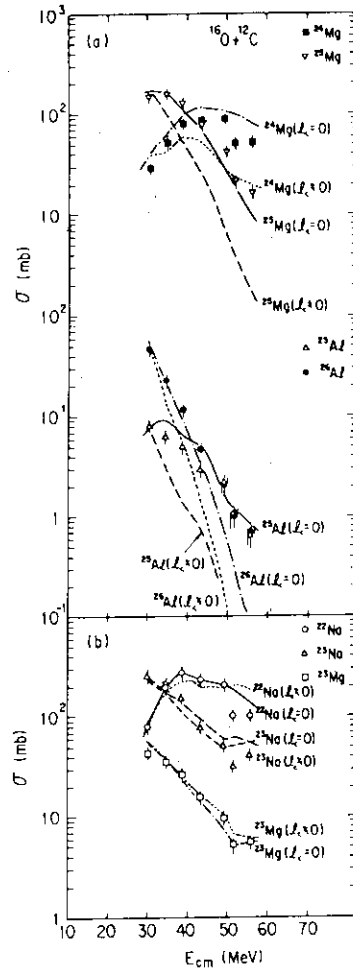


Fig.2 Statistical model predictions assuming the low L cutoff are shown by dashed lines together with data. Solid lines are the calculations without the low L cutoff.

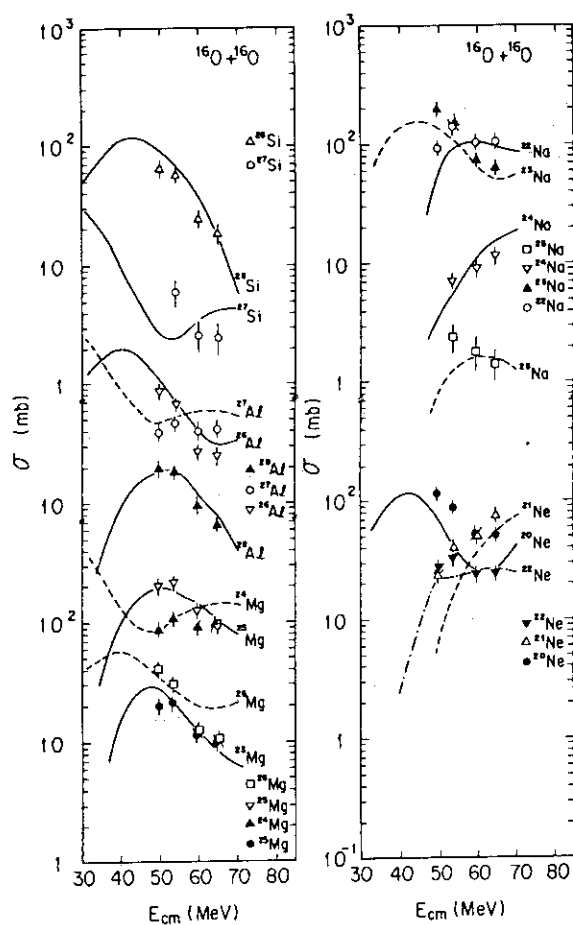


Fig.3 Evaporation residues cross sections produced in the  $^{16}\text{O}$  on  $^{16}\text{O}$  fusion reaction. Solid and dashed lines are the statistical model calculations by CASCADE.

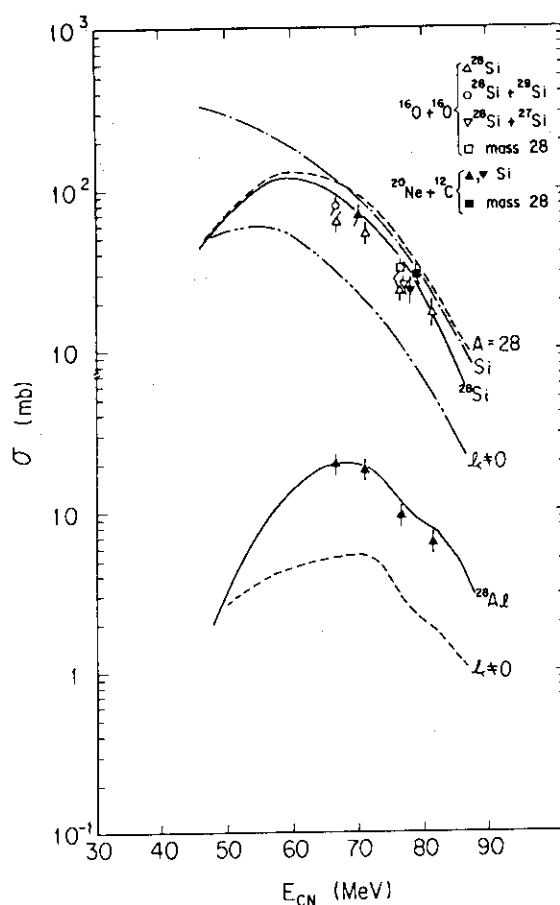


Fig.4 Statistical model calculations assuming the low L cutoff are shown by dashed lines ( $L < 0$ ). Solid lines are the calculations without the low L cutoff. Evaporation residues of  $Z=14$  and  $A=28$  from the  $^{20}\text{Ne}$  on  $^{12}\text{C}$  fusion reaction are also plotted for comparison.

## 5.6 PRE-EQUILIBRIUM EMISSION OF LIGHT PARTICLES IN THE HEAVY-ION REACTIONS

Akira IWAMOTO and Kichinosuke HARADA

Department of Physics, JAERI

From the incomplete fusion experiment, it is suggested that the emission of fast particle is strongly correlated to the velocity of nucleons measured in the center-of mass frame.<sup>1)</sup> Fast particles are thought to be emitted in the early stage of fusion reaction. We made a model which fits such situation.<sup>2)</sup> In the early stage of the fusion, there are two flows of flux with opposite directions, one coming from the projectile and the other from target. Considering the Fermi motion of projectile, target and compound nuclei, the momentum space for nucleon is given in Fig.1. Basic assumption of our model is to assume two sources of particle emission in the formalism of exciton model. Hatched region on the right and dotted region on the left are particle and hole states whose linear momentum are directed to the right and we call them as projectile source. In the same way, target source is defined by the left hatched and right dotted regions. These two sources are assumed to independently emit the fast particle. We define the particle-hole number, energy and linear momentum of these two sources and they are used as the initial condition of the exciton model calculation.

For the momentum dependent part of the level density, we start from the method of Madler and Reif<sup>3)</sup> but the detailed formula are not given here.<sup>2)</sup> An example of the energy spectra of proton at four detection angles for the reaction of 157 MeV  $^{16}\text{O}$  on  $^{40}\text{Ca}$ <sup>4)</sup> is given in Fig.2. The experimental data are taken in coincidence with the evaporation residue at 9 and solid line is our calculation with an overall normalization because the latter is an double differential cross section. From this figure, we see a rather good fit to the data. The enhancement of fast component as we go to the forward angle is clearly reproduced. These calculations are further extended to calculate the alpha emission and several experimental data are analyzed and fairly good agreement between the theory and experiment are obtained.

## References

- 1) H. Morgenstern et al.: Phys. Rev. Lett. 52 (1984) 1104.
- 2) A. Iwamoto: to be published in the Proceedings of 4-th Int. Conf. on Nuclear Reaction Mechanism, Varenna, Italy, June 1985.  
A. Iwamoto: to be published in the Proceedings of 4-th Int. Cont. on Neutron Induced Reaction, Snolenice, Czechoslovakia, June 1985.
- 3) Madler and Reif: Nucl. Phys. A337 (1980) 445.
- 4) H. Ikezoe, JAERI-M 84-085 (1984) 32.

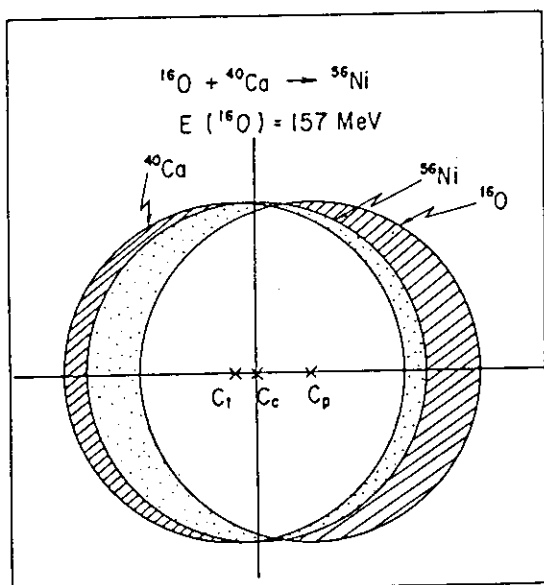


Fig.1 Momentum space relation for the reaction  $^{16}\text{O} + ^{40}\text{Ca}$  of energy 157 MeV at the Coulomb barrier.

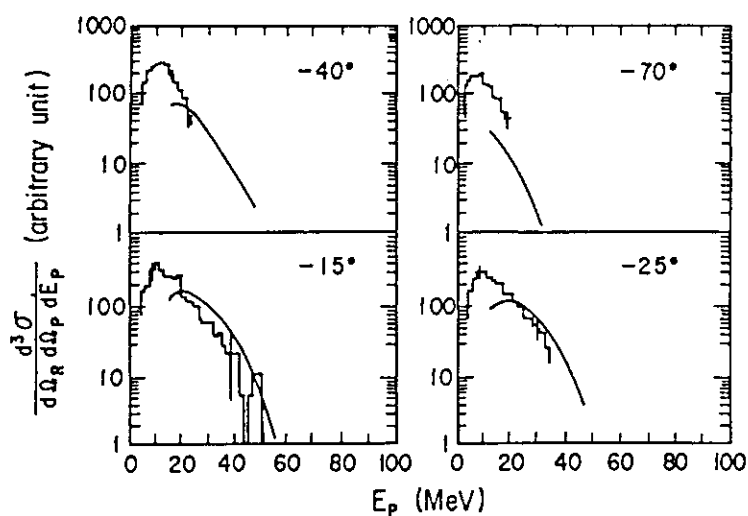


Fig.2 Energy spectra of proton at four detection angles from the reaction 157 MeV  $^{16}\text{O}$  on  $^{40}\text{Ca}$ . Evaporation residue is observed at 9 in the experiment<sup>4)</sup>.

## 5.7 ENHANCEMENT OF SUB-BARRIER FUSION CROSS SECTION DUE TO NECK FORMATION

Akira IWAMOTO and Kichinosuke HARADA

Department of Physics, JAERI

Enhancement of the sub-barrier fusion reaction was calculated by extending the model developed last year.<sup>1)</sup> First new point is the calculation of the potential energy for the neck-formed shape by using the method of Krappe et al.<sup>2)</sup>. The shape of it is defined by the two-center harmonic oscillator parametrization with the value of neck parameter fixed to 0.5. The results show the lowering of the potential energy compared to the no neck shape as is expected. The degree of lowering is about 3 MeV for  $^{40}\text{Ca} + ^{40}\text{Ca}$  system and 12 MeV for  $^{90}\text{Zr} + ^{90}\text{Zr}$  system with the tendency that as the system becomes heavier, the enhancement becomes larger. Another thing resulting from the numerical calculation is that the position of the barrier shifts to larger distance between two nuclei for neck-formed shape compared to the no neck shape, an important point not taken into account by the usual model. The second new point is the calculation of the transition probability from no neck state to neck formed state. It was assumed zero range in the previous treatment<sup>1)</sup> but the finite rangeness is taken into account properly now.

Numerical calculation was done for several systems,  $^{40}\text{Ca} + ^{40}\text{Ca}$ ,  $^{56,64}\text{Ni} + ^{56,64}\text{Ni}$ ,  $^{74}\text{Ge} + ^{74}\text{Ge}$  and  $^{90}\text{Zr} + ^{90}\text{Zr}$ . For all reactions examined we got a fairly good fitting to data by using the same strength of the transition matrix element. Calculation of the asymmetric system was not performed because of the ambiguity of the charge equilibration, but extension to this direction is under way.

### References

- 1) A. Iwamoto and K. Harada: JAERI TANDEM annual report 1983 (1984) 84.
- 2) H.J. Krappe et al.: Phys. Rev. C20 (1979) 992.
- 3) A. Iwamoto: to be published in the Proceedings of the Tsukuba Int. Symposium on Fusion Reaction (1984).

## 5.8 LOW-LYING ISOVECTOR COLLECTIVE STATES AND THE INTERACTING BOSON MODEL

Takaharu OTSUKA and Joseph N. GINOCCHIO\*

Department of physics, JAERI, \*Theoretical Division,  
Los Alamos National Laboratory

Low-lying isovector collective  $2^+$  states are studied in the Samarium isotopes in terms of the Interacting Boson Model version 2 (IBM-2)<sup>1)</sup>. The IBM-2 treats explicitly the proton and neutron degrees of freedom<sup>2)</sup>, and is capable of describing states which are isovector in the proton and neutron quadrupole degrees of freedom<sup>3)</sup>. We searched for isovector states and properties in the low-lying collective state region, taking the samarium isotopes as an example. Based on E2 transition data, it is pointed out that the  $2^+_3$  states of  $^{148,150}\text{Sm}$  are isovector, or F-vector in terms of the F-spin formalism<sup>2,3)</sup>. Fig. 1 shows result of an IBM-2 calculation for the E2 transitions  $0^+_1 \rightarrow 2^+_1$ ,  $2^+_2$  and  $2^+_3$  of  $^{148-154}\text{Sm}$ . The calculation is yet a phenomenological fitting but uses different proton and neutron boson charges (i.e. F-vector boson charge), exhibiting the first comprehensive agreement to experiment. In Fig. 1, the experimental data are compared also to calculation in terms of the IBM-1 which does not distinguish the proton boson from the neutron boson and can describe only isoscalar-type (i.e. F-scalar in the F-spin<sup>3)</sup>) collective states. Clearly, the IBM-1 fails to describe the experimental data, suggesting the importance of the F-vector boson charge which has been ignored in previous studies. Fig. 2 shows values of F-scalar and F-vector boson charges obtained by the fitting calculation, and ratios between proton- and neutron-boson transition matrix elements,  $M_p/M_n$ . The ratio  $M_p/M_n \approx -1$  for the  $0^+_1 \rightarrow 2^+_3$  of  $^{148,150}\text{Sm}$  indicates that these  $2^+_3$  states are almost purely isovector (i.e. F-vector) states.

Some predictions of  $B(M1)^2$  are obtained for further confirmation of the isovector properties. For example,  $B(M1; 2^+_3 \rightarrow 2^+_1)$  are predicted as 0.46, 0.47, 0.06 and 0.02 ( $\mu_N^2$ ) for  $^{148-154}\text{Sm}$ , respectively. The first two large values indicate dominance of isovector (i.e. F-vector) components in the wave function of these  $2^+_3$  states.

This work has been published in Ref. 3.

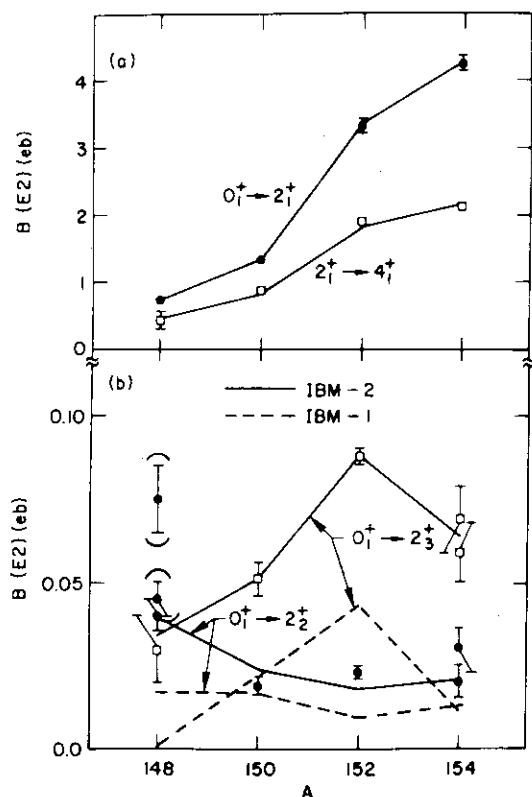


Fig. 1 Calculated (lines) and experimental (symbols)  $B(E2)$  values for four transitions of  $^{A}_{62}\text{Sm}$ . The solid lines are obtained by the present IBM-2 calculation, while the dashed lines are obtained by an IBM-1 calculation<sup>4)</sup>.

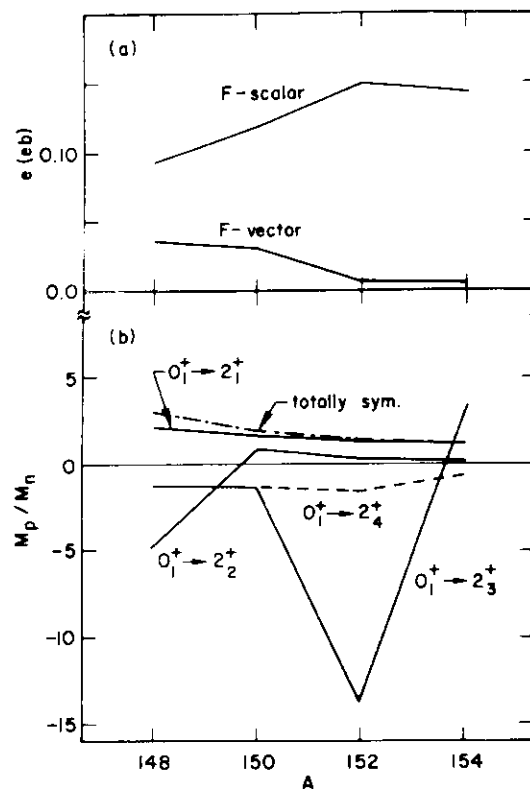


Fig. 2 (a) The F-scalar and F-vector boson charges for  $^{A}_{62}\text{Sm}$ . (b) The proton-neutron ratio  $M_p/M_n$  (See Ref. 3). The dashed-dotted line indicates the ratio for isoscalar-type states. The dashed line shows the  $0^+_1 \rightarrow 2^+_4$  transitions in  $^{152,154}\text{Sm}$ .

#### References

- 1) T. Otsuka, A. Arima, F. Iachello and I. Talmi, Phys. Lett. **76B** (1978) 139.
- 2) A. Arima, T. Otsuka, F. Iachello and I. Talmi, Phys. Lett. **66B** (1977) 205.
- 3) T. Otsuka and J.N. Ginocchio, Phys. Rev. Lett. **54** (1985) 777.
- 4) O. Scholten, F. Iachello and A. Arima, Ann. Phys. (N.Y.) **115** (1978) 325.



## 5.9 RENORMALIZATION OF g-BOSON EFFECTS IN THE INTERACTING-BOSON HAMILTONIAN

Takaharu OTSUKA and Joseph N. GINOCCHIO\*

Department of Physics, JAERI, \*Theoretical Division,  
Los Alamos National Laboratory

There are two major steps in the microscopic derivation of the Interacting Boson Model (IBM). The first step is the mapping from the nucleon system onto the boson system<sup>1)</sup>. Boson states and Hamiltonian are obtained in this mapping as boson images of nucleon states and Hamiltonian<sup>1)</sup>. Since low-lying quadrupole collective states are mainly composed of the  $J=0^+$  (S) and  $J=2^+$  (D) nucleon pairs, the corresponding boson states also mainly consist of the  $J=0^+$  (s) and  $J=2^+$  (d) bosons which are boson images of the S and D pairs. There are, however, non-negligible admixtures of  $J=4^+$  (G) pairs in the low-lying collective states. Consequently, the mapped boson states contain certain amount of the  $J=4^+$  (g) boson which is the boson image of the G pair.

The second major step concerns the treatment of these g-boson admixtures, because only the s and d bosons are explicitly treated in the IBM. In fact, phenomenological analyses do not indicate the need for explicit treatment of g bosons to describe most of the low-lying collective states. We proposed a method for treatment of the g-boson admixtures. The method is based on a unitary transformation between the d and g bosons. By choosing the proper mixing angle in this transformation, the coupling between the new d and g becomes minimal, thereby producing a renormalized s-d boson (or IBM) Hamiltonian starting from a more fundamental Hamiltonian.

We applied this renormalization method to an s-d-g boson system which simulates a rotational nucleus <sup>158</sup>Gd. Fig. 1a shows spectrum obtained by solving this s-d-g boson Hamiltonian directly in terms of the angular momentum projection of the deformed intrinsic state. Fig. 1b shows spectrum obtained by diagonalizing the s-d boson (or IBM) Hamiltonian calculated by our renormalization method. This Hamiltonian contains up to two-body interactions as assumed in the phenomenological IBM. The agreement between these two spectra is remarkable. The spectrum obtained by diagonalizing the s-d boson part of the original s-d-g boson Hamiltonian

(Fig. 1c) deviates from the exact one (Fig. 1a) by a factor three, indicating the importance of the renormalization. The low-lying collective states can now be described within the s-d boson space after the appropriate unitary transformation. The second-order perturbation for the g-boson admixture is not suitable in this case, since the admixture is too large.

The renormalization method can be generalized to problems about strong coupling between two degrees of freedom inside (for example the d boson) and outside (for example the g boson) the truncated space. The major effect is, in general, a reduction of the self-energy of the former degree of freedom. Fig. 2 shows how self-energies (single-particle energies) are changed by the renormalization in the above example.

This work has been published in Ref. 2.

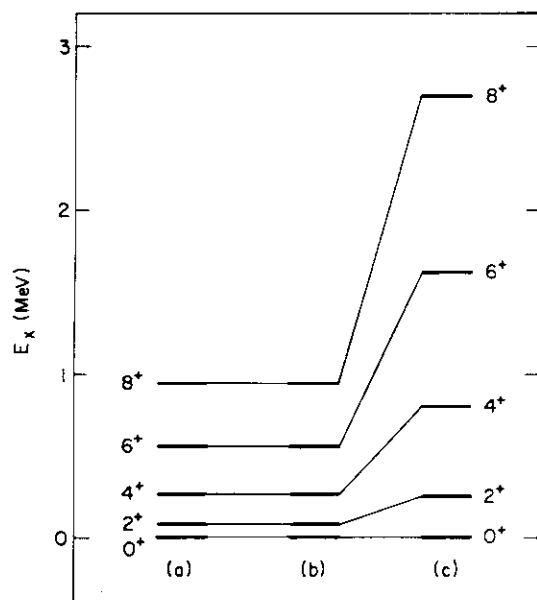


Fig. 1 Spectra of  $^{158}\text{Gd}$  obtained by (a) from an s-d-g boson Hamiltonian, (b) from the renormalized s-d boson (IBM) Hamiltonian, and (c) from the s-d boson part of Hamiltonian in (a).

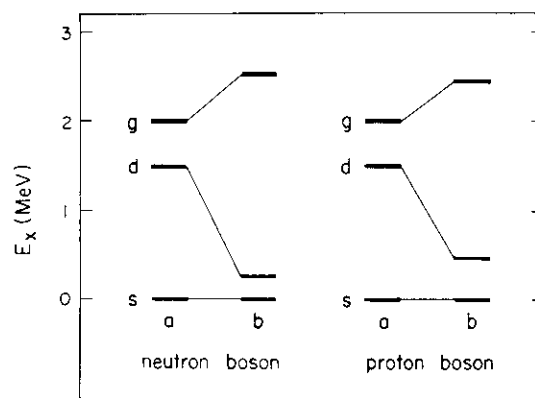


Fig. 2 Single boson energies of the same system in Fig. 1, (a) before and (b) after the renormalization based on the unitary transformation. The large energy gap in (b) separates the collective (i.e. d boson) and non-collective (i.e. g boson) degrees of freedom.

#### REFERENCES

- 1) T. Otsuka, A. Arima, F. Iachello and I. Talmi, Phys. Lett. 76B (1978) 139; T. Otsuka, A. Arima and F. Iachello, Nucl. Phys. A309 (1978) 1.
- 2) T. Otsuka and J.N. Ginocchio, in print in Phys. Rev. Lett. (1985).

## VI NEUTRON PHYSICS

6.1 SCATTERING OF 12.8 MeV NEUTRONS FROM  $^{28}\text{Si}$ 

Yoshimaro YAMANOUTI, Masayoshi SUGIMOTO, Yutaka FURUTA  
Motoharu MIZUMOTO and Mikio HYAKUTAKE\*

Department of Physics, JAERI, \*Department of Nuclear  
Engineering, Kyushu University

Measurements of the nucleon scattering from  $^{28}\text{Si}$  in the energy region above 10 MeV have been reported during the last ten years<sup>1-7)</sup>.

Analyses of these experimental data with the DWBA or coupled-channel methods have revealed the collective behavior of the low-lying excited states of  $^{28}\text{Si}$ . Differential cross sections for the scattering of 12.8 MeV neutrons from  $^{28}\text{Si}$  were measured in order to get deeper understanding of the reaction mechanism in this energy region and collective properties of the low-lying excited states of  $^{28}\text{Si}$ .

In addition to the previous measurements<sup>8)</sup>, differential cross sections at backward angles larger than  $130^\circ$  were obtained, and dead time of the counting electronics was compensated in the present measurements. In order to ascertain the absolute values of the cross sections, time-of-flight spectra at several scattering angles were remeasured. The neutron TOF facility and the experimental methods have been described previously<sup>8)</sup>.

The experimental cross sections were analyzed by the optical model, the DWBA theory and the coupled-channel formalism. In the first step, the elastic scattering data were analyzed by the optical model with the standard potential form by using the code ELIESE3. The form factors for the real part and the imaginary part are of the Woods-Saxon type and the derivative Woods-Saxon type, respectively. The optical potential parameters were searched for automatically to give the best fit between the calculated cross sections for the shape elastic scattering plus the compound elastic scattering and the experimental elastic scattering cross sections. The compound elastic and compound inelastic cross sections were estimated by using the Hauser-Feshbach formalism. The  $(n,n)$  and  $(n,\alpha)$  channels were taken into account, and higher excited levels were assumed to be overlapping and treated through a nuclear level density. The best fit optical potential parameters are listed in table 1. Also included in the table are the volume integrals  $(J/A)_V$  and  $(J/A)_W$  for the real and

Table 1

## Optical potential parameters and volume integrals

(geometrical parameters in fm, potential depth in MeV, J/A in MeV·fm<sup>3</sup>)

V	r	a	W <sub>D</sub>	r <sub>D</sub>	a <sub>D</sub>	V <sub>SO</sub>	r <sub>SO</sub>	a <sub>SO</sub>	(J/A) <sub>V</sub>	(J/A) <sub>W</sub>
55.67	1.132	0.686	8.07	1.259	0.567	6.0	1.15	0.58	471.2	128.7

imaginary potentials, respectively. The volume integrals obtained in the present work were compared with the results of the different experiments to understand the systematics of the optical potentials since the volume integral can be less dependent on the choice of geometrical parameters. The energy dependence of the volume integrals is shown in fig. 1. The volume integrals obtained in the present work are qualitatively consistent with other results.

The DWBA calculations were carried out for the cross sections of the 2<sup>+</sup> and 4<sup>+</sup> states by using the code DWUCK4. The best fit opti-

cal potential parameters in table 1 were used in the calculations. The scattered neutrons leading to the 0<sup>+</sup> state at 4.979 MeV could not be resolved from neutrons to the 4<sup>+</sup> state at 4.617 MeV. The compound inelastic cross sections for the 2nd 0<sup>+</sup> were added to the compound inelastic cross sections for the 4<sup>+</sup> state. The direct contribution from the 2nd 0<sup>+</sup> state was also calculated to obtain the best fit to the experimental cross

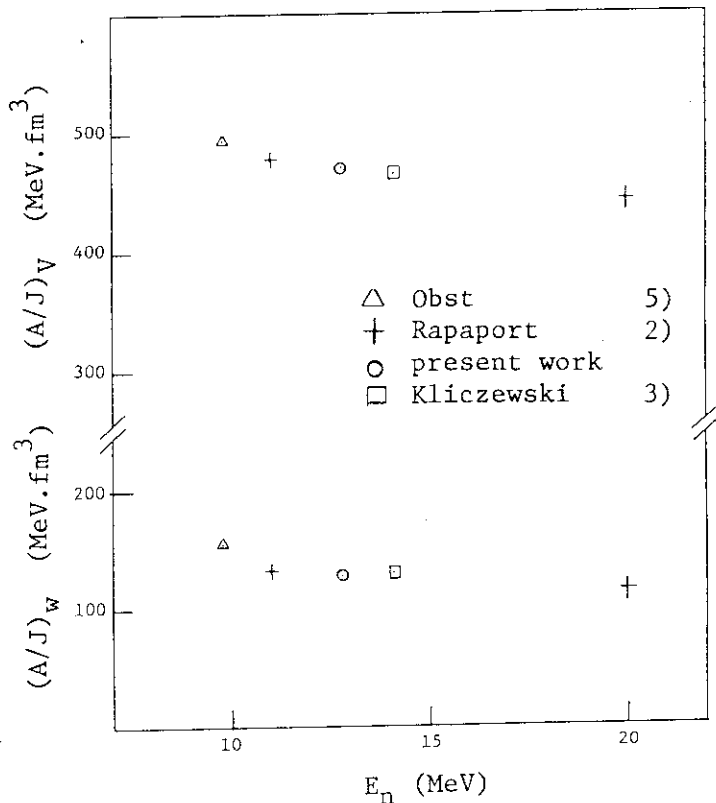


Fig. 1 Energy dependence of the volume integrals for the real and imaginary potentials.

sections by varying the deformation parameters  $\beta_4$  and  $\beta_0$ . The best fit deformation parameters  $\beta_2$ ,  $\beta_4$  and  $\beta_0$  are 0.46, 0.19 and 0.07, respectively. The fits to the experimental cross sections are shown in fig. 3. Each theoretical curve calculated by the DWBA or the coupled-channel formalism in figs. 2 and 3 are the incoherent superposition of the direct contribution and the compound nuclear contribution.

The coupled-channel calculations based on the rotational model were performed by using the code JUPITOR1. In these calculations the  $0^+$  (0.0 MeV),  $2^+$  (1.779 MeV) and  $4^+$  (4.617 MeV) states were assumed to be the members of the ground state rotational band,

and the same optical potential parameters as those in the DWBA calculations except the imaginary potential depth  $W_D$  were used. The imaginary potential depth was adjusted to 4.84 MeV to preserve the fit to the elastic scattering cross sections. The calculations were first performed with the  $0^+-2^+-4^+$  coupling scheme. The result shows that the cross sections calculated for the  $4^+$  state are systematically smaller in magnitude than the experimental cross sections in the whole angular range, and do not reproduce the pattern of the angular distribution. This disagreement might be attributed to neglecting the direct contribution from the 2nd  $0^+$  state. Therefore, the calculations were performed with the  $0^+-2^+-4^+-0^+$  coupling scheme by assuming the 2nd  $0^+$  state as the head of the  $K^\pi = 0^+$  rotational band built on a  $\beta$ -vibrational excitation. The quality of the fit to the  $4^+(0^+)$  cross sections was improved satisfactorily by considering the direct

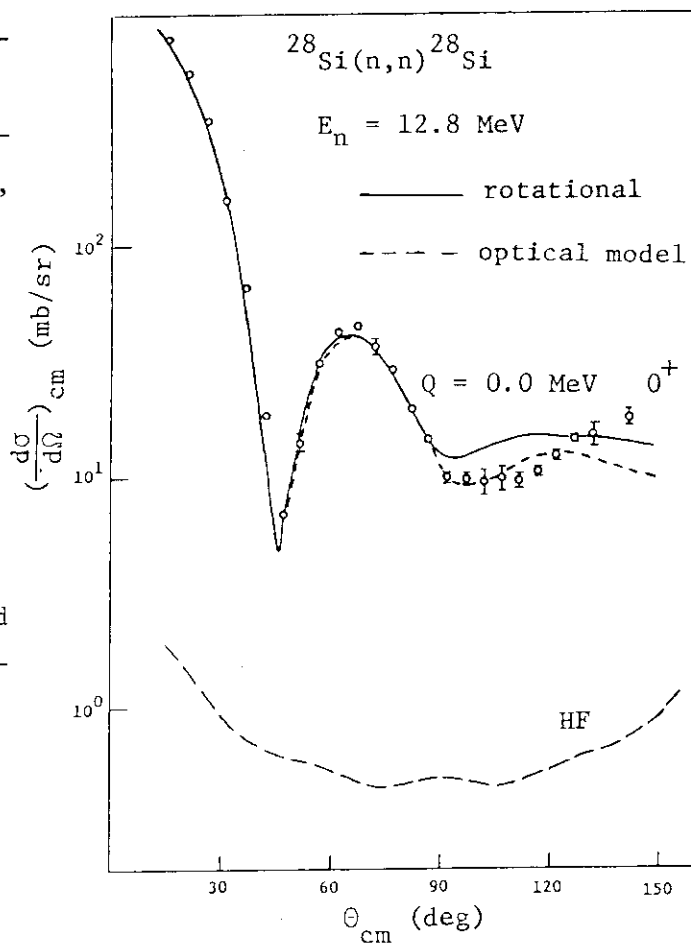


Fig. 2 Experimental cross sections of the elastic scattering and theoretical curves by the optical model and coupled channel calculations.

contribution from the  $0^+$  state (see figs. 2 and 3).

The deformation parameters were adjusted to give the best fit to the experimental cross sections. The best fit quadrupole deformation parameter and the deformation parameter for the  $\beta$  vibration are  $-0.42$  and  $0.29$ , respectively.

The experimental cross sections for the  $0^+$ ,  $2^+$  and  $4^+(0^+)$  states of  $^{28}\text{Si}$  were well reproduced by the coupled-channel calculation based on the rotational model with the oblate quadrupole deformation.

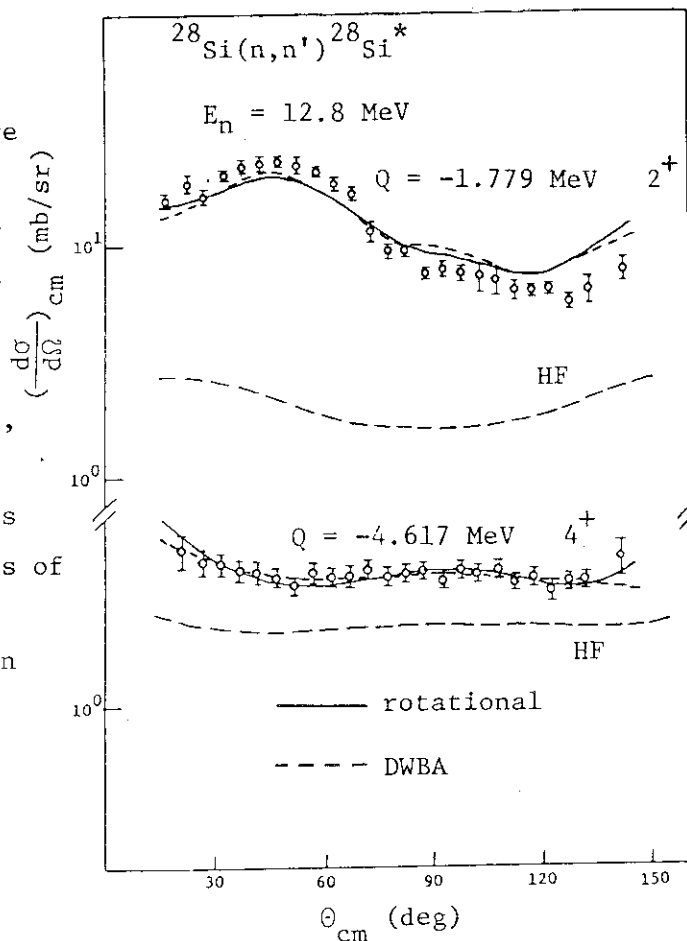


Fig. 3 Experimental cross sections of the inelastic scattering and theoretical curves by the DWBA and coupled-channel calculations.

#### References

- 1) G. Haouat et al, Phys. Rev. C30 (1984) 1795
- 2) J. Rapaport et al, Nucl. Phys. A286 (1977) 232
- 3) S. Kliczewski et al, Nucl. Phys. A304 (1978) 269
- 4) R. De Leo et al, Phys. Rev. C20 (1979) 1244
- 5) A.W. Obst et al, Phys. Rev. C7 (1973) 1076
- 6) R. de Swiniarski et al, Nucl. Phys. A261 (1976) 111
- 7) R. De Leo et al, Phys. Rev. C19 (1979) 646
- 8) Y. Yamanouti et al, JAERI-M 84-129 (1984)

## 6.2 MEASUREMENTS OF FAST NEUTRON SCATTERING CROSS SECTIONS OF ALUMINUM

Masayoshi SUGIMOTO, Yoshimaro YAMANOUTI, Yutaka FURUTA,  
Motoharu MIZUMOTO, Susumu NISHIHARA  
and Mikio HYAKUTAKE\*

Department of Physics, JAERI, \*Faculty of Engineering,  
Kyushu University

### Introduction

The JAERI tandem fast neutron time-of-flight (TOF) spectrometer was used to measure the angular distributions for 13 MeV neutrons scattered from aluminum. The differential cross sections of neutron scattering from Al are of great interest from the theoretical and applied viewpoints. (1) The low-lying excited states of  $^{27}\text{Al}$  can be described as weak coupling of the  $d_{5/2}$  proton hole state to the collective excitations of  $^{28}\text{Si}^{(1)}$ . (2) As aluminum is proposed as the structural material of the fusion reactors, the priorities of nuclear data requests are high. (3) Another purpose of this measurement is technical advancement: the TOF spectra were obtained from the list mode event record data by using the new approach to improve the time resolution of the large-efficiency neutron detectors.

### Measurements

Neutrons were generated through the reaction  $\text{D}(\text{d}, \text{n})^3\text{He}$  by bombarding a deuterium gas target with 10 MeV deuterons extracted from the in-terminal source and accelerated in the single way of the accelerator<sup>(2)</sup>. The average beam current and pulse width were 2  $\mu\text{A}$  and 2 ns, respectively, at a 2 MHz repetition rate. The neutron scatterer was a 3 cm diam and 4 cm high cylindrical aluminum and mounted at a distance of 15 cm from the neutron producing target. The main detector system consisted of four 22 cm diam and 35 cm thick NE213 liquid scintillators contained in the glass vessels which were viewed by the two RCA8854 photomultiplier(PM)s at the front and the rear faces for the purpose of the time-compensation<sup>(2)</sup>. The detectors were placed in the shield-collimator with an 8 m flight path. Two unshielded monitor detectors were set at the 35 deg with respect to the beam direction. Each detector was 2 cm diam and 1.2 cm thick NE213



scintillator mounted on the RCA8575 PM and the Hamamatsu R594 PM, respectively. One of the flux monitors was also used as the beam pulse width monitor.

The scattered neutron TOF spectra were taken at the 15 laboratory angles between 20 and 140 deg at 13 MeV and at the 60 and 100 deg angles in the energy range from 12.3 to 13.5 MeV.

The background spectra, sample-out and gas-out with sample-in, were taken at each angle, and the scattered neutron spectra from silicon were also measured at the several angles to obtain the line shape for the single energy peaks.

The relative detection efficiency was measured by observing the angular distribution of the reaction  $D(d,n)^3\text{He}$  at 10 MeV and comparing with the evaluated cross sections<sup>3)</sup>. The incident neutron flux was measured at 0 deg with the main detectors in order to normalize the relative cross sections. In some cases of these direct source measurements the counting rate at the input to the time-to-amplitude converter(TAC) reached to  $10^5$  cps, so the average beam current was decreased by about an order and the dead-time counting loss at the TAC was monitored.

#### Data acquisition and processing

The data were accumulated using the PDP 11/55 - 11/04 - MBD(Micro-programmed Branch Driver) - CAMAC system with two modes concurrently : 1) the single mode multichannel analysis for the conventional method of the time-compensation<sup>4)</sup> and 2) the list mode event recording for the new approach of the "software" compensation.

The principle of the time-compensation derives the compensating formulae<sup>4)</sup> :  $T_d = T_1 - \alpha T_2$ , where the compensation factor  $\alpha$  is proper to the detector and determined experimentally, and it depends on the neutron velocity. The conventional method can be called the "hardware" compensation because the combination of the electronics modules is used to attain the best time resolution and it employs a constant  $\alpha$  for the representative energy of the measured neutrons. On the other hand, the "software" compensation is the data processing method to manipulate the list mode event data,  $(T_1, T_1-T_2, PH, PS)$ :  $T_1$  is the TOF of the rear-side PM;  $T_1-T_2$  is the difference of TOF between the two PMs; PH is the pulse height; PS is the pulse shape information based on the rise-time difference to discriminate the gamma rays. In the design of the detector

we performed the extensive simulations of the light propagation in the scintillator and the formation of the timing signal at the PM by the Monte Carlo program and found that the  $\alpha$  was also dependent of the radial distance of the detection point. To circumvent the defects of the "hardware" compensation we applied a new approach using the direct information of the detection point, i.e. T1-T2. The list mode events were firstly gated by the lower and upper levels corresponding to the hardware discrimination levels, and secondly selected by the two-dimensional gates defined at the three maps: the PS vs. PH map was used to define the n- $\gamma$  discrimination, the T1 vs. PH map was used for the dynamic biasing<sup>5)</sup> which applied the neutron energy dependent biases to reduce background, and the T1 vs. T1-T2 map showed the detection point and the detector identification. An example of the maps processed by using the VAX 11/780 and E&S Multi Picture System is shown in Fig. 1, for the direct neutron source measurement at 0 deg with no gate. The compensated TOF spectra were obtained by gathering the gated T1 spectra at the every T1-T2 channel to the specific T1-T2 channel and by projecting along the compensation lines shown in Fig. 2. These lines for the energies between 5 and 13 MeV were defined from the observed ridges of the mono-energetic peaks of the  $D(d,n)^3\text{He}$  neutrons measured at the several angles. All the lines were neither straight nor identical in contrast to the assumption of the "hardware" compensation. Fig. 2. shows the enlarged map of the 5.4 MeV neutrons observed in the source measurement at 85 deg. Fig. 3(a) is an example of the compensated spectrum at  $\theta=50$  deg. Some improvements about the peak separation are seen compared with the fig. 3(b), which is obtained from the "Hardware" compensation.

The further processing and analysis of the obtained TOF spectra is in progress.

#### References

- 1) A. de-Shalit: Phys. Rev. 122 (1961) 1530.
- 2) Y. Yamanouti et al.: JAERI-M 84-129 (1984) 92.
- 3) M. Drosch: Nucl. Sci. Engineering 67 (1978) 190.
- 4) J. D. Carlson, R. W. Finlay and D. E. Bainum: Nucl. Instr. Methods 147 (1977) 353.
- 5) J. D. Brandenberger and T. B. Grandy: Nucl. Instr. Methods 93 (1971) 495.

Fig. 1 An example of the maps of source neutron data: (left-up) PS vs. PH (right-up) T1 vs. PH and (right-down) T1 vs. T1-T2. T1 and T2 are time-of-flights obtained from the rear-face and front-face photomultipliers, respectively. PH is the pulse height and PS is the pulse shape information based on the rise-time difference for the n- discrimination. In the PS vs. PH map the neutron is only shown because of the hardware n- $\gamma$  discrimination.

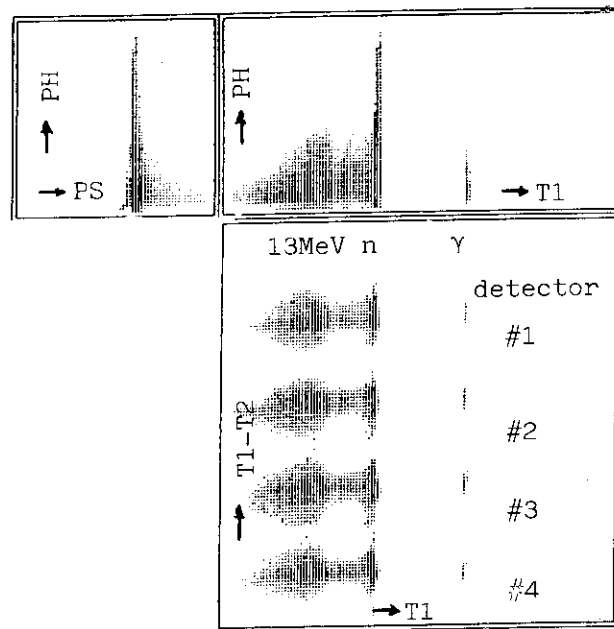
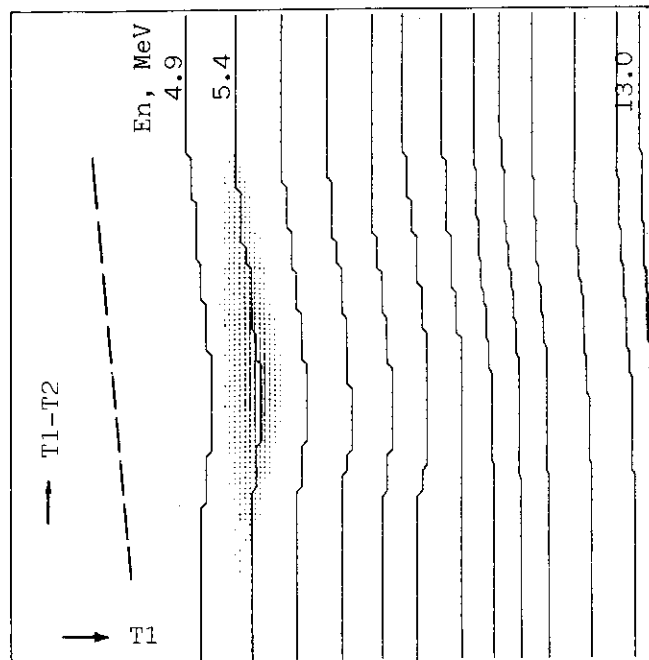


Fig. 2 The compensation lines used in the data processing for the neutron energies between 5 and 13 MeV which were defined by using the mono-energetic neutrons observed at various angles of  $D(d,n)^3\text{He}$  reaction. The dashed line shows the "hardware" compensation factor  $\alpha$ , schematically. The data in the map shows the 5.4 MeV neutrons measured at 85 deg. The spread in the T1 axis represents the intrinsic time resolution and the spread in the T1-T2 axis represents the variation of the detection point in the 35 cm thickness of the detector.



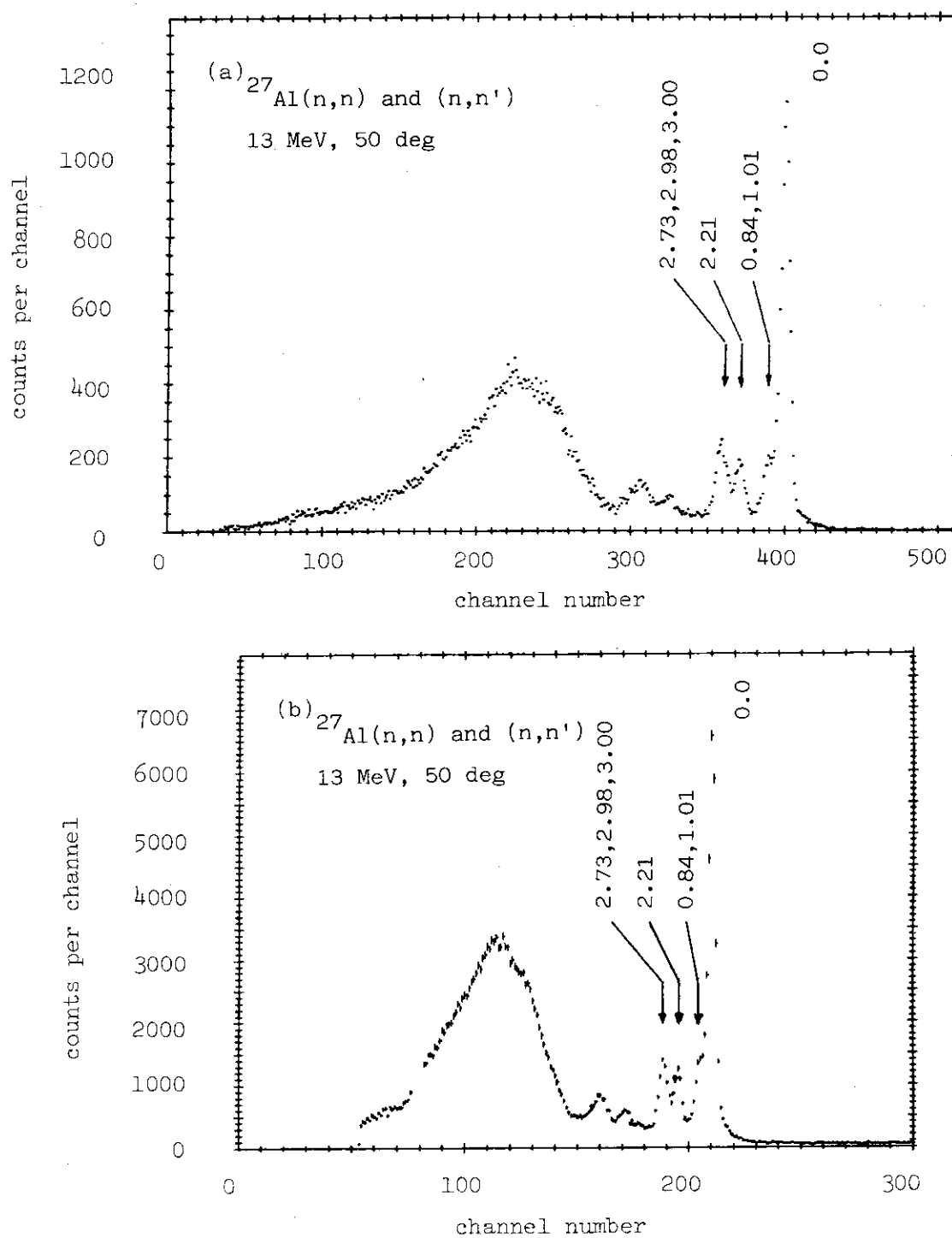


Fig. 3 Neutron time-of-flight spectra for 13 MeV neutrons from Al at 50 deg in laboratory. (a) is processed by the "Software" time compensation method and (b) is obtained from the "Hardware" compensation. The vertical bars at each data point in (b) show the statistical uncertainty. Some lower levels are indicated by their excitation energies.

6.3 NEUTRON RESONANCE PARAMETERS OF  $^{142}\text{Ce}$ 

Makio OHKUBO, Motoharu MIZUMOTO, Yutaka NAKAJIMA,  
Masayoshi SUGIMOTO, Yutaka FURUTA and Yuuki KAWARASAKI

Department of Physics, JAERI

As cerium ( $Z=58$ ) situates near the 4s peak of the s-wave strength function, it is worthwhile to measure the isotopic dependence of the strength function experimentally.  $^{140}\text{Ce}$  is an  $N=82$  closed shell nucleus, in the vicinity of which intermediate structures are often observed.

Also cerium isotopes are FP nuclei. The resonance parameters of  $^{142}\text{Ce}$  are very poorly known.<sup>1)</sup> No measurements were made since Newson et al. did in 1959 using a VDG.<sup>2)</sup> Since cerium is included in the  $^6\text{Li}$ -glass neutron scintillator as an activator, its cross section is important for the accurate efficiency calculation. We have made neutron transmission and capture measurements on natural cerium and separated isotope  $^{142}\text{Ce}$  at the TOF facility of the JAERI electron linear accelerator.

Pulsed neutrons were produced on a tantalum target bombarded by an electron beam of the linac; the beam energy  $\sim 110$  MeV, peak current  $\sim 3\text{A}$ , beam pulse width 25 ns, and repetition rate 600 pps. A neutron transmission detector was a  $1\frac{1}{2}'' \times 1\frac{1}{2}''$   $^6\text{Li}$  glass exposed in a 35 mm  $\phi$  neutron beam at the 47 m station. The capture detector was a 500 l liquid scintillator tank settled at the 55 m station. The signals from these detectors were analyzed by a 4096 channel time analyzer with a 31.25 ns channel width. Separated isotope  $^{142}\text{Ce}$  sample was oxide  $\text{CeO}_2$  with an isotopic content 92.11% of  $^{142}\text{Ce}$  and 7.89% of  $^{140}\text{Ce}$  lent from the ORNL isotope pool. The natural cerium sample was also oxide with a major isotopic content 88.48% of  $^{140}\text{Ce}$  and 11.08% of  $^{142}\text{Ce}$ . Observed total cross sections of  $^{142}\text{Ce}$  nuclide were obtained from the transmissions of  $^{\text{nat}}\text{Ce}$  and  $^{142}\text{Ce}$  samples, and are shown in Fig.1 up to 30 keV. Transmission data of  $^{142}\text{Ce}$  and  $^{140}\text{Ce}$  were analyzed by a multilevel shape fit program SIOB to obtain resonance energy  $E_0$  and neutron width  $\Gamma_n$ .

Resonance parameters of the 40 levels of  $^{142}\text{Ce}$  up to 50 keV are newly determined. A plot of cumulative number of levels vs. neutron energy is

shown in Fig.2, and the average s-wave level spacing was deduced to be  $D_0 = 0.75 \pm 0.12$  keV for the resonances with  $\Gamma_n^0 \geq 0.5$  meV. Cumulative values of  $\Gamma_n^0$  vs. neutron energy are shown in Fig.3, and the overall s-wave strength function of  $^{142}\text{Ce}$  is estimated to be  $S_0 = (2.7 \pm 0.6) \times 10^{-4}$  below 50 keV. This value is about 2.5 times larger than the  $^{140}\text{Ce}$  strength function of  $1.1 \times 10^{-4}$  reported by Camarda from 20 to 240 keV region. 3) The observed  $S_0$  of  $^{142}\text{Ce}$  is consistent with the systematics of the s-wave strength function vs. mass number. In Fig.3 there seem leaps at 1.3, 24, and 43 keV, indicating strong levels at these energies. For  $^{140}\text{Ce}$ , cumulative value of  $\Gamma_n^0$  vs. neutron energy is shown in Fig.4, where an extraordinary large resonance appears at 21.6 keV, and is thought to be a simpler (intermediate) structure which is not yet thoroughly washed out by residual interactions. On the other hand large levels in  $^{142}\text{Ce}$  cluster near 24 keV, which is thought to be one of the structures often observed in the nuclei in the vicinity of the neutron closed shell.

#### References

1. S.F.Mughabghab, M.Divadeenam and N.E.Holden; "Neutron Cross Sections" Vol 1, Part A, Z=1-60, Academic Press(1981)
2. H.W.Newson, R.C.Block, P.F.Nichols, A.Taylor, A.K.Furr and E.Merzbacher: Ann.Phys.8 (1959) 211
3. H.S.Camarda: Phys.Rev.C18 (1978) 1254

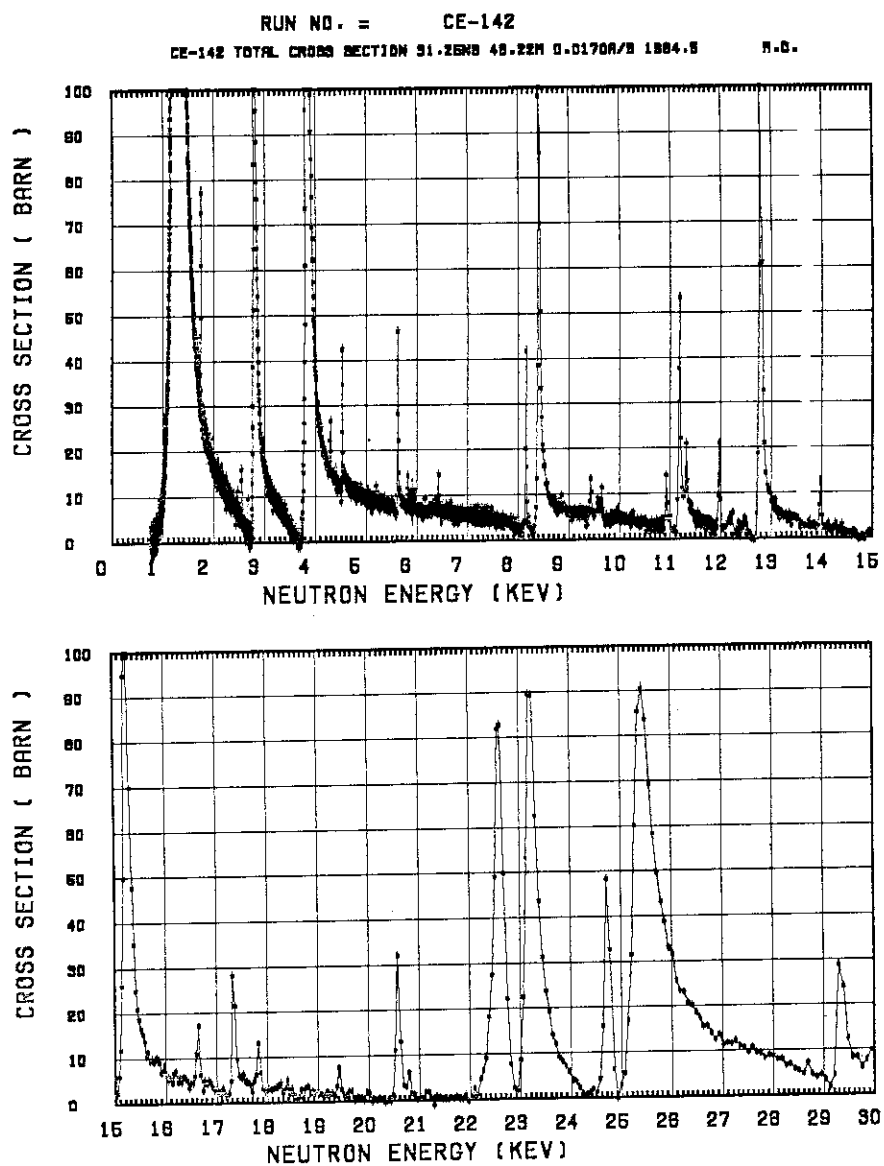


Fig. 1 Observed total cross section(barn) of  $^{142}\text{Ce}$  up to 30 keV.

Fig. 2

A plot of cumulative number of levels vs. neutron energy. Average s-wave level spacing is deduced to be  $0.75 \pm 0.6$  keV. When the very small levels are included, average level spacing is 0.45 keV.

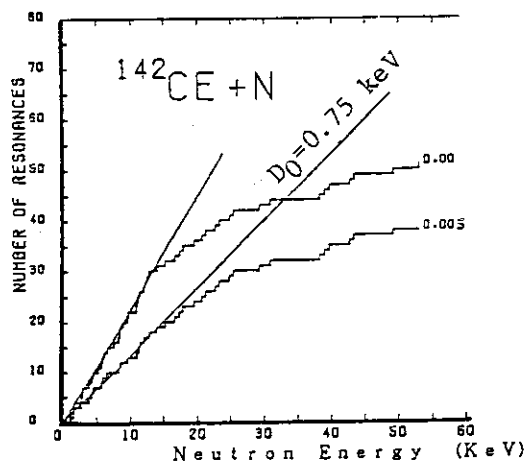


Fig. 3

A plot of cumulative values of  $\Gamma_n^0$  vs. neutron energy for  $^{142}\text{Ce}$ . Overall s-wave strength function is deduced to be  $S_0 = (2.7 \pm 0.6) \times 10^{-4}$ . The leaps are seen at 1.3, 24, and 43 keV with an average distance of 20 keV. Between these leaps,  $S_0$  is  $1.2 \times 10^{-4}$ . (dotted lines)

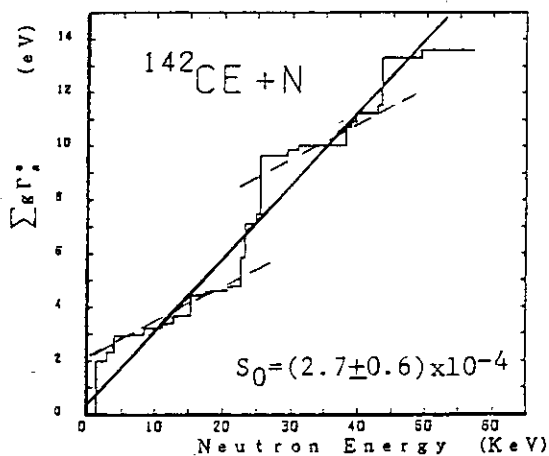
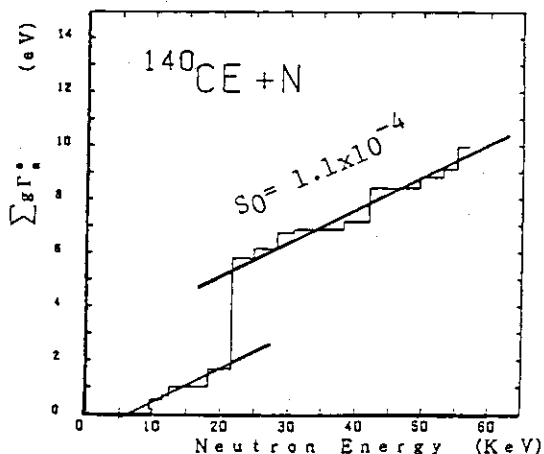


Fig. 4

A plot of cumulative values of  $\Gamma_n^0$  vs. neutron energy for  $^{140}\text{Ce}$ . The solid lines indicate strength function of  $S_0 = 1.1 \times 10^{-4}$ . A leap is seen at 21 keV.





#### 6.4 NEUTRON CAPTURE AND TRANSMISSION MEASUREMENTS AT A 55 M STATION OF THE JAERI LINAC

Motoharu MIZUMOTO, Masayoshi SUGIMOTO, Makio OHKUBO,  
Yutaka NAKAJIMA, Yutaka FURUTA and Yuuki KAWARASAKI

Department of Physics, JAERI

##### Introduction

Accurate neutron cross sections of fission product nuclei are of practical importance for reactor applications. In particular, capture cross sections in the keV region of odd mass nuclei are requested with high priorities, since they contribute significantly to total neutron absorption rate in the reactor core. Average resonance parameters such as strength function and level spacing are also needed to evaluate average cross sections. As a part of our continuing efforts to provide nuclear data of fission products<sup>1)</sup>, capture and transmission measurements for odd Barium isotopes ( $^{135}\text{Ba}$  and  $^{137}\text{Ba}$ ) were carried out at a 55 m station of the JAERI Linac. Several resonance experiments for these nuclei have been previously made in the energy region below 2 keV<sup>2,3)</sup>. The capture experiments have been also carried out at ORELA to extract capture areas for resonances from 2.7 to 12 keV as well as average capture cross sections below 200 keV<sup>4)</sup>. In the present experiment, we have determined neutron widths for  $^{135}\text{Ba}$  and  $^{137}\text{Ba}$  in the energy region up to 4 keV and up to 9 keV, respectively. Average capture cross sections for  $^{135}\text{Ba}$  were deduced from 4 to 300 keV. Capture cross sections for some other nuclei such as Fe, Ce, Sn and Ta were also measured using the same facility at the 55 m station during the past year.

##### Experiment and analysis

Measurements were carried out with the neutron time-of-flight methods. The linac was operated at 300 pps and 600 pps with an electron burst width of 30 ns. Capture events were detected with a 500 l liquid scintillator tank at 54.46 m. The characteristics of this scintillation detector were investigated in some detail<sup>5)</sup> and the experimental pulse height distribution was compared with the Monte-Carlo calculation as shown in Fig. 1. The neutron flux shape was monitored with a  $^6\text{Li}$  glass detector. Beam

filters were inserted permanently in neutron beam; 5 mm boron nitrate to absorb low energy neutrons and 9 mm Pb to reduce gamma flash. Metallic Na of 8 mm thick encapsulated in an Al container was used for capture measurements to normalize back-

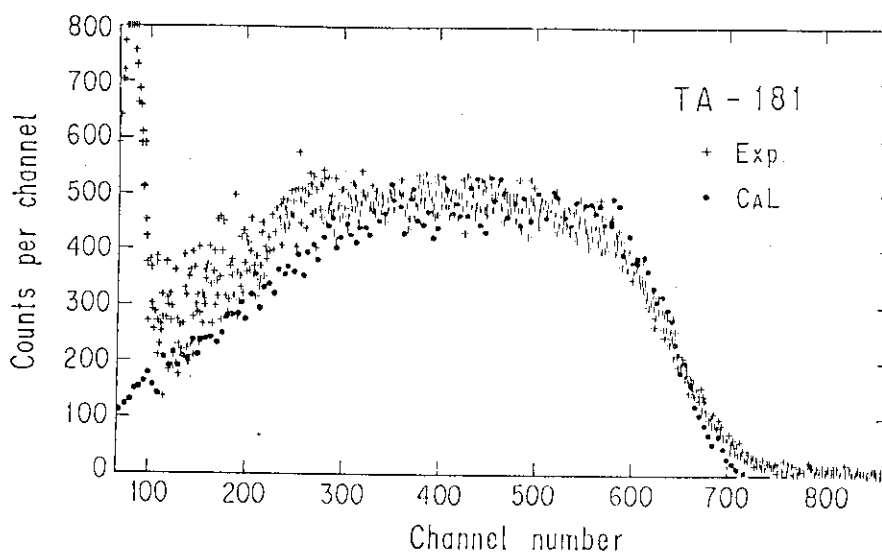


Fig. 1 Experimental and calculated pulse height distributions of Ta(n,γ)

grounds at the 2.85 keV resonance. Transmission were measured with an 11.1 cm  $\phi$  x 0.635 cm thick  $^6\text{Li}$ -glass detector at 56.32 m. Enriched samples such as  $^{135}\text{Ba}$ (79.04 %) and  $^{137}\text{Ba}$ (81.9%) were provided in the form of carbonate and nitrate powder, respectively, from the Isotope Division of ORNL.

The capture count rates were converted to relative capture cross

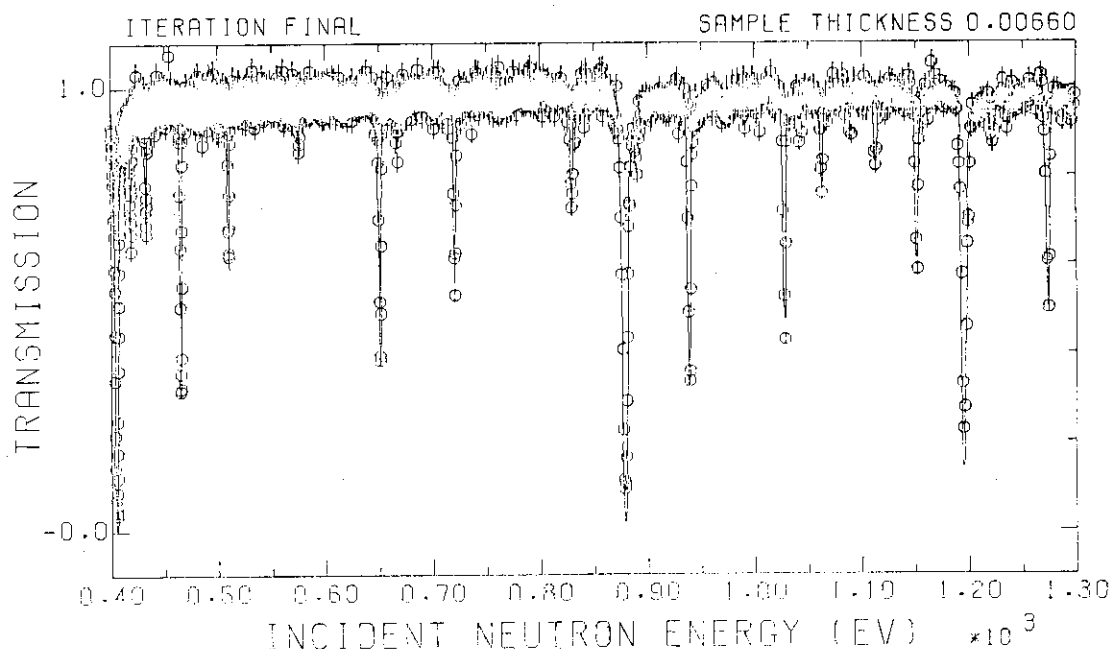


Fig. 2 An example of resonance analysis of the transmission data. The solid line is the calculated curve with the multi-level Breit-Wigner formula.

sections by using conventional techniques for dead time correction, background subtraction and sample thickness correction. The transmission data were analyzed with a multi-level Breit-Wigner code SIOB<sup>6)</sup>. An example of the analysis is shown in Fig. 2.

### Result and discussion

The neutron widths of 63 resonances for  $^{135}\text{Ba}$  and 24 resonances of  $^{137}\text{Ba}$  were obtained from the transmission analyses. Our values are significantly smaller than those in BNL-325<sup>7)</sup> below 1 keV both for  $^{135}\text{Ba}$  and  $^{137}\text{Ba}$ , where the previous data<sup>2,3)</sup>

are available. The s-wave strength functions for  $^{135}\text{Ba}$  and  $^{137}\text{Ba}$  were obtained to be  $S_0 =$

$(0.96 \pm 0.30) \times 10^{-4}$  and  $S_0 =$   
 $(0.16 \pm 0.07) \times 10^{-4}$ , respective-

ly. Our level spacing  $D_0 = 44 \pm 6$  eV for  $^{135}\text{Ba}$  is in good agreement with  $D_0 = 40 \pm 7$  eV given in BNL-325<sup>7)</sup>. But our value of  $D_0 = 150 \pm 80$  eV for  $^{137}\text{Ba}$  corrected for missing resonances is somewhat ambiguous due to the limited number of resonances in our energy region. The s-wave strength functions for odd mass nuclei in the region  $A = 150$  are plotted in Fig. 3. Our experimental values<sup>1)</sup> and the values used for evaluations for JENDL-2<sup>8)</sup> are shown in the figure. Their values are based on the optical model calculation taking into account the experimental data such as average radiation widths.

The average capture cross sections for  $^{135}\text{Ba}$  obtained in the neutron energy region from 4 to 300 keV are shown in Fig. 4. Previous ORELA data<sup>4)</sup> and the evaluated data<sup>8,9)</sup> are also shown in the figure. Overall agreement between the experimental data and the JENDL-2 data is satisfactory, while the ENDF/B-V data are smaller by about 30 %.

The further works for the data of Barium isotopes are still continued to provide accurate information of the experimental uncertainties. Analyses of capture cross sections for other fission product nuclei which were measured with our facility are also in progress.

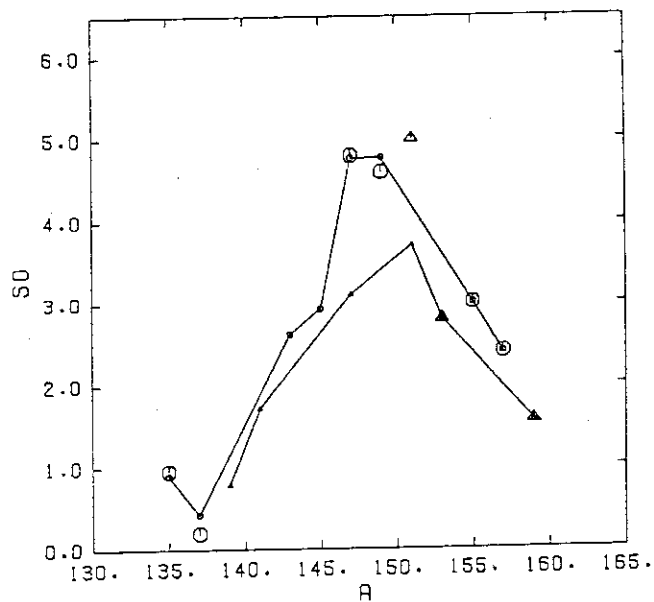


Fig. 3  $S_0 \times 10^4$  vs. A for odd nuclei.

The curves are from JENDL-2

$\circ$  even Z odd N,  $\triangle$  odd Z even N

## References

- 1) N. Yamamuro and A. Asami: NEANDC(E)-209 (1979)19 M.Mizumoto et al.: JAERI-M 84-184 (1984) 75.
- 2) R.N. Alves et al.: Nucl. Phys. A134 (1969) 118.
- 3) R.E. Van de Vyver and N.J. Pattenden: Nucl. Phys. A177 (1971) 393.
- 4) A.R. de L. Musgrove, B.J. Allen and R.L. Macklin: AAEC/E327 (1974), A.R. de L. Musgrove, B.J. Allen, J.W. Boldeman and R.L. Macklin: Aust. J. Phys. 29 (1976) 157.
- 5) M. Mizumoto, M. Sugimoto and T. Shoji: JAERI-M 84-211(1984).
- 6) G. de Saussure, D.K. Olsen and R.B. Perez: ORNL-TM 6286 (1978).
- 7) S.F. Mughabghab, M. Divadeenam and N.E. Holden: BNL-325 4th edition, Neutron Cross Sections, Vol 1, Resonance parameters (1981).
- 8) T. Nakagawa: JAERI-M, 84-103 (1984). S. Iijima and M. Kawai: J. Nucl. Sci. Technol. 20 (1983) 77.
- 9) Evaluated Nuclear Data File - Version V, National Nuclear Cross Section Center, Brookhaven National Laboratory.

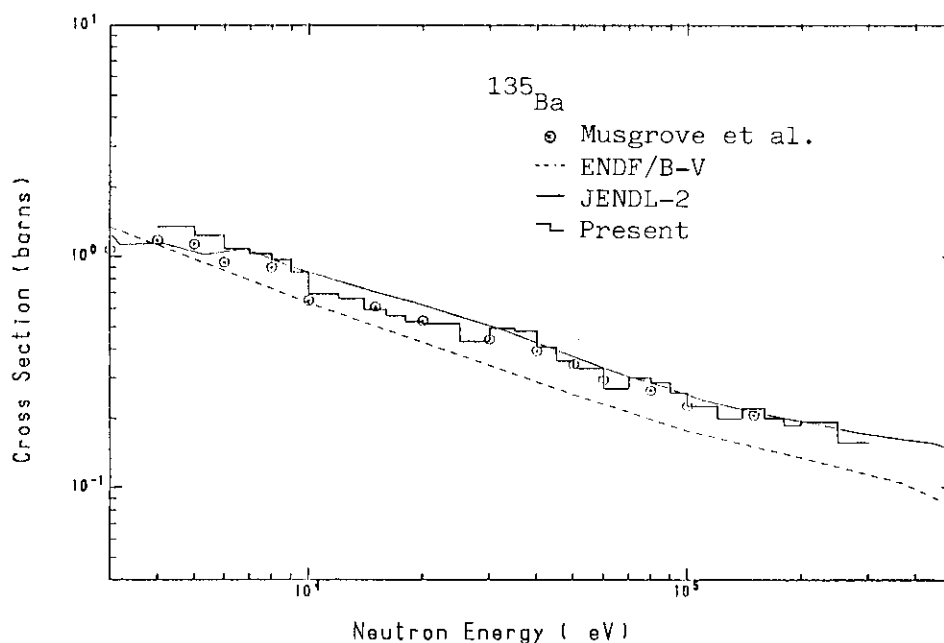


Fig. 4 Neutron capture cross sections of  $^{135}\text{Ba}$ .

## VII PUBLICATIONS

## 7.1 Publications in Journals and Proceedings

1. Appleton, B.R., Naramoto, H., White, C.W., Holland, O.W., McHargue, C.J., Farlow, G.C., Narayan, J. and Williams, J.M.  
Ion Implantation, Ion Beam Mixing and Annealing Studies of Metals in  $\text{Al}_2\text{O}_3$ ,  $\text{SiC}$  and  $\text{Si}_3\text{N}_4$ .  
Nucl. Instr. and Meth. B1 (1984) 167.
2. Baba, S., Hata, K., Izumo, M., Motoki, R. and Sekine, T.  
Preparation of  $^{237}\text{Np}$  Irradiated with Deuterons.  
Int. J. Appl. Radiat. Isot. (1985) in press.
3. Baba, Y. and Sasaki, T.A.  
Application of X-Ray-Induced Auger Electron Spectroscopy to State Analyses of Hydrogen Implanted in Y, Zr and Nb Metals.  
Surf. Interface Anal. 6 (1984) 171.
4. Baba, Y. and Sasaki, T.A.  
Chemical States and Thermal Stability of Hydrogen-Implanted Ti and V Studied by X-Ray Photoelectron Spectroscopy.  
J. Nucl. Mater. 132 (1985) in press.
5. Fukuda, T., Ishihara, M., Ogata, H., Miura, I., Shimoda, T., Katori, K., Shimoura, S., Tanaka, M.-K., Takada, E. and Otsuka, T.  
Light Particle Emission in the Reaction of  $^{93}\text{Nb} + ^{14}\text{N}$  at 132, 159 and 208 MeV.  
Nucl. Phys. A425 (1984) 548.
6. Hamada, S., Sawai, T. and Shiraishi, K.  
Measurement of Mean Projected Ranges for 40-90 MeV Carbon Ion Irradiated into Stainless Steel.  
J. Nucl. Mater. 133&134 (1985) in press.
7. Hamada, S., Sawai, T. and Shiraishi, K.  
Measurement of Mean Projected Range for Carbon Ion Irradiated into Stainless Steel.  
J. Atomic Energy Soc. Jpn. 26 (1984) 695.

8. Iwamoto, A. and Harada, K.  
Enhancement of the Fusion Cross Section Due to the Neck Formation.  
Proc. of the Tsukuba International Symposium on Fusion Reaction (1985)  
in press.
  
9. Iwase, A., Sasaki, S., Iwata, T. and Nihira, T.  
Calorimetric Measurements of Stopping Power of Al and Ni for  $^{35}\text{Cl}$  and  $^{12}\text{C}$  Ions.  
J. Phys. Soc. Jpn. 54 (1985) 1750.
  
10. Iwase, A., Sasaki, S., Iwata, T. and Nihira, T.  
Defect Production by Energetic Heavy Ions in Aluminum and Copper.  
J. Nucl. Mater. 133&134 (1985) in press.
  
11. Kase, M., Kikuchi, A., Yagishita, A. and Nakai, Y.  
Single- and Double-Electron Capture Cross Sections for  $\text{Ne}^{2+}$  in He, Ne  
and Ar.  
J. Phys. B17 (1984) 671.
  
12. Katano, Y., Aruga, T. and Shiraishi, K.  
Precipitates Induced in Austenitic Stainless Steel by Nitrogen  
Injection.  
J. Nucl. Mater. 133&134 (1985) in press.
  
13. Kazumata, Y., Yugo, S. and Kimura, T.  
ESR of Pyrolytic Graphite Irradiated by Ions.  
Proc. of International Carbon Conference (Bordeaux, France) (1984)  
92.
  
14. Kolata, J.J., Rehm, K.E., Kovar, D.G., Stephans, G.S.F., Rosner, G.,  
Ikezoe, H. and Vojtech, R.  
Quasielastic Processes in the  $^{28}\text{Si} + ^{208}\text{Pb}$  Reaction at 8 MeV per  
Nucleon.  
Phys. Rev. C30 (1984) 125.
  
15. Makishima, A., Ishii, M., Ohshima, M., Adachi, M. and Taketani, H.  
EO Transition in  $^{74}\text{Se}$ .  
Nucl. Phys. A425 (1984) 1.

16. McHargue, C.J., Naramoto, H., White, C.W., Williams, J.M., Appleton, B.R., Sklad, P.S. and Angelini, P.  
Structure of Ceramic Surfaces Modified by Ion Beam Techniques.  
Emergent Process Methods for High Technology Ceramics 17 (1984) 519.
  
17. McHargue, C.J., Farlow, G.C., White, C.W., Williams, J.M., Appleton, B.R. and Naramoto, H.  
The Amorphization of Ceramics by Ion Beams.  
Mater. Sci. and Eng. 69 (1985) 123.
  
18. Mikumo, T., Yokota, W., Lee, S.M., Nagashima, Y., Nakagawa, T., Fukuchi, Y., Ideno, K., Tomita, Y., Takeuchi, S., Hanashima, S. and Galster, W.  
The Reactions  $^{37}\text{Cl} + ^{27}\text{Al}$  and  $^{16}\text{O} + ^{48}\text{Ti}$  in the Energy Region of (100-200) MeV. Fission of a Composite System.  
Nuovo Cimento 81A (1984) 79.
  
19. Minehara, E., Yoshida, T., Abe, S., Kanazawa, S., Hanashima, S., Horie, K. and Tsukihashi, Y.  
Proc. of 5th Symposium on Accelerator Science and Technology.  
(1984) 422.
  
20. Mizumoto, M., Nakajima, Y., Ohkubo, M., Sugimoto, M., Furuta, Y. and Kawarasaki, Y.  
Fission Product Nuclear Data Measurements at the JAERI Linac.  
Proc. of the NEANDC Topical Conference on Measurements and Evaluations of Nuclear Data and Decay Heat for Fission Products.  
JAERI-M 84-182 (1984).
  
21. Mizumoto, M., Sugimoto, M. and Shoji, T.  
A 500 % Large Liquid Scintillation Detector for Neutron Capture Cross Section Measurements.  
JAERI-M 84-211 (1984).
  
22. Noda, K., Tanifuji, T., Ishii, Y., Matsui, H., Masaki, N., Nasu, S. and Watanabe, H.  
Irradiation Effects on Lithium Oxide.  
J. Nucl. Mater. 122&123 (1984) 908.



23. Noda, K., Ishii, Y., Matsui, H. and Watanabe, H.  
Irradiation Damage in Lithium Oxide.  
J. Nucl. Mater. 133&134 (1985) in press.
  
24. Ootsuka, A., Fujimoto, F., Komaki, K., Kawatsura, K., Ozawa, K. and Terasawa, M.  
Molecular Effect of Al K $\alpha$  X-Ray Yields from Aluminum Oxide Films for H<sup>+</sup> and H<sub>2</sub><sup>+</sup> Ion Bombardments.  
Phys. Lett. 97A (1983) 191.
  
25. Ootuka, A., Kawatsura, K., Fujimoto, F., Komaki, K., Ozawa, K. and Terasawa, M.  
Single and Double K-Shell Ionization Cross Sections of Beryllium by C, N, O and Ne Ion Bombardments.  
J. Phys. Soc. Jpn. 53 (1984) 1001.
  
26. Ootuka, A., Kawatsura, K., Fujimoto, F., Komaki, K., Ozawa, K. and Terasawa, M.  
Projectile Dependence of KL<sup>L</sup> Vacancy Production Cross Sections of Al by H and He Ion Bombardments.  
J. Phys. Soc. Jpn. 53 (1984) 2215.
  
27. Otsuka, T.  
Independent-Pair Property of Condensed Coherent Fermion Pairs and Derivation of the IBM Quadrupole Operator.  
Phys. Lett. 138B (1984) 1.
  
28. Otsuka, T.  
Microscopically Derived Interacting Boson Model.  
"Capture Gamma-Ray Spectroscopy and Related Topics - 1984"  
S. Raman, Editor (AIP Conference Series No. 125, 1985) p.10.
  
29. Otsuka, T. and Ginocchio, J.N.  
Low-Lying Isovector Collective States and the Interacting Boson Model.  
Phys. Rev. Lett. 54 (1985) 777.

30. Otsuka, T.  
Microscopic Calculation for Deformed Nuclei.  
"Interacting Boson-Boson and Boson-Fermion Systems"  
O. Scholten, Editor (World Scientific, Singapore, 1985) p.3.
  
31. Ozawa, K. and Naramoto, H.  
Ion Beam Analysis on Radiation Damage and Light Impurities at Near  
Surface Region.  
Proc. of 8th Symposium on ISIAT84 (1984) 433.
  
32. Ozawa, K.  
Ion Beam Analysis of Solid Surface by NRA, PIGME and PIXE Methods.  
Proc. of 8th Symposium on ISIAT84 (1984) 503.
  
33. Ozawa, K., Yamaguchi, H., Kawatsura, K., Sataka, M., Kitahara, T.,  
Kikuchi, A., Komaki, K., Ootuka, A. and Fujimoto, F.  
Beam-Foil Interaction of Highly Ionized Chlorine Ions in High Energy  
Region.  
Nucl. Instr. and Meth. B9 (1985) in press.
  
34. Sakamoto, M.  
TOF Neutron Diffraction on Liquid  $\text{CCl}_4$ .  
JAERI-M 84-121 (1984).
  
35. Sakamoto, M.  
TOF Neutron Diffraction on  $\text{PbF}_2$ .  
JAERI-M 84-134 (1984).
  
36. Sakurai, T., Hinatsu, Y., Takahashi, A. and Fujisawa, G.  
Adsorption of Ruthenium Tetroxide on Metal Surfaces.  
J. Phys. Chem. 89 (1985) 1892.
  
37. Sasaki, T.A. and Baba, Y.  
Chemical-State Studies of Zr and Nb Surfaces Exposed to Hydrogen Ions.  
Phys. Rev. B31 (1985) 791.

38. Sasaki, T.A., Baba, Y., Hojou, K. and Aruga, T.  
Transmission Sputtering of Titanium by 114 MeV Fluorine Ions.  
J. Nucl. Mater. 132 (1985) in press.
  
39. Sato, K., Yamaguchi, S., Fujino, Y., Hirabayashi, M., Naramoto, H.,  
Ozawa, K. and Otani, S.  
Deuterium Retention in TiC Crystals Prepared by Chemical Vapor  
Deposition and Floating Zone Methods.  
J. Nucl. Mater. 128&129 (1984) 698.
  
40. Sugiyama, Y., Shikazono, N., Tomita, Y., Ikezoe, H., Tachikawa, T.,  
Takekoshi, E., Kubono, S. and Tanaka, M.  
Measurement of the Spin Alignment in the  $^{12}\text{C} + ^{12}\text{C}$  Inelastic  
Scattering via Recoil.  
Proc. of 1984 INS-RIKEN International Symposium on Heavy Ion Physics,  
Mt. Fuji (1984) 165.
  
41. Sugiyama, Y., Shikazono, N., Tomita, Y., Ikezoe, H., Tachikawa, T. and  
Takekoshi, E.  
Kinematical Correction Capability of JAERI Magnetic Spectrograph  
"ENMA".  
Conference on Instrumentation for Heavy-Ion Nuclear Research, Oak  
Ridge, Tennessee (1984) 67.
  
42. Suzuki, K., Katano, Y., Aruga, T. and Shiraishi, K.  
Miniaturized Target Chamber for 2 MV Van de Graaff Accelerator.  
JAERI-M 84-181 (1984).
  
43. Suzuki, K., Katano, Y., Aruga, T., Hamada, S. and Shiraishi, K.  
Effects of Carbon on Microstructure in Ti-Modified Type 316 Stainless  
Steels Irradiated with Helium Ions.  
J. Nucl. Mater. 133&134 (1985) in Press.
  
44. Takekoshi, E., Sugiyama, Y., Ikezoe, H., Tomita, Y., Shikazono, N.,  
Sawada, M., Nagano, K. and Tachikawa, T.  
A Large Hybrid Focal-Plane Detector with the JAERI Magnetic  
Spectrograph for Heavy-Ion Research.  
Nucl. Instr. and Meth. A (1985) in press.

45. Tsubone, I., Nakajima, Y., Furuta, Y. and Kanda, Y.  
Neutron Total Cross Sections of  $^{181}\text{Ta}$  and  $^{238}\text{U}$  from 24.3 keV to 1 MeV  
and Average Resonance Parameters.  
Nucl. Sci. Eng. 88 (1984) 579.
  
46. Yoshinaga, N., Arima, A. and Otsuka, T.  
A Microscopic Approach to a Foundation of the Interacting Boson Model  
by Using Angular Momentum Projection.  
Phys. Lett. 143B (1984) 5.
  
47. Yugo, S., Kimura, T. and Kazumata, Y.  
A Study on Ion-Irradiation Damage of Graphite Surface.  
Carbon 23 (1985) 147.

## 7.2 Contributions to Scientific and Technical Meetings

1. Aruga, T., Katano, Y., Suzuki, K. and Shiraishi, K.  
Radiation Damage in Vanadium Irradiated with 14 MeV Neutrons (II).  
Fall Meeting of the Japan Institute of Metals in Hiroshima (Oct. 9-11, 1984).
2. Aruga, T., Katano, Y. and Shiraishi, K.  
Effect of Depth Profile of Implanted Helium on Damage Structure in Electron Irradiated Stainless Steel.  
Spring Meeting of the Japan Institute of Metals in Tokyo (Apr. 1-3, 1985).
3. Baba, S., Hata, K., Sekine, T., Ichikawa, S., Shinohara, N., Suzuki, T., Baba, H., Saito, T. and Yokoyama, A.  
Decay of the Compound Nuclei Produced in the Interaction of  $^{197}\text{Au}$  with  $^{16}\text{O}$  and  $^{12}\text{C}$ .  
The 1984 International Chemical Congress of Pacific Basin Societies in Hawaii (Dec. 16-20, 1984).
4. Baba, S., Hata, K., Izumo, M., Motoki, R. and Sekine, T.  
Preparation of  $^{237}\text{Np}$  Irradiated with Deuterons.  
The 1984 International Chemical Congress of Pacific Basin Societies in Hawaii (Dec. 16-20, 1984).
5. Baba, Y. and Sasaki, T.A.  
XPS Observations of Materials Exposed to Hydrogen Ions (III); Surface of Ti and V.  
Fall Meeting of the Atomic Energy Society of Japan in Tokai (Oct. 23-26, 1984).
6. Baba, Y. and Sasaki, T.A.  
Trapping States of Hydrogen Implanted in Metals and Its Dose-Dependences.  
Annual Meeting of the Atomic Energy Society of Japan in Tokyo (Mar. 28-30, 1985).

7. Furuno, S., Izui, K. and Otsu, H.  
Damage Productions through Electron Excitation Process by High Energy Heavy Ion Irradiations.  
Fall Meetings of the Physical Society of Japan in Toyama (Oct. 2-5, 1984).
8. Furuno, S.  
Mechanism for Track Formation in Solid Materials Irradiated with High Energy Heavy Ions.  
The Joint Seminar on Atomic Physics, Solid State Physics and Material Science in the Energy Region of TANDEM Accelerator in Tokai (Jan. 9-11, 1985).
9. Hamada, S., Sawai, T. and Shiraishi, K.  
Measurement of Mean Projected Range for Carbon Ion Irradiated into Stainless Steel.  
Spring Meeting of the Japan Institute of Metals in Tokyo (Apr. 1-3, 1984).
10. Hamada, S., Sawai, T. and Shiraishi, K.  
Measurement of Ranges in Ion Irradiation  
Fall Meeting of the Japan Institute of Metals in Hiroshima (Oct. 9-11, 1984).
11. Hamada, S., Suzuki, K. Sawai, T. and Shiraishi, K.  
Temperature Dependence of Damage Profile in Helium-Irradiated Stainless Steel.  
Fall Meeting of the Japan Institute of Metals in Hiroshima (Oct. 9-11, 1984).
12. Hamada, S., Suzuki, K. and Shiraishi, K.  
Helium-Ion Irradiation Effects Cold-Worked Ti-Modified 316 Stainless Steels.  
Spring Meeting of the Japan Institute of Metals in Tokyo (Apr. 1-3, 1983).

13. Hamada, S., Suzuki, K., Sawai, T. and Shiraishi, K.  
 Temperature Dependence of Damage Profile in Helium-Irradiated  
 Stainless Steel.  
 Fall Meeting of the Japan Institute of Metals in Hiroshima (Oct. 9-11,  
 1984).
  
14. Ichikawa, S., Sekine, T., Hata, K. and Takahashi, N.  
 Experimental Study of Short-Lived Cs and Fr Isotopes by Using ISOL.  
 The 28th Symposium on Radiochemistry in Kobe (Oct. 3-5, 1984).
  
15. Ichikawa, S., Sekine, T., Hata, K., Tamura, T., Minehara, E.,  
 Takahashi, N., Fujiwara, I. and Imanishi, N.  
 A Study of the Decay of  $^{119}\text{Cs}$  Isomers by JAERI ISOL.  
 The 1984 International Chemical Congress of Pacific Basin Societies in  
 Hawaii (Dec. 16-20, 1984).
  
16. Ikezoe, H., Shikazono, N., Tomita, Y., Ideno, K., Sugiyama, Y. and  
 Takekoshi, E.  
 Incomplete Fusion in the  $^{16}\text{O} + ^{27}\text{Al}$  Reaction at 150 MeV.  
 Tsukuba International Symposium on Heavy-Ion Fusion Reaction (Sept.  
 3-5, 1984).
  
17. Ikezoe, H., Shikazono, N., Tomita, Y., Ideno, K., Sugiyama, Y. and  
 Takekoshi, E.  
 Measurements of Incomplete Fusion in the  $^{16}\text{O} + ^{27}\text{Al}$  Reaction.  
 Fall Meeting of the Physical Society of Japan in Mito (Sept. 29 - Oct.  
 2, 1984).
  
18. Ikezoe, H., Shikazono, N., Tomita, Y., Sugiyama, Y., Ideno, K.,  
 Takekoshi, E., Tachikawa, T. and Nomura, T.  
 Measurements of the  $^{16}\text{O}$  on  $^{12}\text{C}$  Fusion Reaction.  
 Annual Meeting of the Physical Society of Japan in Kyoto (Mar. 31 -  
 Apr. 3, 1985).
  
19. Iwamoto, A. and Harada, K.  
 Effect of the Coulomb Excitation on the Sub-Barrier Fusion Reaction.  
 Spring Meeting of the Physical Society of Japan in Fukuoka (Apr. 1-4,  
 1984).

20. Iwamoto, A. and Harada, K.  
 Effect of the Neck Formation on the Sub-Barrier Fusion Reaction.  
 Fall Meeting of the Physical Society of Japan in Mito (Sep. 29 - Oct.  
 2, 1984).
  
21. Iwase, A., Sasaki, S., Iwata, T. and Nihira, T.  
 Electrical Resistivity Changes and Defect Production Cross Sections in  
 Aluminum for Energetic Heavy Ion Irradiations.  
 Spring Meeting of the Physical Society of Japan in Fukuoka (Apr. 1-4,  
 1984).
  
22. Iwase, A., Sasaki, S., Iwata, T. and Nihira, T.  
 Defect Production by Energetic Heavy Ions in Several Metals.  
 First International Conference on Fusion Reactor Materials in Tokyo  
 (Dec. 3-6, 1984).
  
23. Iwase, A.  
 Calorimetric Measurements of Stopping Power for  $^{35}\text{Cl}$  and  $^{12}\text{C}$  Ions in  
 Al and Ni.  
 The Joint Seminar on Atomic Physics, Solid State Physics and Material  
 Science in the Energy Region of TANDEM Accelerator in Tokai (Jan.  
 9-11, 1985).
  
24. Iwase, A.  
 Defect Production by Energetic Heavy Ions in Al and Cu.  
 The Joint Seminar on Atomic Physics, Solid State Physics and Material  
 Science in the Energy Region of TANDEM Accelerator in Tokai (Jan.  
 9-11, 1985).
  
25. Iwase, A., Sasaki, S., Iwata, T. and Nihira, T.  
 Defect Production and Recovery in FCC Metals Irradiated with Energetic  
 Heavy Ions.  
 Spring Meeting of the Physical Society of Japan in Kyoto (Mar. 31-Apr.  
 3, 1985).



26. Katano, Y., Aruga, T., Suzuki, K., Nakata, K. and Shiraiishi, K.  
Effect of Nitrogen on Secondary Defects in N-Ion Irradiated  
Stainless Steel.  
Fall Meeting of the Japan Institute of Metals in Hiroshima (Oct. 9-11,  
1984).
  
27. Katano, Y., Nakata, K., Aruga, T., Suzuki, K. and Shiraishi, K.  
Effect of Nitrogen Injection on Depth Profile of Damage Structure in  
Stainless Steel.  
Fall meeting of the Japan Institute of Metals in Hiroshima (Oct. 9-11,  
1984).
  
28. Katano, Y., Aruga, T. and Shiraishi, K.  
Helium Bubble Behavior in Electron Irradiated Stainless Steel after  
Helium Implantation.  
Spring Meeting of the Japan Institute of Metals in Tokyo (Apr. 1-3,  
1985).
  
29. Kazumata, Y., Yugo, S. and Kimura, T.  
ESR of Pyrolytic Graphite Irradiated by Ions.  
The Joint Seminar on Atomic Physics, Solid State Physics and Material  
Science in the Energy Region of TANDEM Accelerators in Tokai  
(Jan. 9-11, 1985).
  
30. Kikuchi, A., Naramoto, H. and Ozawa, K.  
Depth Distribution of Radiation Damage by High-Energy Heavy Ions in  
Alkali Halides.  
Fall Meeting of the Physical Society of Japan in Toyama (Oct., 2-5,  
1984).
  
31. Kikuchi, A., Naramoto, H. and Ozawa, K.  
Depth Distribution of Radiation Damage by High-Energy Heavy Ions in  
Alkali Halides (II).  
Spring Meeting of the Physical Society of Japan in Kyoto (Mar.31 -  
Apr.3, 1985).

32. Kuroda, K., Saka, H., Imura, T., Noda, K., Ishii, Y. and Watanabe, H.  
Electron Microscopic Observation of Defects in  $\text{Si}_3\text{N}_4$ .  
Fall Meeting of the Japan Institute of Metals in Hiroshima (Oct. 9-11, 1984).
  
33. Makishima, A., Ishii, M., Kohno, T., Adachi, M. and Taketani, H.  
Nuclear Structure of  $^{136,138}\text{Sm}$ .  
Fall Meeting of the Physical Society of Japan in Mito (Sept. 29 - Oct. 2, 1984).
  
34. McHargue, C.J., Farlow, G.C., White, C.W., Appleton, B.R., Angelini P. and Naramoto, H.  
The Structure and Properties of Ion-Implanted  $\text{Al}_2\text{O}_3$ .  
8th Conf. on the Application of Accelerators in Research and Industry in Denton (Nov. 1-3, 1984)
  
35. McHargue, C.J., Farlow, G.C., Farlow, G.C., White, C.W., Williams J.M., Appleton, B.R. and Naramoto, H.  
The Amorphization of Ceramics by Ion Beams.  
Inter. Conf. on Surface Modification of Metals by Ion Beams in Heidelberg (Sept. 17-21, 1984).
  
36. Mizumoto, M., Sugimoto, M. and Shoji, T.  
A Gamma-Ray Response Function of a 500 % Liquid Scintillator for Neutron Cross Section Measurements.  
Fall Meeting of the Atomic Energy Society of Japan in Tokai (Oct. 23-26, 1984).
  
37. Naramoto, H.  
Ion-Implanted Ceramics.  
25th Symp. on Lattice Defects in Toyama (Oct. 6, 1984).
  
38. Noda, K., Ishi, Y. and Watanabe, H.  
Optical Absorption Spectra of Oxygen Ion Irradiated  $\text{Li}_2\text{O}$ .  
Fall Meeting of the Atomic Energy Society of Japan in Tokai (Oct. 23-26, 1984).

39. Noda, K., Ishi, Y., Matsui, H. and Watanabe, H.  
Irradiation Damage in Lithium Oxide.  
1st International Conference on Fusion Reactor Materials in Tokyo  
(Dec. 3-6, 1984).
  
40. Noda, K., Ishi, Y., Matsui, H. and Watanabe, H.  
Irradiation Effect of  $\text{Li}_2\text{O}$  with High Energy Oxygen Ions.  
The Joint Seminar on Atomic Physics, Solid State Physics and Material  
Science in the Energy Region of TANDEM Accelerator in Tokai (Jan.  
9-11, 1985).
  
41. Ootuka, A., Komaki, K., Fujimoto, F., Kawatsura, K., Ozawa, K. and  
Terasawa, M.  
Molecular Effect of O and Al K $\alpha$  X-Ray Yields from  $\text{Al}_2\text{O}_3$  Films for  $\text{H}^+$   
and  $\text{H}_2^+$  Ions.  
Intern. Conf. on X-Ray and Inner-Shell Processes in Atoms, Molecules  
and Solids in Leipzig (Aug. 20-24, 1984).
  
42. Otsuka, T.  
Microscopic Calculation for Deformed Nuclei.  
International Workshop on Interacting Boson-Boson and Boson-Fermion  
Systems in Gull Lake (May 28-30, 1984).
  
43. Otsuka, T.  
Invited Discussions on the Interacting Boson Model.  
East Coast Summer Physics Center in Lewis (June 15-28, 1984).
  
44. Otsuka, T.  
Microscopically Derived Interacting Boson Model.  
Fifth International Conference on Capture Gamma-Ray Spectroscopy and  
Related Topics in Knoxville (Sept. 10-14, 1984).
  
45. Otsuka, T.  
Low-Lying Isovector Collective States and the Interacting Boson Model.  
International Symposium on the Nuclear Shell Model in Philadelphia  
(Oct. 29 - Nov. 1, 1984).

46. Ozawa, K., Yamaguchi, H., Kawatsura, K., Sataka, M., Kitahara, T., Kikuchi, A., Komaki, K., Ootuka A. and Fujimoto, F.  
Beam-Foil Interaction of Highly Ionized Chlorine Ions in High Energy Region.  
International Conference on Physics of Highly Ionized Atoms in Oxford (July 2-6, 1984)
  
47. Ozawa, K. and Naramoto, H.  
Ion Beam Analysis on Radiation Damage and Light Impurities at Near Surface Region.  
8th Symp. on Ion Sources and Ion-Assisted Technology in Tokyo (June 4-6, 1984).
  
48. Ozawa, K.  
Ion Beam Analysis of Solid Surface by NRA, PIGME and PIXE Methods.  
8th Symp. on Ion Sources and Ion-Assisted Technology in Tokyo (June 4-6, 1984).
  
49. Sakai, E.  
Induced Radioactivities in Various Materials for Solid-State Physics Research Irradiated with High-Energy Heavy Ions.  
The 21st Annual Meeting on Radioisotopes in the Physical Sciences and Industry, in Tokyo (July 4, 1984).
  
50. Sasaki, T.A., Baba, Y., Hojou, K. and Aruga, T.  
Transmission Sputtering of Ti by High-Energy Heavy Ions.  
Fall Meeting of the Atomic Energy Society of Japan in Tokai (Oct. 23-26, 1984).
  
51. Sasaki, T.A. and Baba, Y.  
XPS Observations of Materials Exposed to Hydrogen Ions (IV); Changes in Chemical Composition of SiC, Si<sub>3</sub>N<sub>4</sub> and SiO<sub>2</sub>.  
Annual Meeting of the Atomic Energy Society of Japan in Tokyo (Mar. 28-30, 1985).

52. Sataka, M., Ozawa, K., Kawatsura, K., Masai, K., Ishii, K., Ootuka, A., Komaki, K., Fujimoto, F., Kikuchi, A. and Kitahara, T.  
Beam-Foil Spectroscopy of Multi-Charged Chlorine Ions.  
Fall Meeting of the Physical Society of Japan in Toyama (Oct. 2-5, 1984).
  
53. Sataka, M.  
Beam-Foil Spectroscopy at JAERI Tandem.  
The Joint Seminar on Atomic Physics, Solid State Physics and Material Science in the Energy Region of TANDEM Accelerator in Tokai (Jan. 9-11, 1985).
  
54. Sato, K., Fujino, Y., Yamaguchi, S., Naramoto, H., Ozawa, K. and Hirabayashi, M.  
Deuterium Retention in C-Implanted TiC Single Crystal.  
6th Int. Conf. on Plasma Surface Interactions in Controlled Fusion Devices in Nagoya (May 14-18, 1984).
  
55. Sekine, T., Baba, S., Hata, K., Ichikawa, S. and Shinohara, N.  
Formation and Decay of  $^{105}\text{Ag}$  Compound Nuclei (2) the  $^{37}\text{Cl}+^{68}\text{Zn}$  Reaction.  
The 28th Symposium on Radiochemistry in Kobe (Oct. 3-5, 1984).
  
56. Shinohara, N., Ichikawa, S., Suzuki, T., Usuda, S., Okashita, H., Sekine, T., Hata, K., Horiguchi, T., Yoshizawa, Y., Shibata, S. and Fujiwara, I.  
A Study of Transuranium Elements from Interaction of  $^{16}\text{O}$  with  $^{238}\text{U}$ .  
The 28th Symposium on Radiochemistry in Kobe (Oct. 3-5, 1984).
  
57. Shinohara, N., Ichikawa, S., Usuda, S., Suzuki, T., Okashita, H., Sekine, T., Hata, K., Horiguchi, T., Yoshizawa, Y., Shibata, S. and Fujiwara, I.  
Synthesis of Transuranium Nuclides from Interaction of  $^{16}\text{O}$  with  $^{238}\text{U}$ .  
The 1984 International Chemical Congress of Pacific Basin Societies in Hawaii (Dec. 16-20, 1984).

58. Shiraishi, K.  
Radiation Damage in High-Energy-Ion Irradiated Stainless Steel.  
The Joint Seminar on Atomic Physics, Solid State Physics and Material  
Science in the Energy Region of TANDEM Accelerator in Tokai (Jan.  
9-11, 1985).
  
59. Suzuki, K., Katano, Y., Aruga, T. and Shiraishi, K.  
Microstructure of Ti-Modified Type 316 Stainless Steel Irradiated with  
1 MeV He Ions.  
Fall Meeting of the Japan Institute of Metals in Akita (Oct. 4-6,  
1983).
  
60. Suzuki, K., Katano, Y., Aruga, T., Hamada, S. and Shiraishi, K.  
Microstructure of Ti-Modified Type 316 Stainless Steel Irradiated with  
He Ions (II).  
Spring Meeting of the Japan Institute of Metals in Narashino (Apr.  
1-3, 1984).
  
61. Suzuki, K., Katano, Y., Aruga, T., Hamada, S. and Shiraishi, K.  
Microstructure of Ti-Modified Type 316 Stainless Steel Irradiated with  
He Ions (III).  
Fall Meeting of the Japan Institute of Metals in Hiroshima (Oct. 9-11,  
1984).
  
62. Suzuki, K., Katano, Y., Aruga, T., Hamada, S. and Shiraishi, K.  
Effects of Carbon on Microstructure in Ti-Modified Type 316 Stainless  
Steels Irradiated with Helium Ions.  
First International Conference on Fusion Reactor Materials in Tokyo  
(Dec. 3-6, 1984).
  
63. Yamanouti, Y., Sugimoto, M., Tanaka, S., Hyakutake, M., Furuta, Y. and  
Mizumoto, M.  
 $^{28}\text{Si}(n,n)$  and  $(n,n')$  Reactions at  $E_n=12.8$  MeV.  
Spring Meeting of the Physical Society of Japan in Fukuoka (Apr. 1-4,  
1984).

64. Yokota, T., Taji, Y. and Iwata, T.  
Molecular Dynamic Simulation of Point Defects Formation.  
Spring Meeting of the Physical Society of Japan in Kyoto (Mar. 31-  
Apr. 3, 1985).
  
65. Yokota, W., Ideno, K., Ogihara, M., Komatsubara, T., Nakagawa, T.,  
Fukuchi, Y., Nagashima, Y., Furuno, K., Lee, S.M., Mikumo, T., Tomita,  
Y., Ikezoe, H., and Hanashima, S.  
Fission-like Reaction in the System of  $^{37}\text{Cl} + ^{48}\text{Ti}$ .  
Fall Meeting of the Physical Society of Japan in Mito (Sep. 29- Oct.  
2, 1984).
  
66. Yokoyama, A., Baba, H., Saito, T., Shinohara, A., Shoji, M., Baba, S.,  
Hata, K., Sekine, T., Ichikawa, S., Nagame, Y., Fujiwara, I. and  
Imanishi, N.  
Nucleon Transfer Reaction of  $^{197}\text{Au}$  Induced by Heavy Ions.  
The 28th Symposium on Radiochemistry in Kobe (Oct. 3-5, 1984).
  
67. Yokoyama, A., Baba, H., Saito, T., Shinohara, A., Baba, S., Hata, K.,  
Sekine, T., Ichikawa, S., Nagame, Y., Fujiwara I. and Imanishi, N.  
Nucleon Transfer in the Heavy-Ion Reactions of Gold.  
The 1984 International Chemical Congress of Pacific Basin Societies in  
Hawaii (Dec. 16-20, 1984).
  
68. Usuda, S., Shinohara, N. and Okashita, H.  
Anion Exchange Behavior of Transplutonium Elements in Mineral Acid -  
Aqueous Alcohol Mixed Solvents.  
The 28th Symposium on Radiochemistry in Kobe (Oct. 3-5, 1984).

## VIII PERSONNEL AND COMMITTEES



## 8.1 Personnel

## Department of Physics

Kichinosuke Harada	Director
Yoichi Suto	Administrative Manager

## Accelerators Division

Scientific Staff	Michio Maruyama <sup>*</sup>
	Yuuki Kawarasaki ( - September 1984)
	Shiro Kikuchi
	Suehiro Takeuchi
	Eisuke Minehara
	Susumu Hanashima
Technical Staff	Chiaki Kobayashi <sup>**</sup>
(Tandem, V.D.G.)	Isao Ohuchi
	Yutaka Sato
	Tadashi Yoshida
	Susumu Kanda
	Katsuzo Horie
	Satoshi Tajima
	Yoshihiro Tsukihashi
	Shinichi Abe
	Shuhei Kanazawa
Technical Staff	Katuo Mashiko <sup>**</sup>
(Linac)	Nobuyoshi Akiyama
	Yukio Nobusaka
	Tokio Shoji
	Nobuhiro Ishizaki

## Nuclear Physics Laboratory

Scientific Staff	Naomoto Shikazono <sup>***</sup>
	Eiko Takekoshi
	Mitsuhiko Ishii

\* Head, Accelerators Division

\*\* Leader, Technical Staff

\*\*\* Deputy Director, Department of Physics and Head of Nuclear Physics Laboratory

## Nuclear Physics Laboratory (continued)

Scientific Staff	Yoshiaki	Tomita
	Yasuharu	Sugiyama
	Akira	Iwamoto
	Kazumi	Ideno
	Hiroshi	Ikezoe
	Masumi	Ohshima
	Takaharu	Ohtsuka
Scholarship Fellow	Toshiki	Tachikawa (Kyushu University)

## Linac Laboratory

Scientific Staff	Shigeya	Tanaka <sup>*</sup>	( - September 1984)
	Yuuki	Kawarasaki <sup>*</sup>	(October 1984 - )
	Yutaka	Furuta	
	Makio	Ohkubo	
	Yutaka	Nakajima	
	Motoharu	Mizumoto	
	Yoshimaro	Yamanouchi	
	Masayoshi	Sugimoto	
Scholarship Fellow	Susumu	Nishihara (Tohoku University)	

## Solid State Physics Laboratory I

Scientific Staff	Kazuo	Gesi <sup>**</sup>
	Yukio	Kazumata
	Hiroshi	Naramoto
	Hiroshi	Tomimitsu

## Solid State Physics Laboratory II

Scientific Staff	Tadao	Iwata <sup>***</sup>
	Saburo	Takamura
	Hiroshi	Maeda
	Shigemi	Sasaki
	Akihiro	Iwase
	Terufumi	Yokota

\* Head, Linac Laboratory

\*\* Head, Solid State Physics Laboratory I

\*\*\* Head, Solid State Physics Laboratory II

## Solid State Physics Laboratory III

Scientific Staff	Masanobu	Sakamoto
------------------	----------	----------

## Atomic and Molecular Physics Laboratory

Scientific Staff	Kunio	Ozawa *
	Yohta	Nakai
	Kiyoshi	Kawatsura
	Masao	Sataka
Scholarship Fellow	Kuniaki	Masai (Nagoya University)

## Department of Chemistry

## Nuclear Chemistry Laboratory

Scientific Staff	Hiroshi	Okashita **
	Toshio	Suzuki
	Shigekazu	Usuda
	Nobuaki	Kono
	Shin-ichi	Ichikawa
	Nobuo	Shinohara
Scholarship Fellow	Hideki	Yoshikawa (Tokyo Metropolitan University)

## Analytical Chemistry Laboratory

Scientific Staff	Yuji	Baba
------------------	------	------

## Physical Chemistry Laboratory

Scientific Staff	Mutsuhide	Komaki
------------------	-----------	--------

## Solid State Chemistry Laboratory

Scientific Staff	Kazuhiko	Izui ***
	Shin-ichi	Ohno
	Teikichi	Sasaki
	Shigemi	Furuno
	Hitoshi	Ohtsu
	Kiichi	Hojou

\* Head, Atomic and Molecular Physics Laboratory

\*\* Head, Nuclear Chemistry Laboratory

\*\*\* Head, Solid State Chemistry Laboratory

Department of Radioisotope Production

Production Development Division

Scientific Staff	Sumiko	Baba
	Kentaro	Hata
	Toshiaki	Sekine
	Yuichiro	Nagame

Department of Fuels and Materials Research

Scientific Staff	Kensuke	Shiraishi
------------------	---------	-----------

Physical Metallurgy Laboratory

Scientific Staff	Akimichi	Hishinuma <sup>*</sup>
	Takeo	Aruga
	Shozo	Hamada
	Tomotsugu	Sawai
	Kenji	Suzuki
	Yoshio	Katano
	Katsumaro	Fukai

Fuel Property Laboratory

Scientific Staff	Hitoshi	Watanabe <sup>**</sup>
	Kenji	Noda
	Yoshinobu	Ishii

Function Materials Laboratory

Scientific Staff	Hiroji	Katsuta <sup>***</sup>
	Hideo	Ohno
	Takanori	Nagasaki

Department of Reactor Engineering

Reactor Instrumentation Laboratory

Scientific Staff	Eiji	Sakai
------------------	------	-------

\* Head, physical Metallurgy Laboratory

\*\* Head, Fuel Property laboratory

\*\*\* Head, Function materials Laboratory

Department of Health Physics

Technical Staff	Shoji	Izawa <sup>*</sup>
	Toshihiro	Miyamoto
	Takeo	Seki

\* Chief of Radiation Control Group, Department of Health Physics

## 8.2 Tandem Steering Committee

(Chairman)	Manabu	Katsuragi	(Deputy Director General, Tokai Research Establishment)
	Takumi	Asaoka	(Director, Department of Reactor Engineering)
	Kazumi	Iwamoto	(Director, Department of Fuels and Materials Research)
	Kichinosuke	Harada	(Director, Department of Physics)
	Kaoru	Ueno	(Director, Department of Chemistry)
	Yukio	Obata	(Director, Department of Thermonuclear Fusion Research)
	Toshihiko	Abe	(Director, Department of Radioisotope Production)
(Secretary)	Naomoto	Shikazono	(Deputy Director, Department of Physics)
(Secretary)	Michio	Maruyama	(Head, Accelerators Division)
(Secretary)	Yoichi	Suto	(Administrative Manager, Department of Physics)

## 8.3 Tandem Consultative Committee

(Chairman)	Tetsuo	Aochi	(Executive Director)
(Vice Chairman)	Manabu	Katsuragi	(Deputy Director General, Tokai Research Establishment)
(Vice Chairman)	Kichinosuke Harada		(Director, Department of Physics)
	Hiromichi Kamitsubo		(Principal Scientist, Institute of Physical and Chemical Research)
	Kōzi	Nakai	(Professor, National Laboratory for High Energy Physics)
	Hiroyasu Ejiri		(Professor, Osaka University)
	Shiori Ishino		(Professor, University of Tokyo)
	Nobuo Oda		(Professor, Tokyo Institute of Technology)
	Kohzoh	Masuda	(Professor, University of Tsukuba)
	Shiro	Iwata	(Professor, Kyoto University)
	Ichiro	Fujiwara	(Associate Professor, Kyoto University)
	Kenji	Sumita	(Professor, Osaka University)
	Itsuro	Kimura	(Professor, Kyoto University)
(Secretary)	Naomoto	Shikazono	(Deputy Director, Department of Physics)
(Secretary)	Michio	Maruyama	(Head, Accelerators Division)
(Secretary)	Yoichi	Suto	(Administrative Manager, Department of Physics)

## 8.4 Tandem Program Advisory Committee

(Chairman)	Kichinosuke	Harada	(Director, Department of Physics)
	Hirokazu	Umezawa	(Senior Staff, Office of Planning)
	Shoji	Izawa	(Chief, Radiation Control Group, Department of Health Physics)
	Hitoshi	Watanabe	(Head, Fuel Property Laboratory, Department of Fuels and Materials Research)
	Hiroshi	Okashita	(Head, Nuclear Chemistry laboratory, Department of Chemistry)
	Kunio	Ozawa	(Head, Atomic and Molecular Physics Laboratory, Department of Physics)
	Naomoto	Shikazono	(Deputy Director, Department of Physics)
	Yuuki	Kawarasaki	(Head, Linac Laboratory, Department of Physics)
	Michio	Maruyama	(Head, Accelerators Division, Department of Physics)
	Chiaki	Kobayashi	(Leader, Tandem Operation Group, Department of Physics)



## IX CO-OPERATIVE RESEARCHES

Title	Co-Operating Institution
2.1 Beam-Foil Spectra of Chlorine Ions in High Energy Region (II)	College of General Education, University of Tokyo <sup>*</sup> Department of Engineering Science, Kyoto University Faculty of Engineering, Ibaraki University <sup>*</sup>
2.2 Ion Beam Analysis on Nb-Mo Alloy with Energetic Heavy Ions	Department of Nuclear Engineering, Tohoku University <sup>*</sup>
2.3 Defect Production and Recovery in Copper Irradiated with Energetic Ions	Faculty of Engineering, Ibaraki University <sup>*</sup>
2.7 Molecular Effect of O and Al K $\alpha$ X-Ray Yields from Al <sub>2</sub> O <sub>3</sub> Films for H <sup>+</sup> and H <sub>2</sub> <sup>+</sup> Ions	College of General Education, University of Tokyo <sup>*</sup>
2.8 Deuterium Retention in TiC Crystals Prepared by Zone Melting Methods	Department of Nuclear Engineering, Tohoku University <sup>*</sup>
2.11 Electron Capture and Loss Cross Sections for 300 keV to 1.50 MeV Carbon Atoms in Collision with Helium	Faculty of Engineering, Ibaraki University <sup>*</sup>
3.1 Irradiation Effects with Heavy Ions on Alkali Halides (II)	Faculty of Engineering, Ibaraki University <sup>*</sup>
3.2 Irradiation Damage in Lithium Oxide	Faculty of Engineering, Nagoya University <sup>*</sup>
3.4 Residual Radioactivities in Silicon and Germanium Irradiated with Various High-Energy Heavy-Ions	Faculty of Engineering, Toyama University <sup>*</sup>

- |  |  |
|--|--|
| 3.6 Radiation Damage of Materials<br>Ion-Irradiated at Low Temperature   | Faculty of Engineering, Ibaraki<br>University*   |
| 3.8 TEM Observation of Cascade Damage<br>Structure in Pure Nickel  | Department of Nuclear Engineering,<br>University of Tokyo*   |
| 3.9 Irradiation Induced Defects of Dual<br>Phase (Austenite and Ferrite;<br>Duplex) Stainless Steel                                  | Department of Materials Science,<br>University of Tokyo*   |
| 3.14 Damage Structure in Ion-Irradiated<br>$\text{Si}_3\text{N}_4$   | Faculty of Engineering, Nagoya<br>University*  |
| 4.1 Nuclear Chemistry of Actinoids<br>(III) $^{16}\text{O} + ^{238}\text{U}$ and $^{12}\text{C} + ^{242}\text{Pu}$<br>Reactions      | Department of Physics, Hiroshima<br>University*<br>Institute of Atomic Energy, Kyoto<br>University*<br>Institute for Nuclear Study,<br>University of Tokyo |
| 4.2 Decay of the Compound Nuclei<br>Produced in the Reactions of $^{197}\text{Au}$<br>Induced by $^{16}\text{O}$ and $^{12}\text{C}$ | Institute of Atomic Energy, Kyoto<br>University*<br>Faculty of Science, Osaka University*  |
| 4.3 Nucleon Transfer Reaction of Gold<br>Induced by Heavy Ions   | Institute of Atomic Energy, Kyoto<br>University*<br>Faculty of Science, Osaka University*  |
| 4.4 A Study of the Decay of $^{121}\text{Ba}$  | Faculty of Science, Osaka University   |
| 5.1 Studies of Nuclei with Proton and<br>Neutron Numbers of 50 to 82   | Department of Applied Physics, Tokyo<br>Institute of Technology*   |
| 5.2 Inclusive and Coincidence Measure-<br>ments for Strongly Damped Reactions<br>in the System $^{37}\text{Cl} + ^{48}\text{Ti}$     | Tandem Accelerator Center, University<br>of Tsukuba*   |

- |     |   |  |
|-----|---|--|
| 5.3 | Magnetic Substate Population in<br>$^{12}\text{C} + ^{12}\text{C}$ Inelastic Scattering | Institute for Nuclear Study,<br>University of Tokyo* |
| 5.5 | A Study of Limiting Angular Momenta<br>in Fusion Reaction                               | Institute for Nuclear Study<br>University of Tokyo*  |
| 6.1 | Scattering of 12.8 MeV Neutrons<br>from $^{28}\text{Si}$                                | Faculty of Engineering, Kyushu<br>University*        |
| 6.2 | Measurements of Fast Neutron<br>Scattering Cross Sections of<br>Alumium                 | Faculty of Engineering, Kyushu<br>University*        |

\* Travel expense is supplied by JAERI.